D 2022

U.PORTO
FEUP FACULDADE DE ENGENHARIA
UNIVERSIDADE DO PORTO

DEVELOPMENT OF NEW METHODOLOGIES FOR STRUCTURAL MONITORING OF WIND FARMS

JOÃO MIGUEL SOUSA PACHECO

DOCTORAL THESIS IN CIVIL ENGINEERING
PRESENTED TO THE FACULTY OF ENGINEERING
OF THE UNIVERSITY OF PORTO

U.PORTO
FEUP FACULDADE DE ENGENHARIA
UNIVERSIDADE DO PORTO

DEVELOPMENT OF NEW METHODOLOGIES FOR STRUCTURAL MONITORING OF WIND FARMS

João Miguel Sousa Pacheco

July 2022

Dissertation submitted to the Faculty of Engineering of the University of Porto in fulfilment of the requirements for the degree of Doctor of Civil Engineering

Supervisor: Filipe Magalhães (Associate Professor, FEUP)
Co-Supervidor: Álvaro Cunha (Full professor, FEUP)

REPÚBLICA PORTUGUESA | CIÊNCIA, TECNOLOGIA E ENSINO SUPERIOR
FCT Fundação para a Ciência e a Tecnologia
NORTE2020
POCH
PORTUGAL 2020
UNIÃO EUROPEIA Fundo Social Europeu

"A viagem não acaba nunca. Só os viajantes acabam. E mesmo estes podem prolongar-se em memória, em lembrança, em narrativa. Quando o visitante sentou na areia da praia e disse: "Não há mais o que ver", saiba que não era assim. O fim de uma viagem é apenas o começo de outra. É preciso ver o que não foi visto, ver outra vez o que se viu já, ver na primavera o que se vira no verão, ver de dia o que se viu de noite.... É preciso voltar aos passos que foram dados, para os repetir, e para traçar caminhos novos"

(in "Viagem a Portugal", José Saramago)

À memória do meu Pai e

à minha Mãe e Irmã

ABSTRACT

Wind energy is currently considered one of the most promising sources of renewable and clean energy. It is generally accepted that wind energy is a key element in the energy strategy of the actual economies, having registered a truly remarkable evolution in the last two decades. This evolution, practically on a worldwide scale, is verified in terms of installed capacity, as well as in terms of technological evolution. In 2016, wind become the second largest form of power generation capacity in the European Union. It is foreseeable that installed capacity will continue to increase in the coming years. Accompanying the increase of installed wind power capacity, the new wind turbines have also continuously grown in size and output, mainly motivated by economic aspects. As result of this rapid growth, new challenges have arisen at the same time and other ones that will arise in the coming years can be predict. Among them, the cost of energy production, the management of the wind energy assets at the end of their operational lifetime and the limited technical knowledge at design phase stand out in this work.

In that sense, the management of these assets can strongly benefit from the development of cost effective monitoring strategies. A vibration-based structural monitoring system integrated into a preventive maintenance strategy and capable of evaluating the condition of structural elements, such as foundation, tower and blades, is seen as a suitable response to address the mentioned challenges. The reduction of the *Levelized Cost of Energy* (optimizing operation and maintenance strategies and reducing insuring costs by reducing the operation risk through monitoring), the extension of the lifespan of existing wind turbines components (monitoring the evolution of asset wear and defining repair strategies) and the better acquaintance of the structural behaviour of turbines (optimizing the design of the structures), will certainly contribute to increase the competitiveness of this energy source.

Therefore, the first part of this thesis describes the main results obtained with alternative instrumentation strategies tested in a 2.0 MW onshore wind turbine (Torrão Wind Farm) to reduce the costs of the monitoring equipment and at the same time ensure an adequate accuracy in structural condition evaluation. The data processing strategy encompasses the use of operational modal analysis combined with algorithms that deal with the particularities of operation of the wind turbines to continuously track the main vibration modes. After this automated online identification, the influence of the environmental and operating conditions on the tracked natural frequencies is mitigated, making the detection of abnormal variations of the natural frequencies possible, which might flag the appearance of damage. A database of continuously collected acceleration time series during one year is adopted to test the efficiency of alternative monitoring system layouts in detecting simulated damage scenarios. The tested alternative monitoring layouts present a varying number of sensors, alternative distributions in the wind turbine tower, and different sensor noise levels (to replicate

sensors with different costs). Finally, the work also includes the definition of optimized architectures that allow the earlier damage detection, considering different budgets.

Afterwards, this thesis is focused on the development, implementation, validation and optimization of new monitoring strategies to be applied at the level of the wind farm for evaluation of the consumed fatigue life of the main structural components. These are based on the use of optimized instrumentation layouts at a subgroup of wind turbines, taking profit from the data provided by the SCADA system already available in all wind turbines, for the application of extrapolation techniques to assess all the wind turbines of the same wind farm.

In this context, an experimental campaign was implemented at Tocha Wind Farm, an onshore wind farm located in Portugal. This extensive experimental campaign includes the simultaneous instrumentation of two wind turbines (loaded by winds with different turbulence intensities motivated by the neighbouring turbines), adopting strain gauges, clinometers and accelerometers distributed in the tower and blades. Throughout this program, a database was collected during more than two years. This pioneering experimental setup allowed the following achievements: implementation and validation of algorithms for the evaluation of the consumed fatigue life of tower and blades based on the direct measurement of the strains; development of tools to extrapolate the accumulated fatigue damage identified in the monitored period to the full life of the wind turbine; and algorithms to extrapolate fatigue results obtained for instrumented wind turbines to non-instrumented wind turbines of the same farm. A deep analysis of the experimental results permitted to characterize the effect of wind wakes on fatigue consumption in both tower and blades.

Keywords: Wind Energy, Wind Turbines, Structural Monitoring, Operational Modal Analysis, Damage Detection, Fatigue Analysis, Farm-wide Fatigue Assessment.

RESUMO

A energia eólica é considerada atualmente uma das fontes mais promissoras de energia verde e renovável. É amplamente aceite que a energia eólica é um elemento chave na estratégia energética das atuais economias, tendo registado uma evolução verdadeiramente notável nas últimas duas décadas. Esta evolução, praticamente à escala mundial, verifica-se em termos de capacidade instalada, bem como em termos de evolução tecnológica. Em 2016, o vento tornou-se a segunda maior forma de capacidade de geração de energia na União Europeia. Prevê-se que a capacidade instalada continue a aumentar nos próximos anos. Acompanhando o aumento da capacidade eólica instalada, os novos aerogeradores têm continuamente aumentado em termos de tamanho e potência, motivados principalmente por aspetos económicos. Como resultado deste rápido crescimento, surgiram novos desafios, sendo que outros que irão surgir nos próximos anos podem ser conjeturados. Entre os quais se destacam, neste trabalho, o custo de produção de energia, a gestão dos ativos eólicos no final de sua vida útil e o conhecimento técnico limitado na fase de projeto.

Nesse sentido, a gestão destes ativos pode fortemente beneficiar do desenvolvimento de estratégias de monitorização de baixo custo. Um sistema de monitorização estrutural baseado em vibrações, integrado numa estratégia de manutenção preventiva e capaz de avaliar o estado de elementos estruturais, como fundação, torre e pás, é considerado como uma resposta adequada para enfrentar os desafios mencionados anteriormente. A redução do *Levelized Cost of Energy* (otimizando as estratégias de operação e manutenção e reduzindo os custos dos seguros reduzindo o risco de operação através da monitorização), o prolongamento da vida útil dos componentes dos aerogeradores existentes (acompanhando a evolução do desgaste dos ativos e definindo estratégias de reparação) e o melhor conhecimento do comportamento estrutural dos aerogeradores (otimizando o projeto das estruturas), certamente contribuirá para aumentar a competitividade desta fonte de energia.

Desta forma, a primeira parte da presente tese dedicada à pesquisa original descreve os principais resultados obtidos com estratégias alternativas de instrumentação testadas em um aerogerador onshore de 2,0 MW (Parque Eólico do Torrão) com o objetivo de reduzir os custos do equipamento de monitorização, garantindo ao mesmo tempo precisão adequada na avaliação condição estrutural. Uma base de dados de séries temporais de aceleração continuamente medidas durante um ano é utilizado para testar a eficiência de layouts alternativos de sistemas de monitorização na deteção de cenários de danos simulados. Os layouts alternativos de monitorização testados apresentam número variável de sensores, distribuições alternativas na torre do aerogerador e diferentes níveis de ruído do sensor (a fim de simular sensores com diferentes custos). Por fim, o presente trabalho inclui também a definição de arquiteturas otimizadas que permitem a deteção precoce de danos, considerando diferentes orçamentos.

Posteriormente, a presente tese centra-se no desenvolvimento, implementação, validação e otimização de novas estratégias de monitorização a aplicar ao nível do parque eólico para avaliação da vida útil de fadiga consumida dos principais componentes estruturais. Essa avaliação baseia-se em layouts de instrumentação otimizados num subgrupo de aerogeradores, aproveitando os dados fornecidos pelo sistema SCADA disponível em todos as turbinas, para a aplicação de técnicas de extrapolação para avaliar todos os aerogeradores do mesmo parque eólico.

Neste contexto, está a ser desenvolvida uma campanha experimental no Parque Eólico da Tocha, um parque eólico onshore localizado em Portugal. Esta extensa campanha experimental inclui a instrumentação simultânea de dois aerogeradores (solicitados por ventos com diferentes intensidades de turbulência, motivada pela influência dos aerogeradores vizinhos), adotando extensómetros, clinómetros e acelerómetros distribuídos na torre e pás. Ao longo deste programa, foi recolhida uma base de dados com mais de dois anos. Esta configuração experimental pioneira permitiu alcançar os seguintes objetivos: desenvolvimento de algoritmos para avaliação da vida de fadiga consumida da torre e das pás, com base na medição direta de extensões; desenvolvimento de ferramentas para extrapolar o dano de fadiga acumulado ao longo do período de monitorização para toda a vida útil do aerogerador; e desenvolvimento de algoritmos para extrapolar os resultados de fadiga obtidos nos aerogeradores instrumentados para aerogeradores não instrumentados do mesmo parque eólico. A análise exaustiva dos resultados experimentais obtidos permitiu caracterizar o efeito das esteiras de vento no consumo de fadiga tanto na torre como nas pás.

Palavras-chave: Energia Eólica, Geradores Eólicos, Monitorização Estrutural, Análise Modal Operacional, Deteção de Dano, Análise de Fadiga, Avaliação de Fadiga em todo o Parque.

ACKNOWLEDGEMENTS

The feelings put into words here may not make justice to the endless support and guidance given by many individuals and institutions to whom I owe my genuine gratitude. To all my family, friends and colleagues, who through their friendship and support helped me prepare this thesis, here I present my sincere gratitude. Nevertheless, I want to express a special thanks:

To Professor Filipe Magalhães, my advisor, for all the efforts in providing me with the necessary conditions to successfully perform this work, for all the support, the commitment, the time, the sympathy, the precious pieces of advice and for the positive words of encouragement, always believing in a positive outcome for every situation. I am especially grateful for the friendship established between us.

To Professor Álvaro Cunha, my co-advisor, for challenging me with such an interesting topic and always making sure I had the necessary resources to develop my work. I would like to express my genuine gratitude for the close, gentle and constant support, motivation and guidance.

To INEGI, in particular to Eng. José Carlos Matos, Eng. Miguel Marques, Eng.ª Silvina Guimarães, Luís Mendes and Eng. Gil Castro for the opportunity to work within the experimental campaign, specially, in the instrumentation of the rotor and blades of two wind turbines and their contributions, for the sharing of ideas and collaboration in experimental works.

To Nuno Pinto and Eng. Luís Noites for their kindness and prompt assistance in every experimental campaign, planning and performing the in situ tasks.

To EDP Renewables, in particular to Eng. Adelino Barbosa, António Carmo and Luís Carlos Fernandes for their willingness to provide the conditions to perform the experimental campaign in Tocha Wind Farm. Also, for their helpful contributions to the development of the proposed integrated methodology and for the recommendation of such a stepwise procedure for future applications, given undeniable value to the current work.

To several engineers at the VESTAS Porto Design Center for all the support and the conversations about the specific behaviour of the VESTAS wind turbines but in particular to Eng. Miguel Teixeira.

To VESTAS O&M Portugal for the availability shown by their teams to support, execute and monitor the wind turbine instrumentation works.

To Professor Carlos Moutinho, for developing the MEMS sensors, adapting them to our needs in the experimental field and guaranteeing their production in the time. And also for the good time spent with him working with sensors around bridges.

To the Foundation for Science and Technology (Fundação para a Ciência e Tecnologia, FCT), for the funding of this work through the scholarship SFRH/BD/129688/2017. This work was also financially

supported by: Base Funding - UIDB/04708/2020 and Programmatic Funding - UIDP/04708/2020 of the CONSTRUCT - Instituto de I&D em Estruturas e Construções - funded by national funds through the FCT/MCTES (PIDDAC).

To Doctor Sérgio Pereira, for welcoming me into this research group and helping and advising me throughout this stage of my life, and for the opportunity to participate on the preparation and performance of ambient vibration tests on dams.

To Francisco Pimenta, for the availability and knowledge shared regarding the developed algorithms for fatigue assessment of wind turbine towers and the analyses implemented during this work.

To my friends and colleagues from the WindFarmSHM research project team, Sérgio Pereira, Francisco Pimenta, Maryana Berezyak and Mário Sobrinho, for their availability to share their knowledge and experience when I needed the most.

To my work colleagues and friends Sérgio Pereira, Aires Colaço, André Furtado, Alexandre Pinto, Ana Luísa Ramos, Cássio Gaspar, Cláudio Horas, Rodrigo Falcão Moreira, Francisco Pimenta, João Lázaro and Paulo Soares, for the great time that was working in our H304, and for the team spirit, friendship, willingness to help and for the memorable times.

To the other friends and colleagues whom I had the great pleasure to meet and spent time, during the last years in FEUP: João Magalhães, Rui Ribeiro, Inês Ribeiro and Catarina Oliveira. For being part of the beginning of my path in FEUP and for the friendship they show all these years.

To my closest friends, João Sousa, Pedro Ferreira, André Moreira, António Seixal, Pedro Torres, Joel Magalhães, Rui Nunes, Paulo Sousa, Rogério Alves and Firmino Leal for accompanying me during these years, for all the good laughs, kind words, positive energy and for all those hours discussing meaningless topics and getting older together.

À Daniela, por me acompanhar nesta jornada de forma dedicada e atenta. Pelo carinho, alento, motivação extra e, sobretudo, por aguentar o meu mau humor e, mesmo assim, sempre me animar. Pelo conforto que me dá quando se senta ao meu lado e olha o futuro de frente comigo.

À minha família mais próxima, em particular à minha tia Isabel, tia Rosa, tia Céu e tia Fernanda por todo o apoio e suporte prestado ao longo desta jornada, o que me permitiu estar focado e concentrado no trabalho que desenvolvi.

À Noémia e à sua família, por me ter acompanhado desde o berço e me ter transmitido todos os seus ensinamentos e valores que em muito contribuíram para a pessoa que sou hoje.

Ao meu tio Francisco, que, embora já não esteja fisicamente comigo, sempre me acompanhou com imenso carinho e preocupação e que de forma incansável sempre me apoiou a atingir os meus objetivos. Aos meus avós Conceição e José pelo amor incondicional. Todos eles demonstraram ser os meus maiores fãs.

Finalmente, mas não menos importante, aos meus pais, Marília e António, pelo amor, pelo tempo, por me colocarem sempre em primeiro lugar, por me darem tudo aquilo que tenho e sou. À minha irmã, Mariana, pelo amor, pelo carinho e por me ensinar a ver e valorizar tudo de uma outra forma. As suas demonstrações contínuas de força, motivação e confiança foram imprescindíveis para levar esta tese a bom porto. São sem dúvida os principais impulsionadores dos meus sonhos e do que já conquistei até hoje, e por esse motivo lhes dedico este documento.

NOMENCLATURE

For clarity purposes, all the abbreviations, notations and symbols presented in this list are defined in the text when first used. Generally, the use of the same symbol for different entities is avoided. However, in situations in which such procedure proved to be inadequate, the risk of misunderstanding is minimized by preventing the simultaneous use of the same symbol for different entities in the same context. The following list is ordered alphabetically.

LATIN SYMBOLS

A	Area of cross section Scale factor of Weibull distribution
A_i	Calibration coefficients
C_d	Drag coefficient
C_l	Lift coefficient
C_P	Power/energy coefficient
C_T	Thrust coefficient
D	Rotor diameter Drag force
$D_{endured}$	Endured damage
D_i	Damage scenarios
D_{Total}	Total damage
D_{10},	Short-term damage
E	Young modulus
F_N	Normal force
I	Second moment of inertia of the cross section
J_R	T^2 variation
L	Lift force
M_E	Edgewise bending moment

M_F	Flapwise bending moment
N_B	Number of blades
N_i	Permissible number of cycles in fatigue load i
P	Power
Q	Torque
R	Radius Stress ratio
$R_{k,t}$	Characteristic short term structural member resistance in tension
$R_{k,c}$	Characteristic short term structural member resistance in compression
Re	Reynolds number
S	Stress/strain
$S_{k,amp}$	Load amplitude
$S_{k,mean}$	Load mean
SR	Success rate
T	Period of time Axial rotor thrust force
TI	Turbulence intensity
$T_{operating}$	Number of years since the wind turbine started operation
$T^2_{t>t_d,D}$	T^2 Mean value in the damage period but for the scenario without damage
$T^2_{t>t_d,uD}$	T^2 Mean value in the damage period
TSR_{local}	Local speed ratio
TSR	Tip speed ratio
U	Wind speed
V	Relative velocity between the blade element and the wind
V_{ave}	Average annual wind speed at hub height
V_{rated}	Wind turbine rated wind speed
V_{ref}	Reference wind speed
$V(z)$	Horizontal wind speed at height z
V_{hub}	Wind speed at hub height
V_{in}	Cut-in wind speed
V_{out}	Cut-out wind speed
V_{ω}	Flow rotational speed
W	Section modulus
WS	Wind speed

X, Y	Tower reference coordinates
X', Y'	Nacelle reference coordinates

a	Axial induction factor
a'	Angular induction factor
c	Airfoil chord
f	Natural frequency
f_{CV}	Variation coefficient
$f_{out,D}$	Percentage of outliers in the damage period
k	Gauge factor
$\dot{m}$	Mass flow rate
m	Slope parameter of the S-N curve
n	Glass refraction index
n_{eff}	Effective refractive index
n_i	Number of load cycles in fatigue load bin i
$n_{out\|t>t_d}$	Number of outliers observed in the damaged period
$n_{T^2\|t>t_d}$	Number of control points observed in the damaged period
p	Pressure
r	Position of the blade under consideration
$rot(Yaw)$	Rotating matrix taking in account the wind direction
s_{A_i}	Type A uncertainty
t_d	Time when damage occurs
u_{A_i}	Type B uncertainty
u_{cA_i}	Combined type A and B uncertainties in the calibration coefficients
z_{hub}	Hub height in relation to ground

GREEK SYMBOLS

$\Delta\lambda$	Wavelength shift
$\Delta\sigma_i$	Stress differences
$\Delta\sigma_c$	Stress strength
ΔT	Temperature shift from the zero moment
Λ	Grating pitch (or grating period)
Ω	Rotational frequency of the rotor

α	Angle of attack Wind shear exponent
α_{glass}	Thermal expansion coefficient of the fiber
α_{δ}	Change of the refraction index
α_{sp}	Expansion coefficient of the structure material
β	Blade pitch angle
γ_{Ff}	Partial factor for equivalent constant amplitude stress range
γ_{Mf}	Partial factor for fatigue strength
$\gamma_{m,fatigue}$	Reduction factor γ_m for fatigue verification
$\gamma_{m,short\ term}$	Reduction factor γ_m for short-term verification
ε	Total strain
ε_E	Signal of the strain gauge bridge in edgewise direction
ε_{Load}	Strain due to loading
ε_{FBG}^{Temp}	Strain due to temperature effects on the sensors
ε_F	Signal of the strain gauge bridge in flatwise direction
$\varepsilon_{Structure}^{Temp}$	Strain due to temperature effects on the structure
ε_Z	Longitudinal strain signal
θ	Angle between the tower sensors referential and nacelle orientation
θ_i	Angle of the i-th sensor from the x-axis
λ_0	Wavelength of the sensor at the zero moment
λ_{0T}	Wavelength of the temperature-measuring FBG sensor at the zero moment
λ_{0m}	Wavelength of the strain-measuring FBG sensor at the zero moment
λ_B	Bragg wavelength
λ_m	Measured wavelength on strain-measuring FBG sensor
λ_T	Measured wavelength on temperature-measuring FBG sensor
ξ	Damping ratio
ρ	Mass density
σ	Standard deviation
σ_{amp}	Stress amplitude
σ_{max}	Maximum stress
σ_{min}	Minimum stress
σ_{mean}	Mean stress
σ_{range}	Stress range

σ_Z	Longitudinal stress
φ	Inflow angle
ω	Circular frequency

OTHER SYMBOLS

$*_\infty$	Section far ahead of the rotor
$*_W$	Section far wake of the rotor
$\langle * \rangle$	Estimated value

ABBREVIATIONS

$2D$	Two-dimensional
$3D$	Three-dimensional
ANPSD	Average normalized power spectral density function
BE	Blade element theory
CAPEX	Capital Expenditure
CLD	Constant Life Diagram
CM	Condition Monitoring
EU	European Union
FA	Fore-Aft
FBG	Fiber Bragg grating strain sensors
GPS	Global Positioning System
HP	High pressure
IEC	International Electrotechnical Commission
LCL	Lower Control Limit
LCOE	Levelized Cost of Energy
LE	Leading edge
LP	Low pressure
MA	Moment analysis
MAC	Modal Assurance Criterion
MEMS	Micro Electro-Mechanical System
NTP	Network Time Protocol
OMA	Operational Modal Analysis

OPEX	Operational Expenditure
PP	Power production
RUL	Remaining useful lifetime
SCADA	Supervisory Control And Data Acquisition
SF	Safety factor
SHM	Structural Health Monitoring
SS	Side-Side
SSI-COV	COVariance-driven Stochastic Subspace Identification
SSI-DATA	DATA-driven Stochastic Subspace Identification
TE	Trailing edge
UCL	Upper Control Limit
UCS	Ultimate compression strength
UTS	Ultimate tension strength
UK	United Kingdom
p-LSCF	Poly-reference Least Squares Complex Frequency Domain
WTi	Wind turbine number i

CONTENTS

1. INTRODUCTION 1
1.1 Research Context 1
1.2 Objectives and Main Contributions 6
1.3 Organization of the Thesis 9

2. BASICS OF WIND TURBINES BEHAVIOUR AND STRUCTURAL MONITORING 11
2.1 Main Components of Wind Turbines 11
2.2 Aerodynamic Behaviour 16
2.2.1 Wind Action 16
2.2.2 Rotor Aerodynamic Behaviour 18
2.2.3 Aerodynamic Control Strategies 24
2.3 Monitoring of Wind Turbines 26
2.3.1 Introduction 26
2.3.2 Environmental and Operational Conditions 32
2.3.3 Structural Health Monitoring 33
2.3.4 Operational Modal Analysis of Wind Turbines 34
2.3.4.1 Time-variance due to Nacelle Rotation 34
2.3.4.2 Time-variance due to Rotor Rotation 35
2.3.4.3 Periodic Nature of the Excitation Forces 36
2.4 Final Considerations 37

3. VIBRATION-BASED MONITORING OF WIND TURBINES FOR DAMAGE DETECTION 39
3.1 Introduction 39
3.2 Case Study Description 41
3.3 Strategy for Vibration-Based SHM 44
3.3.1 Automated Modal Analysis 45
3.3.1.1 Modal Results 47
3.3.1.2 Database Characterization 48
3.3.2 Minimization of Environmental and Operational Effects 49
3.3.3 Damage Detection 51
3.4 Optimization of the Vibration-Based Monitoring System 53

3.4.1 Strategies: Sensors Layout and Sensors Noise 53
3.4.1.1 Sensors Layout 53
3.4.1.2 Sensors Quality 54
3.4.2 Influence of the sensors layout and noise on the modal tracking 55
3.5 Performance Evaluation of Alternative Monitoring Strategies 57
3.5.1 Criteria for Performance Evaluation 57
3.5.2 Damage scenarios 58
3.5.3 Results 60
3.5.3.1 Total number of points on the control chart 61
3.5.3.2 Percentage of outliers in the damage period 62
3.5.3.3 Variation of the T^2 index between damage and undamaged scenarios 62
3.5.3.4 Time for damage identification 63
3.5.3.5 Conclusions 64
3.6 Final Considerations 67

4. MONITORING CAMPAIGN AT TOCHA WIND FARM 69
4.1 Introduction 69
4.2 Tocha Wind Farm and VESTAS V100-1.8 MW 70
4.3 Preliminary Evaluation of the Modal Properties of the Wind Turbines 72
4.3.1 Numerical Models 72
4.3.2 Ambient Vibration Tests 73
4.4 Monitoring System and Preliminary Monitoring Results 76
4.4.1 Tower Monitoring System: Accelerometers 77
4.4.2 Tower Monitoring System: Strains and Rotations 79
4.4.3 Rotor Monitoring System: Accelerometers 82
4.4.4 Rotor Monitoring System: Strains 83
4.4.5 Complementary Data and Synchronization 85
4.5 Final Considerations 91

5. FATIGUE ASSESSMENT OF WIND TURBINE TOWER 93
5.1 Introduction 93
5.2 Brief State of the Art 95
5.3 Processing Steps for Fatigue Assessment from Strains Gauges Measurements 98
5.3.1 Bending Moments at Instrumented Section 99
5.3.2 Extrapolation of the Bending Moments 99
5.3.2.1 Critical construction details 99
5.3.2.2 Extrapolation of the Bending Moments to any Section 100
5.3.3 Axial Stress Variation in the Cross-Section 102
5.3.4 Rainflow Counting 102
5.3.5 Fatigue Damage During the Monitoring Period 102
5.3.6 Extrapolation of the Fatigue Damage in Time 104

5.4 Experimental Evaluation of Bending Moments at the Tower 106
5.4.1 Processing Methodology 106
5.4.2 Bending Moments Validation 108
5.4.3 Bending Moments vs Operating Conditions 111
5.5 Fatigue Assessment of Wind Turbine Tower 117
5.6 Evaluation of Fatigue Life Consumption Within the Wind Farm 121
5.6.1 Introduction 121
5.6.2 Fleet Leader Concept 122
5.6.3 Damage Capture Matrix Construction 123
5.6.3.1 Damage Binning 123
5.6.3.2 Bin Reduction 129
5.6.3.3 Fill up Empty Bins 130
5.6.4 Damage Extrapolation in the Instrumented Wind Turbine 135
5.6.4.1 Damage Capture Matrix Validation 135
5.6.4.2 Total Endured Damage of the Instrumented Wind Turbine 138
5.6.5 Fatigue Damage Extrapolation within the Farm 144
5.7 Final Considerations 149

6. ANALYSIS OF WIND TURBINE BLADES EXPERIMENTAL DATA 153
6.1 Introduction 153
6.1.1 Blade Structure and Composite Materials 154
6.1.2 Loads and Damage Mechanisms 156
6.1.3 Structural Health Monitoring 157
6.2 Strain Measurements with Fiber Bragg Granting Sensors 160
6.2.1 Experimental Application at Tocha Wind Farm 160
6.2.2 Fiber Bragg Granting Strain Sensors 162
6.2.3 Calibration of Strain Gauges 166
6.3 Experimental Determination of Bending Moments 169
6.3.1 Methodology and Data Processing 169
6.3.2 Bending Moments vs Operating Conditions 174
6.3.2.1 Transient Events 175
6.3.2.2 Power Production 178
6.4 Preliminary Fatigue Analysis 184
6.4.1 Fatigue Modelling of Composite Wind Turbine Blades 184
6.4.1.1 Constant Amplitude Fatigue Models 185
6.4.1.2 Variable Amplitude Fatigue Models 187
6.4.2 Fatigue Results 189
6.4.2.1 Rainflow Matrix Histograms 190
6.4.2.2 Fatigue Damage 193
6.4.2.3 Effect of Wakes in Fatigue Damage of Wind Turbine Blades 198
6.5 Final Considerations 206

7. CONCLUSIONS AND FUTURE RESEARCH 209
7.1 Conclusions 209
7.2 Future Research 211

REFERENCES 213

LIST OF FIGURES

Figure 1.1 – Total power generation capacity in the EU 2005-2017 (adapted from (WindEurope, 2018)). 2

Figure 1.2 – New onshore and offshore wind installations in Europe for 2016-2020 and WindEurope's scenarios for 2021-2025 (adapted from (WindEurope, 2021)). 3

Figure 1.3 – Monitoring strategy to be applied in the context of a wind farm. 6

Figure 2.1 – Main wind turbines components of horizontal-axis upwind onshore wind turbines. 11

Figure 2.2 – Upwind onshore wind turbine: (a) Variation of the airfoil blade length; (b) Main mechanical components inside the nacelle (adapted from (Wagner, 2020)). 12

Figure 2.3 – Campbell diagram of: (a) Senvion MM82-2 MW wind turbine; (b) Vestas V100-1.8 MW wind turbine (the diagonal dashed lines represent the harmonic frequencies associated with the rotor rotation). 14

Figure 2.4 – Wind resource characterization: (a) Vertical profile of wind speeds considering the turbulence effect (adapted from (M. Hansen, 2015)); (b) Distribution of mean wind speed frequencies measured at Tocha Wind Farm and respective fit of Rayleigh and Weibull distributions. 17

Figure 2.5 – The energy extracting stream tube of a wind turbine (adapted from (Burton et al., 2011)). 18

Figure 2.6 – Actuator disc with stream tube (adapted from (Cruz & Atcheson, 2016)). 19

Figure 2.7 – Angular momentum theory: (a) Rotational flow model after the passage of the air mass through the rotor plane; (b) Angular ring geometry of wake wind flow (adapted from (Manwell et al., 2010)). 21

Figure 2.8 – Relative wind velocity applied to the airfoil and the subsequent lift and drag forces (adapted from (Oliveira, 2016)). 23

Figure 2.9 – Monitoring strategy developed to be applied in the context of a wind farm. 27

Figure 2.10 – Influence of different maintenance strategies on wind turbine performance (adapted from (Coronado & Fischer, 2015)). 28

Figure 2.11 – Expectation of maintenance costs as a function of inspection intervals for different condition assessment strategies (adapted from (Besnard & Bertling, 2010)). 29

Figure 2.12 – Damage assessment levels. 30

Figure 2.13 – Illustration of the θ angle between the sensors referential (in black) and nacelle orientation. 35

Figure 3.1 – Senvion MM82-2MW: (a) Picture of the wind turbine; (b) Wind turbine power curve. 41

Figure 3.2 – Position of the accelerometers at three levels of the wind turbine tower. 42

Figure 3.3 – Main steps of the vibration monitoring strategy to damage detection. 44

Figure 3.4 – Modal analysis of a setup with the wind turbine in operation: (a) Control diagram (SSI-COV); (b) Characterization of clusters in average frequencies and number of poles. 46

Figure 3.5 – Campbell diagram of considered clutters of stable poles, including vibration modes and external harmonic excitation (p-LSCF algorithm). 47

Figure 3.6 – Campbell diagram with the nine tracked vibration modes (p-LSCF algorithm) and corresponding mode shapes. 47

Figure 3.7 – Natural frequency of 2 SS* mode vs rotor speed (regime 4). 50

Figure 3.8 – Natural frequency 1 SS* vs pitch angle (regime 5). 50

Figure 3.9 – Identified and predicted frequency value of 1 SS* and 4 FA mode for Period 2. 50

Figure 3.10 – Histograms of the natural frequencies of 1 SS* and 2 FA modes before (red line) and after (blue bars) mitigation of environmental and operational effects. 51

Figure 3.11 – T^2 control chart of a generic process. 52

Figure 3.12 – Alternative sensors layouts. 53

Figure 3.13 – Power spectra of typical acceleration time series measured at the tower top for varying wind velocities: original signal (Acc) and original signal contaminated with different levels of noise (Acc+Noise1,2,3). . 54

Figure 3.14 – Campbell diagram with the tracked vibration modes with: (a) Layout 4 N2; (b) Layout 4 N3; (c) Layout 1 N0; (d) Layout 2 N2. 55

Figure 3.15 – Success Rate [%] obtained witch different layouts (1 to 4) and increasing noise level for layout 4 (N0 to N3) (Layout 1 and 2, MAC limit of 0.5; Layout 3 and 4N1 to 4N3, MAC limit of 0.8). 56

Figure 3.16 – Procedure implemented to identify abnormal deviations of the natural frequency values. 57

Figure 3.17 – T2 control charts corresponding to layout 1 to 4 and for noise levels N0, N1 and N2 considering a scenario undamaged and three damage scenarios D1, D2 and D3 (the horizontal lines represent the UCL of each solution). 60

Figure 3.18 – Number of points of the T^2 control charts. 61

Figure 3.19 – Relative frequency of outliers: (a) for damage D1; (b) for damage D2; (c) for damage D3. 62

Figure 3.20 – Performance indicator J_R index: (a) Damage scenario D1; (b) Damage scenario D2; (c) Damage scenario D3. 63

Figure 3.21 – The response time of optimized monitoring strategies: (a) Damage scenario D1; (b) Damage scenario D2; (c) Damage scenario D3. 64

Figure 4.1 – Tocha Wind Farm: (a) Geographic location in Portugal; (b) Wind turbines and auxiliary structures; (c) Characterization of the wind conditions observed from 2013 to 2018, based on data provided by meteorological mast (100 m high measurements). 70

Figure 4.2 – Vestas V100-1.8MW: (a) Wind turbine at Tocha Wind Farm; (b) Numerical model developed using ROBOT STRUCTURAL ANALYSIS. 72

Figure 4.3 – Ambient vibration tests: a) Instrumented section; b) Sensors; c) Operating scenarios and power curve of Vestas V100 wind turbine (https://en.wind-turbine-models.com). 73

Figure 4.4 – Ambient Vibration test results for wind turbine 1: (a) Average power spectra for FA and SS directions; (b) Stabilization diagram produced by the SSI-COV method; (c) Two zooms of this diagram for first (left) and second (right) pairs of tower bending modes. 74

Figure 4.5 – Mode shapes and natural frequencies identified with the ambient vibration test and numerical model of wind turbine 1. 74

Figure 4.6 – Ambient Vibration test results for wind turbine 1 in operating and non-operating conditions: (a) Average power spectra; (b) Natural frequencies (results obtained from 10 minutes single observation setups with very low variance of the environment and operational parameters). 75

Figure 4.7 – Comparison of the natural frequencies of four wind turbines in non-operational conditions: (a) 1st pair of bending moments; (b) 2nd pair of bending modes. 75

Figure 4.8 – Tower sections instrumented with accelerometers: (a) Photo of the force balance sensors (connected to cables) and of the MEMS based acquisition system (grey box with antenna); (b) Force-balance sensors; (c) MEMS sensors. 77

Figure 4.9 – Power spectra from force balance (blue line) and MEMS (orange line) sensors ($1\Omega, 3\Omega, \ldots, 12\Omega$ marked with dashed vertical lines). 78

Figure 4.10 – Colour maps with singular-value spectra for the FA and SS directions in January 2019. 78

Figure 4.11 – Colour map with natural frequencies over rotor speed in March 2020 (the diagonal dashed lines represent the harmonic frequencies associated with the rotor rotation). 79

Figure 4.12 – Tower strains monitoring system: (a) Instrumented section of the tower; (b) Position of the strain gages (◊) and temperature sensors ( ) at the section; (c) Photo of strain and rotation sensors. 80

Figure 4.13 – Tower Monitoring System Strains and Rotations: (a) Example of strain time series; (b) Strain and rotations during nacelle yawing, SG – strains; CL - rotations (see sensor positions in Figure 4.12). 80

Figure 4.14 – Averaged power spectra: six force-balance accelerometers (first row), longitudinal strains A to D (second row) and rotation at clinometer 3 (third row) in non-operating condition (left column) and operating condition (right column). 81

Figure 4.15 – MEMS based system installed inside one blade and direction of measurements (X approximately aligned with edgewise direction). 82

Figure 4.16 – Example of acceleration time series and corresponding operation parameters and power spectra. 83

Figure 4.17 – Strain measurement at the blade root: wiring and photo. 84

Figure 4.18 – Example of detrended strain time series (static component was removed) and corresponding operation parameters and power spectra (S1 and S3 bending in the edgewise direction; S2 and S4 bending in the flapwise direction). 84

Figure 4.19 – Environmental SCADA data measured at WT1 from January 2013 to June 2021: Wind speed, wind direction and nacelle temperature (the monitoring period is in grey). 86

Figure 4.20 – Operational SCADA data measured at WT1 from January 2013 to June 2021: Power output, blade pitch angle, and rotor speed (the monitoring period is in grey). 87

Figure 4.21 – Comparison between SCADA 10-min and SCADA high-resolution at WT1 during a start-up and shutdown event: (a) Wind speed; (b) Blade pitch angle; (c) Rotor speed; (d) Power output. 88

Figure 4.22 – Synchronization of the KMI system (force-balance S3) and cRIO system (strain gauge B). 89

Figure 4.23 – Synchronization of the SCADA data (yaw angle high-resolution) and cRIO system (strain gauge A) (the vertical dashed lines correspond to the singular points used for synchronization). 90

Figure 5.1 – Fatigue Assessment procedure based on strains measurements. 98

Figure 5.2 – S-N curves defines in GL-2010 and Eurocode 3 (category detail 80 MPa). 103

Figure 5.3 – Daily temperature effects on strains measurements at the bottom section: (a) Strains signals zeroed during the nacelle rotation; (b) Strains signals zeroed during the nacelle rotation with compensation of the temperature effects; (c) Temperature measurements. 107

Figure 5.4 – Strain-gauge calibration check: (a) Yaw angle nacelle; (b) Strain signals; (c) Mean value of the full rotation signals observed from Frebuary-2019 to April-2020 (see sensor positions in Figure 4.12). 108

Figure 5.5 – 10-min average strains signal of strain gauges A to D (see sensor positions in Figure 4.12). 109

Figure 5.6 – Bending moments variations at the base of the tower estimated from accelerations and strains time series during a rotor stop event. 110

Figure 5.7 – Experimental and numerical bending moments time series for FA and SS directions in the bottom instrumented section of the tower considering two different operating conditions. 110

Figure 5.8 – Variation of 10-min average bending moments at the tower base as a function of the wind speed and turbulence intensity, considering normal power production: (a) Fore-aft direction; (b) Side-to-side direction (x scale omitted due to confidentiality agreements). 111

Figure 5.9 – Variation of 10-min average power output during normal power production, as a function of the FA bending moment at the tower and turbulence intensity. 112

Figure 5.10 – Bending moments measured at tower base during normal power production, considering different wind speed and turbulence intensities. Wind speed and blade pitch angle provided by SCADA high resolution. 113

Figure 5.11 – Bending moments measured at tower base and wind speed and blade pitch angle time series during parked/idling condition for: (a) Wind speed below the cut-in speed; (b) During a storm. 114

Figure 5.12 – Bending moments measured at tower base and wind speed and blade pitch angle time series during an emergency shutdown event. 115

Figure 5.13 – Bending moments measured at tower base and wind speed and blade pitch angle time series during the start-stop of the turbine around the cut-in wind speed. 115

Figure 5.14 – 10-min average (left) and maximum (right) thrust loads as a function of 10-min average wind speed, considering: (a) Power production conditions; (b) Parked periods. 116

Figure 5.15 – Influence of the window length: (a) Damage distribution over the half of the section (y scale omitted due to confidentiality agreements); (b) Histogram of the stress cycles. 117

Figure 5.16 – Influence of the rainflow histogram resolution: (a) Relative difference of the calculated damage (the 1 MPa bin amplitude is the reference); (b) Stress cycles histogram. 118

Figure 5.17 – Influence of the S-N curve parameters: (a) Damage distribution over the section (y scale omitted due to confidentiality agreements); (b) Histogram of the stress cycles and S-N curve provided by Eurocode 3. . 119

Figure 5.18 – Influence of signal sampling frequency. Stress cycles amplitude as a function of the accumulated damage for a sampling frequency of 25 Hz (with zoom) (x scale omitted due to confidentiality agreements). 119

Figure 5.19 – Influence of signal sampling frequency: (a) Damage distribution over the section considering 4 methods ($f_s = 25\ Hz$); (b) Damage distribution over the section for all sampling frequency (Butterworth filter) (y scale omitted due to confidentiality agreements). 120

Figure 5.20 – Overview of damage extrapolation method form the fleet leader to the entire wind farm. 122

Figure 5.21 – Tocha Wind Farm: (a) Layout of the wind farm and identification of the fleet leader and its wake directions; (c) Characterization of the wind conditions. 123

Figure 5.22 – Short-term damage for FA direction: (a) Time evolution over the monitoring period; (b) Cumulative damage distribution. 124

Figure 5.23 – Short-term damage for FA direction as a function of: (a) Wind speed; (b) Turbulence intensity; (c) Wind direction; (d) Pitch angle; (e) Rotor speed; (f) Power output. 124

Figure 5.24 – Short-term damage for FA direction as a function of the wind speed for the six load cases. 126

Figure 5.25 – Accumulated and relative damage and total time for different load cases. 126

Figure 5.26 – Average 10-min damage for power production, binned based on: (a) Wind speed; (b) Turbulence intensity. 127

Figure 5.27 – Turbulence intensity and average damage for different wind sectors: (a) Difference between the turbulence intensity measured at WT1 and the average turbulence intensity in the five turbines of the farm; (b) Average damage and turbulence intensity at WT1 for wind speed bin of 7-9 m/s. 128

Figure 5.28 – Damage distribution within two wind speed and turbulence intensity bins (histogram) fitted with a normal distribution (orange curve). 129

Figure 5.29 – Damage distribution within four wind speed and turbulence intensity bins (histogram) fitted with a normal distribution before (orange dashed distribution) and after (orange distribution) applying bootstrapping. . 130

Figure 5.30 – Matrix with the number of recorded 10 minutes time series during power production in the monitoring period. 131

Figure 5.31 – Two alternative approaches followed to fill up the empty bins of the capture damage matrix (red rectangles in the matrices represents higher damage). 133

Figure 5.32 – Distribution of the damage over the tower cross-section as a function of: (a) Wind speed for $TI \in [11-13[\ \%$; (b) Turbulence intensity for $WS \in [9-10[\ m/s$. 134

Figure 5.33 – Comparison of real and extrapolated fatigue damage over the instrumented tower cross-section considering the monitoring period. 136

Figure 5.34 – Extrapolated damage at the critical point of the instrumented cross-section for each combination of monitoring and extrapolation periods, normalized to the actual damage measured in the respective monitoring period. 137

Figure 5.35 – Distribution of the number of 10-min periods measured by SCADA system at WT1, before and in the monitoring period according the: (a) Wind speed bins; (b) Turbulence intensity bins. 138

Figure 5.36 – Turbulence intensity measured at WT1 (Jan-2013 to Jun-2021): (a) Turbulence intensity variation (10-min and 30-day moving average); (b) 30-day moving average of measured and corrected turbulence intensity. 139

Figure 5.37 – Reconstructed fatigue damage for the critical angle of the cross-section (May 2012 to June 2021): (a) Wind speed variation (10-min and 30-day average) over the wind turbine lifetime; (b) 10-min damage values and 30-day moving average damage; (c) Cumulative damage. 141

Figure 5.38 – Distribution of the extrapolated endured damage at the critical point of the tower instrumented cross-section based on the three alternatives of the damage capture matrix, normalized to the D_{3D} (the vertical dash lines shows the damage mean values normalized to the D_{3D} mean value). 142

Figure 5.39 – Distribution of the extrapolated endured damage at critical point of the tower cross-section under alternative operating conditions. 142

Figure 5.40 – Turbulence intensity correction (Jan-2013 to Jun-2021): (a) 30-day moving average of measured and corrected turbulence intensity for all wind turbines; (b) Control software version of each wind turbine. 144

Figure 5.41 – Identification of the wakes and difference between the wind speed/turbulence intensity measured at WT1 and WT5 and the respective average values in the five turbines of the farm, from Jan-2013 to Jun-2021. 145

Figure 5.42 – Identification of the wakes and difference between the wind speed/turbulence intensity measured at WT2, WT3 and WT5 and the respective average values in the others five turbines (Jan-2013 to Jun-2021). 146

Figure 5.43 – Cumulative estimated damage (D_{3D}) for the critical angle of each wind turbine of the wind farm. . 147

Figure 5.44 – Distribution of the extrapolated endured damage at critical angle of the tower cross-section for all wind turbines of the wind farm and normalized to the WT1 (vertical dash line shows the mean value). 148

Figure 6.1 – Schema of the components of a wind turbine blade (adapted from (Lund & Stegmann, 2005)). 154

Figure 6.2 – Schema of section of wind turbine blade with two internal webs and definition of load cycles (adapted from (Mishnaevsky et al., 2017)). 155

Figure 6.3 – Classification of the three areas of the wind turbine blades. 155

Figure 6.4 – Main structural damage mechanisms of wind turbine blades (adapted from (Katnam et al., 2015)). 157

Figure 6.5 – Variation of flapwise ($EI_{flapwise}$) and edgewise ($EI_{edgewise}$) stiffness and drag (C_d) and lift (C_l) coefficients along the blade (normalized values). 161

Figure 6.6 – FBG monitoring system adopted within the framework of Tocha Wind Farm monitoring project. 162

Figure 6.7 – FBG sensor location at blade root (instrumented blade cross-section in line). 162

Figure 6.8 – FBG index profile and the spectrum of the incident, reflected and transmitted beams (adapted from (Campanella et al., 2018)). 163

Figure 6.9 – Signal pre-processing of strain gauges: (a) Raw signal; (b) Cleaned signal; (c) Temperature compensated strain gauge measurements after senor calibration (blade 1 of the WT1). 169

Figure 6.10 – Temperature effects on strain gauges signal: (a) Time series without temperature compensation; (b) Time series with temperature compensation; (c) Temperature measurements (blade 1 of the WT1). 170

Figure 6.11 – Determination of the calibration coefficients (blade B of the WT5). 171

Figure 6.12 – Blade root bending moments of the wind turbine 1 during a stop event: (a) Flapwise bending moments; (b) Edgewise bending moments; (c) Pitch angle (blue line) and rotor speed (orange line). 172

Figure 6.13 – Blade root bending moments of the wind turbine 5 during a stop event: (a) Flapwise bending moments; (b) Edgewise bending moments. 173

Figure 6.14 – Power curve and variation of the blade pitch angle as a function of the wind speed, considering the flapwise and edgewise bending moments at root of blade A of the WT5. 174

Figure 6.15 – Flapwise and edgewise bending moments at the blade roots of the wind turbine 1, during park/idling conditions: (a) Wind speed below the cut-in speed; (b) During a storm. 175

Figure 6.16 – Flapwise and edgewise bending moments at the blade roots of the wind turbine 1, during a shutdown event (wind speed above the cut-out speed). 176

Figure 6.17 – Flapwise and edgewise bending moments at the blade roots of the wind turbine 1, during a start-up event after a maintenance operation (wind speed above the cut-in speed). 176

Figure 6.18 – Flapwise and edgewise bending moments at the blade roots of the wind turbine 1 during the start and stop of the turbine around the cut-in wind speed. 177

Figure 6.19 – Variation of 10-min average flapwise bending moments at the root of blades A, B and C of the wind turbines 1 and 5 as function of the 10-min average wind speed provided by the SCADA system, considering variable levels of turbulence intensity, during power production. 178

Figure 6.20 – Flapwise bending moments at the root of blade A (WT1) during power production: (a) Bending moment time series for the 9-10 m/s wind speed bin; (b) Variation of 10-min average flapwise bending moment with the 10-min average wind speed and turbulence intensity; (c) Bending moment time series for the $7 - 9\ \%$ turbulence intensity bin. 180

Figure 6.21 – Variation of 10-min average edgewise bending moments at the root of blades A, B and C of the wind turbines 1 and 5 as function of the 10-min average wind speed provided by the SCADA system, considering variable levels of turbulence intensity, during power production. 181

Figure 6.22 – Variation of the 10-min bending moments at the root of blade B of the WT5 during power production ('o': mean, '∗': maximum and '×': minimum values): (a) Flapwise direction; (b) Edgewise direction. 182

Figure 6.23 – Variation of the 10-min flapwise and edgewise bending moments at the root of blade B of the WT5 during power production, as a function of rotor speed and pitch angle, where the colour of the points indicate the 10-min average wind speed. 183

Figure 6.24 – Fatigue damage evolution: (a) Damage as a function of the number of cycles for composites and metals; (b) Stages of damage modes development in composite materials. Adapted from (Kaminski et al., 2015). 184

Figure 6.25 – Constant amplitude fatigue models: (a) Basic fatigue terminology; (b) Typical S-N curve trends for composite materials (adapted from (Roger, 2006)). 185

Figure 6.26 – Fatigue life prediction models: (a) Schematic constant life diagram for composites; (b) Linear Goodman Diagram (adapted from (Roger, 2006)). 187

Figure 6.27 – Fatigue assessment of wind turbine blades based on strain measurements. 189

Figure 6.28 – Rainflow counting cycles at root of the blade A of WT1 for edgewise direction: (a) 3D rainflow for TE and LE sensors; (b) Number of cycles as a function of strain amplitude; (c) Number of cycles as a function of mean strain. 191

Figure 6.29 – Rainflow counting cycles at root of the blade A of WT1 for flapwise direction: (a) 3D rainflow for LP and HP sensors; (b) Number of cycles as a function of strain amplitude; (c) Number of cycles as a function of mean strain. 192

Figure 6.30 – Time variation of the normalized short-term damage for flapwise and edgewise direction for WT1 and WT5 over the monitoring period and corresponding histogram (all figures have the same vertical scale). 194

Figure 6.31 – Variation of the average damage at flapwise and edgewise directions (mean values for blade A of WT5) as a function of the environmental and operational parameters considering five load cases (all figures have the same vertical scale). 195

Figure 6.32 – Total time and relative damage at wind turbines 1 and 5 for different load cases (average values for all blades of each wind turbine, according to each damage main direction). 196

Figure 6.33 – Average 10-min damage at flapwise and edgewise directions at WT1 and WT5 considering power production, as a function of the wind speed and turbulence intensity, with zooms for the edgewise direction. 197

Figure 6.34 – Identification of the analysed yaw sectors and difference between the turbulence intensity measured at WT1 and WT5 and the respective average values in the five turbines of the farm, from Jan-2013 to Jun-2021. 199

Figure 6.35 – Relation between environmental and operational parameters at WT1 and WT5 considering the yaw sector 1 (WT1: upstream turbine and WT5: downstream turbine). 200

Figure 6.36 – Comparison of accumulated damage on blade roots of the WT1 and WT5 considering the yaw sector 1 (WT1: upstream turbine and WT5: downstream turbine). All plots with the same vertical scale. Vertical scale values not included due to confidentiality constraints. 200

Figure 6.37 – Relation between environmental and operational parameters at WT1 and WT5 considering the yaw sector 2 (WT1: downstream turbine and WT5: upstream turbine). 201

Figure 6.38 – Comparison of accumulated damage on blade roots of the WT1 and WT5 considering the yaw sector 2 (WT1: downstream turbine and WT5: upstream turbine). All plots with the same vertical scale. Vertical scale values not included due to confidentiality constraints. 202

Figure 6.39 – Relation between environmental and operational parameters at WT1 and WT5 when both wind turbines are loaded by an unperturbed flow (yaw sector 3). 202

Figure 6.40 – Comparison of accumulated damage on blade roots of the WT1 and WT5 when both wind turbines are loaded by an unperturbed flow (yaw sector 3). All plots with the same vertical scale. Vertical scale values not included due to confidentiality constraints. 203

Figure 6.41 – Distribution of the number of observations for each yaw sector, considering wind speed and turbulence intensity. 204

LIST OF TABLES

Table 2.1 – Basic SCADA parameters for structural health monitoring. 32

Table 3.1 – Regimes considered for reference modal properties of the wind turbines. 42

Table 3.2 – Statistics related to the results obtained with the three modal identification algorithms. 48

Table 3.3 – Variation of the natural frequencies associated with tested damage scenarios [%]. 59

Table 3.4 – Comparison of the analysed instrumentation solutions. 65

Table 4.1 – Technical specification of the Vestas V100-1.8 MW wind turbine. 71

Table 4.2 – Tower monitoring systems of WT1 and corresponding timing protocols. 89

Table 5.1 – Relative differences of accumulated damage at the critical angle of the cross-section of the tower considering the different sampling methods and sampling frequencies. 120

Table 5.2 – Cumulative damage obtained from the experimentally characterized and extrapolated bins for the critical angle [%]. 137

Table 5.3 – Extrapolated endured mean damage obtained from the real and extrapolated bins of the damage capture matrix for the critical angle [%]. 148

Table 6.1 – Material properties of the wind turbine blades adopted in this work. 190

Table 6.2 – Total energy production at upstream and downstream wind turbines and relative variation for each yaw sector over the monitoring period. 205

1 INTRODUCTION

1.1 RESEARCH CONTEXT

Energy plays a central role in modern economic and social development models. This is a key element that not only affects the internal dynamics of countries, but also shapes the strategies of international relations, whether at the political or even military level. Currently, with the growth of the world population and technological development, the energy demand continues to increase. Satisfying this demand at the time and in the place where it is required, in a safe and adequate manner, requires having sufficient and diversified primary energy sources, an efficient and economically viable system for converting these same sources into the different forms of energy, as well as a system capable of making it accessible to consumers. The current development paradigm is most likely unsustainable in the medium/long term. In addition to factors such as the growing scarcity of natural resources, especially fossil fuels, the energy dependence of some countries, environmental degradation and climate change are factors that largely contribute to this scenario. However, a system that is not geared towards continued economic growth is unstable and leads to the risk of collapse of economies as they are currently organized.

Limiting global warming in line with the Paris Agreement (UNFCCC, 2015) to significantly reduce the risks and impacts of climate change fundamentally requires transforming our energy system and adjusting our energy production and consumption patterns in a short period. This transformation is based mainly on two main points: the commitment to energy efficiency and the production of carbon neutral energy. With regard to the production of low carbon energy, renewable energy is a fundamental pillar in realizing the decarbonisation priority, in fulfilling the commitments agreed under the Paris Agreement and in supporting the transition to greener, efficient and more competitive economies and societies.

Aware of this issue, most of the world's economies have made efforts to introduce clean energy into their global energy balance. Taking the example of the European Union (EU), a wide range of complementary climate and energy policies support the evolution of low carbon energy and aim to stimulate innovation in this field. The main objectives are to guarantee a safe, accessible and environmentally friendly energy supply. The progress achieved since 2005 is largely attributed to the presence of binding national targets for 2020 under the Renewable Energy Directive (EU, 2009) and to the national support instruments applied in response to these same goals. After the conclusion of this program, a new program for 2030 is currently under implementation (EU, 2018). The EU's climate vision for 2050 was also recently presented (EC, 2018), which confirms the intention to lead global efforts to mitigate climate change and achieve absolute carbon neutrality by 2050.

As result of the policies adopted, there has been a steady growth of investment in renewable energy sources for over a decade, leading to a doubling of global capacity between 2005 and 2017. In 2017, for

the third consecutive year, more than an half of all newly installed energy capacity worldwide was from renewable sources, with an estimated contribution of 70% for that year. Seen from a technological and market perspective, the global development of renewable energy sources in 2017 was dominated by high investment in solar and wind energy for electricity generation, which together accounted for more than 80% of total global investments (Frankfurt School-UNPE, 2018; IRENA, 2018).

Taking the example of the EU once more, Figure 1.1 shows the evolution of the total power generation capacity between 2005 and 2017. It is clear that wind was the energy source with the greatest growth in this period, overtaking coal as the second largest form of power generation capacity in 2016.

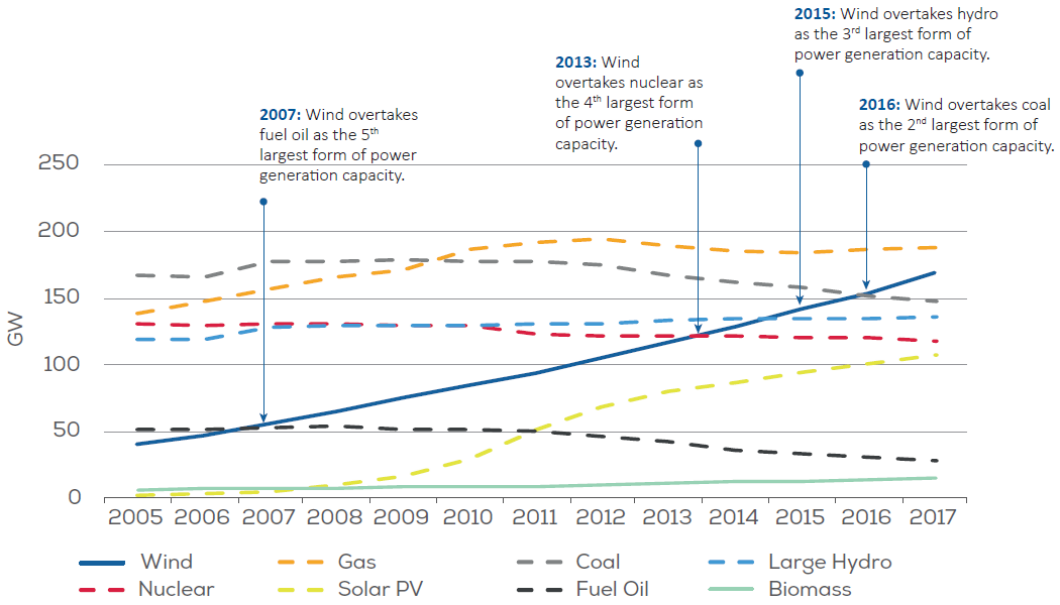


Figure 1.1 – Total power generation capacity in the EU 2005-2017 (adapted from (WindEurope, 2018)).

As show in Figure 1.2, in 2020 Europe installed 14.7 GW of new wind power capacity, being 10.5 GW of the new installations in the EU-27. In fact, 2020 was the third largest year in term of overall installations, following on from 2017, the record year, and 2019, the second largest year. It is important to note that 80% (11.8 GW) of wind installations in 2020 came from onshore wind. At the end of 2020, Europe had 220 GW of installed wind power capacity, 194 GW onshore and 25 GW offshore (WindEurope, 2021).

It is generally accepted that wind energy is a key element in the energy strategy, taking into account the evolution of the wind market. In terms of the future, the outlook is equally optimistic. Figure 1.2, shows two scenarios (realistic expectations scenario and low scenario) for the development of wind power capacity in the Europe. Both scenarios reflect potential developments in European regulatory frameworks, national policies, project development timelines and the ability of wind to secure further capacity through upcoming auctions and tenders (WindEurope, 2021).

According to the best estimate of the installed capacity over the next five years, it is expected that Europe will build 105 GW of new capacity by 2025, which represent an annual installation rate of 21 GW. Onshore will probably represent 72% of new installations in the next five years. Although new installations are forecasted to grow year on year, the rate of onshore installations will begin to stall. On the other hand, offshore installations are expected to see new records beaten each year. 29 GW of new offshore wind expected over the next five years. That is almost a doubling of the annual installation rate from 3 GW to 5.8 GW.

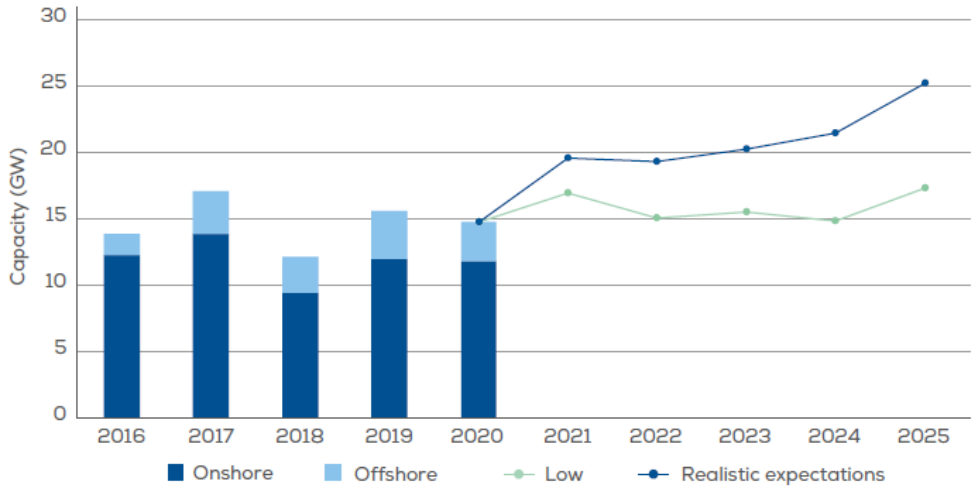


Figure 1.2 – New onshore and offshore wind installations in Europe for 2016-2020 and WindEurope's scenarios for 2021-2025 (adapted from (WindEurope, 2021)).

Portugal has also registered a trend similar to other European countries. Currently, Portugal has an accumulated installed wind energy capacity of 5.3GW, in a total of 240 wind farms. In 2020, this sector avoided the emissions of 6 million tons of CO_2-eq (APREN, 2021). It is important to highlight the first floating semi-submersible wind farm in the world, the WindFloat Atlantic, with a 25 MW of installed capacity (Marine Insight, 2021).

According to the Portuguese Renewable Energy Association, in 2020 the share of renewable electricity in the overall electricity generation was 60%, where wind energy met 24% of the demand (APREN, 2021). In fact, Portugal was the fifth country in terms of share of wind, in a ranking led by Denmark with 48%. It is important to note that, in Europe (EU27+UK) wind farms covered 16% of the electricity demand in 2020 (WindEurope, 2021).

The scenarios outlined allow demonstrating the importance of the wind sector contribution to the current energy problem. It is foreseeable that the installed capacity will continue to increase in the coming years. Accompanying the increase of installed wind power capacity, the new wind turbines have also continuously grown in size and output. The wind turbines will have powers considerably higher than the current common values, mainly motivated by economic aspects. Furthermore, the offshore sector will be the one that will grow the most and where technological development will be more relevant. The manufacturer Siemens Gamesa recently launched SG 14-222 DD prototype. This new wind turbine is world's largest and most powerful offshore wind turbine, with 14 MW of capacity and a 222 m diameter rotor (39000 m^2 swept area) (Siemens Gamesa, 2021).

Based on the current scenario and the most likely development model, it is possible to identify various challenges that will arise in the coming years. Among them, the following stand out in this work:

- Cost of energy production;
- Management of the wind energy assets at the end of their operational lifetime, in particularly:
  - Repowering and lifetime extension;
  - Decommissioning and end-of-life management of wind turbine components/materials;
- Limited technical knowledge.

Reducing the unit cost of wind energy is a key to ensuring the competitiveness and growth of the wind sector (Dao, Kazemtabrizi and Crabtree, 2019). In addition to the relevance of reducing the cost of installation of the wind power plants (CAPEX - Capital Expenditure), the reduction of the costs over the period of their operation (OPEX - Operational Expenditure) also represents an important vector for competitiveness. Due to the downtime, operation and maintenance interventions can take 3% of wind turbine total production lifetime (Tchakoua *et al.*, 2014). In this way, the operation and maintenance costs have an important impact on wind power's Levelized Cost of Energy (LCOE), constituting 10% to 20% of the LCOE, and reaching up to 35% at the end of life (Walford, 2006).

It is important to reduce these costs where possible, by optimizing the operational and maintenance strategies of the wind farms, based on monitoring system that can remotely assess the condition of several components of the wind turbines. In this way, it is possible to optimize the maintenance interventions according to loss of production, availability of replacing components and meteorological conditions. Note that, if a corrective maintenance strategy is adopted, unplanned downtime reduces the wind turbine efficiency, since it is difficult to predict, and can make up 30% to 40% of total operation and maintenance costs (Walford, 2006; Reder, Gonzalez and Melero, 2016). On other hand, recognition of the role of monitoring systems in reducing the risks of the assets by insurance institutions will lead to a reduction in insurance premiums.

As every energy technology, wind energy assets have an end of their operational lifetime. In EU, a significant proportion of the installed wind turbines, the generation installed in the 2000s, will come to the end of its lifetime between 2020 and 2030. It is expect that on the next five years (2021-25), 38 GW in Europe will reach the end of their design life and will require a decision on whether to repower, extend the life of the asset or decommission. It is estimated that about 2.4 GW will be repowered and 7 GW will be fully decommissioned. All decommissioned and repowering capacities came from onshore wind. Complex permitting rules are the key factor behind the slow acceptance of repowering projects in Europe. As an example, Austria had a net negative installation of -39 MW in 2020, with 64 MW decommissioned and only 25 MW commissioned (WindEurope, 2021). Out of the 14 GW of onshore wind installed in 2021, only 515 MW came from repowering projects. Most repowering took place in Germany, which have included rules for repowering in their national legislation (WindEurope, 2022).

Tapping into the potential of repowering depends on the existence of a robust regulatory framework, which creates the business case for such projects. Therefore, it is essential to create a regulatory framework that defines the rules for the actions to be taken at the end of the useful life of these assets and put in place effectives strategies for repowering and lifetime extension. The continuous monitoring of these assets allows to assess the evolution of the wear of the wind turbine support structure over time. Information that is essential in decision making when reaching the maximum expected lifetime.

On the other hand, decommission is the last owners' decision, based on the site-, project- and country-specific economic case. In Europe, 396 MW of onshore wind power was decommissioned in 2021 (WindEurope, 2022). Many parts of wind turbines can be recycled. However, this is hardly ever the case for the composite wind blades. Due to their structural and material complexity, blades are composed of various materials elements that are extremely difficult to separate and recycle. Consequently, composite fibreglass in blades is the most difficult, and the most expensive part of turbines to recycle (Rani *et al.*, 2021). The weight of the blades of a typical 2.0 MW wind turbine is 19.5 tonnes (Ortegon, Nies and Sutherland, 2013). Composites account for more than 90% of the weight of wind turbine blades (Liu and Barlow, 2016). The blade waste provides from three types of sources: manufacturing, service and end-of-life waste. Considering all these sources, a total of 43 million tons of blade waste will be accumulated worldwide by 2050, being 25% of the waste in Europe (Liu and Barlow, 2017).

Several strategies for end-of-life management of wind turbine blades can be adopted, from disposal (landfilling and incineration), via life extension, reuse and recycling, to the development of new generation of blade materials (smart, bio-based and biodegradable materials) (Mishnaevsky, 2021). The European Waste Hierarchy (2008/98/EC directive) illustrates the preferred waste management processes, based on sustainability (EC, 2008). The majority of life cycle assessments assume either landfilling or incineration of used wind blades in their analyses (Sakellariou, 2018).

Focusing on service time extension, there exist several options to increase the service time of wind turbine blades, among them, using more durable materials, ensure better maintenance, repair and reuse. The development of new extra-durable wind blades (designed to survive additional years) can be implemented only in following years with the new wind turbines generation. The reactive options to increase the service time of already installed blades requires improving maintenance and repair. This includes health monitoring, damage reporting and identification (inspection and non-destructive tests) and repair procedures. The condition-based maintenance is a very promising approach to identify damage at an early stage, define repair strategies and extend blade lifetime. This will provide a transitional solution for coming years, until the new recycling technologies and new generation of wind turbine blade materials come on the market (Mishnaevsky, 2021).

Finally, the increase of wind turbine dimensions, in particularly the increase of the height of tower and of the blades length, and the exploration of offshore locations lead to significant uncertainties. More flexible structures subject to difficult-to-predict actions make structural analyses more complex, which translates into greater difficulties in order to avoid resonance problems and rapid wear of the components. The impossibility of significantly optimizing the design of the structures, translates into more expensive final solutions. In this way, experimental data continuously recorded by monitoring system contributes to improve the knowledge on:

- The real loads acting on the rotor and the resulting forces on the blades and tower for different wind speeds and turbulence intensities;
- The effect of the foundation stiffness and the tower-foundation connection stiffness on the overall behaviour of the wind turbine;
- The interaction between neighbouring wind turbines and its effect on fatigue life consumption;
- The aerodynamic damping component and how it is influenced by the wind speed, turbulence intensity, rotor speed and blade pitch angle.

In conclusion, large investments in the implementation of wind turbines were made in the last decades, which increased the importance of this source in the national electricity systems. The management of this asset can strongly benefit from the development of cost effective monitoring strategies. Furthermore, it is crucial to prepare the scientific community and the industry for several challenges, such as the evaluation of the need of replacement of wind turbine components at the end of their design life. The extension of the lifespan of the existing wind turbines, the possibility of the reducing insuring costs by reducing the operation risk through monitoring and reducing uncertainties and optimizing the design of wind turbines will certainly contribute to increase the competitiveness of this energy source.

1.2 OBJECTIVES AND MAIN CONTRIBUTIONS

The thesis here presented is framed by the WindFarmSHM Research Project, which aims at the development, implementation, validation and optimization of new methodologies to continuously assess the structural elements of wind turbines, tower, blades and foundation. The main goal is the development of a monitoring strategy to identify structural changes in the support structure and to estimate the fatigue damage evolution of a family of wind turbines, using optimized monitoring schemes involving only a subset of wind turbines. Figure 1.3 gives an overview of the monitoring strategy under development.

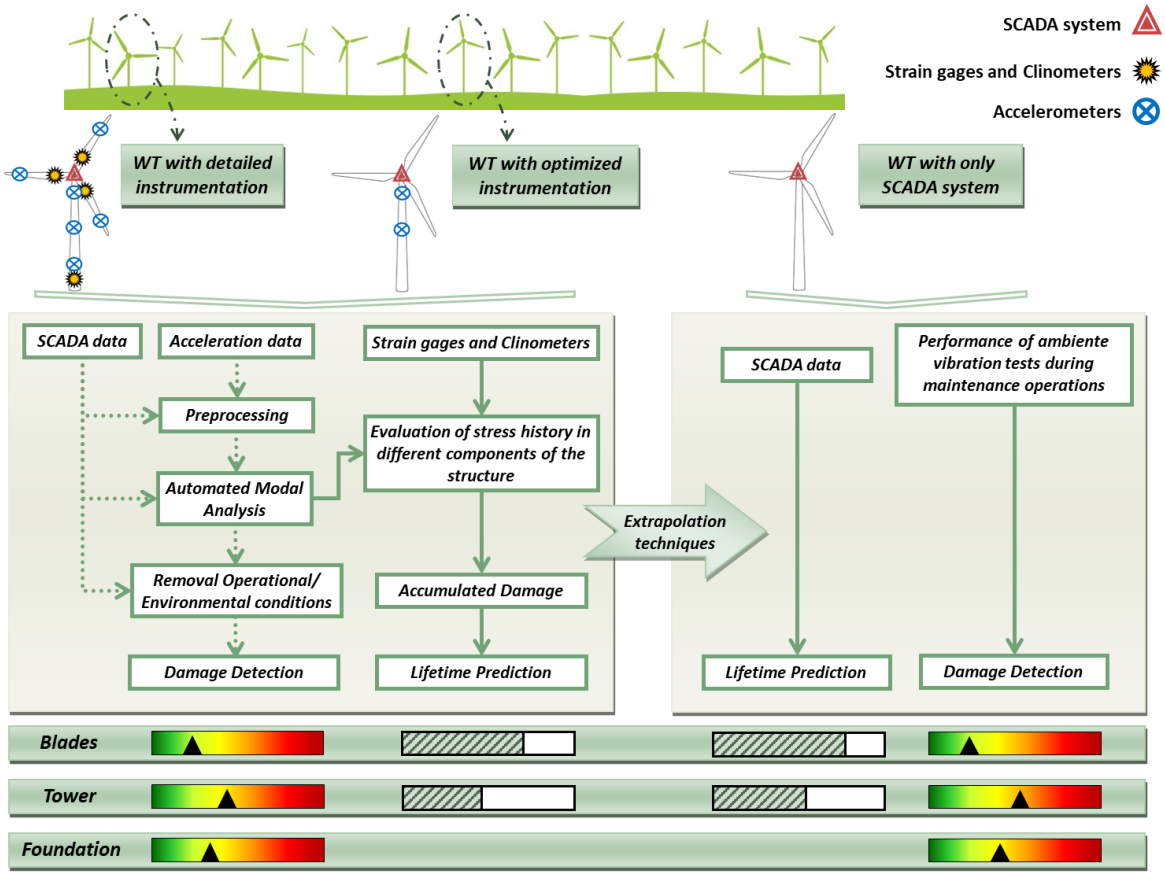


Figure 1.3 – Monitoring strategy to be applied in the context of a wind farm.

The monitoring strategy was designed to be applied in the context of a wind farm. Using optimized instrumentation layouts at a subgroup of wind turbines and taking profit from the data provided by the acquisition systems already available in all the wind turbines, the SCADA system that characterizes the environmental and operational parameters, for the use of extrapolation techniques to assess all the wind turbines of the same wind farm.

This work has a large experimental component and includes the simultaneous instrumentation of several wind turbines of an onshore wind farm, comprehending accelerometers, strain gages and clinometers, distributed in the blades, tower and foundation, and the development of numerical models for the generation of complementary data. The data processing has in mind two main goals:

- Detection of stiffness reductions motivated by the appearance of damage;
- Evaluation of the remaining fatigue life of the main structural components.

To achieve these goals, the development of a complete monitoring system addresses the following objectives:

- Innovative monitoring software adequate to permanently check the structural health of the tower, blades and foundation, taking into account the automatic tracking of their modal parameters;
- Algorithms for the evaluation of the remaining fatigue life of the main structural components based on direct measurements with strain gages or/and supported by a virtual sensors approach;
- Algorithms to extrapolate results obtained for instrumented wind turbine to non-instrumented wind turbines of the same farm, using SCADA data;
- Proposal of an optimized monitoring system at the level of the wind turbine, considering alternative monitoring layouts with different number of sensors and with different noise levels;
- Proposal of an optimized monitoring system at the level of the wind farm, analysing the minimum number of wind turbines to be instrumented in order to obtain a reliable extrapolation of the obtained results to the full wind farm.

It is expected that the outcomes presented in this thesis may represent an important step in the development of such systems to monitor the most important components of wind turbines, contributing also to better understand the dynamic behaviour of these structures and to increase their safety and lifetime. In this context, the main contributions of the present work are the following:

- Monitoring system optimization analysis, regarding the capacity for damage detection, considering alternative monitoring layouts with different numbers of sensors and sensors with different costs, and so with different noise levels (Chapter 3);
- Conception and assembly of a vibration-based dynamic monitoring system, specially designed to meet the requirements of a wind turbine, able to perform: (1) the online automatic identification of the modal parameters under all operating conditions, to remove the influence of operational and environmental effects and to compute indices permitting to detect the presence of small structural anomalies and, (2) estimate the fatigue condition in tower and blades cross sections (Chapter 4);
- Operation of a monitoring system at Tocha Wind Farm for a period of two years, where the developed routines were tested, demonstrating the ability of the system to estimate the accumulated fatigue damage (Chapter 5);
- Implementation of a strategy to estimate the fatigue state of a wind turbine tower cross section based on strains measurements (Section 5.3);
- Development of tools to extrapolate the accumulated fatigue damage identified in the monitored period to the full life of the wind turbine, using past SCADA data (Section 5.6.4);
- Implementation of a strategy to extrapolate results obtained for one instrumented wind turbine to non-instrumented wind turbines of the same farm, using SCADA data (Section 5.6.5)
- Implementation of a strategy to extract strain signals from fiber optic strain gauges installed at blade roots, considering the temperature effects and an experimental calibration procedure (Chapter 6);
- Validation of tools to estimate the bending moments at blade roots and the accumulate fatigue damage for different operating conditions, based on strains measurements (Section 6.3).

- Analysis of the wake effects on the fatigue consumption of the blades of two instrumented rotors of the same wind farm (Section 6.4).

1.3 ORGANIZATION OF THE THESIS

The objectives described in the previous section conducted to an outline of the present thesis divided in seven chapters. It was the intention of the author to start with a global perspective of the wind turbine behaviour and the text is then progressively oriented towards more detailed aspects of the implementation of the vibration-based analysis and fatigue evaluation. A summarized description of the contents addressed in each chapter is presented in the following paragraphs.

Chapter 1 introduces the present work together with important background and motivation, properly justified by the evolution of the wind sector. The main objectives of the thesis are presented, as well as the principal contributions associated with the research, followed by a brief description of the organization of the text throughout the chapters.

Chapter 2 is essentially dedicated to the description of the components of current wind turbine models. The operation of a wind turbine is explained according to the Blade Element Theory, serving as a mean for a better understanding of some operational aspects of these power plants. Important aspects concerning the dynamic characteristics of wind turbines, typical dynamic behaviour of the tower and rotor blade elements and the most important aspects concern to control strategies are also described. Finally, the topic of structural health monitoring is introduced along with methodologies to process data obtained from the continuous dynamic monitoring of structures. The main challenges associated with their application to wind turbines are also addressed.

Chapter 3 describes the main results obtained with alternative instrumentation strategies tested in a 2.0 MW onshore wind turbine to reduce the costs of the monitoring equipment and at the same time ensure an adequate accuracy in structural damage detection. The work presented here serve as a follow-up of the monitoring campaign conducted in Torrão Wind Farm (Oliveira, 2016), the first experimental campaign presented in this thesis. In order to reduce investment in the acquisition of monitoring equipment, while ensuring adequate accuracy in detecting damage, the original data is manipulated in order to recreate alternative monitoring solutions, designed considering different budgets. The tested alternative monitoring layouts present a varying number of sensors, alternative distributions in the wind turbine tower, and different sensor noise levels.

Chapter 4 introduces a detailed description of the extensive monitoring program performed at the Tocha Wind Farm, the second experimental campaign presented in this thesis. This chapter presents the different layouts adopted in the instrumentation of the wind turbines and shows some results from the fully instrumented wind turbine.

Chapter 5 begins with a brief state-of-the-art and the description of a methodology to estimate the fatigue condition of the tower based on strain measurements. The chapter continues with the analysis of the impact of several processing parameters on the fatigue results using the monitoring data collected at the Tocha Wind Farm. The chapter ends with the application of tools to extrapolate the fatigue damage. The accumulated fatigue damage identified in the monitored period is extrapolated to the full life of the wind turbine, using SCADA data and the results from the instrumented wind turbine are extrapolated to non-instrumented wind turbines, using the SCADA.

Chapter 6 is dedicated to the development of tools to assess the fatigue condition of wind turbine blades from strains measurements with a set of fibre optic strain gages installed at blade roots. This chapter describes the data processing needed to obtain an accurate experimental estimation of the bending moments applied to the blade roots and the procedure to obtain the fatigue damage. The instrumentation of the two wind turbine rotors allows quantifying the interaction between neighbouring wind turbines and its effect on fatigue life consumption.

Finally, **Chapter 7** summarizes the most important conclusions reached after the current work and highlights some potential future research topics.

2
BASICS OF WIND TURBINES BEHAVIOUR AND STRUCTURAL MONITORING

2.1 MAIN COMPONENTS OF WIND TURBINES

Historically, wind turbines can be defined according to several design configurations. The first wind turbines came almost directly from windmill concepts, where wind power has been exploited for mechanical purposes. Although there are several possible configurations for wind turbines, almost all of them that currently contribute to energy production are turbines with upwind rotors and horizontal axis of rotation. Only this typology of wind turbines are analysed in this work. A detailed description of the various configurations and typologies of wind turbines, including less common solutions, can be found in (Hau, 2006).

The main components that are included in most common wind turbines are the nacelle, the rotor and the tower. Figure 2.1 labels the main elements of the typology of onshore wind turbines covered in this work. In a very simple way, the configuration of the blades allows capturing the energy of the wind, transforming it into kinetic energy of rotation. Through a system of shafts, the rotation of the rotor allows activating the generator where electrical energy is produced. Following, the main components are briefly described, as well as the modes of operation.

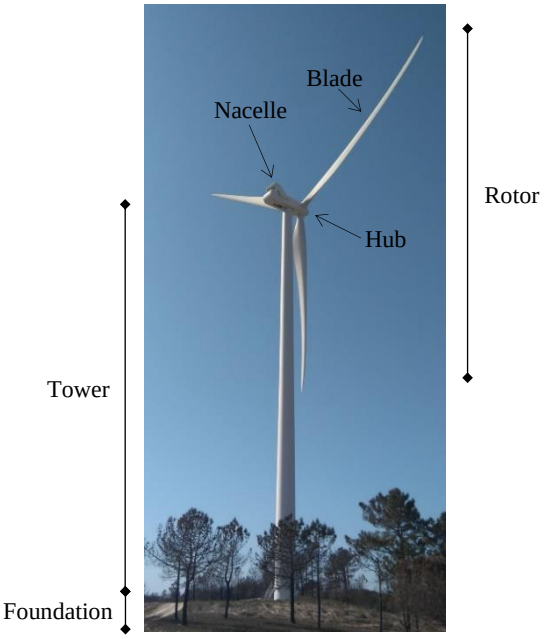


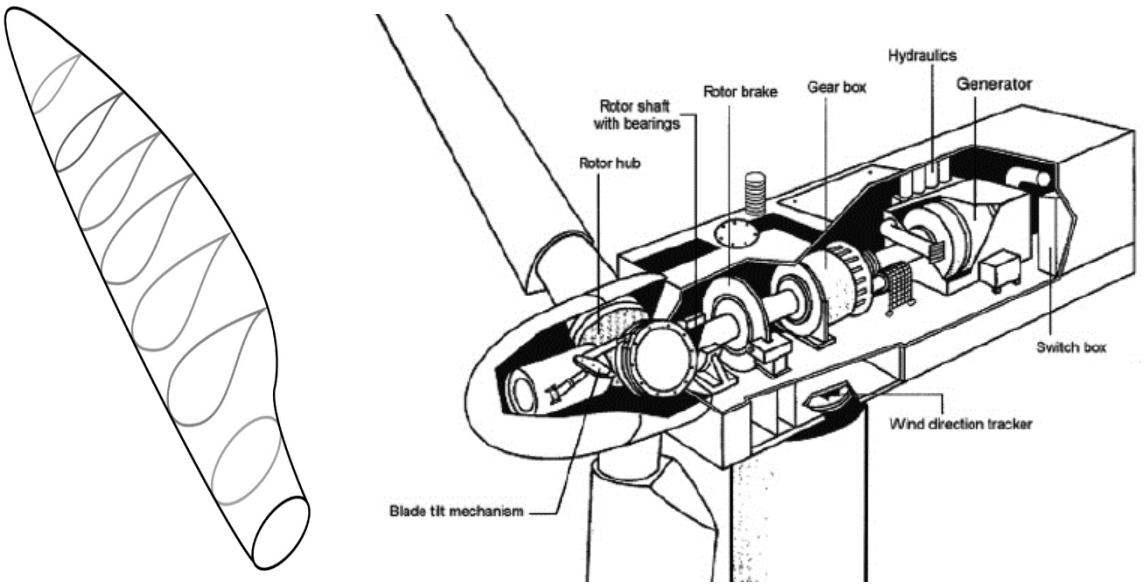
Figure 2.1 – Main wind turbines components of horizontal-axis upwind onshore wind turbines.

Before going on to the description of the main components, it is important to mention that recent wind turbines are usually equipped with a system called SCADA (Supervisory Control and Data Acquisition system). This system allows the operation control of the entire system, as well as the monitoring and recording of several environmental and operational variables, such as wind speed and direction, rotor rotation speed, nacelle orientation, blades pitch angle, wind speed, generator rotation, power output, ambient temperature, among others. Thus, the SCADA system consists of a processing centre together with a wide range of sensors that provide fundamental indicators that will be of paramount importance for the analysis of the data recorded by the structural monitoring systems covered in this work (see Chapters 3 to 6).

The rotor is composed of the blades and the hub (where the blades are connected) and represents the key element of wind turbines, converting the energy of the wind flow into kinetic energy of rotation.

Since the blades capture the energy of the wind, defining their aerodynamic characteristics is extremely important in order to optimize this extraction process. In this sense, these elements have complex cross-sections (called airfoils) that vary along the length of the blade (Figure 2.2a). In addition to the aerodynamic requirements, it is necessary to take into account the physical and mechanical characteristics of the blades, in order to ensure high strength (support operating conditions and cyclical movements during the lifetime), reduced mass (avoid that high efforts are transmitted to the structure) and sufficient rigidity (avoiding efficiency losses and collisions with the tower). The materials most used in the production of these elements are composite materials and carbon fibres, in order to meet the above requirements.

Note that there are rotors with different number of blades (generally 1 to 3 blades). The main difference is in the vibration level that these rotors present for the same excitation, resulting from the variation of the rotor's moment of inertia with the revolution of the blades. In fact, it is the 3-blade rotors that present the best performance at this level, being currently the most used typology (Hau, 2006). In this work, only rotors composed of three blades are discussed.



(a) (b)

Figure 2.2 – Upwind onshore wind turbine: (a) Variation of the airfoil blade length; (b) Main mechanical components inside the nacelle (adapted from (Wagner, 2020)).

The nacelle, represented schematically in Figure 2.2b, is located at the top of the tower and comprises several mechanical and electrical components that allow the production of electrical energy by the generator through mechanical energy transmitted from the rotor. For most turbines, the nacelle has a split shaft system, in which the main shaft (rotor shaft) rotates together with the hub at a reduced speed, transmitting torque to the high-speed secondary shaft (generator shaft) through the gearbox. The need to increase the speed of rotation of the generator shaft (factors around 100 are common) is justified by the difference between the operating speeds of most generators and the rotor.

There are also several mechanisms in the nacelle, such as the mechanical brake (allows interrupting the turbine operation in an emergency), the yaw system (mechanically orienting the nacelle with the direction of the wind) and the blade pitch angle system (controls the wind energy captured by the rotor). Although these are not described in this work, there are alternative concepts for nacelle configurations, among which direct drive generators stand out. It is a typology in which there is no gearbox and in which the hub and the generator are connected by a single low-speed shaft.

The main function of the wind turbine tower is to support the nacelle and the rotor, while allowing the necessary elevation of the rotor to a certain height, in order to maximize the use of the system according to the characteristics of the wind flow, which presents higher speeds and less turbulence for higher heights (vertical wind speed profile described in the next section).

Nowadays, the most used material in the construction of this component is steel, although prestressed reinforced concrete solutions have also been used. The construction's weight, strength, slowness of construction process and complexity are the downsides of concrete solutions and make it less common. There are four main types of towers: tubular steel, metallic truss, tubular reinforced concrete and hybrid solutions (Hau, 2006). The most used solution is tubular steel towers. Generally, these are composed of steel plates, moulded in a circular fashion and welded together, forming segments with 20 m to 30 m in length. The various segments are then joined using bolted connections on the flanges at the ends, thus eliminating welding processes at the construction site. Due to the greater concentration of efforts at the bottom of the tower, its diameter increases from top to bottom, as does the thickness of the shells.

The high level of acceptance of this typology is mainly due to two factors: at the assembly level (reduced assembly times and its transport is facilitated as assembly is carried out on site) and at the design level (uniform behaviour in all directions and knowledge of this type of solution). However, it is important to emphasize that the tendency for the turbines to grow in size has caused difficulties both in transporting the tower segments with larger diameters, as well as in guaranteeing the necessary stiffness values using tubular steel sections.

Finally, it is important to highlight the importance and complexity of the design of this structural component. Taking into account the slenderness of the tower, the mass located on its upper part and the movements of the rotor, the design of this structural element requires the study of very complex dynamic problems. Tower stiffness is an important factor in wind turbine system dynamics due to the possibility of coupled vibrations between the rotor and tower subsystems.

In fact, the tower stiffness is a major consideration in the overall design of a wind turbine. In order to prevent resonant problems in the wind turbine system, it is imperative to avoid a match of the natural frequency of the tower with the frequency of rotor rotation and its harmonics. To achieve this goal, three configurations can be followed:

- Stiff-stiff tower: frequency of rotation of the rotor is lower than the tower natural frequency;
- Soft-stiff tower: tower natural frequency is tuned in order to be placed between the operating rotational frequency (1Ω) and its first integer multiple (3Ω for three-blades rotors);

- Soft-soft tower: tower natural frequency lower than operating rotor rotational frequency.

For fixed-speed wind turbines, the range of possible values for the tower natural frequency is wider. However, current wind turbines are equipped with variable-speed rotors. In this case, the range for the tower natural frequency becomes much narrower and the range of operation of the rotor needs to be constrained.

To exemplify the relationship between the tower stiffness and the range of rotor operation, two models of wind turbines studied in the scope of this work are considered. The Senvion MM82-2MW wind turbine that will be introduced in Chapter 3 and the Vestas V100-1.8MW wind turbine installed at Tocha Wind Farm that will be introduced in Chapter 4. Both models operate at variable rotor speeds. However, Senvion model has a wider operating range (from 8.5 to 17.1 rpm) while Vestas model operates between 8.8 to 14.9 rpm. Colour maps with the signal spectra are show in Figure 2.3, where the dominant frequencies of the wind turbine towers are characterized as a function of the rotor speed. The operating range of the rotor is also specified.

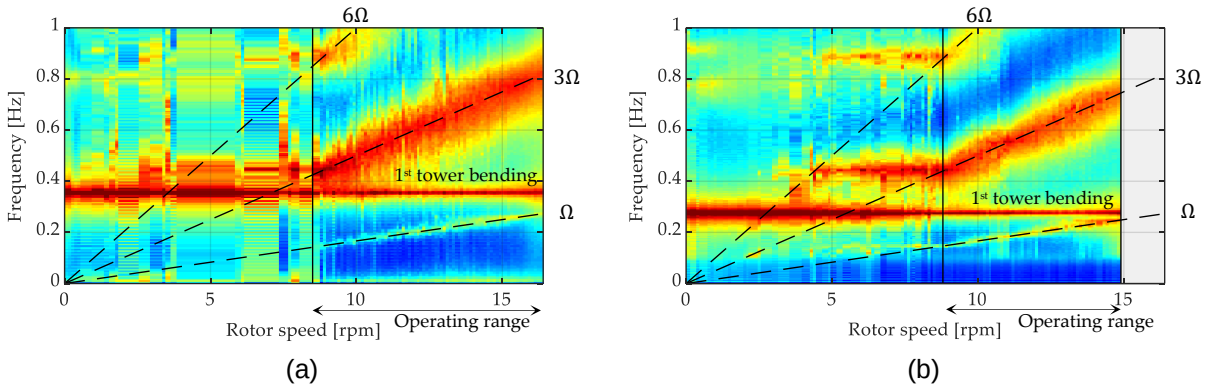


Figure 2.3 – Campbell diagram of: (a) Senvion MM82-2 MW wind turbine; (b) Vestas V100-1.8 MW wind turbine (the diagonal dashed lines represent the harmonic frequencies associated with the rotor rotation).

In the figures, the two well defined horizontal alignments around 0.35 Hz (Senvion model) and 0.27 Hz (Vestas model) are clearly visible along the whole rotor speed regimes. In fact, they both correspond to the first pair of closely spaced vibration modes of the towers in the FA and SS directions. In both cases, the first natural frequency of the tower remains above the rotational speed (1Ω) and below the integer multiple 3Ω. Thus, both models are classified as soft-stiff towers.

Note that it is imperative to avoid a match of the natural frequency of the tower with the frequency of rotor rotation in order to prevent resonant problems. Taken in to account that the first natural frequency of the tower bending is smaller for Vestas model (around 0.27 Hz), the maximum rotor speed is limited in order to avoid that the rotational speed crosses the first natural frequency of the tower. The diagonal alignment corresponding to 1Ω grows with the rotor speed, from 0.147 Hz, when rotor speed is around 8.8 rpm, to 0.248 Hz for 14.9 rpm. However, it never reaches the first natural frequency of the tower in order to avoid tower resonance phenomena. On the other hand, the first harmonic at Senvion model grows from 0.142 Hz (8.5 rpm) to 0.285 Hz (17.1 rpm).

Finally, the foundation has the function of ensuring the stability of the structure and directing its loads to the ground, that is, preventing the structure from settling due to gravitational loads, preventing it from sliding due to horizontal loads and preventing collapse due to moments in the base. Furthermore, it is important to note that the definition of the foundation's design and construction will influence the dynamic behaviour of the entire structure.

At this point, it is important to distinguish the foundation type of onshore and offshore wind turbines. In fact, while the foundations of onshore solutions follow the traditional concepts of most civil engineering structures, offshore solutions have adopted much of the knowledge that has been developed in the offshore oil and natural gas exploration industry.

Foundations for onshore wind turbines are based on well-known and widely explored concepts in civil engineering, with two main solutions: slab foundations (direct foundations) or pile foundations (indirect foundations).

Slab foundations are used when the soil close to the surface is of sufficient quality to support the anticipated loads. In this type of solution, the turning moments at the base are compensated by the eccentricity of the reaction, while the vertical loads are distributed over the foundation area and the friction developed in the surface of the soil-foundation interaction balances the horizontal loads. This solution consists of a reinforced concrete slab that generally has a polygonal geometry and variable thickness. On the other hand, pile foundations are used for soils of lower quality, or with insufficient quality to meet the necessary requirements. They are also made up of a reinforced concrete slab from which a number of piles are joined and extended until a soil layer of sufficient quality is reached. For this case, all the loads are absorbed by the ground through the lateral and/or tip resistance of the piles.

2.2 AERODYNAMIC BEHAVIOUR

2.2.1 WIND ACTION

The characterization of wind conditions is a key factor in the entire process of designing a wind project, from the identification of suitable locations and forecasts of economic viability, through the design of the park and turbines, to the assessment of the consequences on the network for distribution and on consumers. Thus, this section presents a brief description of the parameters that allow characterizing the wind resource. This description is mainly supported by the standard IEC 61400-1 (International Electrotechnical Commission, 2014), which can be consulted for further details of these concepts.

This standard divides the wind regimes for the calculation of loads and safety checks under normal wind conditions, whose probability of occurrence is high during the useful life of the structure, and extreme conditions, which are defined considering return periods of 1 or 50 years. All models are based on a parameter called reference wind speed (V_{ref}). A wind turbine designed for a given V_{ref}, will be able to withstand conditions where the extreme value of the average wind speed for periods of 10 minutes at the height of the hub, in a 50-year payback period, is less than or equal to V_{ref}.

From the point of view of wind energy exploration, the high variability of the wind, both geographically and temporally, is its main singularity and makes its characterization complex. To overcome this difficulty, the characterization of the wind resource is generally supported by the evaluation of the following parameters: flow turbulence, flow slope, vertical velocity profile, extreme winds, velocity frequency distribution and air density.

The wind always presents turbulent characteristics, that is, the flow is chaotic, with random periods that vary in the order of a few seconds. Turbulence can be understood as the fluctuation of wind speed and direction around its mean values. The main sources of turbulence are the friction of the air mass with the earth's surface and thermal effects.

Thus, wind speed can be decomposed into its average component and the three turbulent components (longitudinal, lateral and vertical). The most used statistical parameter in the characterization of turbulent wind components is the standard deviation. From the ratio between the standard deviation of each turbulent component and the average velocity at a given level, the turbulence intensity of each component can be obtained. In the field of wind energy, turbulence intensity curves are defined as a function of the wind speed at the hub height. Turbulence intensity is defined by random variations in wind speed for 10-minute time interval averages.

An important aspect in the characterization of turbulence is the configuration of wind farms. The wake effect has two main consequences on wind turbine located in the wake of their neighbours: the decrease in wind energy and the increase in the experienced turbulence. Thus, the IEC 61400-1 standard defines effective turbulence intensity as the sum of ambient turbulence plus wake effects.

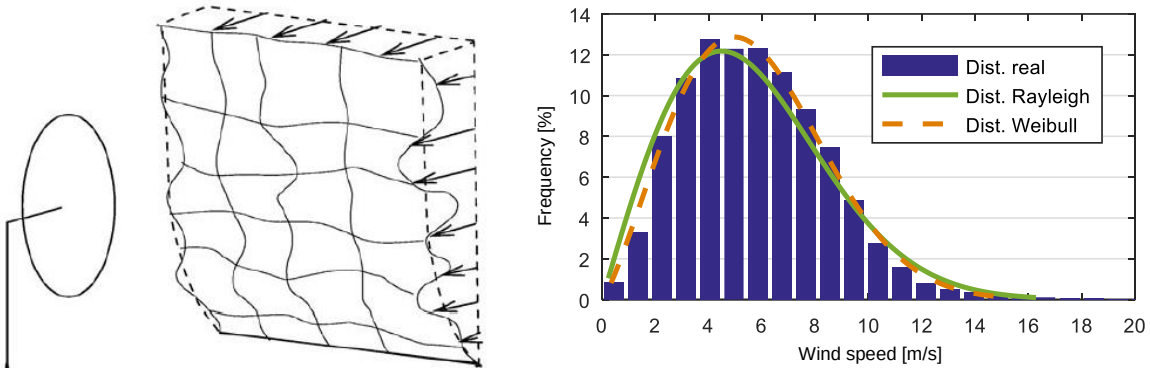
The slope of the flow, in relation to the horizontal, is mainly motivated by the slope of the terrain. The standard indicates that mean angles of the flow in relation to the horizontal plane between -8º and 8º must be considered, assuming that this angle does not vary with height.

The vertical profile of wind speeds is in accordance with the boundary layer theory that assumes a practically null value at the surface, which increases with height until reaching the undisturbed flow velocity. In Figure 2.4a, the velocity profile is schematically represented considering the influence of turbulence. The shape of the profile is conditioned by the roughness of the terrain, the orography and the heat flow. According to the same standard, the velocity profile is approximated by a power law model, in which the wind velocity $V(z)$ is given as a function of the z height above the ground by the expression:

$$V(z) = V_{hub} \cdot \left(\frac{z}{z_{hub}}\right)^{\alpha} \tag{2.1}$$

with:

V_{hub}	Wind speed at hub height
z_{hub}	Hub height in relation to ground level
α	Shear factor: $\alpha = 0.2$ according to IEC 61400-1 standard for normal wind conditions



(a) (b)

Figure 2.4 – Wind resource characterization: (a) Vertical profile of wind speeds considering the turbulence effect (adapted from (M. Hansen, 2015)); (b) Distribution of mean wind speed frequencies measured at Tocha Wind Farm and respective fit of Rayleigh and Weibull distributions.

The frequency distribution of wind speeds is an important parameter in the design of a wind turbine, mainly because it allows determining the frequency of each individual load considering normal design conditions. For the statistical analysis of the wind speed distribution, there are two models that can be used: the Rayleigh distribution and the Weibull distribution. The corresponding mathematical formulations are presented in the following equations.

$$P_{Rayleigh}(V_{hub}) = \frac{\pi}{2}\left(\frac{V_{hub}}{V_{ave}^2}\right) exp\left\{-\frac{\pi}{4}\left(\frac{V_{hub}}{V_{ave}}\right)^2\right\} \tag{2.2}$$

$$P_{Weubull}(V_{hub}) = \frac{k}{A}\left(\frac{V_{hub}}{A}\right)^{k-1} exp\left\{-\left(\frac{V_{hub}}{V_{ave}}\right)^{k}\right\} \tag{2.3}$$

with:

V_{ave}	Average annual wind speed at hub height: $V_{ave} = 0.2 \cdot V_{ref}$
k	Form factor
A	Scale factor

In this way, the average value of the wind speed at the hub's elevation, in periods of 10 minutes, may assume one of the previous distributions. Figure 2.4b represents the wind speed frequency distribution obtained from measurement at the meteorological tower of the Tocha Wind Farm in 2017 (histogram), to which a distribution was fitted according to the Rayleigh model (green line) and according to the

Weibull model (dashed orange line). A good similarity between the two distributions adopted and the experimental distribution is confirmed.

Wind turbines must be able to withstand extreme wind conditions, which include extreme wind speeds, gusty winds due to storms and extreme variations in wind speed and direction. These extreme conditions must be characterized considering different periods of recurrence. According to the standard, the following must be adopted: the average speed (extreme values of the average speed at intervals of 10 minutes) and maximum burst (average speed at intervals of 3 seconds), in both cases considering a recurrence period of 50 years. Changes are also introduced to the calculation models that define the vertical velocity profile and the velocity distribution, in order to consider the different characteristics of this type of flow. Various transient events are also defined for which an adequate response of the structure must be guaranteed.

Finally, the density of the air mass, despite being a parameter with reduced variance, influences the aerodynamic loads applied to the structure, so it must be correctly characterized. The standard indicates the value of $1{,}225\ kg/m^3$.

2.2.2 Rotor Aerodynamic Behaviour

After completing the introduction on the characterization of wind action, the next step focuses on the process of extracting energy from a free flow of air by the rotor. The Axial Momentum Theory allows explaining this process, assuming that the kinetic energy of the flow is extracted when passing through a disk, formed in the plane of the rotor and delimited by the length of the blades, and that this process affects only the mass of air that passes through this disk. As shown in Figure 2.5, considering the mass flow rate constant, as the airflow approaches the disk, it decreases its velocity and, consequently, expands its cross-sectional area.

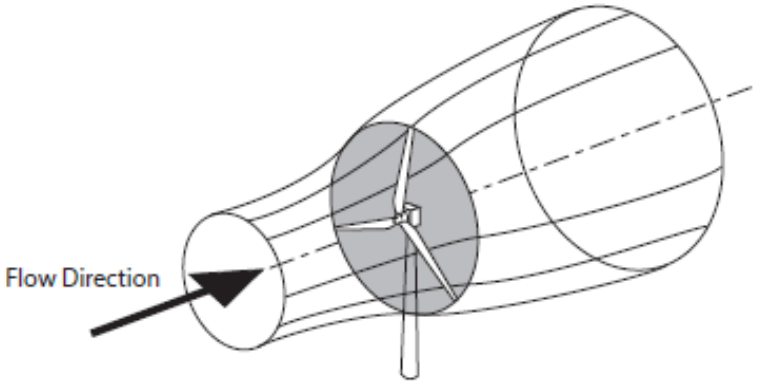


Figure 2.5 – The energy extracting stream tube of a wind turbine (adapted from (Burton et al., 2011)).

In Figure 2.6, a control volume corresponding to an ideal wind turbine is represented, in which it is assumed that the flow is stationary and that the external pressure surrounding the control volume is zero (volume involved by the ambient pressure). Applying the axial moment theory, the axial thrust force (T) acting on the rotor is given by:

$$T = \rho \cdot U_{\infty}^2 \cdot A_1 - \rho \cdot U_W^2 \cdot A_2 \quad (2.4)$$

with:

T	Axial thrust force of the rotor
ρ_{ar}	Mass density of air
U_*	Wind velocity (in section * of Figure 2.6)
A_*	Area of cross section (in section * of Figure 2.6)
$*_{\infty}$,$*_1$	Section far ahead of the rotor
$*_W$,$*_2$	Section far wake of the rotor

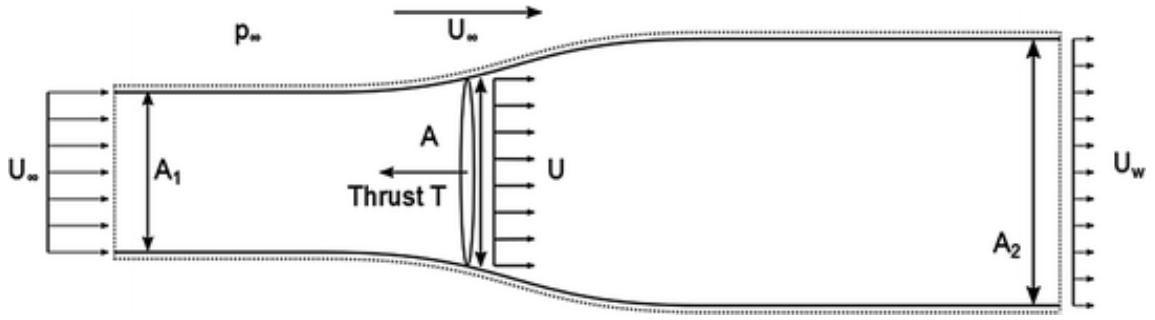


Figure 2.6 – Actuator disc with stream tube (adapted from (Cruz & Atcheson, 2016)).

Bearing in mind the principle of conservation of mass and the fact that the flow is considered to be in the steady state:

$$\dot{m} = \rho \cdot U \cdot A = \rho \cdot U_{\infty} \cdot A_1 = \rho \cdot U_W \cdot A_2 \quad (2.5)$$

with:

$\dot{m}$	Mass flow rate

In this way, the impulse force can then be defined as:

$$T = \dot{m} \cdot (U_{\infty} - U_W) = \rho \cdot U \cdot A \cdot (U_{\infty} - U_W) \quad (2.6)$$

Since the flow velocity should be equal immediately upstream and downstream of the rotor disk and the pressure is identical in the sections sufficiently spaced upstream and downstream of the disc, the pressure variation (Δp) in the vicinity of the disk is given by:

$$\Delta p = {}^1/_2 \cdot \rho \cdot (U_{\infty}^2 - U_w^2) \quad (2.7)$$

In this way, defining the impulse force according to the pressure variation in the vicinity of the disk:

$$T = A \cdot \Delta p = {}^{1}/_{2} \cdot \rho \cdot A \cdot (U_{\infty}^{2} - U_{w}^{2}) \tag{2.8}$$

Since the value of extracted power (P) is obtained from the rate of work performed by the thrust force on the rotor disk, then:

$$P = T \cdot U = {}^{1}/_{2} \cdot \rho \cdot U \cdot A \cdot (U_{\infty}^{2} - U_{w}^{2}) \tag{2.9}$$

In an attempt to define the degree of deceleration of the air mass in the rotor disc vicinity, it is common to introduce the axial induction factor (a), given by:

$$a = \frac{U_{\infty} - U}{U_{\infty}} \rightarrow \begin{cases} U = (1 - a) \cdot U_{\infty} \\ U_{w} = (1 - 2 \cdot a) \cdot U_{\infty} \end{cases} \tag{2.10}$$

Analysing the relationships presented in the equation (2.10), it is concluded that if $a > 1/2$ then $U_w < 0$, which would mean a flow reversal (an invalid phenomenon for this case study). That is, considering an extreme situation, the flow is stopped for $a = 1/2$.

Starting from the relationships presented in the equation (2.10), equation (2.9) can be rewritten as follows:

$$P = T \cdot U = \left[{}^{1}/_{2} \cdot \rho \cdot U_{\infty}^{3} \cdot A\right] \cdot 4a(1 - a)^{2} \tag{2.11}$$

In this equation, the first term of the multiplication (square brackets) represents the power available that is present in the flow, while the second term represents the efficiency of capturing this power. This term is usually called the power coefficient (C_p). It is easily verified that the maximum value of C_p is (Manwell et al., 2010):

$$a = \frac{1}{3} \Rightarrow C_{p}^{Máx} = \frac{16}{27} \approx 59.3\% \tag{2.12}$$

The value of $16/27$ is called the Betz limit and is considered the theoretical maximum limit of power extracting from a given flow. This means that, regardless of the machine's efficiency, no wind turbine can extract more than 59.3% of the power available of the wind.

Although the axial moment theory is quite useful for understanding the extraction of power by the rotor, it has several limitations that derive from the assumptions on which it is based, listed in (Manwell et al., 2010). Among these limitations is the assumption that the wind flow remains as an undisturbed axial flow after passing through the rotor. In fact, when the air flow mass passes through the rotor, part of its

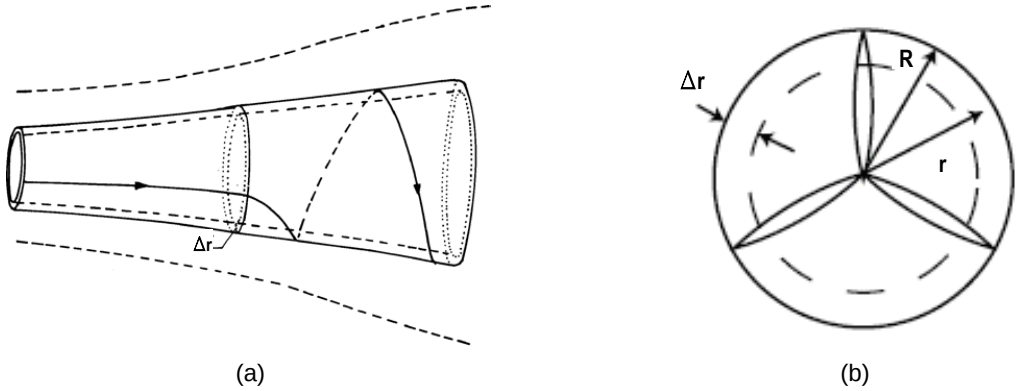
energy is transformed into torque applied to the generator shaft to produce electrical energy. The fundamental laws of mechanics imply that a reaction of equal magnitude and opposite direction is applied to the wind flow (Figure 2.7a). A rotational conveyor flow is thus generated, with a direction opposite to the rotation of the rotor, in reaction to the moment exerted by the flow on the rotor. Following the theory of angular momentum, it is possible to overcome this limitation.

Since the tangential rotor speed is not constant for all radial positions, rings of radius r and thickness Δr are considered that define areas equal to $2 \cdot \pi \cdot r \cdot \Delta r$, as shown in Figure 2.7b). Thus, the tangential velocity of the belt flow at a distance r from the center of the rotor (component of the velocity of the air flow tangential to the rotation of the rotor in the radius ring r) is given by:

$$V_{\omega} = 2 \cdot r \cdot \Omega \cdot a' \tag{2.13}$$

with:

V_{ω}	Flow rotational speed
r	Radius of the annular rings
Ω	Angular velocity of the rotor
a'	Angular induction factor $a' = \frac{\omega}{2 \cdot \Omega}$



(a) (b)

Figure 2.7 – Angular momentum theory: (a) Rotational flow model after the passage of the air mass through the rotor plane; (b) Angular ring geometry of wake wind flow (adapted from (Manwell et al., 2010)).

The disc is then formed by annular rings, which independently contribute to the rotation of the fluid passing through the disc. Thus, the torque (ΔQ) in each rotor ring is defined as the change in the angular momentum of the fluid that passes through the ring, expressed by:

$$\Delta Q = \rho \cdot 2 \cdot \pi \cdot r^2 \cdot U_{\infty}(1 - a) \cdot V_{\omega} \cdot \Delta r \tag{2.14}$$

Once the rotor torque is defined, it is possible to determine the corresponding extracted power:

$$\Delta P = \Delta Q \cdot \Omega \tag{2.15}$$

Equating the power extracted by the rotor (equation (2.15)) with the power derived from the theory of axial momentum (equation (2.11)) it is possible to obtain the relationship between the axial and tangential induction factors, called local speed ratio (TSR_{local}). Considering the outer radius of the rotor (R), the tip speed ratio (TSR) is obtained.

$$TSR_{local} = \frac{\Omega \cdot r}{U_\infty}, \qquad TSR = \frac{\Omega \cdot R}{U_\infty} \tag{2.16}$$

$$a(1-a) = TSR_{local}^2 \cdot a'.(1+a') \tag{2.17}$$

The power extracted by each ring of radius r and thickness Δr is given by:

$$\Delta P = \left[\frac{1}{2} \cdot \rho \cdot U_\infty^3 \cdot 2\pi \cdot r \cdot \Delta r\right] \cdot [4 \cdot a'(1-a) \cdot TSR_{local}^2] \tag{2.18}$$

In the equation (2.18), the term defined in the first parentheses represents the power of the flow, while the second term refers to the efficiency of the element that captures the power.

Although the axial and angular momentum theories already explain the extraction of power from the wind flow, the problem is not yet complete as the axial and angular induction factors (a and a') are still unknown. Thus, a final step is needed, which is to determine the aerodynamic power of the rotor of a wind turbine by applying the Blade Element Theory, which combines the previous moment analysis (axial and tangential directions) with the blade element theory.

Following the blade element theory, it is possible to relate the aerodynamic lift $\vec{L}$ and drag $\vec{D}$ forces that act on a blade element of width Δr and section chord length c for a wind mass velocity equal to $\vec{V}$, by the following expressions:

$$\Delta\vec{D} = \frac{1}{2} \cdot C_d \cdot \rho \cdot \vec{V}^2 \cdot c \cdot \Delta r, \qquad \vec{D} \parallel \vec{V} \tag{2.19}$$

$$\Delta\vec{L} = \frac{1}{2} \cdot C_l \cdot \rho \cdot \vec{V}^2 \cdot c \cdot \Delta r, \qquad \vec{L} \perp \vec{V} \tag{2.20}$$

with:

C_d	Drag coefficient
C_l	Lift coefficient
$\vec{V}$	Relative velocity between the blade element and the wind: $\vec{V} = \sqrt{[U_\infty(1-a)]^2 + [\Omega \cdot r(1+a')]^2}$

The drag C_d and lift C_l coefficients are a function of the angle of attack α and of the blade cross-section shape (arifoil), although surface roughness may also have some influence. These coefficients are usually determined using tests in wind tunnels or through numerical simulations.

In Figure 2.8, the relationship between the relative wind speed (V) (axial and angular component) and lift (L) and drag (D) forces is schematically illustrated. In the same figure, β represents the pitch angle, α is the angle of attack and φ represents the inflow angle. The length of the blade section chord c is given by the maximum distance along the longitudinal axis of the section.

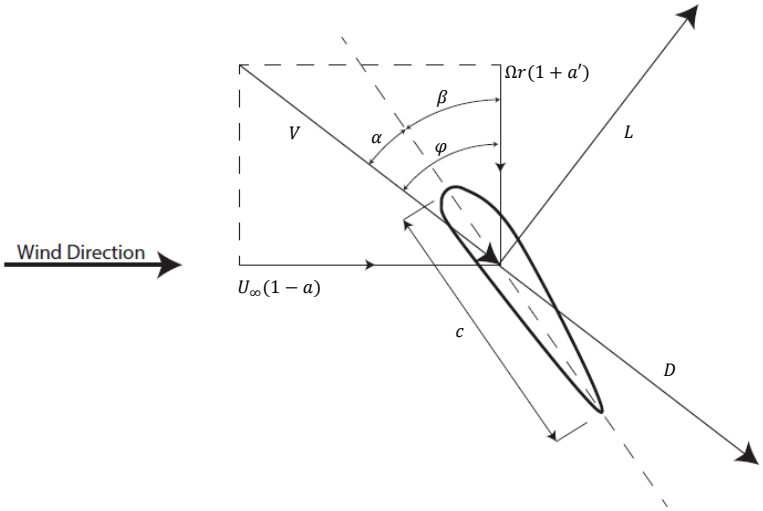


Figure 2.8 – Relative wind velocity applied to the airfoil and the subsequent lift and drag forces (adapted from (Oliveira, 2016)).

In blade element theory, the forces acting on the rotor are expressed as a function of its configuration and orientation. Thus, each blade is discretized into n elements along its longitudinal axis, forming rings of width Δr. From what has been exposed so far, it appears that for a given blade element belonging to the radius ring r, the inlet angle of the flow can be determined by:

$$tan\,\varphi = \frac{U_\infty(1-a)}{\Omega \cdot r(1+a')} \tag{2.21}$$

The aerodynamic characterization of the rotor is completed with the application of the blade element theory. For each of the rings in which the blades were discretized, the impulse force and torque equations derived from the blade element theory (BE) are equated with the corresponding equations derived from the moment analysis (MA).

$$\Delta T_{MA} = 4 \cdot \pi \cdot r \cdot \rho \cdot U_\infty^2 \cdot a(1-a) \cdot \Delta r \tag{2.22}$$

$$\Delta Q_{MA} = 4 \cdot \pi \cdot r^3 \cdot \rho \cdot U_\infty \cdot \Omega \cdot a'(1-a) \cdot \Delta r \tag{2.23}$$

$$\Delta T_{BE} = n \cdot [L(C_l) \cdot cos\,\varphi + D(C_d) \cdot sin\,\varphi] \cdot \Delta r \tag{2.24}$$

$$\Delta Q_{BE} = n \cdot [L(C_l) \cdot sin\,\varphi - D(C_d) \cdot cos\,\varphi] \cdot r \cdot \Delta r \tag{2.25}$$

In conclusion, and seeking to facilitate the interpretation of the presented methodology, the six main steps for the implementation of a BEM algorithm are now listed (only the main steps are presented, additional details can be found in (Cruz & Atcheson, 2016):

1. Assume initial values for the axial (a) and angular (a') induction factors;
2. Determine the angle of inflow φ (eq. (2.21) and the local angle of attack $\alpha = \varphi - \beta$;
3. Determine the lift and drag coefficients: $\{C_{1,}C_d\} = f(\alpha, Airfoil)$;

4. Obtain updated values for the axial (a) and angular (a') induction factors from the blade element theory: $\Delta T_{MA} = \Delta T_{BE}$ and $\Delta Q_{MA} = \Delta Q_{BE}$;
5. If the new induction factors obtained present a variation greater than a certain pre-established tolerance, comparing with the initial values, repeat steps 2 to 4 considering the new induction factors;
6. Upon completion of the previous iterative process, the local forces acting on the blades are determined with the final values of a and a'.

Finally, it is important to mention some of the limitations of the presented method that can considerably affect the results. On the one hand, the theory presented considers that the adjacent blade sections, defined by the various rings, are independent of each other. Although this is a simplification, the error is acceptable when considering normal operating conditions.

Contrary to what was concluded with equation (2.10), conveyor flow reversal to $a > 0.5$, it appears that for high values of TSR, which correspond to high values of a, the permeability of the rotor is almost comparable to a disk. Thus, it is proposed in (Glauert, 1926) a correction of the curve of the axial induction factor that takes into account the described effect.

Finally, the loss of power production near the tip of the blades (tip loss factor) is another important limitation of the method. This behaviour is due to the discrete number and finite length of the blades and can be overcome using the Prandtl approximation (Burton et al., 2011).

2.2.3 Aerodynamic Control Strategies

Currently, all commercial wind turbines are equipped with control systems that ensure their proper functioning throughout the various operating conditions, having as main objectives: to maximize power production and avoid overloading the structure. Control systems are divided into passive and active systems. Simply put, passive systems use natural phenomena to ensure that a given variable stays within certain established limits. For example, loss of rotor aerodynamic efficiency when wind speed exceeds a certain critical level, known as stall control. Active systems, on the other hand, use sensors to monitor the evolution of certain variables and electrical, mechanical, hydraulic or pneumatic means that perform the necessary control actions.

Having introduced the main aspects related to the aerodynamic performance of wind turbines, this section has as main objective to describe the operation control systems of variable speed wind turbines (designed to achieve maximum aerodynamic efficiency in a wide range of wind speeds). As these are the most common systems, the aerodynamic control of the blades (pitch angle control) or the control of the rotational speed of the rotor using the generator torque will be described.

The control of the pitch angle is a system that allows changing the geometry of the rotor, through the rotation of the blades around their longitudinal axis, using mechanical systems installed in the respective roots. The pitch angle variation allows adjusting the blade attack angle, thus regulating the rotor rotation speed, keeping the moment applied to it constant. It is possible with this system to reach pitch angles of $\beta = 90°$, making the lift force acting on the rotor practically null. The main advantage of this system is that it is very effective in controlling the rotor rotation speed, resulting in a more constant power output. On the other hand, this system requires more expensive equipment than other passive systems.

Even before introducing other rotor speed control system, it is important to describe how it is possible to obtain the maximum aerodynamic power of a variable speed wind turbine. From the equations presented in the previous section, the maximum aerodynamic power is obtained considering the

optimum value of the top speed ratio (TSR_{opt}), and the maximum power coefficient (C_p^{Max}) in the following equations:

$$P = k \cdot \Omega^3 \qquad Q = k \cdot \Omega^2 \tag{2.26}$$

$$k = \frac{1}{2} \cdot \rho \cdot \pi \cdot R^5 \cdot \frac{C_P}{TSR^3} \tag{2.27}$$

Assuming constant operating conditions and that the variables in equation (2.27) have the respective optimal values, it is possible to conclude that the maximum efficiency can be achieved by varying the torque (Q) according to the quadratic value of the rotor rotation speed. This is the control strategy that maximizes turbine efficiency.

Variable speed wind turbines that integrate pitch angle control systems also have a complementary rotor speed control system. Under partial load operating conditions, the pitch angle remains constant, while the rotor operates with variable speed in order to guarantee the optimum value of the tip speed ratio. In this operating regime, the previous relationship is respected (thus obtaining the optimal power coefficient), which means the extraction of maximum power. However, due to limitations of the structure itself, it is not possible to follow the previous relationship for all wind speed regimes, with the maximum allowable rotor speed being reached for a relatively low wind speed (Burton et al., 2011).

As the wind speed increases and the nominal power is reached, the turbine torque is used to control the electric power production, while the pitch angle allows to keep the rotor speed within acceptable limits. During gust events, generator power remains constant while rotor speed increases. If wind speed decreases, rotor torque is reduced while generator power remains constant. If the wind speed remains high, the pitch angle increases in order to reduce the aerodynamic efficiency of the rotor (and its torque), consequently reducing the rotor speed. In this way, it is possible to guarantee the high aerodynamic efficiency of the generator, without overloading the system by the action of the wind.

2.3 MONITORING OF WIND TURBINES

2.3.1 INTRODUCTION

Civil engineering structures are generally designed to operate over long lifetimes. During the long period of operation, the structures are subjected to a wide range of factors, mainly human and environmental, which degrade their condition and performance capacity. Gradually, this continuous "wear and tear" may result in the appearance of damage that jeopardizes the capacity of the structure to meet the minimum requirements for safety, operation and sustainability, which could ultimately lead to its collapse. However, the deterioration of the structure's conditions can be avoided and/or repaired by following maintenance and rehabilitation actions as corrective or preventive measures.

This question is particularly relevant when addressing the safety and operability of wind turbines. These are machines that involve complex and unusual structural issues in the field of civil engineering, mainly due to the interaction between the action of the wind, the rotating movement of the rotor and its support structure (tower and foundation). In addition to their structural complexity, there is also an economic component. Since, these are structures that represent large investments of promoters, and when these are not operational, imply considerable losses of revenue. In order to ensure that these systems are not damaged during their operation, or that after the occurrence of a certain failure, the operation is interrupted in order to avoid its deterioration, the turbines are equipped with a primary safety system that ensures emergency stops in critical situations. In nowadays wind turbines, this monitoring and control system is called SCADA system.

Currently, there is a growing interest in the study of solutions to assess the integrity of wind turbines and their components. The main objective is to minimize turbine downtime, as these periods of non-production, together with the costs of repairing and replacing components, entail large economic losses. Thus, reducing wind energy costs involves making turbines more intelligent, in other words, developing systems that allow the collection of a wide range of data, which can be used to maximize the efficiency of the turbine itself and of the entire farm.

Among these intelligent systems, structural monitoring systems stand out, which in recent times have become more attractive. These systems allow the acquisition a large amount of data, which can be used for varied purposes. Obviously, its viability is only guaranteed if the benefits obtained make it possible to overcome its inherent costs: implementation and maintenance costs, data storage, processing and analysis. However, the benefits of a monitoring system are complex and quite difficult to quantify. Still, these benefits are easily understandable in terms of maintenance and management of wind farms.

Considering the role of monitoring systems in the maintenance of wind turbines, the different types of maintenance strategies that can be followed according to (BSI, 2017) are schematically represented in Figure 2.9. According to this document, maintenance expresses the combination of all technical, administrative and management actions during the life cycle of a unit aimed at preserving it, or repairing it, in a state in which it can perform the required function.

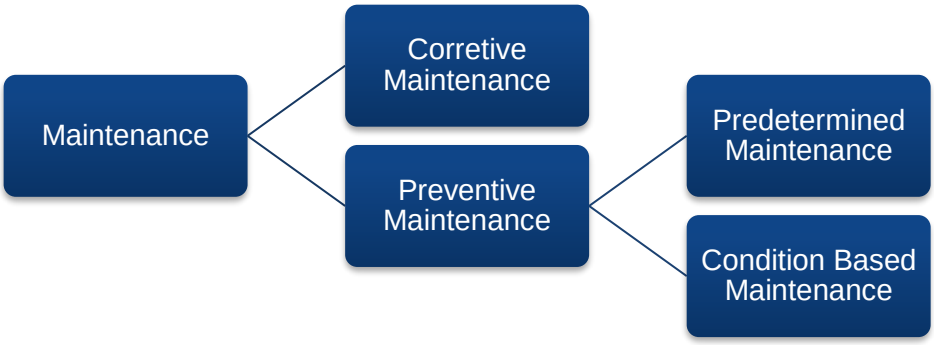


Figure 2.9 – Monitoring strategy developed to be applied in the context of a wind farm.

According to the figure shown and applying these same concepts to the theme of monitoring wind turbines, maintenance is divided into two large groups:

- Corrective Maintenance, in which maintenance measures are only activated after the failure has been identified and with the objective of restoring the wind turbine's state that allows for normal operation (the SCADA system fits into this maintenance strategy);
- Preventive Maintenance that is carried out at pre-established time intervals, or according to prescribed criteria, and which is intended to reduce the probability of failures and the degradation of the structure functioning;

Preventive Maintenance, in turn, is divided into:

- Pre-determined maintenance, which represents preventive maintenance carried out in accordance with established time intervals, but without prior investigation of the condition. Time intervals can be established from knowledge of the main failure mechanisms;
- Condition Based Maintenance, which includes a combination of condition monitoring, data analysis and subsequent maintenance actions. Condition monitoring includes at least one of the following actions: measurements, inspections, analysis and testing. These actions may be programmed, requested or carried out continuously over time.

Monitoring the structural condition of wind turbines aims to detect changes that reveal deviations from their normal operating behaviour and that indicate the development of a failure. Condition Monitoring (CM) can be subdivided into:

- "Online-CM" when monitoring is carried out during turbine operation, with no impact on its performance. Monitoring equipment is permanently installed in the structure (such as measuring time series of accelerations at specific points in the tower);
- "Offline-CM" when monitoring requires the interruption of turbine operation (such as laboratory analysis of oil samples collected in the gearbox).

Figure 2.10 illustrates the evolution of the performance index of a wind turbine over time according to the different maintenance strategies. As can be seen from the analysis of the figure, the corrective maintenance strategy has as its main advantage the fact that the useful life of the components is fully consumed. However, it can also represent long periods of downtime, risk of secondary damage and, ultimately, lead to catastrophic failures. Pre-determined preventive maintenance has the advantage of being scheduled in time, facilitating the management of maintenance teams and the stock of the various replacement components. However, it can become a more expensive strategy as it wastes part of the lifetime of some components.

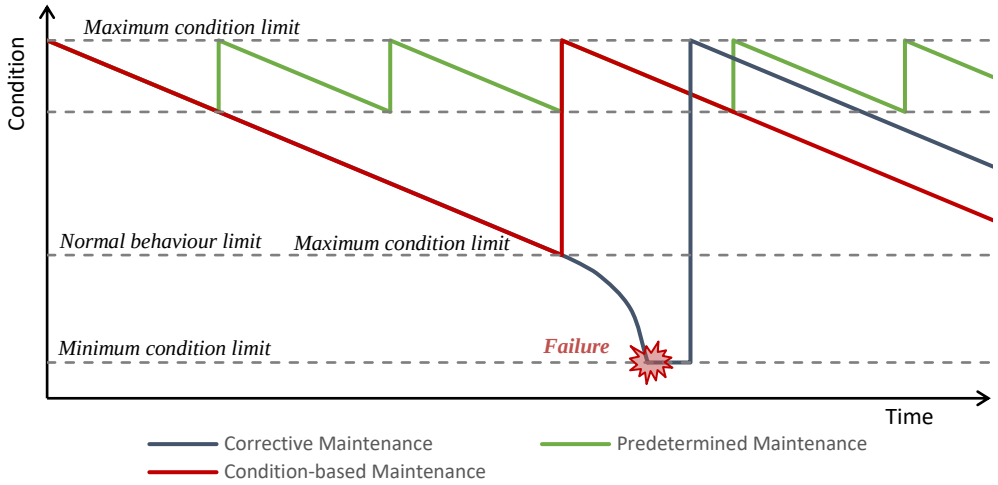


Figure 2.10 – Influence of different maintenance strategies on wind turbine performance (adapted from (Coronado & Fischer, 2015)).

The condition-based maintenance strategy is based on the fact that a large part of failures affecting equipment and structures are preceded by certain signs, conditions or indications that a failure will occur (Ahmad & Kamaruddin, 2012). Thus, through early identification of failures, preventive measures are taken that can prevent severe damage to the monitored components, the propagation of damage to other components and, in certain cases, damage can even be avoided (Hyers et al., 2006). In this way, not only will repair costs be reduced, but it will also allow for better scheduling of maintenance tasks, which usually translates into reduced turbine downtime (Adams et al., 2011). In addition to shorter downtimes, these may occur during periods when wind turbine production is expected to be reduced, based on wind farm production estimates using wind forecasts. In fact, the careful management of maintenance work in this type of structures is a preponderant factor, as it allows to avoid or minimize the loss of revenue related to these tasks. In contrast to pre-determined preventive maintenance, condition-based maintenance has the advantage of optimizing the useful life of components, avoiding unnecessary replacements, as maintenance tasks are only performed when there is evidence of abnormal behaviour.

Based on the conclusions just presented, condition-based maintenance clearly appears to be the maintenance strategy with the greatest economic benefit. As an example, some studies that prove this same advantage are describe below.

In (McMillan & Ault, 2007) the economic advantages between a condition-based maintenance strategy (considering a condition monitoring system for the generator, gearbox, blades and electrical system) and pre-determined maintenance for a 5 MW offshore wind turbine are analysed. The results show that the first strategy introduces economic benefits from 60% to 80%.

In (ECN, 2007) the costs associated with preventive and corrective maintenance of offshore wind turbines were studied. It was concluded that corrective maintenance costs are twice as high as preventive maintenance.

Very interesting results were obtained in (Yang et al., 2014). In this work, the economic advantage of installing a condition monitoring system in the gearbox of a 3.0 MW wind turbine that had a failure in the inner ring of the same component was evaluated. According to the results, the costs of the monitoring system would be covered 2 to 3 times for each year of turbine operation.

In (Besnard & Bertling, 2010) a cost-benefit analysis of a system for monitoring the condition of the rotor blades of a 5MW offshore wind turbine is presented. The analysis compares the cost of maintaining

the blades throughout the turbine's life cycle, considering the following condition assessment strategies: 1) Regular visual inspections, 2) Regular inspections according to non-destructive tests, 3) Permanent monitoring through an online-CM system. Figure 2.11 shows the expected values of the maintenance cost of the blades as a function of the inspection intervals. Considering the first two scenarios, it can be seen that inspection intervals have a strong impact on the total cost of these strategies. It is also concluded that the third scenario is associated with the lowest maintenance cost.

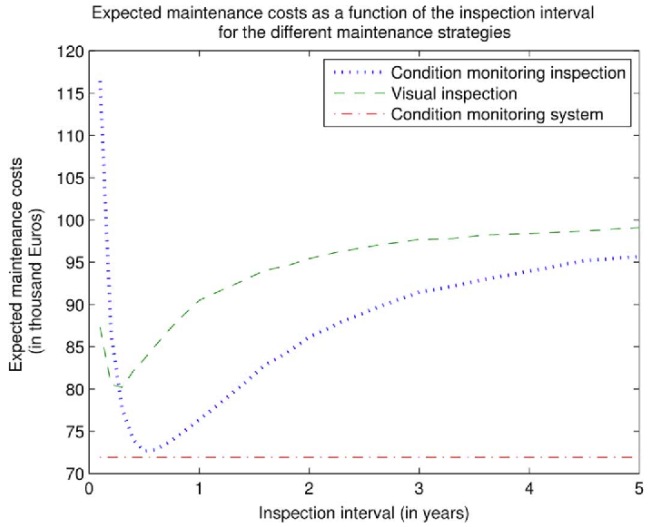


Figure 2.11 – Expectation of maintenance costs as a function of inspection intervals for different condition assessment strategies (adapted from (Besnard & Bertling, 2010)).

Monitoring the condition of the various components of a wind turbine represents a very broad field. However, it can be divided into two main groups according to the field of application: Condition Monitoring (CM) and Structural Health Monitoring (SHM). Condition Monitoring is oriented towards the evaluation of the turbine's mechanical components, especially the rotating components such as the transmission system shafts. Structural Health Monitoring, on the other hand, is aimed at structural components, such as the foundation, tower and blades. Despite this separation of concepts, it is common in many other works to use, in a simplified way, the term Condition Monitoring to encompass the monitoring systems of all components.

The present work focuses on the monitoring of the structural condition of the supporting structure (tower and foundation) and of the rotor blades of wind turbines. Based on the different challenges offered by different structural systems, several techniques, algorithms and methods were developed over time that allowed the practical application of these concepts. An important idea presented in (Rytter, 1993) concerns the different levels of damage detection, as presented in Figure 2.12.

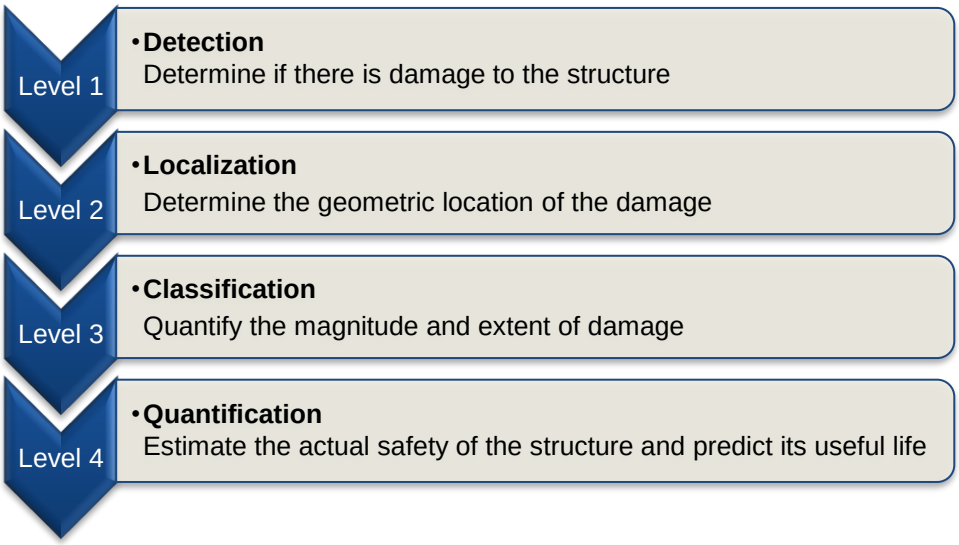


Figure 2.12 – Damage assessment levels.

Damage to structures can also be approached in terms of magnitude and in terms of time scale (Farrar & Worden, 2007; Worden et al., 2007). The time scale refers to the period of time the damage takes to occur, divided into deferred damage (fatigue damage, degradation of coatings, corrosion of metal towers and erosion and cracking of blades) and rapid damage (impacts, extreme winds). On the other hand, magnitude classifies damage according to its scope, that is, damage can be at the material level or at the structural level.

A monitoring system should be able to at least identify the damage (level 1), with the remaining assessment phases being carried out later by maintenance teams. The same system will also have to be able to detect damage with different evolution time scales, which may require the consideration of several detection methods. Finally, it is important that the damage is corrected at the element's local level, before the total failure of that component occurs, so the response time should be minimized.

Focusing now on the various SHM methods, aimed at applications in wind turbines, from which it is possible to obtain indicators in relation to structural performance, in (Wymore et al., 2015), an overview of the various methods is presented. In (Boller et al., 2009; Ciang et al., 2008) it is possible to find a description of the methods aimed at monitoring the rotor. In all these works, methods based on measuring vibrations are the most common type in SHM systems for monitoring the condition of supporting structures of wind turbines.

Vibration-based methods seek to relate the dynamic properties of structures with the presence of damage. These methods are based on the fact that the structure's response to external forces (such as wind) depends on its mechanical properties. As a given damage develops in the structure, its material and dynamic properties will also change, which consequently also modifies the response to external excitations. Vibration-based SHM systems are designed to detect these response changes, with the aim of characterizing the damage that may arise (Farrar et al., 2001). The dynamic parameters most often used as indicators of change in response are natural frequencies. However, it is also possible to consider other indicators, such as the configuration of vibration modes, damping coefficients and strain energy (Carden & Fanning, 2004). The main advantages of these methods are the fact that they allow detection of damage on a global scale, requiring a relatively small number of sensors and without prior knowledge of the location of the damage.

However, alternative non-vibration-based methods have been developed, especially with the aim of being applied to structural components made of composite materials, such as rotor blades. Below are some of the most used methods. A more detailed description of the principles of SHM systems applied to rotor blades can be found in (Rolfes et al., 2014).

- Methods based on acoustic waves: allow detecting local damage, such as cracks in blades (Gellermann, 2013). They have the disadvantage of requiring the sensors to be close to the point of damage, which may not be feasible in large structures where the location of damage is not known in advance;
- Methods based on the propagation of ultrasonic waves: consists of introducing ultrasonic waves into the blades by means of an actuator and capturing the transmitted signal with a receiver. Any damage located perpendicular to the direction of wave propagation will change its characteristics. It is not possible to accurately determine where the damage occurs;
- Methods based on stress measurement: this is one of the approaches with the highest number of applications to monitor the load applied to the rotor blades. It is also suitable for damage detection and deformation measurement. Measurements are carried out with strain gauges (such as fibre optic strain gauges) that are installed in the critical areas of the blades. However, identifying small damage requires a large number of sensors. This type of instrumentation allows the identification of stress concentration points, which can be used to infer the stability of the structure or to estimate the useful life through fatigue analysis.

On the other hand, the SHM systems developed to be applied in towers and foundations of wind turbines, in addition to methods based on vibrations, stand out, the measuring of strains, measuring of inclination angles (with clinometers) and measuring displacements. An example of the joint application of several measurement systems integrated in the monitoring of a wind tower of a Senvion MM92 wind turbine can be found in (Commission et al., 2012). In this study, 9 accelerometers, 92 strain gauges, 4 temperature sensors and 2 inclinometers were used, in addition to the SCADA system data.

There are several case studies in the literature in which SHM methods were applied in the monitoring of wind turbines, which allowed to obtain very positive results. In (Pelayo et al., 2011) methodologies based on vibrations were applied to detect damage in the supporting structure of wind turbines. This work allowed to identify abnormal levels of vibration in a turbine that had cracks in the foundations.

The sensitivity of the dynamic properties of the blades to the occurrence of damage does not seem to be so relevant. In (Marulo et al., 2014) it is shown that the variation in natural frequencies is only relevant when analysing significant damage scenarios.

In recent years, there has been a significant advance in several technologies within the scope of SHM systems. For example, acquisition systems have been developed with reduced dimensions, capable of wireless communication with sensors that can be powered with solar energy, making them fully autonomous. Furthermore, MEMS (micro-electromechanical sensors) have been developed with high levels of precision and at very competitive prices. Despite the advances registered, the implementation of SHM systems still presents many challenges. In addition to the cost and selection of sensors, the processing, analysis and management of collected data are some examples. Furthermore, SHM is an interdisciplinary field that imposes a wide range of knowledge. As an example, the complete project of a SHM system for the blades of a wind turbine requires knowing the physical parameters to be monitored, the type of instrumentation equipment to be used, the location of this equipment, ensuring the correct functioning of the entire the system and autonomy and the processing and analysis of the acquired data.

2.3.2 Environmental and Operational Conditions

The wind turbines and the associated equipment in the wind farm are connected to a SCADA system (Supervisory Control and Data Acquisition), which includes a number of transducers that support the operation and control of the turbines.

In fact, SCADA data includes a complete record of the operating history of the turbines, through which the reliability of these machines can be fully understood. However, this information is still not fully used for wind turbine condition monitoring, because of its low sampling rate in older wind turbines models, typically one sample every 10 minutes. Currently, the new generation of turbines are equipped with mode sophisticated SCADA systems, which provide data with time intervals of a 1 second to 10-min.

An overview of commercially available SCADA systems as well as of the parameters typically recorded can be found in (Crabtree et al., 2014; Yang et al., 2014). In general, SCADA records are 10-min averages, maximum, minimum and standard deviation of 1 Hz sampled values of several parameters of the wind turbine's operation and atmospheric conditions. The number of starts and stops and alarm logs recorded by the SCADA system can also be available. The parameters recorded by SCADA systems that are typically used for structural monitoring are listed in Table 2.1.

Table 2.1 – Basic SCADA parameters for structural health monitoring.

Environmental	**Operation**
Wind speed	Pitch angle
Wind direction	Yaw angle
Barometric pressure	Rotor shaft speed
Ambient temperature	Generator speed
Nacelle temperature	Active power output

In recent years, the use of SCADA data has become a very relevant topic for condition monitoring and structural health monitoring (Dai et al., 2018; Wei-Hua Hu et al., 2015; Iliopoulos et al., 2016; Schlechtingen & Santos, 2014). It is also used on failure detection and diagnosis by principal component analysis (Jin et al., 2019), support vector regression (Tang et al., 2019), artificial neural networks (Bangalore & Patriksson, 2018; Kong et al., 2020), improved deep neuronal networks and other learning algorithms (Helbing & Ritter, 2018).

The monitoring strategy developed in this work is complemented by the data provided by the SCADA system, taking profit from its availability since the wind turbine installation.

2.3.3 STRUCTURAL HEALTH MONITORING

As mentioned in the introductory chapter, the aim of this work is to develop, implement, validate and optimize new methodologies that allow the continuous assessment of the structural elements of wind turbines, supported by a monitoring system of the structural condition. This system will have to be able to respond to two relevant problems in the field of evaluating the structural condition of the main structural components of wind turbines: the identification of damage at an early stage and the estimation of the fatigue life of the structure. Thus, the system will consist of two modules: Damage Detection and Fatigue Assessment.

The first module follows a modal approach (Fritzen, 2005), in which the modal parameters of the structure (natural frequencies, damping coefficients and configuration of vibration modes) are continuously estimated over time. As damage is usually associated with reductions in stiffness, and assuming that the mass variation is negligible (which is perfectly acceptable for wind turbines), anomalous reductions in the value of natural frequencies are assumed as a result of the presence of damage. Some examples of similar monitoring systems implemented in civil engineering structures can be found in (W-H Hu, 2011; F Magalhães, 2010; Peeters, 2000).

However, it is important to note that vibration-based monitoring systems require a "learning" process, with a specific duration of time. During this period, the SHM system identifies and records the performance of the structure considered “healthy”, in particular, the dependence of the modal parameters on external factors (environmental and operational). Acceptable deviation limits are also established in order to exclude false damage alarms, for example, due to seasonal temperature variation. This means that these systems do not assess the integrity of the structure once they are installed. The monitoring system can only be considered operational once the analysis algorithms are implemented, at the end of the “learning” period. As it is possible to understand, these are systems based on the continuous comparison of the monitored characteristics with the “normal” characteristics obtained during the training period. The identification of deviations is considered an indicator of potential damage. In this way, intrinsic faults that do not significantly contribute to the stiffness of the overall structure, such as manufacturing errors, are not effectively detected by these systems.

Chapter 3 is dedicated to the application of tools for vibration based damage detection in a 2MW wind turbine, so further details about the practical application of these tools are presented there.

The second module of the monitoring system concerns the estimation of the fatigue life condition of wind turbines. Once the structural load cycles are continuously estimated, it is possible to assess the increase in damage to all structural elements. In this way, it is possible to make an estimate of the actual consumed life period due to fatigue of the structure.

In fact, the fatigue analysis of a wind turbine is a fundamental task, but quite complex. Firstly, turbines are made up of large structural components, designed with different materials, which require different assessment procedures. On the other hand, wind turbines are structures predominantly subjected to dynamic loads, with considerable uncertainty in their quantification and frequency of occurrence. Finally, these are structures made up of a large rotating element (rotor), supported on the top of a slender structure (tower), prone to resonance problems.

Chapter 5 is dedicated to the fatigue analysis of the wind turbines of Tocha Wind Farm, so further details about the practical application of fatigue analyses are presented there.

2.3.4 Operational Modal Analysis of Wind Turbines

In a very succinct way, Operational Modal Analysis (OMA) can be understood as an experimental identification methodology, in which, from the measurement of the structure response to ambient excitation, it is possible to estimate its dynamic properties. The most commonly used algorithms are described in reference (Filipe Magalhães & Cunha, 2011). This section is just dedicated to a brief discussion of the particularities found in wind turbines.

In previous sections, some case studies were referred in which modal identification techniques were applied to wind turbines, which demonstrated the ability of OMA tools to extract the dynamic characteristics of the structure under real operating conditions. However, the application of OMA tools is only valid if the following assumptions are met (Tcherniak et al., 2010):

- Structure characteristics are time-invariant;
- The forces should have broadband frequency spectra;
- The forces have to be uncorrelated;
- The forces have to be distributed over the entire structure.

The temporal invariance of the structure is the most difficult premise to respect. The relative movements between the various substructures that make up the turbine, such as the rotating movement of the rotor, the rotation of the nacelle and the variation in the pitch angle of the blades, does not allow this hypothesis to be fully respected.

As for the assumptions made in relation to the excitation forces, it is valid to admit that these are respected whenever the turbine is in non-production. When in production, the rotor rotation induces a harmonic excitation that translates into an excitation spectrum with several peaks coincident with the rotor rotation frequency and its harmonics. This subject will be further discussed in the next chapter.

Finally, it is valid to admit that excitation forces are equally distributed throughout the structure. In reality, the action of the rotor when in operation causes a greater concentration of forces in the upper part of the wind turbine. Even though the intensity of the excitation on the remaining structure is lower than that acting on the rotor, it is realistic to assume that the last assumption is satisfied.

In conclusion, under operating conditions, OMA identification algorithms cannot be directly applied to wind turbine signals in the same way as when under parked conditions. The application of identification algorithms to wind turbines in operation is only valid if auxiliary pre-processing tools are adopted in order to overcome the previous violations. Reference should be made that for some strategies presented below, some input information, usually obtained with the data collected by the SCADA system, is required.

2.3.4.1 Time-variance due to Nacelle Rotation

Considering sensors installed in the tower, framed into a global stationary reference, it is necessary to apply a coordinate transformation to the collected signals so that these will follow the nacelle orientation, defined by the fore-aft (FA) and side-side (SS) directions (moving reference). There are some alternative procedures to handle the problem of structure time-variance due to nacelle rotation, which should be selected according to the quality of the data available from the SCADA system.

Normally, the data from yaw angles is only available in the form of time-averaged values (e.g. 10 minutes mean values). In this case, the same rotation matrix should be applied to the entire raw data

collected during that period. In fact, this approach provides adequate results because in current operating conditions the nacelle does not suffer important rotations during the adopted time interval.

The raw data obtained from the sensors should suffer a coordinate transformation according to:

$$\begin{bmatrix} X'(t,\theta) \\ Y'(t,\theta) \end{bmatrix} = \begin{bmatrix} cos(\theta) & sin(\theta) \\ -sin(\theta) & cos(\theta) \end{bmatrix} \cdot \begin{bmatrix} X(t) \\ Y(t) \end{bmatrix} \tag{2.28}$$

with:

X', Y'	Nacelle reference coordinates (moving)
X, Y	Tower reference coordinates (stationary)
θ	Angle between the tower sensors referential and nacelle orientation (Figure 2.13)

This transformation leads to the projection of the collected acceleration time series in the FA and SS directions, as show in Figure 2.13.

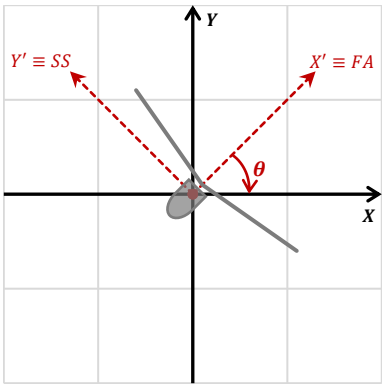


Figure 2.13 – Illustration of the θ angle between the sensors referential (in black) and nacelle orientation.

This coordinate transformation guarantees that the registered signals are coherent with the time-moving reference frame. In this way, the temporal invariance of the structure due to the orientation of the rotor is guaranteed.

2.3.4.2 Time-variance due to Rotor Rotation

The spinning rotor, as referred earlier, is another source of violation of the structure time-invariance requirement. In experimental testing, a coordinate transformation is required in situations where sensors are located in the rotating components of the rotor (such as blades), under operating conditions.

This violation can be overcome through the Coleman transformation (M. H. Hansen, 2007). In this way, the movement of each blade is integrated in the same tower coordinate system. A routine for the application of Coleman transformation to records from sensors located on the rotor is proposed in (Allen et al., 2011). It is important to note that, although it removes the periodicity due to the rotation, it does not eliminate the periodicity character of the excitation forces.

2.3.4.3 Periodic Nature of the Excitation Forces

Due to rotor rotation, the structural response contains harmonic components and the modal identification process can become difficult.

Several methodologies have been proposed to overcome this limitation, for example, Kurtosis-based methods were proposed in (Jacobsen, Andersen et al., 2006; Andersen, Brincker et al., 2007; Jacobsen, Andersen et al., 2008); Cepstral method was proposed in (Randall & Sawalhi, 2011); and Peeters et al (Peeters, Cornelius et al., 2007) introduced the time synchronous averaging method.

Although different methodologies to identify and remove the effect of harmonics in vibration signals have been developed, some difficulties are expected regarding the application of these methods to the modal identification of wind turbines. In that sense, other type of strategy is now briefly introduced, since this was employed in the data processing presented in Section 3.3.1.

This procedure is based on comparison of the modal properties identified in each dataset (obtained from the modal identification algorithms) with reference properties of the vibration modes intended to be monitored. These reference properties (usually frequency value and mode shape) are defined based on results obtained during a training period. As can be seen comparing Figure 3.5 and Figure 3.6 (Chapter 3), this simple tracking procedure allows eliminating the influence of the harmonics in the modes under analysis.

2.4 FINAL CONSIDERATIONS

This chapter starts with basic and fundamental knowledge about the constitution, operation and dynamic behaviour of wind turbines. These concepts are fundamental for the development of the work that was briefly introduced in the previous chapter.

Then, it is dedicated to a brief description of the wind turbine rotor aerodynamic behaviour. This theoretical background represents a helpful insight for the comprehension and definition of the various operational conditions of a wind turbine. The variation of the operating conditions requires the definition of control strategies. In that sense, the description of simplified aerodynamic and rotor torque control strategies is also included in this chapter

Finally, concepts related to the monitoring of structures are presented, framing the system that is intended to be developed in this work within the scope of maintenance and management of wind farms by promoters. A brief description of the processing methodology for monitoring the structural condition of wind turbines is also presented.

This chapter is especially important to frame the scope of the present work. A monitoring system, able to detect structural damage at an early stage and perform an estimation of the fatigue condition of the main structural elements, represents an important tool to remotely control the condition of the wind turbines and, thus, its reliability. At the same time, this continuous assessing provides helpful information to timely prepare maintenance actions and to optimize operation and maintenance procedures.

3
VIBRATION-BASED MONITORING OF WIND TURBINES FOR DAMAGE DETECTION*

3.1 INTRODUCTION

As mentioned in the previous chapter, the correct definition of the Operation and Maintenance strategy is a key aspect for all industry agents involved in wind energy production. Therefore, the assessment of the integrity of the wind turbines and their components is a field of study with a high level of interest.

In this sense, this chapter focuses on the analysis of the results obtained within the scope of a monitoring campaign on a 2 MW onshore wind turbine, having in mind the optimization of the monitoring layout. It is a research driven expensive experimental campaign, in which seven force-balance accelerometers with reduced noise levels were installed in three sections along tower high, during more than one year.

The processing of the collected data is based on Operational Modal Analysis techniques (Magalhães and Cunha, 2011) briefly introduced in Chapter 2 and aims to identify the dynamic properties of the structure (natural frequencies, damping ratios and mode shapes) over the different operating conditions of the wind turbine. In (Oliveira *et al.*, 2018a) the validity and suitability of the monitoring system is demonstrated, as well as of the algorithms implemented for data processing.

In a next step, starting from the results database obtained with Operational Modal Analysis, tools are developed with the objective of identifying structural changes, or damage, in an initial stage of development, from the analysis of abnormal variations in the modal properties. The effectiveness of the developed tools is proven through the simulation of four damage scenarios. The theoretical foundations related to the methodology used and the results obtained can be found in (Oliveira *et al.*, 2018b).

The work presented in this chapter appears as a follow-up to the previous works. As mentioned, the installed monitoring system is considerably expensive. In order to reduce the investment in the acquisition of monitoring equipment, while ensuring adequate accuracy in detecting damage, the original data is manipulated in order to recreate alternative monitoring solutions, designed considering different budgets. Thus, two different strategies are applied to optimize costs: (1) reduce the number of sensors to be used; (2) use lower quality sensors. These two strategies can also be combined in order to obtain instrumentation solutions that maximize the benefit / cost ratio.

Regarding the first strategy, four alternative layouts are tested for the distribution of a variable number of accelerometers along the height of the tower. The second strategy involves adding noise levels to the recorded acceleration time series. In total, four different noise levels were tested.

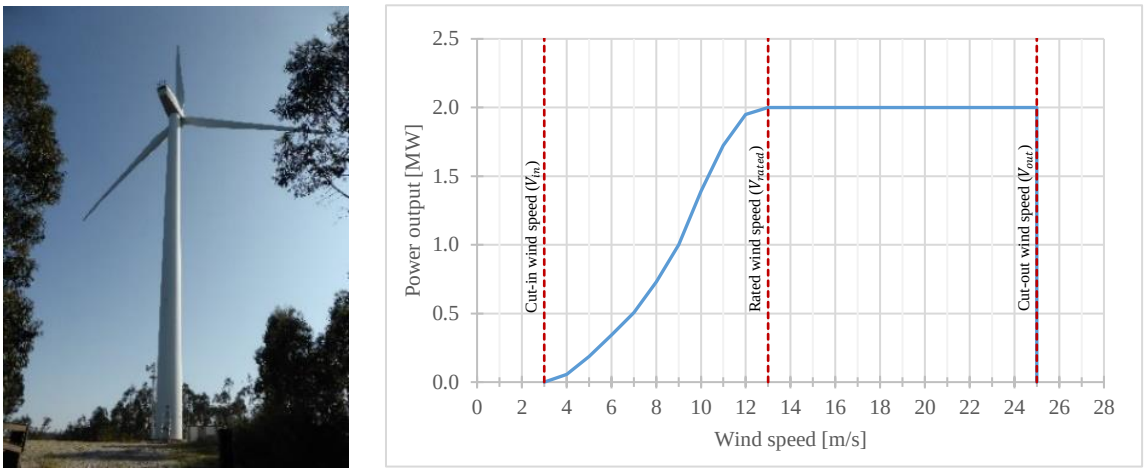
* This chapter is based on the paper:
Pacheco, J., Oliveira, G., Magalhães, F., Moutinho, C., Cunha, Á. (2021) *Vibration-Based Monitoring of Wind Turbines: Influence of Layout and Noise of Sensors*. Energies, 14(2), 441. https://doi.org/10.3390/en14020441.

In this way, the main goals of this study are:

- To compare the efficiency of the two alternatives adopted to reduce costs (reducing the number of sensors and reducing their quality);
- Define the maximum noise level of the sensors, which allows obtaining estimates of the modal properties of current wind turbines;
- Define an optimal instrumentation solution (layout and noise level) that can be applied to current wind turbines.

3.2 CASE STUDY DESCRIPTION

The case study addressed in this work is a Senvion MM82 wind turbine located in the Torrão Wind Farm, in the north of Portugal, which started operating in 2007 (Figure 3.1a). It is a 2.0 MW wind turbine, with an 82 m diameter up-wind rotor, three pitch controlled blades, variable speed operating and the hub is located at 80 m high. The support structure consists of a 76 m high tubular steel tower composed by three segments and a reinforced concrete slab foundation.



(a) (b)

Figure 3.1 – Senvion MM82-2MW: (a) Picture of the wind turbine; (b) Wind turbine power curve.

The wind turbine operates for wind speeds between 3 m/s (V_{in}) and 25 m/s (V_{out}) and achieves the rated power output for wind speeds of about 13 m/s (V_{rated}), as seen in the power curve illustrated in Figure 3.1b. It is important to note that wind turbines are highly time-varying structures, dependent on environmental and operating conditions. If it is desired to track the modal properties of the wind turbine over its period of life, it is important to identify and remove the effect of harmonics in vibration signals, as mentioned in Section 2.3.4.3. In this sense, six operating regimes were adopted to define the reference properties of the monitored vibration modes. For each regime, reference values are chosen for each vibration mode to be tracked. In a simple way, the operating regimes are related to the different structural configurations adopted by the turbine over the different operating conditions. These regimes are characterized in Table 3.1.

As described in the table, regimes 1 and 2 are referred to non-operating conditions since the wind speed is too low for production. The pitch angle of the blades is set to values around 90° and lower than 90° for regime 1 and 2, respectability. When wind speed is higher than the cut-in speed, the pitch decreases and the generator starts operating. Regime 3 is defined as a transition state from non-operation and operation. The 10-min rotor speed mean values are between 0 rpm and the lowest operating rotor speed. Setups in which the rotor speed is higher than the lowest operating rotor speed, and before the pitch actuator is actively varying the angle of attack of the blades, are clustered as regime 4. Regime 5 starts when pitch angle increases in order to avoid excessive rotor speed values and extends to the limit operating conditions of the turbine. Lastly, regime 6 is similar to regime 1, but the wind speed is higher than the turbine cut-out wind speed.

Table 3.1 – Regimes considered for reference modal properties of the wind turbines.

	Operating regime	Wind turbine condition
1	Parked or idling	Pitch angle values is at its maximum level (≈ 90°)
2	Parked or idling	Wind speed lower than cut-in speed Pitch angle values is kept at is higher level for rotor rotation (< 90°)
3	Transition regime from non-operation to operation	Rotor speed between 0 rpm and lowest operating rotor speed Pitch angle values close to its lower level
4	Operating regime	Rotor speed between lowest and maximum rotor speed Pitch angle values is kept at its lower level
5	Operating regime	Rotor speed close to maximum operating rotor speed Pitch angle values starts to increase
6	Parked	Wind speed higher than cut-out speed Pitch angle values is at its maximum level (≈ 90°)

It is important to note that the definition of the six operating regimes is based on a statistical analysis conducted on the SCADA data. Employing environmental and operational data the 10-min series are clustered into different operating regimes. These six regimes are used further in for automated model analysis (Section 3.1.1).

The experimental data used in this study was collected through a vibration-based monitoring system composed of seven uniaxial force-balance accelerometers, distributed in pairs in three sections along the tower height (measuring acceleration along two horizontal direction), according to the scheme presented in Figure 3.2. In the section at a height of 2/3 of the tower height (+48.393 m), a third sensor was added that allows characterizing the torsional movements. However, pure torsion modes of the tower were not identified.

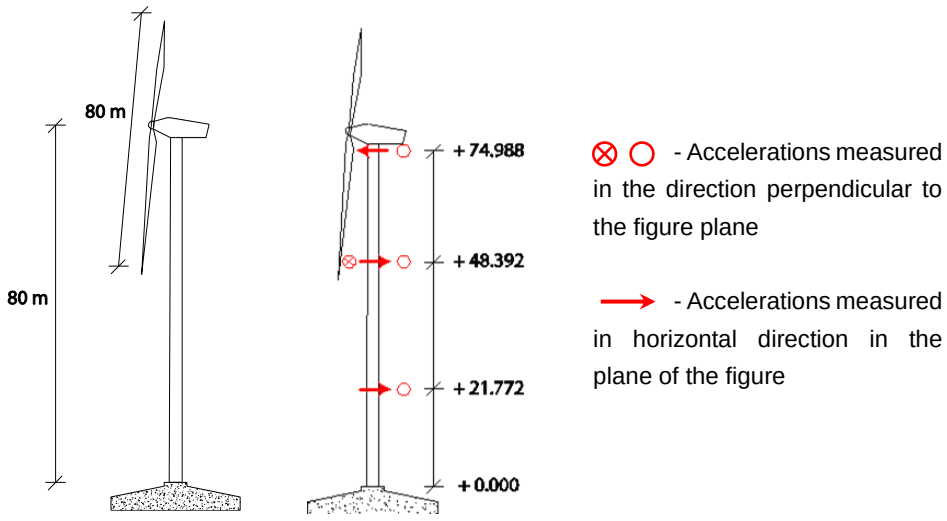


Figure 3.2 – Position of the accelerometers at three levels of the wind turbine tower.

All instrumentation equipment is located inside the tower. The central acquisition system includes a field computer and a digitizer with a 24-bit analog-to-digital converter. The digitizer was configured to continuously record 10 minutes acceleration time series with a sampling frequency of 50 Hz, later decimated to 12.5 Hz.

The collected data is complemented with the information provided by the SCADA system, which continuously characterizes the wind turbine's environmental and operational parameters. Maximum, minimum and average values are recorded for each 10-minute interval of several parameters, including wind speed and direction, rotor speed, nacelle orientation, blades pitch angle and outdoor temperature, these are important for the identification of the regions marked in Figure 3.1b.

A more detailed description of the case study, of the corresponding monitoring system and of operating regimes of the wind turbine can be found in (Oliveira *et al.*, 2018a, 2018b).

3.3 STRATEGY FOR VIBRATION-BASED SHM

As described, damage detection will be carried out based on the identification of abnormal variations in the value of the natural frequencies of the structure. The main goal is to develop a totally autonomous processing methodology, in which the data continuously collected allows the identification of damage situations. The application of the methodology to the case study under analysis is briefly described in this section.

The accelerations time series and the parameters provided by the SCADA system are the input data of the processing algorithms. As show in Figure 3.3, for each 10-minute periods, the data acquired is processed according to the following four main steps:

1. **Pre-processing**: the recorded acceleration data are decimated (low pass filter and resampling from 50 to 12.5 Hz) to focus the analysis on the frequency range of interest, between 0 Hz and 6 Hz. Then, a coordinate transformation is applied (Equation 2.28), using the yaw angle provided by the SCADA system, in order to align the signals according to the FA and SS directions (horizontal, perpendicular and parallel to the rotor plane, respectively);
2. **Automated Operational Modal Analysis**: the time series of accelerations are processed using three alternative modal identification algorithms: SSI-COV (Magalhães and Cunha, 2011), SSI-DATA (Van Overschee and De Moor, 1996) and p-LSCF (Peeters *et al.*, 2004) combined with post-processing routines to automate the analysis (Devriendt *et al.*, 2014);
3. **Minimization of the environmental and operational effects**: after the dynamic characterization of the structure, it is essential to minimize the influence of the operational and environmental effects on the dynamic parameters. In this sense, multivariate linear regression models are applied to reduce their variability. The detailed description of the models implemented in this stage is presented in (Oliveira *et al.*, 2018b);
4. **Damage detection**: the last step is to identify damage by assessing significant deviations from the reference values of natural frequencies. The implemented procedure is based on the analysis of T^2 multivariate control diagrams (Magalhães, Cunha and Caetano, 2012). This method allows detecting variations of the various natural frequencies in a single chart.

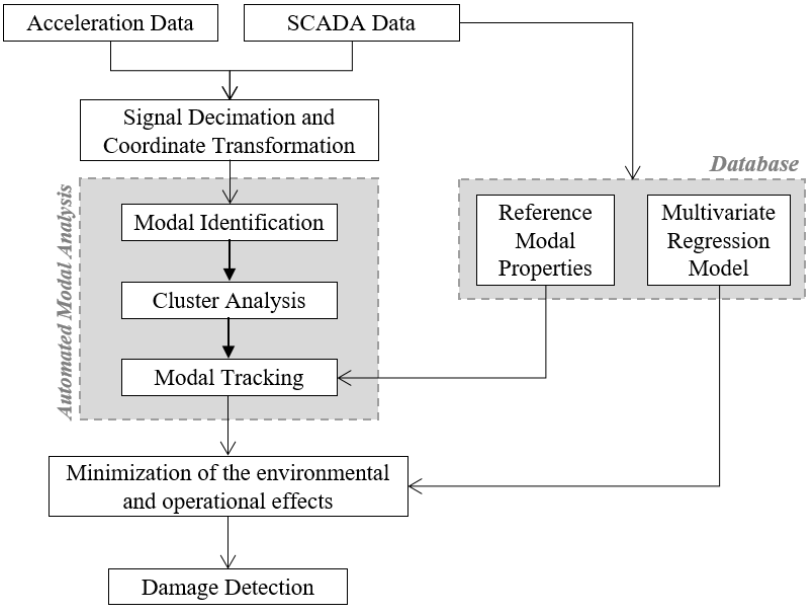


Figure 3.3 – Main steps of the vibration monitoring strategy to damage detection.

In the following sections, each of the steps is described in detail and accompanied with intermediate results of the Torrão case study. Some preliminary pre-processing steps were discussed in Chapter 2.

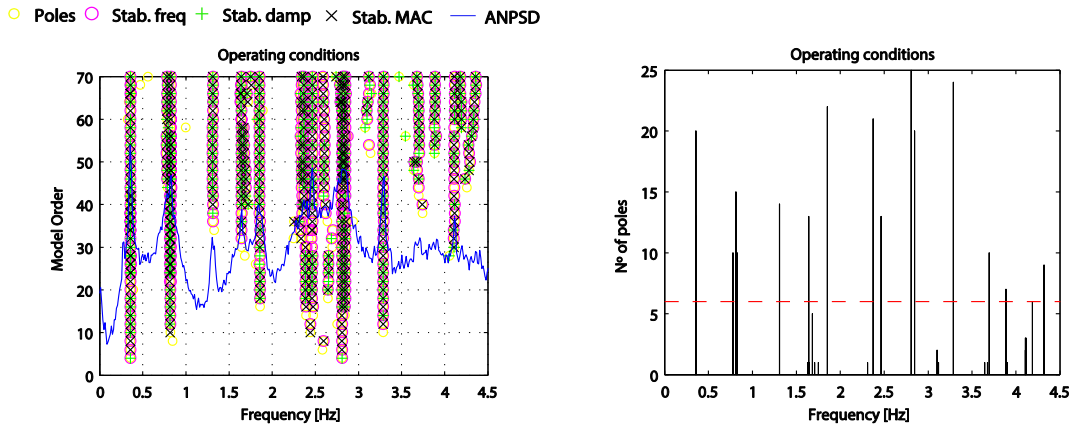
3.3.1 AUTOMATED MODAL ANALYSIS

After the initial pre-processing, the data is processed by dynamic identification algorithms, in order to estimate the modal properties of the structure. In applications developed in ViBest, two algorithms are normally considered in the time domain: SSI-COV – "Covariance driven Stochastic Subspace Identification", SSI-DATA – "Data driven Stochastic Subspace Identification" and a frequency domain algorithm: p-LSCF – "poly-reference Least Squares Complex Frequency Domain".

It is intended that the dynamic monitoring system is as autonomous as possible, without the need for the intervention of an experienced operator who continuously monitors the processing of the collected data. In fact, the steps and sub-goals of the data processing chain described so far make it possible to obtain the dynamic parameters of the structure. However, an additional procedure is needed that makes it possible to automatically detect the desired modal parameters.

The results obtained from the identification methods referred to in the previous section are generally represented in the form of stabilization diagrams (Figure 3.4a), in which the poles obtained for models of different orders are located at the frequencies of possible resonance peaks. In this way, if the properties of a pole (modal parameters) remain constant over the consecutive orders of the models, the pole is considered stable and this frequency will most likely correspond to a vibration mode. In the application to the Torrão wind turbine, a pole is considered stable if it respects the following limits between consecutive orders: maximum variation of natural frequencies and damping coefficients of 1% and 5%, respectively, and a minimum value of 0.97 for the parameter of MAC (parameter that measures the similarity of the settings of the vibration modes) (Allemang, 2003).

Automatic interpretation of stabilization diagrams is performed based on hierarchical cluster analysis (Gordon, 1999; Magalhães, Cunha et al., 2009). This technique divides the objects (poles) into a certain number of individual classes (clusters), grouping the poles belonging to the same vibration mode. The natural frequencies and modal configurations are the parameters used to calculate the distance between poles, while the evaluation of the similarity between the clusters uses the criterion of minimum connection. Given the uncertainty about the final number of clusters, the cut-off criterion was defined by imposing a degree of homogeneity within the cluster (maximum distance between any point and its closest point in the same cluster). After analysing a reprehensible dataset, the value of 0.02 has proved to be suitable for many applications. Once the hierarchical analysis is finished, it is important to eliminate the clusters related to spurious modes. Assuming that the poles belonging to the physical modes are consistent across the different orders of the models, an initial cut-off criterion is applied that eliminates clusters with a reduced number of poles. For the Torrão wind turbine, after careful data analysis, clusters with six or fewer poles are eliminated. In Figure 3.4b the clusters are characterized, representing the number of poles as a function of the average frequency.



(a) (b)

Figure 3.4 – Modal analysis of a setup with the wind turbine in operation: (a) Control diagram (SSI-COV); (b) Characterization of clusters in average frequencies and number of poles.

After selecting the clusters that satisfy the imposed criteria, it is necessary to differentiate the vibration modes intended to be identified (main modes of the structure) from the clusters that refer to the dynamic response of the structure due to harmonic excitation. With this objective, a methodology is followed in which the properties of the clusters (natural frequencies and modal configurations) are compared with the modal properties of the reference vibration modes that are intended to be identified over time.

As referred in the previous Section 2.3.4.3, the external excitation created by the rotor rotation introduces new challenges to the modal identification of wind turbines, when compared to other more common structures. The operation of the rotor introduces a harmonic excitation into the structure that translates into well-defined peaks in its response spectrum. These harmonics can be interpreted by modal identification algorithms as structural vibration modes. Considering a typical generator with a three-blade rotor and rotation speed P, these peaks have frequency values equal to nP, where n can take values equal to $1, 3, 6, 9, ...$

Considering the data acquired over a year of monitoring, the selected clusters, even before this last stage, are represented in a Campbell diagram (Figure 3.5). The Campbell diagram is understood as the graphical representation of the evolution of the average frequencies of selected clusters along the different operating regimes as a function of the rotor speed. In the same figure, the vertical lines divide the diagram into 4 regions: a non-production region, a transition region and two operating regimes. Diagonal dashed lines represent harmonics associated with rotor rotation. The points are represented according to the main vibration direction of the mode: FA (for-after): perpendicular to the plane of the rotor; SS (side-side): parallel to the plane of the rotor.

Analysing the figure, it is possible to identify resonance phenomena due to the excitation created by the rotor rotation, that is, the cases in which the harmonics have a frequency identical to that of the real vibration mode. These clusters tend to appear around the dashed diagonal lines in the production regions (rotor speeds greater than 8.7 rpm). In contrast, the real vibration modes are easily identified through the horizontal alignments of clusters, across all operating regimes. In addition, this diagram also allows analysing possible variations in the value of natural frequencies as a function of rotor speed.

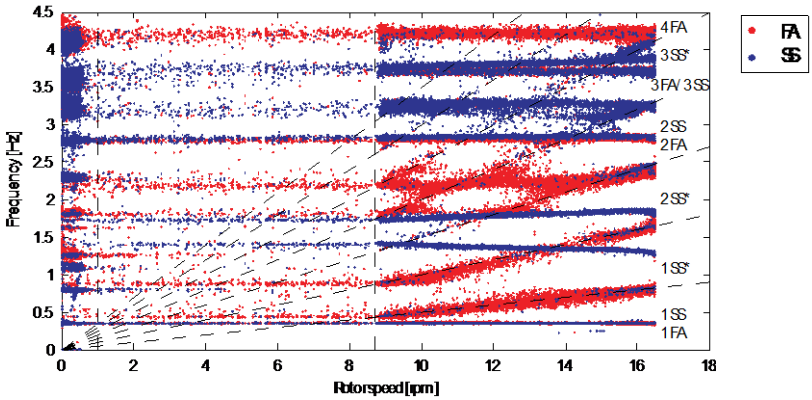


Figure 3.5 – Campbell diagram of considered clutters of stable poles, including vibration modes and external harmonic excitation (p-LSCF algorithm).

As mentioned in Section 2.3.4.3, this type of structure is highly variable over time, with different structural configurations according to the operating conditions. In this way, for each of the operating regimes (defined in Section 3.2), the modal reference properties of the vibration modes are defined. Therefore, the data files recorded in each 10-min setup are classified according to the six regimes. The modal properties of the clusters selected in the previous step are compared with the reference properties, according to the respective regime, in order to associate or not each cluster with a vibration mode.

3.3.1.1 Modal Results

With this procedure, several modes of vibration were identified and nine modes were selected to be continuously tracked by the dynamic monitoring system, including bending modes of the tower and rotor. The evolution of nine vibration modes throughout the different operating regimes is presented in a Campbell diagram (Figure 3.6), where the identified natural frequencies are plotted against the rotor speed. Each mode is identified according to the following nomenclature: order number of the mode followed by the main direction of vibration (FA or SS). If the value of the natural frequency associated with a given mode is clearly dependent on the speed of rotation of the rotor, the graphic sign "*" is added to the name to state that this is driven by the rotor. The configurations of the tracked vibration modes at the tower mode shapes are also represent. The diagram makes it possible to clearly observe the evolution of the value of the natural frequencies of the nine modes of vibration over the operating regimes.

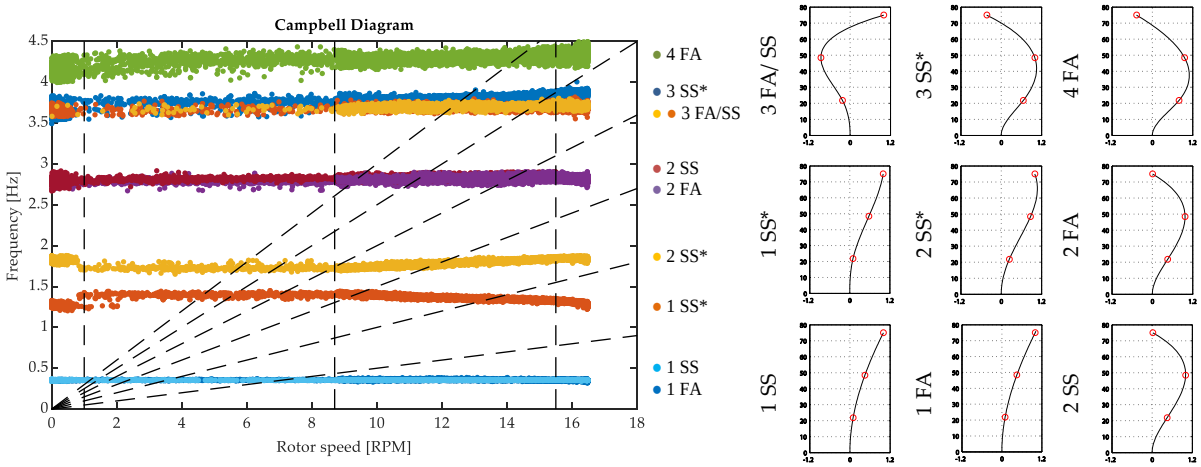


Figure 3.6 – Campbell diagram with the nine tracked vibration modes (p-LSCF algorithm) and corresponding mode shapes.

Table 3.2 presents the average values of natural frequencies (f_{mean}), success rates (SR) and the variation coefficient (f_{cv}) of the nine vibration modes. Success rates are understood as the ratio between the number of times a particular mode is identified and the total number of files processed (setups). Considering the lower success rates associated with the identification of the last 3 modes, these will not be considered for damage identification. The selected 6 modes are also the ones that have the greatest contribution to the dynamic response of the structure.

Table 3.2 – Statistics related to the results obtained with the three modal identification algorithms.

Mode	SSI-COV			SSI-DATA			p-LSCF		
	$f_{mean}[Hz]$	$SR[\%]$	f_{cv}	$f_{mean}[Hz]$	$SR[\%]$	f_{cv}	$f_{mean}[Hz]$	$SR[\%]$	f_{cv}
1 SS	0.354	81.2	0.005	0.355	84.7	0.006	0.354	80.8	0.006
1 FA	0.355	67.4	0.020	0.358	67.4	0.022	0.354	64.7	0.019
1 SS*	1.325	63.4	0.039	1.330	84.9	0.038	1.330	87.4	0.037
2 SS*	1.791	78.3	0.034	1.793	89.8	0.032	1.793	85.5	0.032
2 FA	2.792	75.8	0.009	2.789	74.0	0.009	2.796	80.1	0.006
2 SS	2.828	83.7	0.011	2.829	60.2	0.011	2.831	85.5	0.009
3FA/3SS	3.673	9.1	0.011	3.690	14.9	0.011	3.700	43.2	0.008
3 SS*	3.782	29.5	0.011	3.789	44.9	0.012	3.809	67.8	0.015
4 FA	4.236	38.3	0.017	4.266	82.3	0.019	4.276	95.1	0.019

3.3.1.2 Database Characterization

The installed monitoring system allowed to obtain a database of accelerations during a period of about one year. It is curious to see that only in an insignificant part, around 0.4% of all collected setups, the dynamic parameters of any of the 6 selected modes are not identified. This shows that the monitoring system is totally adequate to the intended objective and that the data processing and methods implemented are sufficiently robust and are correctly calibrated for the present case study.

However, more relevant than identifying the percentage of data files from which it is possible to extract dynamic parameters from the system, is to identify which files permit the simultaneous identification of the first 6 modes presented in Table 3.2. In order to maximize the number of setups to be used in this analysis, tried to understand which of the tested identification methods has the highest success rate (SR) in the simultaneous identification of the 6 selected modes. The following results were obtained: $SR_{SSI-COV} = 32.3\%$, $SR_{SSI-DATA} = 21.4\%$, $SR_{p-LSCF} = 22.5\%$. Despite the fact that the SSI-COV method is the one with the highest success rate, but not as high as pretended, there is a strong interest in increasing the quantity of the available samples. For this purpose, simple arithmetic averages were performed between the results of the various methods for each of the setups. This allowed the success rate to be increased to 60%, approximately double what would be achieved with the best method alone. In this way, took advantage of the complementarity between the methods, that is, extract as much information as possible from each setup. Because, as is easily understood, given the great variability of

operational and environmental conditions, different identification methods are effective in different conditions.

In order to prove the validity of this methodology, statistical analyses were carried out, which involved the study of measures of location, dispersion and distribution of the frequencies obtained with each of the identification algorithms and with the average. These results validated the proposed methodology.

3.3.2 Minimization of Environmental and Operational Effects

Wind turbines are subject to a great variability of environmental and operational effects that represent an important source of variability in the modal properties of the structure (Sohn, 2007). In fact, it is frequent that the variations caused by these external factors present greater amplitude than the variations caused by the structural damage itself. In order to detect small-scale damage at an early stage, it is essential to eliminate the influence of external factors on modal properties, more precisely on natural frequencies, as these will be indicators of the presence of damage. This section presents the methodology implemented in order to mitigate the variability of natural frequencies.

The mitigation of external effects on the modal parameters is feasible following different approaches, and in this work Multivariate Linear Regression Models are adopted. These are models that allow us to assume the values of the response variables (dependent variables) based on the values of the independent variables. A theoretical description of this methodology is found in (Johnson and Wichern, 2002). In this application case, the models are built from the measurement of environmental and operational parameters (independent variables) that try to explain the variation of dynamic properties (dependent variables). Since the SCADA system records a wide variety of external parameters, this methodology is very suitable in the context of monitoring wind turbines, as it does not require the installation of additional sensors.

Despite being a relatively simple approach to implement, the definition of these models requires a reference period (or training period) in which a representative variation of the environmental and operational effects must be included. This period (usually lasting one year) must therefore include the full range of operational and environmental effects with a significant influence on the values of natural frequencies.

In the case of the Torrão study, since only a 1-year data period is available, the following strategy was adopted: the available database was divided into two different periods, each consisting of intercalary days. Period 1 was then used to define a multivariate regression model, while Period 2 was used to assess the existence of damage. In this way, both periods contain results within a period of 1 year, but with alternate days.

In the previous section, it was verified that generators present a significantly different behaviour between the operating regimes. On the other hand, it is valid to admit that within each regime this behaviour is practically homogeneous. For this reason, a multivariate linear regression model must be established for each operating regime. The most relevant operational and environmental data are: wind speed (W.S.), outdoor temperature (Temp.), rotor speed (RPM) and pitch angle (Pitch). A detailed description of the models considered, the methodology and analyses implemented and the results obtained is presented in (Oliveira, Magalhães et al., 2018b).

To exemplify some of the relationships between the natural frequencies and the variables of the SCADA system, the Figure 3.7 and Figure 3.8 show, respectability, the evolution of the natural frequencies of the 2 SS* mode as a function of the rotor speed for operating regime 4 and frequency evolution of mode 1 SS* as a function of pitch angle (regime 5).

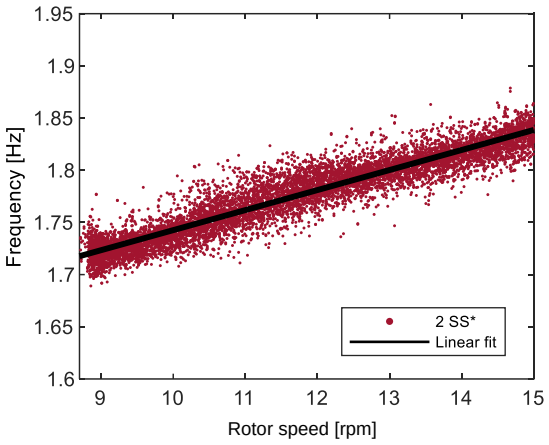


Figure 3.7 – Natural frequency of 2 SS* mode vs rotor speed (regime 4).

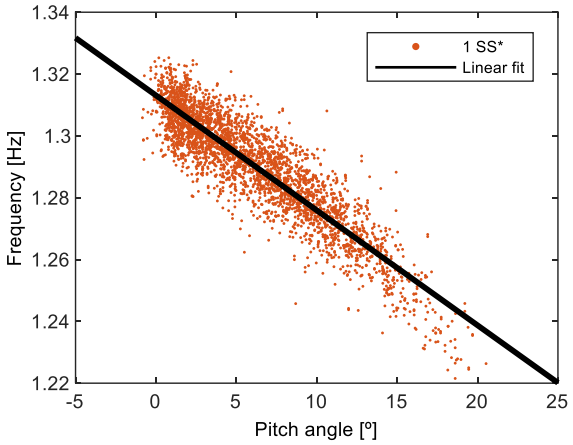


Figure 3.8 – Natural frequency 1 SS* vs pitch angle (regime 5).

After evaluating the influence of external factors on natural frequencies for each of the operating regimes, two alternative approaches can be adopted: consider independent variables with a potential physical relationship with natural frequencies or consider all variables in all regimes, in an attempt to define a more general regression model. In the case of the study under analysis, the second approach was adopted.

Having defined the regression models, it is now possible to predict the values of the natural frequencies of the vibration modes. In Figure 3.9, for modes 1 SS* and 4 FA, the values of the frequencies predicted with the regression model and the values identified from the setups of Period 2 are compared. There is great consistency between the results, which allows validating the developed models.

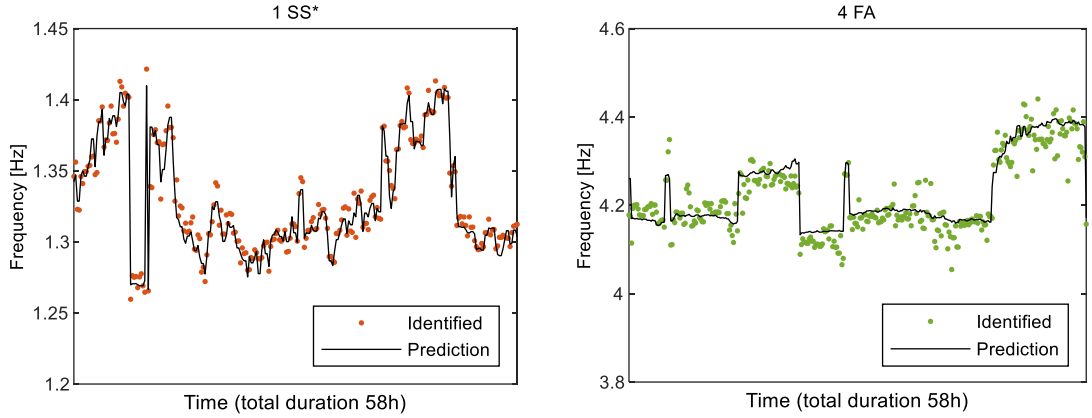


Figure 3.9 – Identified and predicted frequency value of 1 SS* and 4 FA mode for Period 2.

In Figure 3.10, the histograms of the natural frequencies of vibration for the 1 SS* and 2 FA modes are presented. It appears that with this statistical procedure, a clear reduction in the variability of the values of the natural frequencies of the main modes of vibration is obtained, which allows for the identification of damage with greater precision.

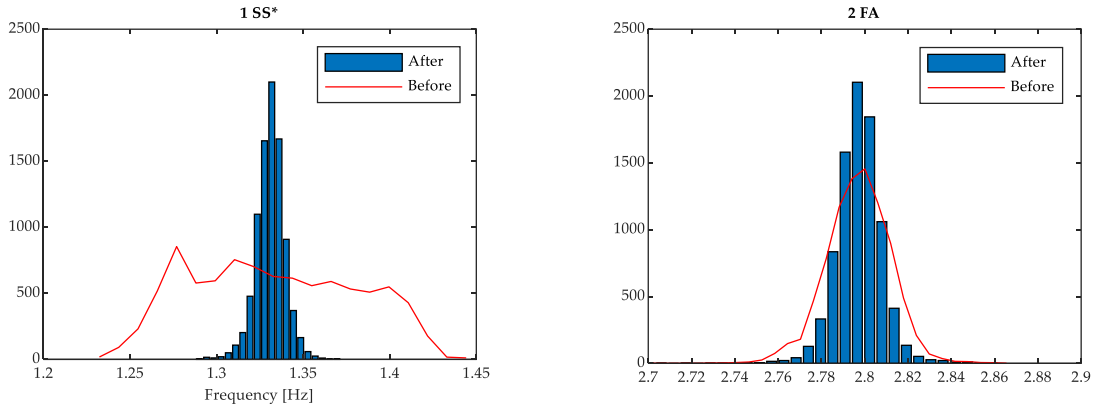


Figure 3.10 – Histograms of the natural frequencies of 1 SS* and 2 FA modes before (red line) and after (blue bars) mitigation of environmental and operational effects.

3.3.3 DAMAGE DETECTION

Finally, the fourth step of the vibration monitoring strategy refers to damage detection. Corrected natural frequencies are used as indicators of abnormal changes in the structure of wind turbine. Thus, a procedure is needed to assess whether the continuously estimated frequencies refer to damage situations or not.

In that sense, a method based on control diagrams can be used. It is a simple statistical tool for process control, which aims to assess whether one or more variables remain within previously established limits, thus indicating that the process unfolds normally. Since it is intended to evaluate the natural frequencies of several vibration modes simultaneously, T^2 control diagrams are used (Johnson and Wichern, 2002). Using this multivariate technique, it is possible to monitor more than one analysis parameter on a single graph. For this reason, control charts are a very suitable technique to identify possible frequency deviations.

In Figure 3.11, a typical T^2 control chart of any generic process is represented. These diagrams consist of the graphical representation of the statistical test called T^2 (vertical axis) for the various observations of a process, generally over time (horizontal axis). After an initial model calibration period, in which the structure is considered to be undamaged, it is possible to set an upper control limit. Then, each new observation is evaluated according to that reference and, if the T^2 value is greater than this threshold, the abnormal event is detected and, most likely, the occurrence of damage. It should be noted that each of the points on the graph could represent a single observation or the average of a group of observations (subsample). A complete description of the application of this tool can be found in (Magalhães, Cunha et al., 2012).

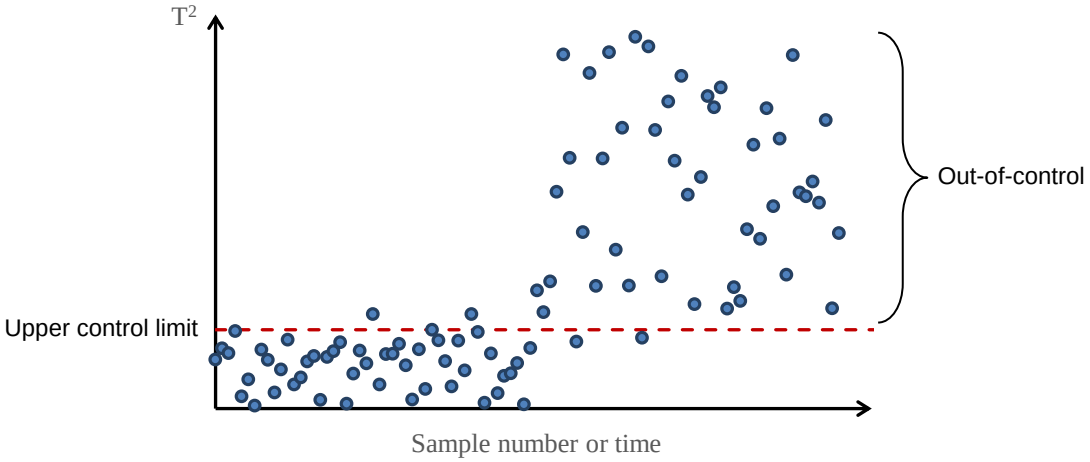


Figure 3.11 – T^2 control chart of a generic process.

3.4 OPTIMIZATION OF THE VIBRATION-BASED MONITORING SYSTEM

3.4.1 STRATEGIES: SENSORS LAYOUT AND SENSORS NOISE

Two strategies were followed in order to reduce the costs related to monitoring equipment: (1) reducing the number of sensors to be used; (2) using lower quality sensors. These two strategies were combined in order to obtain more economical instrumentation solutions, without compromising the quality of the structural evaluation of wind turbines.

3.4.1.1 Sensors Layout

The four tested instrumentation layouts are represented in Figure 3.12. Layout 1 is based on a single pair of sensors located at the top of the tower (+74,988 m). This is an interesting solution as wind turbines are currently equipped with a biaxial accelerometer in this position. The use of this sensor in the evaluation of the structural condition of the tower would represent an important benefit without implying an extra investment.

Although the previous layout has a great advantage in terms of investment in monitoring equipment, it is important to note that due to the reduced amplitude of the modal coordinates associated with the second pair of tower bending modes at this section, it will not be possible to accurately identify these two modes (2 FA and 2 SS). Layout 2 thus emerges as an alternative to layout 1, which optimizes the location of the single instrumentation point. In this case, the pair of sensors is approximately 2/3 of the height of the tower (height +48,392), which theoretically allows the identification of all important vibration modes.

Layout 3 results from the combination of the previous layouts and is thus based on two biaxial sensors located at the top and 2/3 of the tower height. Layout 4 corresponds to the most complete instrumentation situation, based on seven acceleration recording channels, as described in Section 3.2. This layout aims to serve as a reference to evaluate the results of the other layouts.

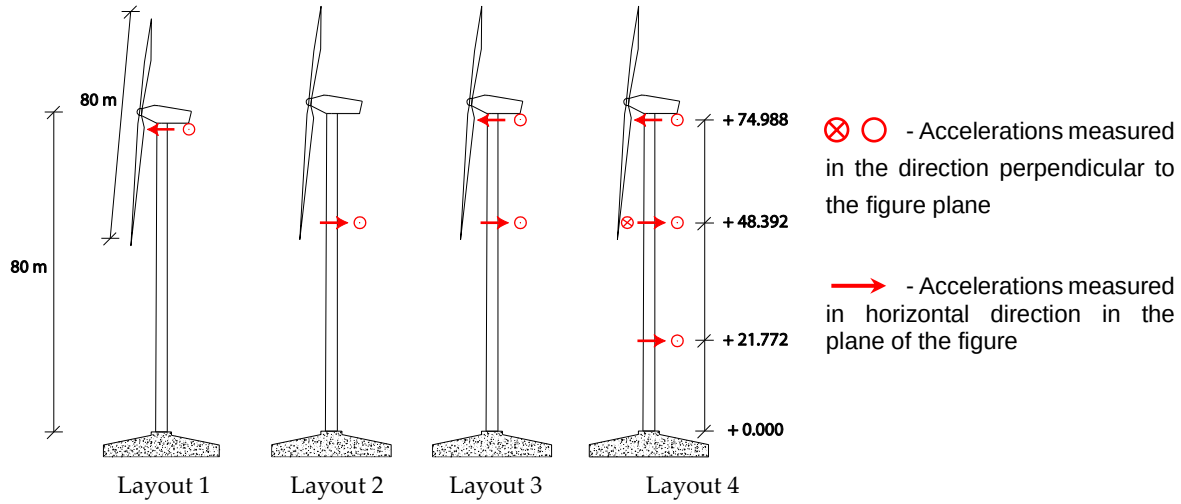


Figure 3.12 – Alternative sensors layouts.

3.4.1.2 Sensors Quality

The sensors adopted in the monitoring system described in Section 3.2 are force-balance accelerometers. These are sensors present very low noise levels and market prices typically exceeding 1500€. In order to simulate the time series that would be obtained with MEMS (microelectromechanical system) sensors, four noise levels were considered: the original noise level of the adopted sensors (N0), and noise levels of $N1 = 1 \cdot 10^{-3}\ m/s^2/\sqrt{Hz}$, $N2 = 1 \cdot 10^{-2}\ m/s^2/\sqrt{Hz}$ and $N3 = 1 \cdot 10^{-1}\ m/s^2/\sqrt{Hz}$. It is important to note that the higher level of simulated noise is a quite conservative upper bound for low cost sensors, and the intermediate noise levels should be also conservative values for mid-range and high quality MEMS sensors with costs between 100 € and 800 € (Evans *et al.*, 2014; Moutinho and Cunha, 2019). With the rapid evolution of these sensors, the noise levels of the MEMS sensors and theirs prices are becoming lower. Still, it should be pointed out that the observed noise is generally higher than the one referred in the specification sheets, since this is also influenced by the complete measuring chain until digitalization.

The new accelerations time series are obtained by adding band-limited white noise time series with different amplitudes (tuned according to the simulated noise level) to the originally measured acceleration time series. This method assumes that the spectral noise of the sensors is constant for the frequency range under analysis, since this is validated by accelerometers testing.

Figure 3.13 represents the spectra of the time series of accelerations recorded at the top of the tower, considering the defined noise levels for different wind speeds. It can be seen that for very low wind velocities, all the adopted noise levels are superior to the measured accelerations, but as soon as the wind velocity reaches values around 2.5 m/s, the accelerations are already above the two first noise levels. The higher noise level is only overcome by the acceleration signal for quite high wind velocities.

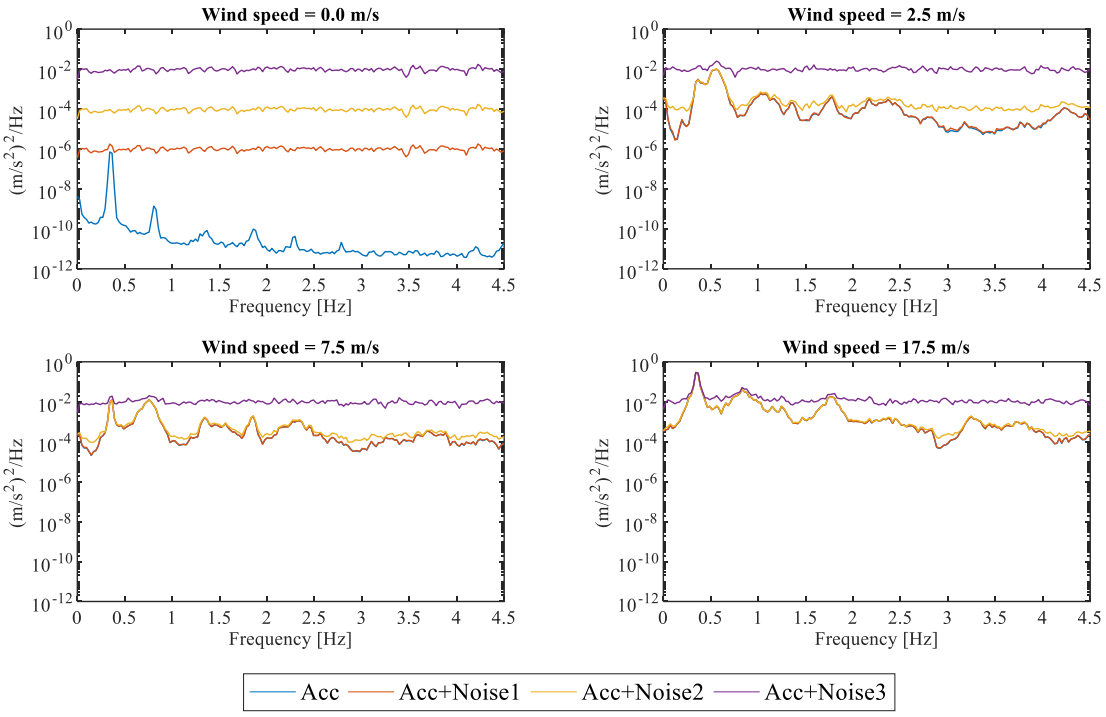


Figure 3.13 – Power spectra of typical acceleration time series measured at the tower top for varying wind velocities: original signal (Acc) and original signal contaminated with different levels of noise (Acc+Noise1,2,3).

In conclusion, sixteen alternative architecture solutions for dynamic instrumentation of wind turbines are to be tested. Having defined the scenarios to be analysed in the scope of this study, the procedure presented in Section 3.3.1 was reproduced for each monitoring solution.

3.4.2 INFLUENCE OF THE SENSORS LAYOUT AND NOISE ON THE MODAL TRACKING

In order to make the interpretation of the results more clearly, their presentation will be carried out in two stages. In a first phase, the implications of the layouts and noise levels in the identification of the 6 vibration modes considered for the identification of damage was evaluated. Then, the performance of each solution is evaluated in relation to the ability to identify damage and the duration of the time interval between the appearance of damage and its detection.

Figure 3.14 shows the Campbell diagrams associated with some of the adopted monitoring solutions. Comparing Campbell diagram of layout 4 N0 (Figure 3.6) with layout 4 N2 and N3 (Figure 3.14a and Figure 3.14b), it observed that as the quality of the sensors decreases (with increased noise), the number of natural frequencies identified for lower rotor speeds (lower excitation levels) are significantly reduced. With noise level N2, it can be seen that the number of identified frequencies for rotor speed lower than 7 rpm significantly reduced, still all the modes can be tracked. For noise level N3, only the second pair of the tower bending modes can be reasonably tracked. For this reason, the noise level N3 will not be considered in future analysis.

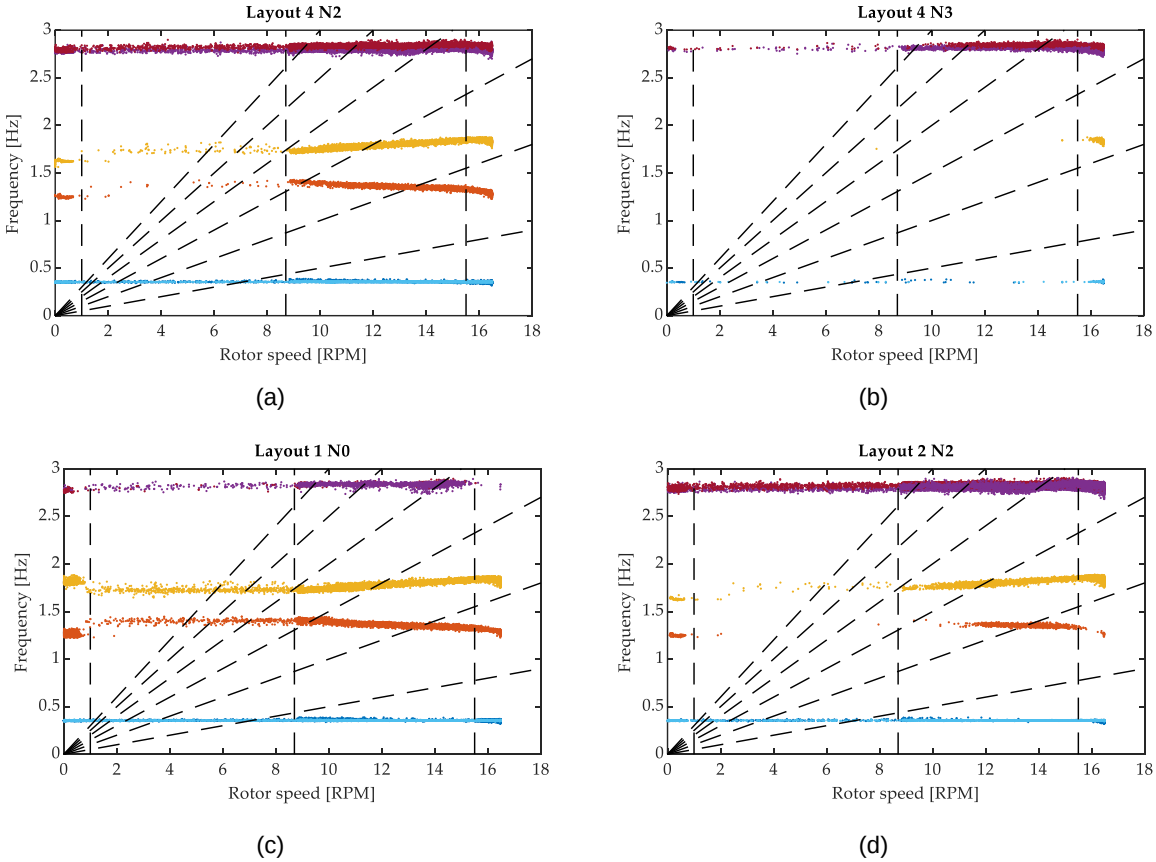


Figure 3.14 – Campbell diagram with the tracked vibration modes with: (a) Layout 4 N2; (b) Layout 4 N3; (c) Layout 1 N0; (d) Layout 2 N2.

Analysing the diagram associated to layout 1 with noise level N0 (Figure 3.14c) it can be seen that and the tracking of the 2nd par of support structure bending modes is less efficient (lower number of points), especially for lower rpm. The reduced modal ordinate of these vibration modes at the top of the tower explains this limitation. For this reason, in this layout these two vibration modes will not be considered in the evaluation of the structural condition (only the modes 1 FA, 1 SS, 1 SS *, and 2 SS * will be considered).

The diagram corresponding to layout 2 with noise level N2 (Figure 3.14d) shows that even using a single poor quality sensor it is possible to obtain a Campbell diagram with reasonable quality.

This qualitative analysis covering different operation conditions is complemented by the results presented in Figure 3.15. In this bar plot, the success identification rate ("number of times a mode is identified" / "number of processed setups") achieved with the different layouts and noise levels for layout 4 is quantified.

For modes 1 SS, 1 FA, 1 SS* and 2 SS* the success rate decreases with the increase of the noise level, the reduction being very drastic for noise level N3. For mode 2 FA (second bending mode of the tower) it is observed a slight increase of the success rate with the increase of noise. This behaviour can be explained by the fact that, being the only mode whose contribution for the response is above the noise level, the identification is only focused on this mode.

Finally, layouts 3 and 4 show very similar success identification rate. For some modes the success rates obtained with layout 1, 2 or 3 are higher than those obtained with the original layout, which indicates that more sensors at the tower may not improve the quality of the results, in particular the sensor at elevation +21,772 m does not have a significant advantage.

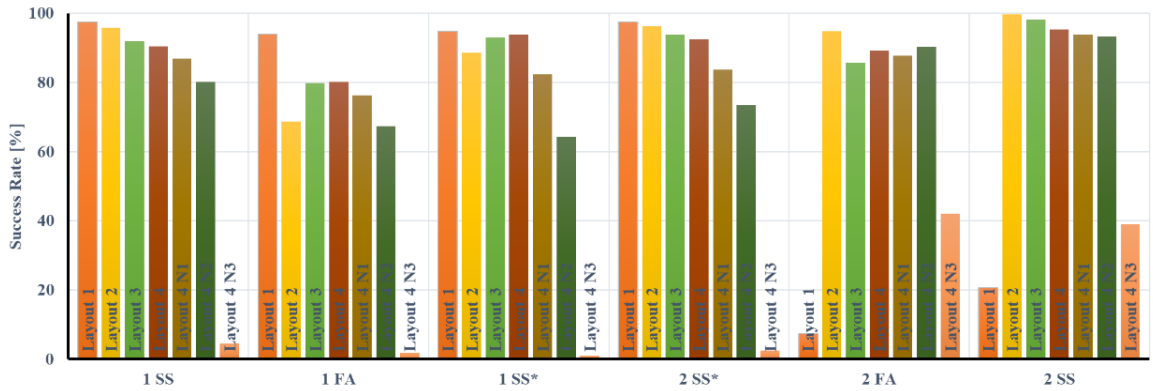


Figure 3.15 – Success Rate [%] obtained witch different layouts (1 to 4) and increasing noise level for layout 4 (N0 to N3) (Layout 1 and 2, MAC limit of 0.5; Layout 3 and 4N1 to 4N3, MAC limit of 0.8).

3.5 PERFORMANCE EVALUATION OF ALTERNATIVE MONITORING STRATEGIES

3.5.1 CRITERIA FOR PERFORMANCE EVALUATION

A statistical procedure based on multivariate control charts was implemented to identify abnormal deviations of the natural frequency values. It consists on a simple tool in which several variables, natural frequency values of several modes in this case, are evaluated according to the statistic test T^2 (Johnson and Wichern, 1988).

This procedure is represented schematically in Figure 3.16. After an initial training period (Period 1), in which it is considered that the structure is not damaged, it is possible to define an upper control limit (UCL) to consider an observation as not damaged (considering that 95 % of the values from this period are within the safety region). Then, each new observation is evaluated according to this reference and, if the T^2 value is larger than this limit, it is considered that an abnormal event is detected (probably due to the occurrence of damage). A complete description of this tool can be found in (Magalhães, Cunha and Caetano, 2012).

In order to have clearer plots (with lower scatter) each point of the control chart is calculated from 36 datasets (equivalent to 6 hours of data). Only the points associated with Period 2 will be represented in the next section and it is considered that the damage occurs in the middle of Period 2 (t_d).

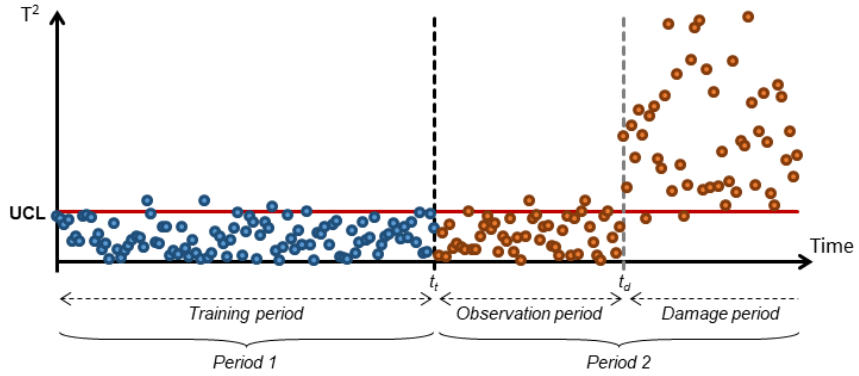


Figure 3.16 – Procedure implemented to identify abnormal deviations of the natural frequency values.

The evaluation of the performance of the alternative monitoring solutions from the visual analysis of the control charts is possible. However, it is essential to define quantitative criteria that allow a more objective evaluation. Thus, four parameters were established:

1. Total number of points on the control chart: it is directly related to the success rates in identifying the selected vibration modes. A greater number of points means a greater number of times that the structure is "examined", considering the same monitoring period;

2. Percentage of outliers in the damage period ($f_{out,D}$) computed as:

$$f_{out,D} = \frac{n_{out|t>t_d}}{N_{T^2|t>t_d}} \tag{3.1}$$

with:

$n_{out\|t>t_d}$	Number of outliers observed in the damaged period
$N_{T^2\|t>t_d}$	Number of control points observed in the damaged period

3. The J_R indicator quantifies the variation of the T^2 index between the scenario without damage and a given damage scenario, and is given by:

$$J_R = \frac{\bar{T}^2_{t>t_d,D}}{\bar{T}^2_{t>t_d,uD}} \tag{3.2}$$

with:

$\bar{T}^2_{t>t_d,D}$	Mean value of T^2 index in the damage period but for the scenario without damage
$\bar{T}^2_{t>t_d,uD}$	Mean value of T^2 index in the damage period

Thus, higher values of J_R indicate a clearer variation of T^2 compared to normal conditions, corresponding to a greater capacity of the layout considered to detect a structural change.

4. Time interval between the occurrence of the damage and the moment when the alert is issued. In fact, quantifying response times is not simple and requires criteria to be established. Considering a real case of continuous monitoring of a wind generator, emitting an alarm signal whenever the natural frequencies present a variation greater than the pre-established limit (point of the control graph above the control limit) would not be feasible given the amount of false alarms that would be issued. Therefore, the difficulty lies in defining an automatic and robust enough method that, based on the analysis of the control graphs, detects the structural change with a high degree of assertiveness.

Since in the present work it is only intended to compare the proposed instrumentation solutions, it was decided to adopt a simple and easy criterion to raise an alarm. Thus, it is assumed that an anomaly is identified when it is found that at least four points on the control chart, in intervals of eight consecutive points, are above the limit. Note that each point corresponds to the observation of 36 data files with a duration of 10-min each. In a perfect monitoring system, each point would correspond to 6 hours of observation of the structure. In conclusion, assuming that the monitoring of the wind turbine does not present data flaws and the success rates in identifying the modes is 100%, the hypothesis that the structure presents anomalies is considered valid whenever, at intervals of 48 hours (8 points, 2 days), at least half of the observations are considered anomalous.

3.5.2 DAMAGE SCENARIOS

In order to evaluate the ability of each alternative monitoring solution to detect the appearance of damage in the wind turbine structure at an early stage, three different damage scenarios were tested:

- D1: Scour problems at the foundation of an offshore monopile wind turbine;
- D2: Foundation problems in onshore wind turbines;
- D3: Damage to the rotor blades.

The detailed description of the procedures used and the three damage scenarios that are defined here can be found in (Oliveira, 2016; Oliveira *et al.*, 2018b). In the following paragraphs, only a brief description of these same scenarios is presented.

Damage scenario D1 can be associated with scour problems at the foundation of an offshore monopile wind turbine (the present case study is an onshore wind turbine but the natural frequencies present values that are similar to the ones found in offshore wind turbines (Devriendt *et al.*, 2014), so this analysis is valid). A small scour depth of around 0.075 times the base diameter of the monopile is considered. Taking into account references (Sørensen and Ibsen, 2013; Prendergast, Gavin and Doherty, 2015), this damage corresponds to the frequency variations presented in Table 3.3. This damage has more impact on the second pair of the tower bending modes.

Damage scenario D2 can be explained by foundation problems in onshore wind turbines, related to the connection between the steel tower and the concrete foundation. It reproduces frequency variations in the tower bending modes that are 5 times smaller than the ones reported in the experimental study presented in (Pelayo *et al.*, 2011). This damage has more impact on the first pair of the tower bending modes.

The last damage scenario (D3) is related to a blade damage. The monitored wind turbine was modelled in the HAWC2 software (Larsen and Hansen, 2007) to assess the sensitivity of the natural frequencies 1 SS* and 2 SS* to structural damage at the blades. The stiffness of the three blades was decreased 15 % over a length of 2 m (5 % of the total length of the blade) around 33 % of the blade length from the blade root. The imposed stiffness reductions led to the variations of the blades frequencies reported in Table 3.3.

The representativeness of the simulated damage may be criticized, but the main goal is to show the ability of alternative monitoring layouts to spot very small frequency variations, as the ones presented in Table 3.3 (all values lower than 1%).

Table 3.3 – Variation of the natural frequencies associated with tested damage scenarios [%].

Modes	Δf_{D1}	Δf_{D2}	Δf_{D3}
1 SS	-0.20	-0.50	0.00
1 FA	-0.20	-0.50	0.00
1 SS*	0.00	0.00	-0.65
2 SS*	0.00	0.00	-0.65
2 FA	-0.40	-0.24	0.00
2 SS	-0.40	-0.24	0.00

Finally, in order to make data processing less complex and to facilitate the analysis and interpretation of results, certain simplifications were adopted. On the one hand, it is considered that the damage occurs in the middle of Period 2, with the values of natural frequencies being reduced according to the percentages shown in the previous table. On the other hand, it is considered that the damage to the structure occurs instantaneously, disregarding the fact that the magnitude of the damage may be increasing over time. In the scenario of a growing damage, it would be identified as soon as the simulated intensity is reached.

3.5.3 RESULTS

In Figure 3.17, the control diagrams for layouts 1 to 4 are represented, considering the noise levels N0, N1 and N2. These diagrams were obtained for the undamaged situation of the structure and for the damage scenarios previously defined as D1, D2 and D3.

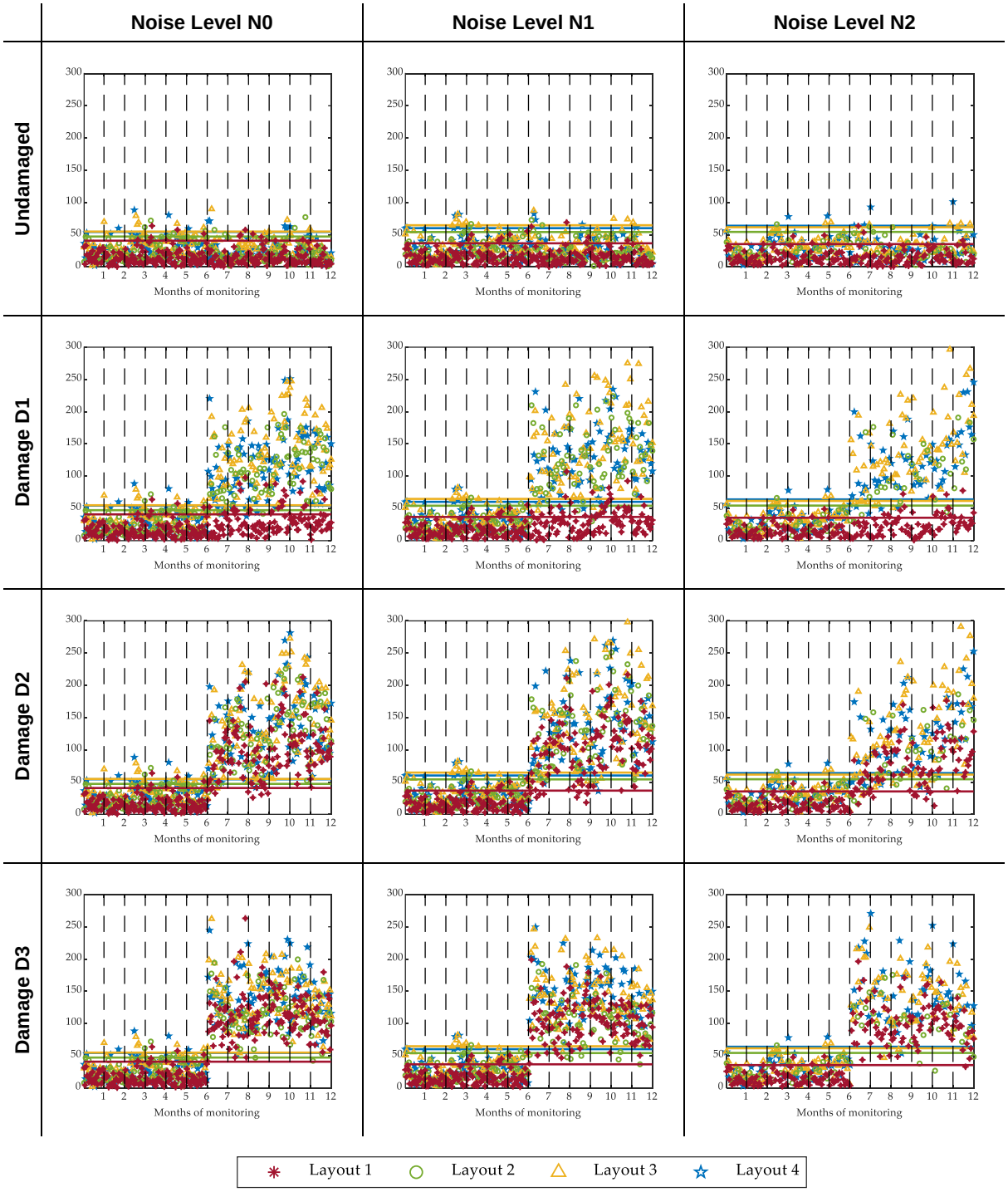


Figure 3.17 – T^2 control charts corresponding to layout 1 to 4 and for noise levels N0, N1 and N2 considering a scenario undamaged and three damage scenarios D1, D2 and D3 (the horizontal lines represent the UCL of each solution).

The analysis of the figure shows that damage scenarios D2 and D3 are identified by all the monitoring solutions under analysis, since after the introduction of the damage most of the points are above the control limit. However, for layout 1 D1 damage scenario, related to erosion problems in the foundation of offshore wind turbines, has not been properly detected. As can be seen from the analysis of Table 3.3, this scenario has more impact on the second pair of tower bending moments and these are not well identified with this instrumentation solution. However, as described in (Evans *et al.*, 2014), increasing the variation of the frequency values of the first pair of bending modes by about 2.5 times (to approximately 0.50%), values associated to still accepted scour, layout 1 is able to detect this damage scenario.

3.5.3.1 Total number of points on the control chart

The reduction in the quality and number of sensors might be associated with a reduction in the density of points in the control charts, as a result of the reduction in the success rates in the identification of all vibration modes under analysis. This is analyzed in Figure 3.18, which represent the total number of points in the control charts for each monitoring solution.

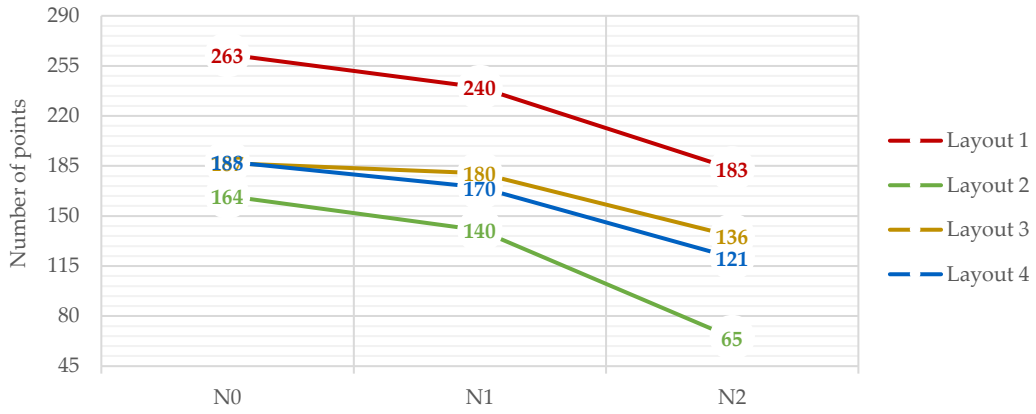


Figure 3.18 – Number of points of the T^2 control charts.

As would be expected, for the same layout, the use of lower quality sensors translates into a reduction in the number of points. This reduction is more pronounced for layouts with only one measurement level (Layouts 1 and 2).

The effect of the reduction in the number of sensors is not so obvious. Layout 2 with only one biaxial sensor is the one with the lowest dot density. At the opposite, layout 1 is the one with the highest density. Although it also has a single measurement level. This is explained by the fact that in its analysis only four of the six main vibration modes are considered, as justified in Section 3.4.2, and by high success rates in the identification of these same four modes, as can be seen in Figure 3.15.

Layouts 3 and 4 present a very similar behavior. It should be noted that for the noise level N0, the difference between them is minimal (Layout 3: 187 points and Layout 4: 188 points). This confirms that the use of an extra measurement level at 1/3 of the height tower (layout 4) does not translate into a significant advantage, and for higher noise levels, it even translates into a disadvantage. This is justified by the lowest measurement level is located in a position of the structure with reduced vibration levels. When using lower quality sensors (noise level N1 and N2), this measurement level only introduces noise into the system.

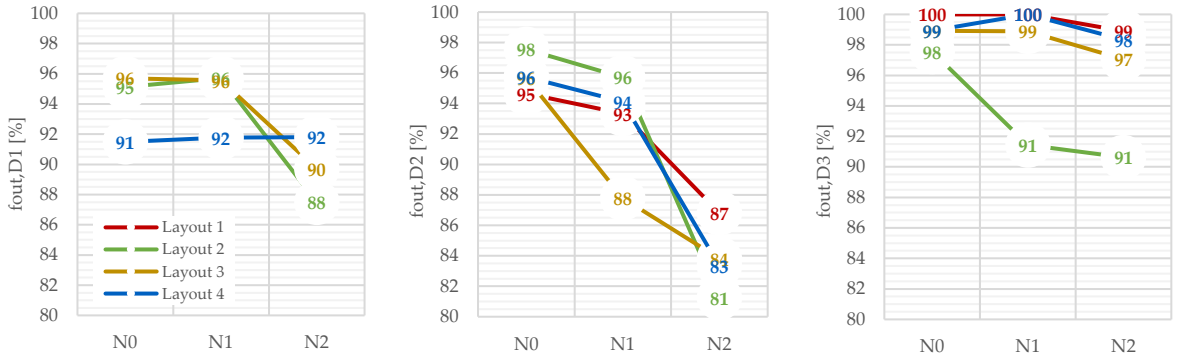
3.5.3.2 Percentage of outliers in the damage period

The relative frequency of outliers in the damage period $f_{out,D}$ for the analyzed solutions are represented in Figure 3.19, for each of the damage scenarios. In general, these results confirm the suitability of the proposed instrumentation solutions in detecting the simulated damage scenarios, with the expectation of layout 1 for damage scenario D1 (values out of the scale adopted for Figure 3.19a.

For damage scenario D1, Layout 4 appears to be insensitive to the reduction of the sensors quality. This behavior is justified by the success rates presented in Figure 3.15, where it is shown that for layout 4 there are no changes in the success rates in the identification of the second pair of tower bending modes with the addition of noise. Still, layouts 2 and 3 exhibit similar behavior to each other and even show better performance than layout 4 for noise levels N0 and N1, which indicates that, for the same noise level of the sensors, it is preferable to use a limited and carefully positioned number of sensors, rather than a large number of sensors.

Now considering the D2 damage scenario, it is possible to understand the loss of precision in the control diagrams with the decrease in the quality of the sensors. For the noise level N0, all solutions have very high $f_{out,D}$ values (greater than 95%) while for the noise level N2 the results are significantly degraded with $f_{out,D}$ values below 90%.

Finally, for damage scenario D3, the majority of the solutions exhibit a high performance with $f_{out,D}$ values greater than 97%. The only exceptions are Layouts 2 N1 and Layout 2 N2, which still presents a good performance.



(a) (b) (c)

Figure 3.19 – Relative frequency of outliers: (a) for damage D1; (b) for damage D2; (c) for damage D3.

3.5.3.3 Variation of the T^2 index between damage and undamaged scenarios

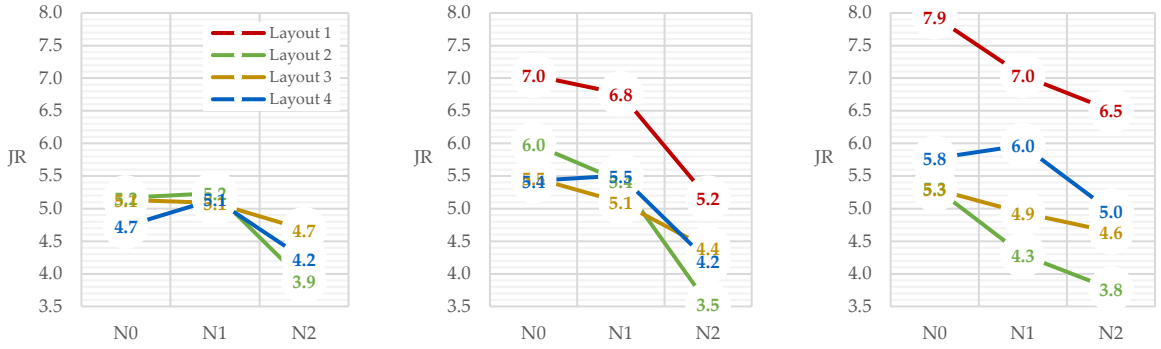
The J_R index was determined for each solution using Equation (3.2). The results obtained for each damage scenario are shown in the Figure 3.20.

The values obtained from the J_R index for the different solutions show once again a good performance in the identification of structural changes. Since the various solutions are being tested in the identification of slight damage and at an early stage, the fact that in all cases $J_R > 3$ is a very positive indicator.

For the D1 scenario, all solutions present a very similar behavior to each other and show little influence of the sensor noise levels. In scenario D2, it turns out that solutions based on layout 1 have a better performance than the other solutions. Again, this behavior can be justified on the basis that for layout 1

only four of the six vibration modes are being used. The rest of the layouts once again show a similar behavior along the increasing noise levels, with reductions in the J_R index.

Considering the D3 damage scenario, the same conclusions can be drawn for solutions based on layout 1. For the remaining layouts, there is a clear distinction in their performance. Layout 4 is the one with the second highest values of J_R while layout 2 is the one with the lowest values.



(a) (b) (c)

Figure 3.20 – Performance indicator J_R index: (a) Damage scenario D1; (b) Damage scenario D2; (c) Damage scenario D3.

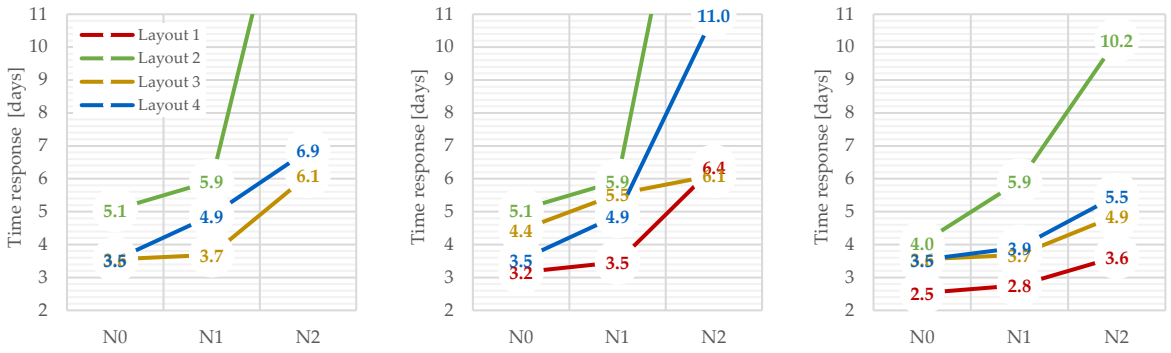
3.5.3.4 Time for damage identification

The response times of the various solutions were calculated using the criteria defined in Section 3.5.1, being the results presented in Figure 3.21. The response times obtained for most of the instrumentation architectures covered in this work are quite satisfactory. It is possible to identify the presence of damage in less than 7 days, in some cases just 3 days. In fact, since structural changes of very small amplitude are being considered, the possibility of detecting them in less than a week is a very interesting result.

The analysis of these figures allows reaching conclusions very similar to those that have already been mentioned during the discussion of the results. As expected, the reduction in sensor quality implies an increase in response times for all systems, with this variation being more pronounced for layout 2. In all damage scenarios, layout 2 is the one with the greatest response times. Layout 1 is the one that allows D2 and D3 damage to be detected more quickly. Once again, it is verified that layouts 3 and 4 present a very similar behavior, taking advantage of layout 3 for higher noise levels (N2 and N3).

The minimum response times obtained were 3.5 days for the D1 damage scenario with Layout 4 N0, while for D2 and D3 damage times of 3.2 and 2.5 days were obtained, respectively, using layout 1 N0. These are very promising values considering the magnitude of the damage considered. These values prove the effectiveness and the importance of the application of vibration monitoring systems in wind generators in order to identify structural changes.

At the opposite extreme, the maximum response times are for Layout 2 N2, with durations of 17.9, 20.4 and 10.2 days for damage scenarios D1, D2 and D3, respectively. Despite being values 4 to 6 times higher than the minimum values, this is not a totally inappropriate solution. Bearing in mind that this solution only requires a low-cost biaxial sensor of the MEMS type and that damage of very small amplitude is being considered.



(a) (b) (c)

Figure 3.21 – The response time of optimized monitoring strategies: (a) Damage scenario D1; (b) Damage scenario D2; (c) Damage scenario D3.

3.5.3.5 Conclusions

In Table 3.4, all the obtained results are summarized, together with a column with indicative costs for the sensors adopted in the relevant layouts and a final evaluation. It is important to highlight that the costs are indicative (there is a large dispersion in the sensors cost that depends not only on the noise floor but also on other properties such as reliability and construction quality), being the final cost also dependent on the adopted acquisition system and cables or wireless devices. The prices of force balance sensors (N0) have been stable over time, whereas, for the MEMS sensors (N1and N2) a price decrease and quality improvement has been observed. For the lower quality sensors the prices present even higher dispersion, so a quite conservative upper bound of 200€ per channel was assumed.

One of the objectives of this work was the definition of an optimal combination of layout and noise level of the sensors in order to conceive a monitoring system sufficiently accurate to detect structural changes of the most common wind turbines. However, as it was possible to perceive throughout the results discussion and with the summary in Table 3, there is no one solution that brings together all the advantages and stands out noticeably before the others. In fact, as expected, the reduction of associated costs implies the loss of some capacity in the dynamic identification of the structure and, consequently, of the performance in the detection of damage.

Thus, maybe more important than the design of an ideal optimized monitoring system, is the definition of criteria and general guidelines that help in the definition of an instrumentation architecture for a particular case, according to the available means and the accuracy of the intended results.

Table 3.4 – Comparison of the analysed instrumentation solutions.

Monitoring Solution		Criterion 1	Criterion 2			Criterion 3			Criterion 4			Sensors Cost (Approx.)	Final Evaluation
			D1	D2	D3	D1	D2	D3	D1	D2	D3		
Layout 1	N0	263	-	95	100	-	7.0	7.9	-	3.2	2.5	3 000 €	▬
	N1	240	-	93	100	-	6.8	7.0	-	3.5	2.8	1 000 €	▬
	N2	183	-	87	99	-	5.2	6.5	-	6.4	3.6	<400 €	▬
	N3	-	-	-	-	-	-	-	-	-	-	-	✗
Layout 2	N0	164	95	98	98	5.2	6.0	5.3	5.1	5.1	4.0	3 000 €	✓
	N1	140	96	96	91	5.2	5.4	4.3	5.9	5.9	5.9	1 000 €	✓
	N2	65	88	81	91	3.9	3.5	3.8	17.9	20.4	10.2	<400 €	✓
	N3	-	-	-	-	-	-	-	-	-	-	-	✗
Layout 3	N0	188	96	96	99	5.1	5.5	5.3	3.6	4.4	3.6	6 000 €	✓
	N1	180	96	88	99	5.1	5.1	4.9	3.7	5.5	3.7	2 000 €	✓
	N2	136	90	84	97	4.7	4.4	4.6	6.1	6.1	4.9	<800 €	✓
	N3	-	-	-	-	-	-	-	-	-	-	-	✗
Layout 4	N0	188	91	96	98	4.7	5.4	5.8	3.5	3.5	3.5	10 500 €	▬
	N1	170	92	94	91	5.1	5.5	6.0	4.9	4.9	3.9	3 500 €	✗
	N2	121	92	83	91	4.2	4.2	5.0	6.9	11.0	5.5	<1 400 €	✗
	N3	-	-	-	-	-	-	-	-	-	-	-	✗

✓ Relative Advantage, ✗ Relative Disadvantage, ▬ Advantage depends on the circumstances

Accordingly, the main ideas that can be transmitted with the analysis of Table 3.4 are described in the following paragraphs.

The noise level N2 represents the maximum noise limit of the sensors to be used in the instrumentation of wind turbines from which it is not possible to obtain acceleration time series with adequate quality. In this way, sensors with noise level N3 are inadequate in any layout.

Layout 1, despite having demonstrated a good performance in the identification of D2 and D3 damage scenarios, does not allow the detection of D1 damage at an early stage of development. The lack of versatility of this layout makes it only advantageous for wind turbines equipped with a biaxial accelerometer at the top of the tower by the manufacturers and when there is no possibility / interest in complementing/chancing the instrumentation. In fact, the great advantage of this solution is the low investment associated with it. However, it is essential to keep in mind its limitations. For situations in

which it is intended to install only one biaxial sensor in the tower, layout 1 should be avoided in favor of layout 2.

Layout 4 represents an extensive instrumentation layout, and consequently with high costs, which allows to accurately characterize the dynamic behavior of the structure. As has been proven, it only makes sense to associate this layout with highly sensitive sensors (low noise level) since for noise levels N1 and N2, layout 3 showed better performance. Thus, Layout 4 N0 is a solution to be adopted, mainly, in research projects or in works in which greater detail is required.

The solutions that in the previous table were marked as having a relative advantage are layouts 2 and 3 associated with noise from N0 to N2. They are a broad group of six combinations of instrumentation to which different budgets and performances are associated.

Several interesting conclusions can be drawn from the analysis of criteria 4 and cost. Reducing the initial cost of the sensors by about 1/3 (Layout 3 N0) is only increasing the response times by 1% for the damage scenarios D1 and D3 and by 26% for the damage D2. Considering the reduction of the same costs by 2/3 of the initial value (Layout 2 N0), response times are increased by 43% for damage D1 and D2 and by 15% for D3. It is also relevant to note that using only a single intermediate quality sensor (Layout 2 N1) the response times are increased by 68% for all damage scenarios. With the nowadays quality of the MEMS sensors, it is clear that in the monitoring of wind turbines the high costs of the force-balance sensors can be avoided.

The previous conclusions allow us to realize that it is possible to optimize the original monitoring system on a large scale without jeopardizing its performance and without compromising the accuracy of the structural condition assessment.

The monitoring system, in addition to allowing structural changes to be identified, may also identify the location in the structure where the damage occurred. In reality, the first step to take after the alert for the presence of damage in the structure is to identify the most likely location where the damage occurred.

The repercussion that a given damage has on the dynamic parameters of the structure depends on the characteristics of that same damage. Taking the present case study as an example, the reduction in blade stiffness mainly affects the modes related to the blades, while the cracking of the foundation of an onshore wind turbine mainly affects the first pair of vibration modes of the tower. Thus, as soon as a structural change is identified from a general control chart (control chart in which the 6 main vibration modes are evaluated simultaneously), the same diagram can be replicated using subset of natural frequencies to identified the natural frequencies that produced the change observed ion the global control chart These methodology presented before was replay for all monitoring solutions and the analysis of the results allows to conclude that through the construction of control diagrams in which variations of specific natural frequencies are evaluated, it is possible to prove indication about the possible location of the damage, verifying a correct relationship between the defined damage scenarios and the information transmitted by the partial control charts.

3.6 FINAL CONSIDERATIONS

The present chapter presents the main results obtained from a vibration-based monitoring system installed on a 2.0 MW onshore wind turbine, with the aim of detecting small structural damage considering different monitoring strategies.

The first important result that can be taken focuses on the quantification of sensor noise above which it is not possible to adequately identify the most relevant modes for the dynamic characterization of a wind turbine.

The main conclusions and considerations that were drawn from the present study are listed below:

- In general, the obtained results demonstrate that the monitoring solutions based on continuous modal identification are adequate to detect structural changes in wind turbines. Even with a small number of sensors installed, it is possible to detect different types of damage at an early stage;
- The reduction in the number of sensors and / or their quality implies lower success rates in the identification of the reference modes and, consequently, more time for the structural change to be confidently detected;
- The definition of optimized layouts mainly influences the degree of success in identifying the different vibration modes. This degree of success depends mainly on the amplitude of the modal configurations of the different modes at the points where the sensors corresponding to each layout are located;
- The solution based on a biaxial sensor at the top of the tower revealed some deficiencies in the identification of the second pair of tower bending modes. Even so, it proved that it is capable of identifying minor damage;
- Even using a single low-cost biaxial sensor of the MEMS type, acceptable results were obtained, as long as the sensor is placed in a suitable section of the tower;
- Solutions based on two and three instrumented sections lead to similar results, so the installation of a biaxial sensor at 1/3 of the height of the tower does not reflect any advantage;
- Comparing the results for the various solutions, it seems advantageous to use a smaller number of sensors, but of good quality and carefully positioned, instead of using a larger number of sensors, but of inferior quality;
- It is possible to effectively optimize the original monitoring system, significantly reducing costs and without impairing performance on an equal scale;
- Six main solutions were selected that were considered to have relative advantages. These solutions are associated with different budgets and performances;
- The proposed solutions, in addition to allowing structural changes to be identified, also make it possible to partially locate the element where they occurred, which translates into added value for the inspections to be carried out later.

The results achieved and the tools developed are very relevant to promote the use of dynamic monitoring systems in wind turbines and for the optimization of dynamic monitoring systems to be installed in these structures, allowing a more sensible choice of the type of sensors to be adopted and distribution along the height of the tower.

4
MONITORING CAMPAIGN AT TOCHA WIND FARM*

4.1 INTRODUCTION

This chapter introduces the Tocha Wind Farm, presents the different layouts adopted in the instrumentation of the wind turbines and shows initial results. The results presented demonstrate the ability of the different monitoring components to track the modal parameters of the system, composed of tower and rotor, and to characterize the internal loads at the tower base and blade roots.

The main goal of this chapter is to describe an experimental setup that can provided reliable information regarding wind forces and wind fatigue damage on the tower and blades of wind turbines. Such monitoring system must be able to capture the mechanical loads acting on the structure and should take into account the environmental and operating data already available through the SCADA.

The data collected and presented in this chapter is the foundation work for developments presented in later chapters, providing a reliable set of wind turbine measurement data used for fatigue damage estimation.

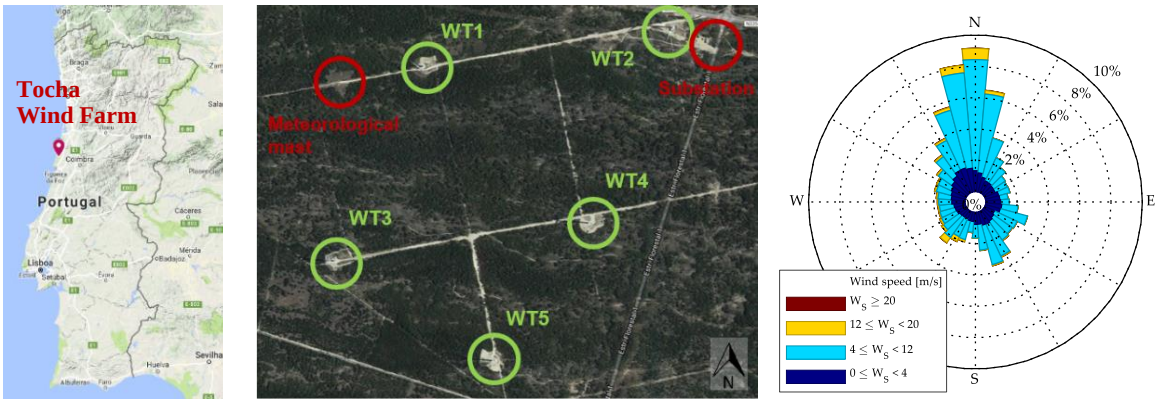
It is important to mention that within the scope of this thesis not all data collected by the monitoring systems installed in the Tocha Wind Farm were processed. One of the objectives of this work was the start of the experimental campaign in this wind farm and the development of the first routines and algorithms for the processing of the recorded data. Taking into account the large volume of measured data and its diversity, future work to be developed are described in Chapter 7.

* This chapter is based on the paper:
Pacheco, J., Guimarães, S., Moutinho, C., Marques, M., Matos, J. C., and Magalhães, F. (2020) *New strategies for optimized structural monitoring of wind farms: experimental campaign.* Wind Energ. Sci., 5, 983–996, https://doi.org/10.5194/wes-5-983-2020.

4.2 TOCHA WIND FARM AND VESTAS V100-1.8 MW

The Tocha Wind Farm is owned by EDP Renewables and started its operation in May 2012. It is located in the central region of Portugal, approximately 3 km from the coastline (Figure 4.1a). It consists of five Vestas wind turbines, model V100 with 1.8 MW of rated power, totalling 9.0 MW of installed power. Figure 4.1b presents a geographic location of the wind farm and the distribution of the five wind turbines, identified with numbers that will be used throughout this work. This figure also identifies a substation position, as well as a meteorological mast.

It is important to note that the wind farm fits into a coastal area, with very soft orography of the terrain and where the foundation's soil is predominantly sandy, which is why deep foundations are used in all wind turbines. Thus, the steel tower of the turbines is connected to a 14-by-14 m concrete slab with variable height, 1.50 m at the ends and 3.00 m in the central area. In turn, sixteen concrete piles with 1 m diameter support the slab.



(a) (b) (c)

Figure 4.1 – Tocha Wind Farm: (a) Geographic location in Portugal; (b) Wind turbines and auxiliary structures; (c) Characterization of the wind conditions observed from 2013 to 2018, based on data provided by meteorological mast (100 m high measurements).

The wind rose (Figure 4.1c) obtained with the wind measured at the meteorological mast between 2013 and 2018 reveals that the predominant wind direction is approximately north. Also reveals a secondary wind direction along the southeast direction. Thus, considering the very smooth terrain and the proximity of the coast, wind turbines 1, 2 and 3 are more frequently exposed to slightly disturb offshore winds, while the remaining turbines are more frequently exposed to wind with additional turbulence caused by wake effects.

Vestas V100-1.8MW wind turbine is a wind turbine designed for low wind onshore sites, so it features a larger rotor diameter, enabling it to deliver higher output at low wind speeds. It is a 3-bladed upwind turbine with a rotor diameter of 100 m (sweep an area of 7850 m^2) and a generator rated at 1.8 MW. The turbine operates at variable speeds from 9.3 to 15 rpm, with individual pitch control for each blade. The energy input from the wind to the turbine is adjusted by pitching the blades according to the control strategy. The pitch system also works as the primary brake system by pitching the blades out of the wind (putting the rotor in idling). As show in Figure 4.3c, the power production increases gradually from cut-in wind speed (4 m/s) to rated wind speed (12 m/s) and is stable up to cut-out wind speed (20 m/s).

The yaw system allows keeping the turbine upwind during power production to maximize the power output and reduce the risks of nacelle misalignment. The nacelle is installed on the yaw plate that is bolted to the turbine tower. Asynchronous yaw motors with brakes enable the nacelle to rotate on top of the tower. Automatic yawing is deactivated when the mean wind speed is below 3 m/s.

The hub supports the three blades and transfers the reaction forces to the main bearing (also supports blade bearings and the pitch cylinder). The hub is placed the height of 95 m and is supported by a steel tower, with a hollow circular cross-section with variable diameter and thickness, composed of four segments that are linked on site with bolted connections (flange connections). Tower internals such as platforms and ladders are support in a horizontal direction by magnets and vertically by mechanical connections. Table 4.1 summarizes the main turbine characteristics.

Table 4.1 – Technical specification of the Vestas V100-1.8 MW wind turbine.

General		**Rotor**	
Rated Power	1800 kW	Diameter	100 m
Cut-in wind turbine	4 m/s	Swept area	7850 m^2
Rated wind speed	12 m/s	Number of blades	3
Cut-out wind speed	20 m/s	Blade length	49 m
Wind Class - IEC	IECS – IEC IIIA	Operation range	8.8 to 14.9 rpm
Generator type	Asynchronous with wound rotor and slip rings	Rotational direction	Clockwise (front view)
Power regulation	Pitch regulated with variable speed	Aerodynamic brakes	Full feathering

Tower and Foundation		**Pitch and Yaw systems**	
Tower type	Conical tubular	Pitch system type	Hydraulic (1 cylinder/blade)
Hub height	95 m	Pitch system range	-5° to 90°
Max. section length	24.6 m	Yaw system type	Plain bearing system with built-in friction
Max. diameter	4.2 m	Yawing speed	≈0.45 °/sec (15 min for a full rotation)
Support foundation	Square slab with piles in reinforced concrete	Hub type	Cast ball shell hub

Focusing on the braking concept, the main brake on the turbine is aerodynamic and is done by pitching the three blades at 90°. In addition, there is a mechanical disc brake on the high-speed shaft of the gearbox. The mechanical brake is only used as a parking brake and when the emergency stop is activated.

As described in Chapter 2, the wind turbines are equipped with a controller system. In this case, the turbine controller is based on an interconnected hardware and software controller. The turbine control system serves the following main functions:

- Monitoring and supervision of overall operation
- Synchronizing of the generator to the grid during connection sequence
- Operating the wind turbine during various fault situations
- Automatic yawing of the nacelle and blade pitch control
- Noise emission control
- Monitoring of ambient conditions and the grid.

4.3 PRELIMINARY EVALUATION OF THE MODAL PROPERTIES OF THE WIND TURBINES

In order to obtain an initial estimate of the wind turbine dynamic properties before the installation of the monitoring systems, a set of ambient vibration tests were performed in four of the five wind turbines in operating and non-operating conditions. Additionally, a simple numerical model of the wind turbines was deployed. In the next sections, the preliminary evaluation of the modal properties of the wind turbines will be described.

4.3.1 NUMERICAL MODELS

In order to better interpret the experimental results, a numerical model of the wind turbine was developed using a software for structural analysis: ROBOT STRUCTURAL ANALYSIS (Autodesk, 2016), following the available technical drawings. It is a simplified model, in which the operation of the turbine is not modelled. Rotational movement of the rotor and all control systems are disregarded, being the main purpose of the numerical model the simulation of the dynamic behaviour of the tower under the test conditions presented in the following section.

It is considered that the foundation does not allow any kind of relative movements and is not considered the opening of the door (a specific numerical model for this detail has shown that it has a reduced influence on global behaviour). Thus, the modelling of the tower was based on 3D bar elements to which the corresponding cross-sections were assigned.

Regarding blade modelling, at the time very detailed information was not available. Alternatively, starting from the NREL 5 MW reference wind turbine (Jonkman *et al.*, 2009), the characteristics of the blades were scaled to be compatible with the wind turbine under study. The blades are modelled by 3D bar elements, divided into multiple sections to which the average mass, stiffness and inertia characteristics have been attributed. Since there is no rotation of the rotor, the blades were modelled with the pitch angle observed during the ambient vibration tests.

The nacelle and hub are represented by concentrated loads applied at their centres of gravity. The connection between the tower, blades and the geometric centres of the nacelle and hub is modelled with rigid links of negligible mass.

Still, it is important to note that more advanced models are currently being developed in FAST (Sprague, Jonkman and Jonkman, 2015) using some structural information that was derived from the previously described model, calibration procedures based on the monitoring data and further information that was disclosed in the context of other research projects. All the details of one of the developed FAST models are presented in (Pimenta *et al.*, 2019).



(a) (b)

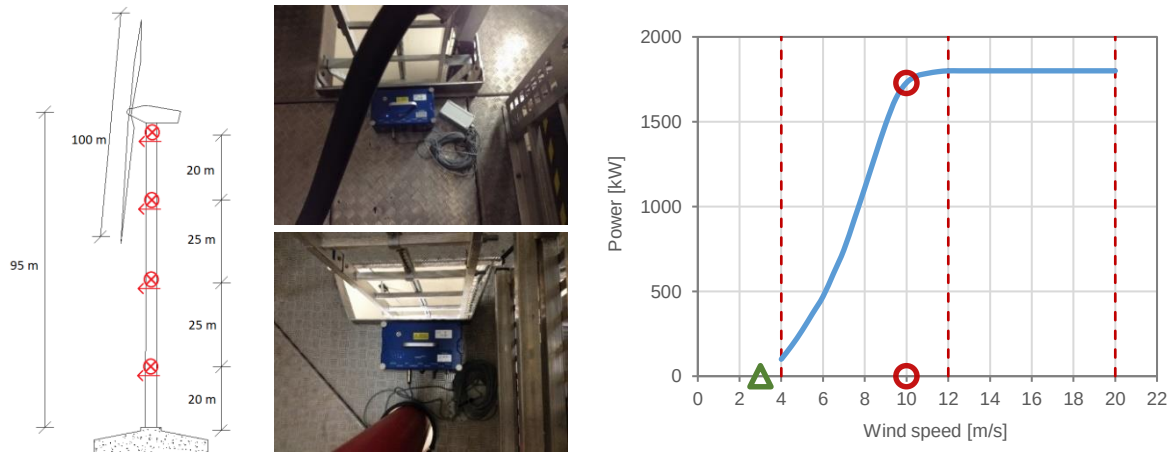
Figure 4.2 – Vestas V100-1.8MW: (a) Wind turbine at Tocha Wind Farm; (b) Numerical model developed using ROBOT STRUCTURAL ANALYSIS.

4.3.2 AMBIENT VIBRATION TESTS

The ambient vibration tests were performed during two visits. In the first campaign, the main goal was to accurately identify the natural frequencies and the configuration of the tower vibration modes, considering two different situations: wind turbine in operating conditions and wind turbines in non-operating conditions (the rotor was stopped or idling). At this stage, only the wind turbine 1 was tested. Several 10 minutes of accelerations time series were measured (sample rate of 100 Hz) with 4 standalone seismographs (Figure 4.3a), with internal tri-axial force balance sensors, that were placed in the horizontal platforms of the tower (Figure 4.3b).

In the second campaign, the main objective was to identify the natural frequencies of all wind turbines of the wind farm, in order to characterize the variability of the natural frequencies. The same equipment was used and with the same data acquisition parameters, but only the two highest sections of the towers were instrumented. It should be noted that in this second tests the rotor of the wind turbines was stopped.

The collected acceleration time series were first analysed in the frequency domain and then processed with the Covariance driven Stochastic Subspace Identification method (SSI-COV) (Magalhães and Cunha, 2011). The operating scenarios observed during the performance of the ambient vibration tests are shown in Figure 4.3c): 1st campaign: red circles, 2nd campaign: green triangle. It can be seen that the wind conditions observed during the two test are quite different. The owner of the wind farm provided SCADA data with mean, maximum and minimum values of relevant variables for each 10-minutes period.



(a) (b) (c)

Figure 4.3 – Ambient vibration tests: a) Instrumented section; b) Sensors; c) Operating scenarios and power curve of Vestas V100 wind turbine (https://en.wind-turbine-models.com).

Figure 4.4 shows some of the results obtained from the first campaign in non-operating condition. The top left plot shows two averaged normalized spectra (ANPSD): one for the for-aft direction, FA, (perpendicular to the rotor plane) and another for the side-side direction, SS, (parallel to the rotor plane). It is possible to identify several abscissa in correspondence with the most relevant peaks of the spectrum, which represent good estimates of natural frequencies. Among the various peaks identified, there are two that clearly stand out: one near 0.25 Hz and another near 1.80 Hz. Comparing the experimental results with numerical ones (Figure 4.5), it is confirmed that these peaks correspond to the first and second pairs of tower bending modes. In the stabilization diagram covering the full frequency range under analysis, the position of the first three pairs of tower bending modes is marked. The two zooms presented at the bottom of the figure show that with the SSI-COV method it is possible to separate the very close modes within the first two pairs of frequencies. There are still other stable pole alignments

relevant to the dynamic characterization of the structure. However, they are probably associated with vibration modes dominated by the rotor, which can only be identified and characterized using the more detailed instrumentation, which will be described in the next section.

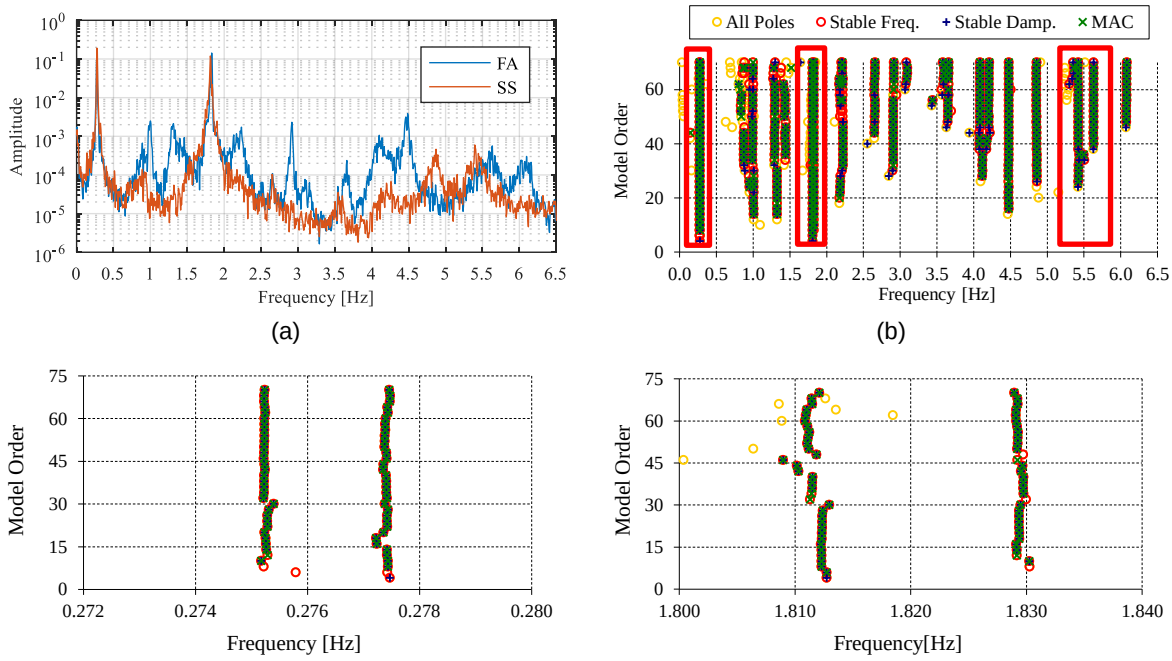


Figure 4.4 – Ambient Vibration test results for wind turbine 1: (a) Average power spectra for FA and SS directions; (b) Stabilization diagram produced by the SSI-COV method; (c) Two zooms of this diagram for first (left) and second (right) pairs of tower bending modes.

Figure 4.5 presents the identified mode shapes and natural frequencies, which are compared to numerical results obtained from the preliminary simple numerical model. There is an excellent relationship between numerical results (blue line) and experimental results (red circles).

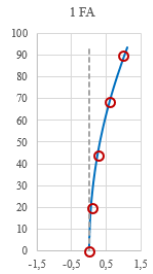
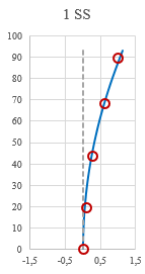
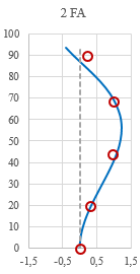
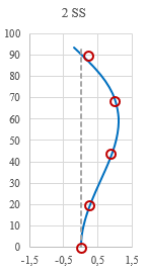
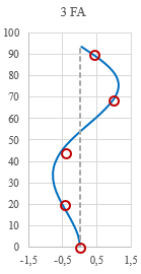
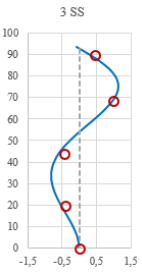
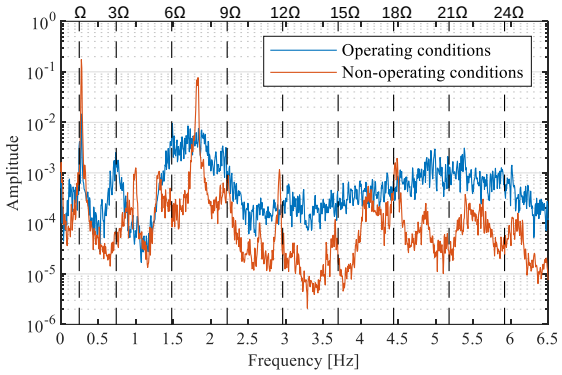
Modes shapes						
	1 FA	1 SS	2 FA	2 SS	3 FA	3 SS
$f_{exp}[Hz]$	0.275	0.277	1.829	1.812	5.635	5.426
$f_{model}[Hz]$	0.269	0.271	1.765	1.834	5.431	5.433
$\Delta f[\%]$	-2.18	-2.17	-3.50	1.21	-3.62	0.13
$MAC[\%]$	99.9	99.9	95.1	95.7	98.9	97.3

Figure 4.5 – Mode shapes and natural frequencies identified with the ambient vibration test and numerical model of wind turbine 1.

Still, for the first test campaign, it is important to understand the influence that the normal operation of the rotor has on the dynamic characteristics of the structure. Thus, Figure 4.6 compares ANPSD (average normalized auto-spectral density function) obtained for stopped rotor and in operation. It should be noted that the represented ANPSD were calculated considering together the signals measured along the FA and SS directions. The dashed vertical lines represent the harmonic frequencies associated with the rotor operation ($\Omega, 3\Omega, 6\Omega, ...$). The results obtained in terms of natural frequencies (f) are also compared for the identified vibration modes for the two analysed situations. For the first tower bending modes there are two very pronounced peaks for the two considered operating conditions. For the second pair of tower bending modes only in non-operating conditions there is a clear peak in ANPSD.



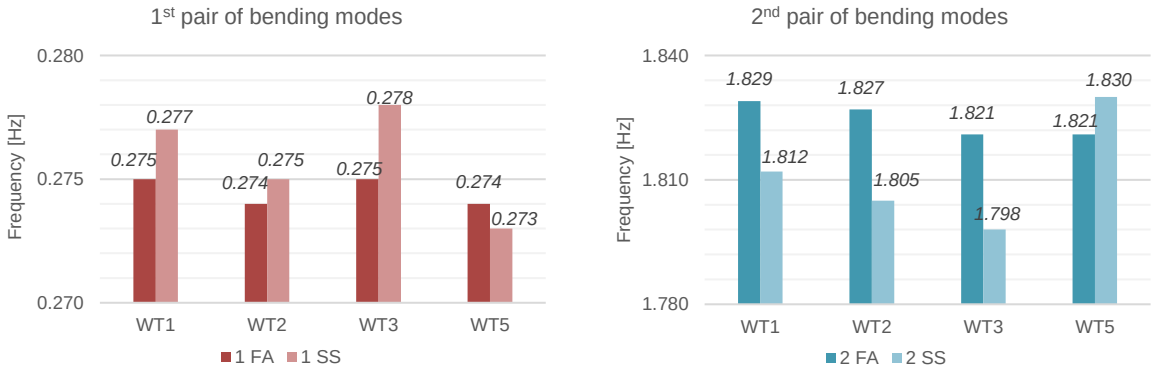
(a)

Vibration Modes	Non-operating f $[Hz]$	Operating f $[Hz]$
1 FA	0.275	0.276
1 SS	0.277	0.275
2 FA	1.829	1.795
2 SS	1.812	1.896
3 FA	5.635	5.489
3 SS	5.426	5.355

(b)

Figure 4.6 – Ambient Vibration test results for wind turbine 1 in operating and non-operating conditions: (a) Average power spectra; (b) Natural frequencies (results obtained from 10 minutes single observation setups with very low variance of the environment and operational parameters).

Figure 4.7 compares the results obtained for the four tested wind turbines. All of them present quite similar natural frequencies, but wind turbine 5 seams to present a slightly different behaviour expressed by the differences observed at the values of the natural frequencies of the first and second tower bending modes associated with the side-side direction (1 SS lower than the others and 2 SS higher than the others). For this reason and also because this is the wind turbine where higher turbulence is expected, it was decided to focus the monitoring camping on wind turbines 1 and 5.



(a) (b)

Figure 4.7 – Comparison of the natural frequencies of four wind turbines in non-operational conditions: (a) 1st pair of bending moments; (b) 2nd pair of bending modes.

4.4 MONITORING SYSTEM AND PRELIMINARY MONITORING RESULTS

The experimental campaign in Tocha Wind Farm involves the simultaneous monitoring of several wind turbines during a period of about three years. In order to obtain data representative of the dynamic behaviour of all wind turbines, the experimental campaign includes the following three instrumentation layouts:

- A complete monitoring layout installed on wind turbine 1;
- An intermediate monitoring layout installed on wind turbine 5;
- A simple monitoring layout to be installed on the other wind turbines, considering shorter instrumentation periods.

The distribution of the monitoring layouts in the wind turbines of the farm was conditioned by the available time slot for installation of equipment, usually scheduled during other maintenance operations, and by the intention to instrument the rotor of one wind turbine that for the predominate wind direction (north) is loaded by an unperturbed flow and another one the is influenced by the wakes of the other turbines (see Figure 4.1c). For this reason, wind turbine 1 was instrumented according to the complete layout, while the intermediate layout was applied in wind turbine 5.

The simple monitoring layout has two main objectives: i) to characterize and identify differences in the dynamic behaviour of wind turbines; ii) to understand the interaction of the wake effects between nearby wind turbines. This simple layout will be applied to all other structures, considering time periods limited to four or six months. If justified or if atypical behaviours are identified, these wind turbines can then be instrumented with a complementary layout, suitable for each situation that is intended to be analysed.

The complete monitoring layout includes the following components:

- Two alternative systems to characterize accelerations at the tower: a commercial system based on a set of low noise force balance accelerometers and a customized low-cost system based on MEMS (micro electromechanical systems) accelerometers designed and assembled in FEUP (Moutinho and Cunha, 2019);
- Strain gages at the tower base to characterize the stresses during different operating conditions;
- Clinometers to characterize the rotations and, indirectly, the bending moments at the base of the tower;
- A set of fibre optic strain gages to estimate bending moments at the blades roots;
- MEMS accelerometers placed at the blades, 10 m from the root, to characterize their dynamics.

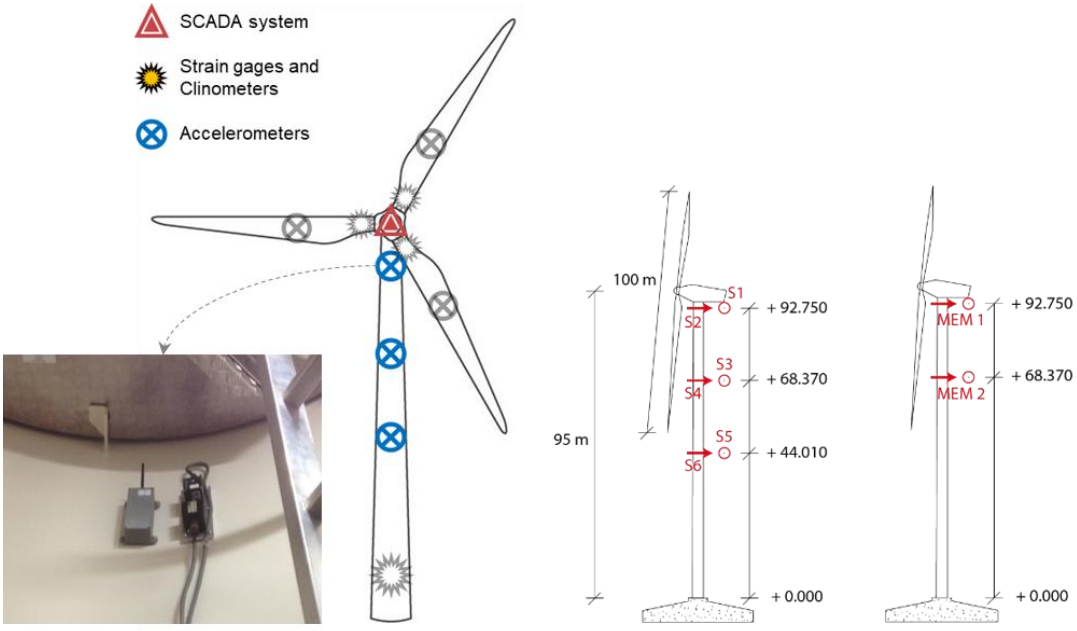
The intermediate layout includes the characterization of the accelerations at the tower through the optimized low-cost MEMS accelerometer system and the characterization of the rotor dynamic behaviour through fibre optic strain gauges and MEMS accelerometers installed on the blades.

Finally, the simple monitoring layout consists solely of using the MEMS accelerometer system to collect data regarding tower vibrations.

The following sections describe the several instrumentation systems adopted, together with the presentation and analysis of preliminary results for wind turbine 1. The results presented here are intended to demonstrate what is being measured, to certify the correct functioning of the systems and to demonstrate the capabilities of the most complete monitoring layout.

4.4.1 TOWER MONITORING SYSTEM: ACCELEROMETERS

In order to obtain the best possible characterization of the tower accelerations a commercial system based on six force-balance unidirectional accelerometers connected to a 24 bits acquisition system was deployed. As depicted in Figure 4.8a, this involved the instrumentation of three sections of the tower along two orthogonal horizontal directions. These three sections coincide with the height of the technical platforms, in order to facilitate the installation and maintenance of the monitoring equipment. The sensors are connected by cables to a central acquisition system that continuously records acceleration time series with a sample rate of 20 Hz. This data is accessible from FEUP through an internet connection.



(a) (b) (c)

Figure 4.8 – Tower sections instrumented with accelerometers: (a) Photo of the force balance sensors (connected to cables) and of the MEMS based acquisition system (grey box with antenna); (b) Force-balance sensors; (c) MEMS sensors.

Complementary, a MEMS based system was also installed. This is a standalone system developed at FEUP that integrates a tri-axial acceleration sensor (in this application just the two horizontal directions are being recorded) with a sample rate of 62.5 Hz, a set of batteries that ensure five months of continuous operation, a memory card for data storage, high-precision clocks and a radio for data transmission (in the present application the data transmission is limited to state-of-health parameters to increase the system autonomy). Two of these devices were installed in the tower in the positions marked in Figure 4.8c. The main goal is the development and test of easy to deploy and cost effective systems for wind turbines testing and monitoring, so the evaluation of the performance of these devices designed and assembled in FEUP is very relevant.

Figure 4.9 shows two examples of spectra obtained from acceleration series recorded by the two alternative sensor under test, considering the wind turbine parked (figure on the left) and in power production (figure on the right). It appears that the system designed at FEUP demonstrates a performance that is comparable to the more expensive and difficult to install commercial system (KMI). These figures are in accordance with the results of the ambient vibration test presented above. Under non-operating conditions, the peak pairs associated with the first two tower mode pairs clearly stand out. In operating

conditions, additional peaks associated with the rotor rotation frequency appear (identified by the dashed vertical lines). The peaks associated with the second pair of bending modes become much more diffuse, which makes their tracking over time quite challenging.

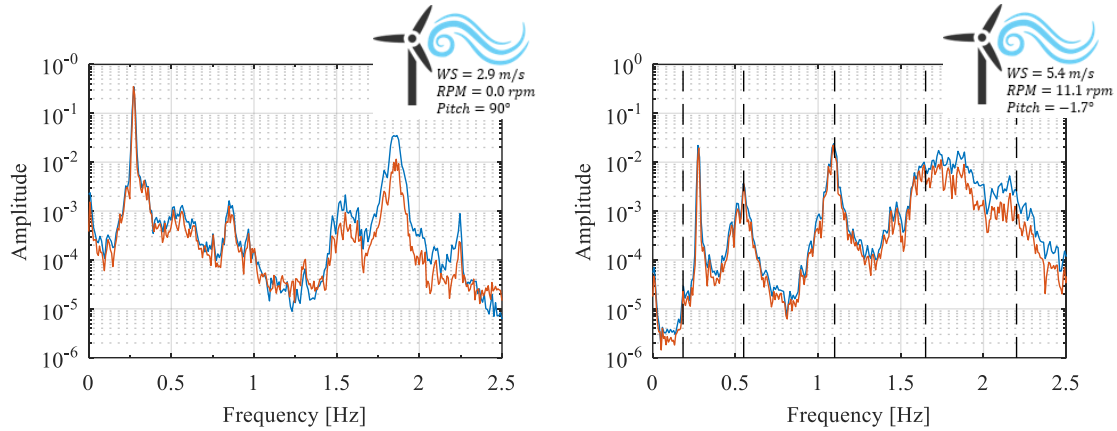


Figure 4.9 – Power spectra from force balance (blue line) and MEMS (orange line) sensors ($1\Omega, 3\Omega, \ldots, 12\Omega$ marked with dashed vertical lines).

Figure 4.10 shows the colormaps obtained from spectra of singular values calculated with the acceleration time series acquired with the commercial system during January 2019, after their projection according to the FA and SS directions. The hotter colours correspond to frequency bands in which the signal has greater energy. As might be expected, variations in frequency content are observed over time due to varying operating conditions. It is also possible to visually track the time evolution of the natural frequencies associated with the first two pairs of tower modes. In the context of the WindFarmSHM project, new algorithms for automated operational modal analysis are being developed taking as reference the ones presented in (Oliveira *et al.*, 2018). These algorithms are being tested in the signals recorded by the two types of sensors.

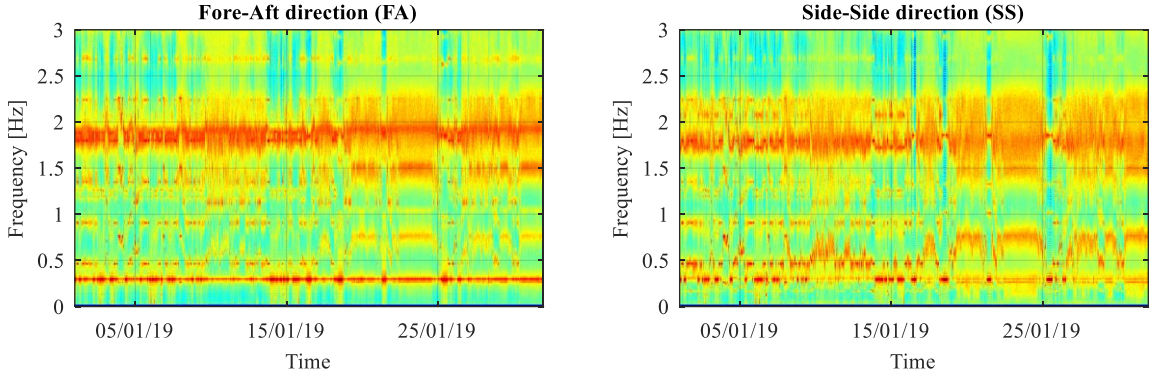


Figure 4.10 – Colour maps with singular-value spectra for the FA and SS directions in January 2019.

The evolution of the natural frequencies over the rotor speed is represented in Figure 4.11. The two well defined horizontal alignments around 0.27 Hz and 1.80 Hz are clearly visible along the whole rotor speed regimes. In fact, they both correspond to two pairs of closely spaced vibration modes in the FA and SS directions. In addition, the other two referred alignments (around 1.30 Hz for 0.0 rpm) are also distinguished in all operating conditions. It is interesting to note that the frequency value of these two modes seems to decrease and increase, respectively, with the increase of the rotor speed. This is an expected behaviour of rotor whirling modes when considering a fixed reference (as is the case of the implemented monitoring system with sensors at the tower).

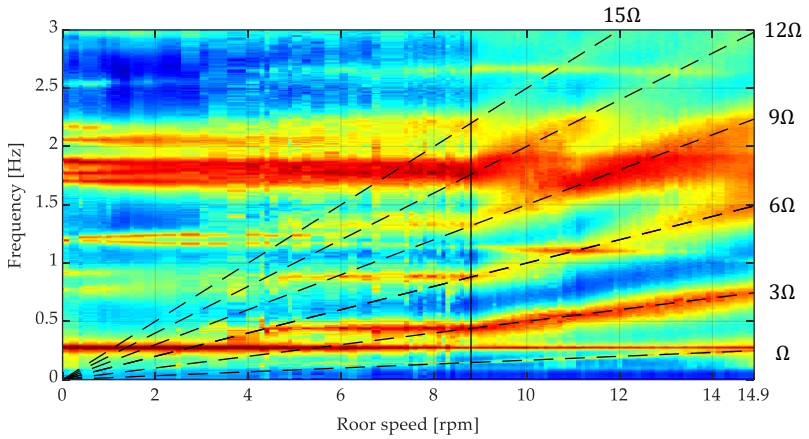


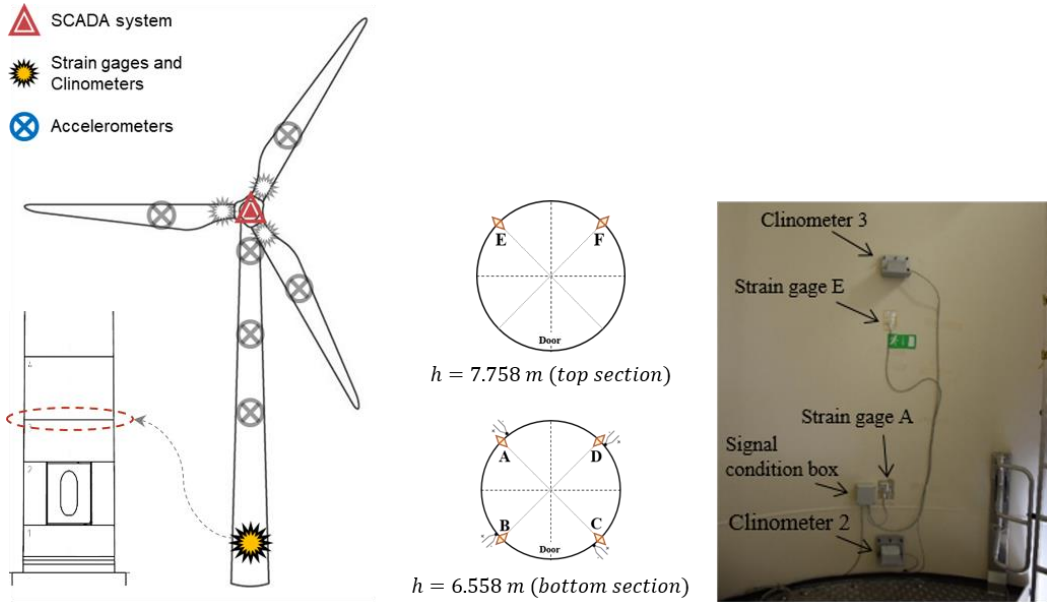
Figure 4.11 – Colour map with natural frequencies over rotor speed in March 2020 (the diagonal dashed lines represent the harmonic frequencies associated with the rotor rotation).

The analysis of the figure is also important to assess the influence of the rotor excitation on the detection of the vibration modes throughout the operating regimes. As referred in Chapter 3, this influence is only present when the turbine is in operation (rotor speed higher than ≈8.8 rpm), motivated by the harmonic excitation.

4.4.2 TOWER MONITORING SYSTEM: STRAINS AND ROTATIONS

This monitoring component is essential for fatigue assessment of the tower. One important goal is the evaluation of alternative monitoring layouts for estimating static and dynamic bending moment diagrams along the tower: using strains and/or rotation measurements, combined with accelerometers.

The strains system is composed of six 2D rosette strain gages (measurement of the strain in two orthogonal directions) and four Pt100 temperature sensors. In order to try to evaluate the static bending moment diagrams evolution along the tower, with all sensors installed from the same tower horizontal platform, the six strain gauges are distributed in two close cross-sections: four sensors at 6.5 m from the base of the tower (bottom section) and two sensors at 7.7 m (top section) as shown in Figure 4.12. The four temperature sensors are located in the bottom section, close to the strain gauges. Measuring deformation in the direction perpendicular to the tower axis and temperatures is important to allow the evaluation of alternative procedures to minimize the influence of temperature on the measured longitudinal deformations.

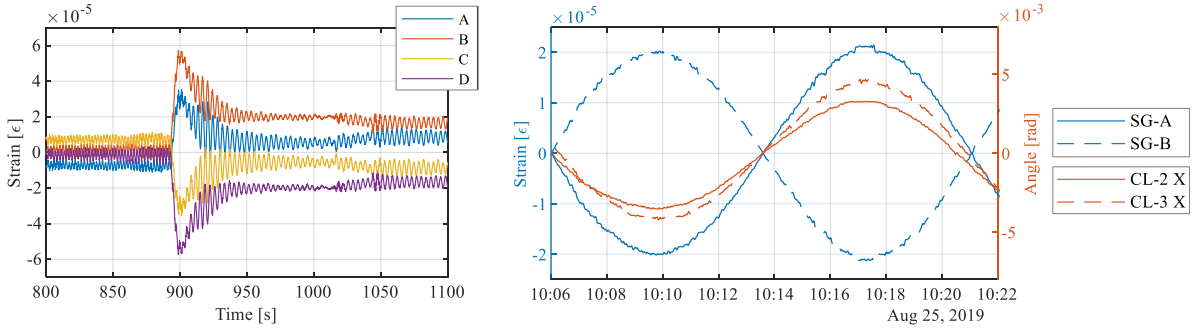


(a) (b) (c)

Figure 4.12 – Tower strains monitoring system: (a) Instrumented section of the tower; (b) Position of the strain gages (◊) and temperature sensors ( ) at the section; (c) Photo of strain and rotation sensors.

The installation of the clinometers aims to measure the rotation at the base of the tower and to alternatively estimate the extensions from the measurement of rotations in two close sections. The main advantage of estimating bending moments from rotations is that the installation of the clinometers is less intrusive than the installation of strain gauges, which involves removing of tower painting. The three clinometers were installed along the vertical alignment formed by strain gauges A and E. One of the clinometers was installed close to the foundation (near the base flange), while the other two are positioned according Figure 4.12c. The two monitoring components are connected to a National Instruments digitizer and processor (model cRio 9056 - http://www.ni.com), installed at the base of the tower. Data acquisition is ensured by a program developed in LabView for this specific application, with a sample rate of 50 Hz.

Figure 4.13 shows an example of the strains time series obtained for a stop event of the rotor. Although the main purpose of this monitoring system was to characterize the static component of the response, it is possible to characterize the dynamic component with good accuracy. This data will be relevant to test and compare various approaches for estimating the dynamic stresses in the tower from acceleration measurements (Maes *et al.*, 2016).



(a) (b)

Figure 4.13 – Tower Monitoring System Strains and Rotations: (a) Example of strain time series; (b) Strain and rotations during nacelle yawing, SG – strains; CL - rotations (see sensor positions in Figure 4.12).

The records obtained from strain gauges are influenced by several factors, including the effect of temperature. Thus, the experimental determination of bending moments in the tower requires the acquired raw data to be pre-processed to obtain the real deformation. The implemented procedure is introduced in Chapter 5.

Figure 4.14 shows the average spectra of the six force-balance accelerometers (first row), of longitudinal deformations recorded by sensors A, B, C and D (second row) and of clinometer 3 (third row), considering the rotor parked (left) and in operation (right). These spectra show excellent agreement of results between the alternative monitoring components and demonstrate that it is possible to perform operational modal analysis from the data collected by all these systems.

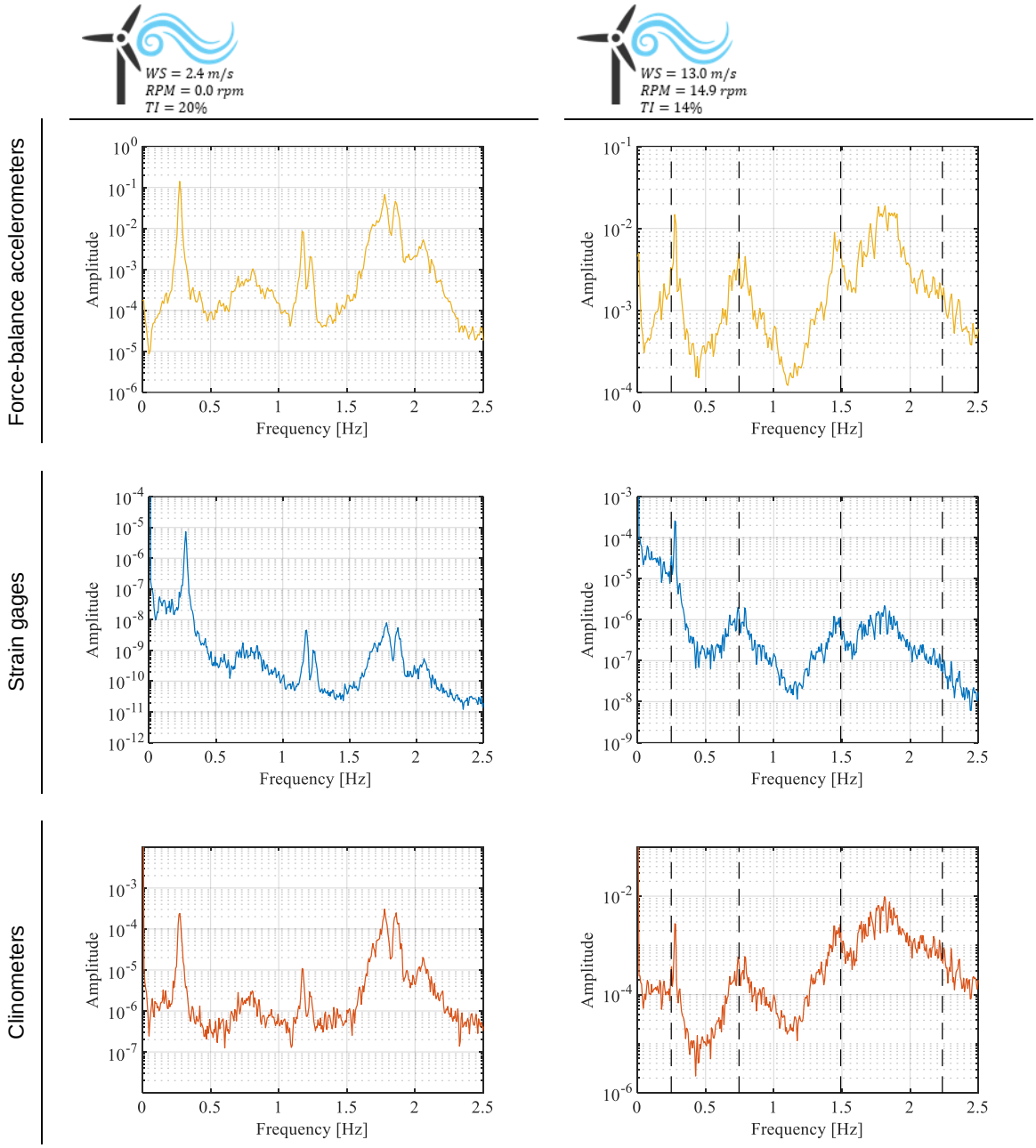


Figure 4.14 – Averaged power spectra: six force-balance accelerometers (first row), longitudinal strains A to D (second row) and rotation at clinometer 3 (third row) in non-operating condition (left column) and operating condition (right column).

4.4.3 ROTOR MONITORING SYSTEM: ACCELEROMETERS

The goal of this monitoring system is the characterization of the rotor dynamic behaviour under different operating conditions. The analysis of the results of the ambient vibration tests showed the existence of several resonance frequencies that could not be attributed to the tower fundamental modes. These are certainly related to modes more dominated by the rotor. In addition, direct identification of rotor modes may be beneficial for automatically detecting blade changes, driven either by reduced stiffness due to damage or by additional masses due to ice formation. In this way, the same MEMS based devices that were installed in the tower were also installed inside the blades, one in each blade, 10 m from the blade root, as shown in Figure 4.15 (sample rate of 62.5 Hz).

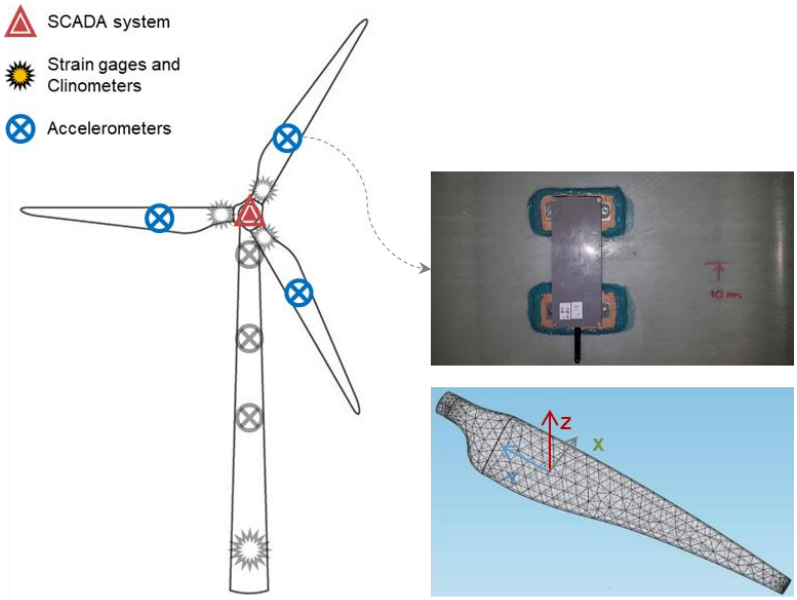


Figure 4.15 – MEMS based system installed inside one blade and direction of measurements (X approximately aligned with edgewise direction).

From the simultaneous recording of the acceleration time series on the blades it should be possible to estimate the modal parameters of the rotor, in particular their modal configurations. However, this is as challenging goal that is outside the scope of the present work, so in the present document only examples of the time series and their spectra are show in Figure 4.16, considering the stopped rotor (left) and in operation (right). Signals X, Y and Z are in accordance with the referential presented in Figure 4.15.

Considering the figures obtained with the rotor parked, in addition to the various peaks corresponding to the main tower modes, peaks are also identified for various other resonant frequencies that are certainly associated with rotor modes. When the rotor is in operation, the adopted sensors measure the gravity, being the registered accelerations dominated by the rotor rotation frequency. Several other frequencies associated with vibration modes in flapwise (Z) and edgewise (X) directions can still be observed.

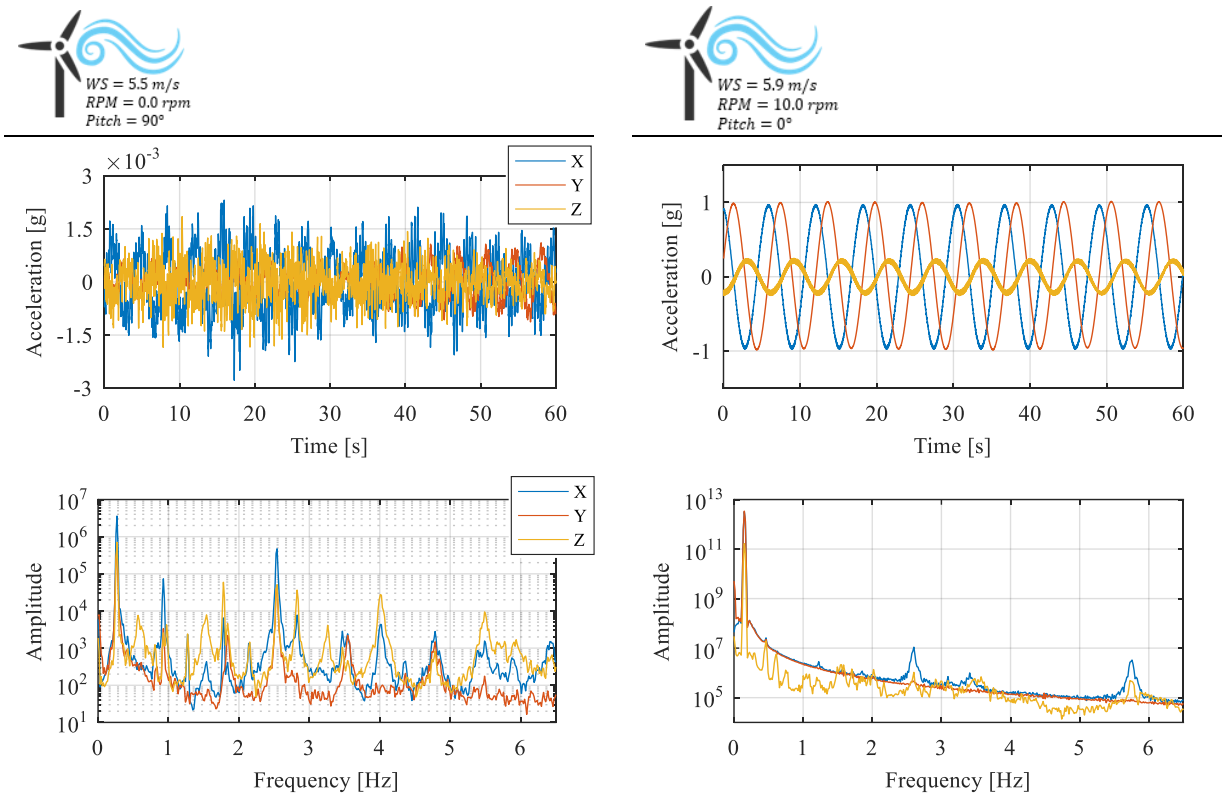


Figure 4.16 – Example of acceleration time series and corresponding operation parameters and power spectra.

4.4.4 ROTOR MONITORING SYSTEM: STRAINS

The main goal of the blades strains monitoring is to collect data to estimate the fatigue condition of these elements, as well as to evaluate their structural performance from the evolution of the continuously estimated modal parameters. On the other hand, the joint analysis of the wind characteristics, the moments acting at the blades and the bending moments at the tower can be relevant to understand the mechanisms of transmission of loads from the rotor to the tower and to validate numerical modelling.

The solution adopted is based on a commercial system provided by HBM / FiberSensing called WindMeter (https://www.hbm.com) that was configured with a sampling rate of 100 Hz. Each blade is instrumented with four fiber optic strain sensors and temperature sensors for compensation of the temperature effects. As shown in Figure 4.17, each set of sensor is connected to a central acquisition system installed at the hub, which in turn allows remote access to data via a 3G modem.

As noted with respect to tower strains processing, a similar methodology was also followed for processing the blade strains records that will be introduced in Chapter 6.

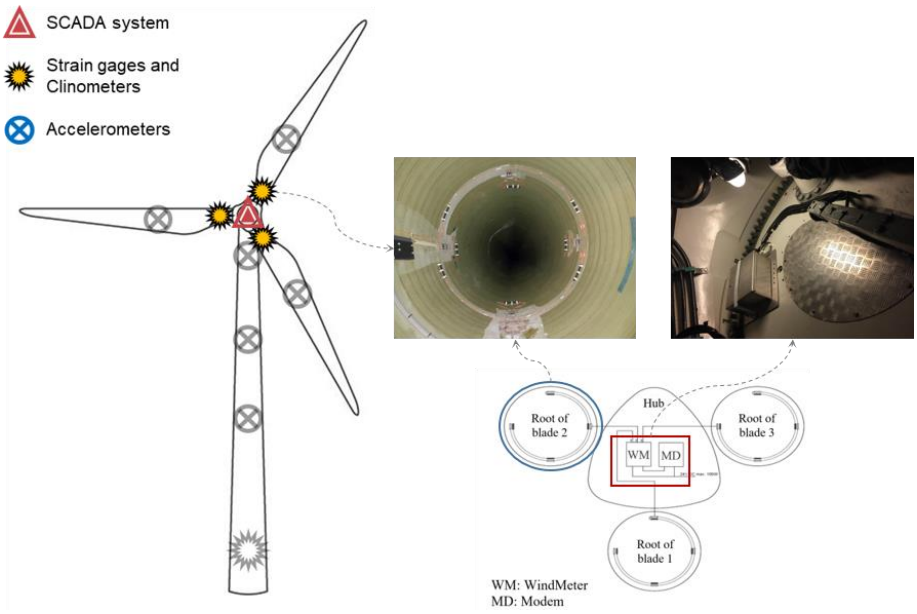


Figure 4.17 – Strain measurement at the blade root: wiring and photo.

As an example, Figure 4.18 shows two strains time series and their spectra, considering the rotor stopped (left) and in operation (right). Sensors $S1$ and $S3$ correspond to blade bending according to edgewise direction, while sensors $S2$ and $S4$ correspond to flapwise direction. These show that the acquired data, besides being fundamental to obtain the stress history for fatigue analyses, can also be used for operational modal analysis of the structure.

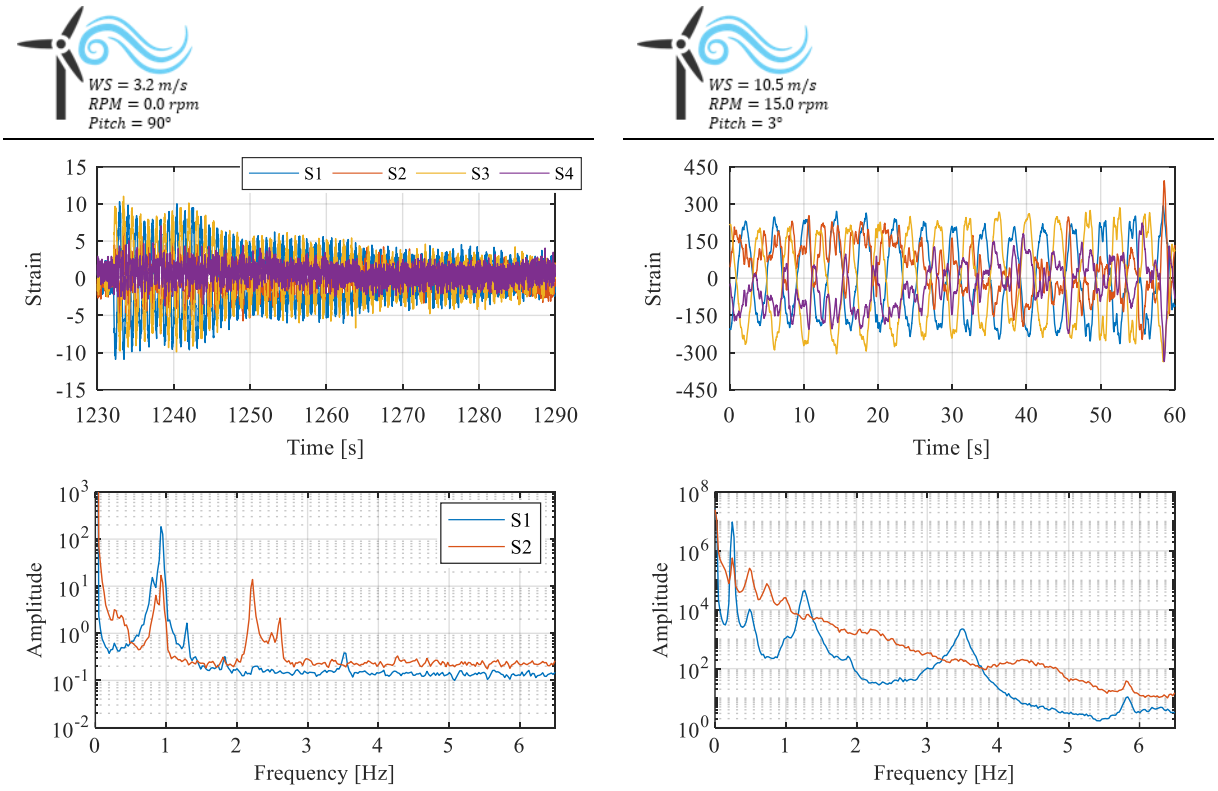


Figure 4.18 – Example of detrended strain time series (static component was removed) and corresponding operation parameters and power spectra (S1 and S3 bending in the edgewise direction; S2 and S4 bending in the flapwise direction).

It should be noted that the deformations measured on the blades are not as sensitive to the tower bending modes as in the case of accelerations, since although tower movement produces blade movements, it does not lead to relevant bending. Thus, the peaks shown in the spectra can only be motivated by the contribution of blade modes.

By comparing the spectra of Figure 4.16 and Figure 4.18 for the parked situation, it is possible to identify several coincident peaks for the same frequencies. While in operation, the observed resonant frequencies depend on the rotor speed of the rotor, so the peaks do not coincide.

4.4.5 Complementary Data and Synchronization

The dynamic monitoring system components described above are complemented by the SCADA system of the wind turbines. As mentioned in Chapter 2, in order to process the data collected from the monitoring systems, it is essential to accurately characterize the environmental and operational conditions in the wind farm. In this study, the owner of the wind farm provides SCADA data with two sample rates of several operational and environmental parameters:

- *SCADA-10min*: These data are composed by the mean, maximum and minimum value from 10 minutes period of several operational and environmental parameters. Among them, the following were important for the context of this project:
    - Wind speed;
    - Wind direction
    - Ambient temperature;
    - Rotor speed;
    - Yaw angle;
    - Blades pitch angle;
    - Power output.
- *SCADA high-resolution*: Data composed by the same parameters listed above, but with a sampling interval of 15 seconds.

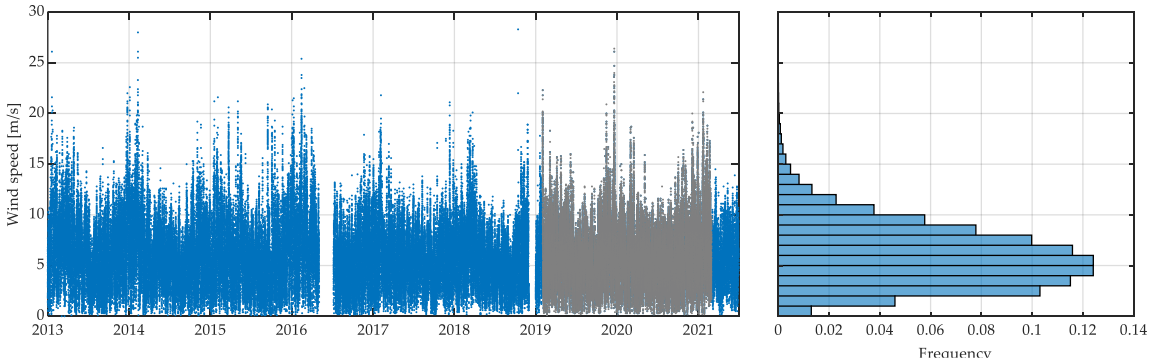
The data acquired with a higher sampling frequency is very useful as it allows accurately monitoring the rapid variations of some parameters, such as wind speed (wind gusts of few seconds), which is not possible to follow from the average values of the SCADA-10min.

The environmental and operational data collected from January 2013 to June 2021 from the SCADA system (SCADA-10min) of wind turbine 1 is show in Figure 4.19 and Figure 4.20, respectively. The corresponding histogram plots are also presented. Note that in the figures there are some periods without SCADA parameters, which occur mainly during power outages. The grey points correspond to the two-years monitoring period analysed in the following chapters of this work.

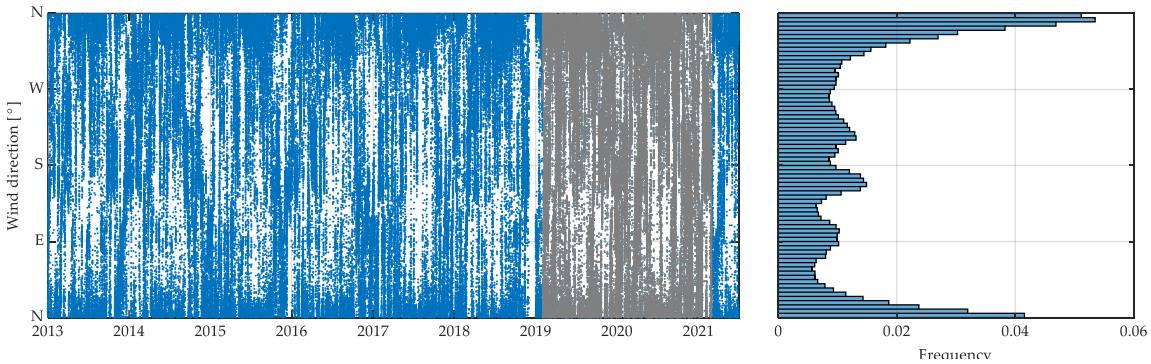
Figure 4.19a indicates the 10-min average wind speed where the annual variations can be observed, with relatively higher wind speeds in winter seasons. A maximum average wind speed of 36.8 m/s was recorded in October 2018 during the Storm Leslie. The histogram adopts the classical shape of a Weibull distribution. Figure 4.19b shows the wind direction, being the main direction identified along the north sector. The annual temperature variation is displayed Figure 4.19c. A minimum temperature of 3°C was recorded in January 2017 and a maximum of 39°C in August 2018. Considering the history of

temperatures recorded in the winter seasons and the proximity of the farm to the sea, ice formation on the blades is not expected.

Wind speed



Wind direction



Nacelle temperature

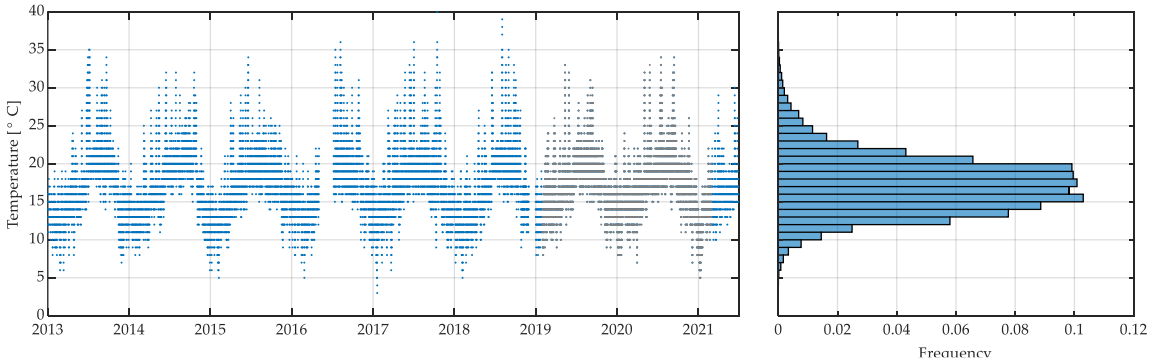


Figure 4.19 – Environmental SCADA data measured at WT1 from January 2013 to June 2021: Wind speed, wind direction and nacelle temperature (the monitoring period is in grey).

Figure 4.20 provides the variation of the operational data and its statistical analysis. The blades pitch angles varies from to -5° to 15° for power production and are pitched at 20° during idling. The idle/shut-down periods correspond to rotor speed bellow 2.5 rpm and production periods correspond to rotor speed higher than 8.8 rpm.

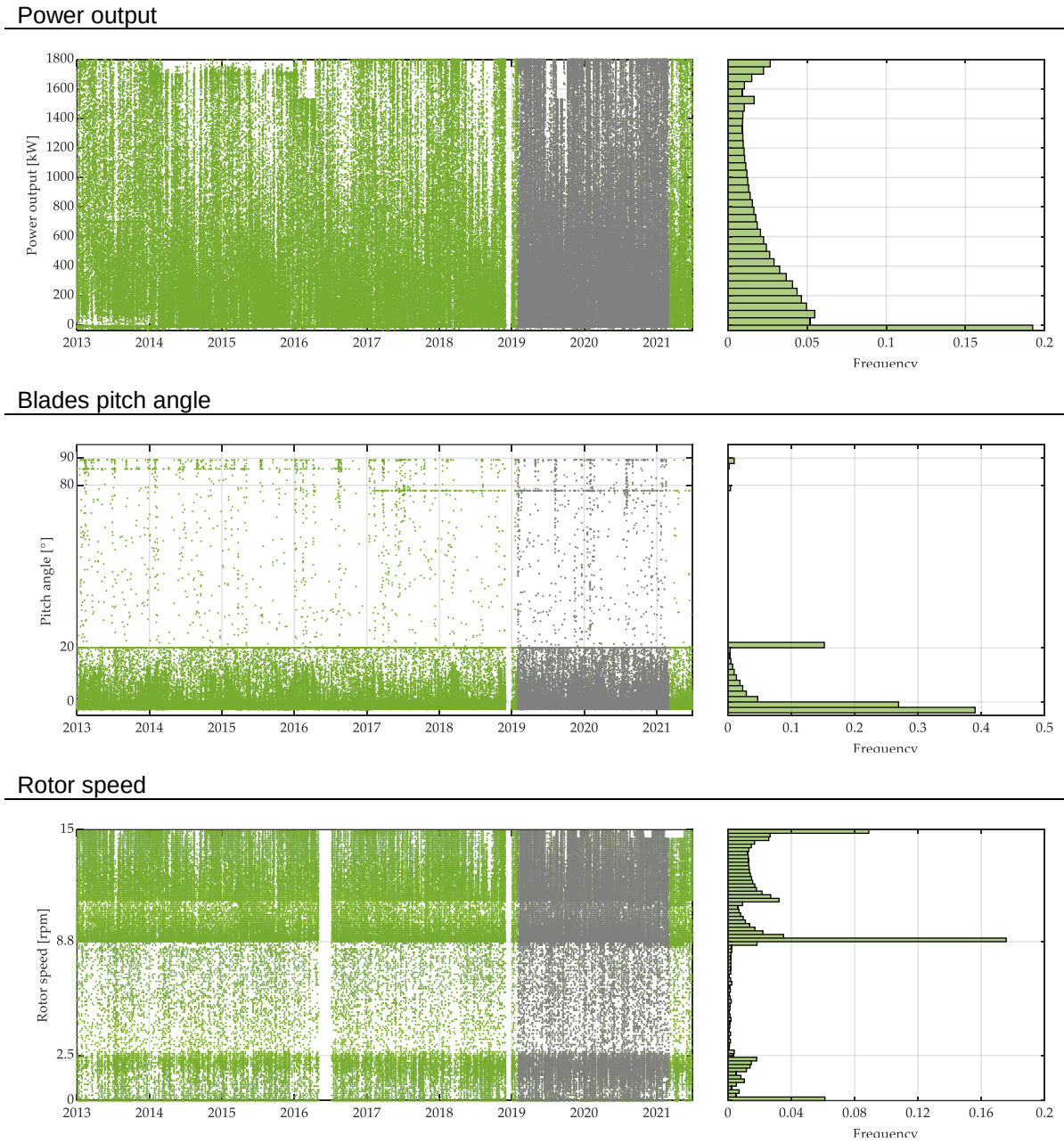


Figure 4.20 – Operational SCADA data measured at WT1 from January 2013 to June 2021: Power output, blade pitch angle, and rotor speed (the monitoring period is in grey).

In order to demonstrate the usefulness of SCADA high resolution, the Figure 4.21 represents the variation of the environmental and operating conditions of WT1 considering the two types of SCADA data available. The figure shows a typical behaviour of the turbine when the average wind speed is oscillating around de cut-in speed. Only considering the SCADA 10-min (maximum, minimum and mean values), it is not possible to describe adequately what happened during this period. However, with high frequency SCADA data is possible to identify a turbine stop event, followed by a start-up.

Focusing on wind speed variation (Figure 4.21a), it appears that from the high-resolution data it is not possible to obtain the same characterization of the wind conditions compared to the 10-min data

(maximum, minimum, mean and standard deviation). For the remaining variables, the two SCADA data types describe the behaviour of the variables similarly.

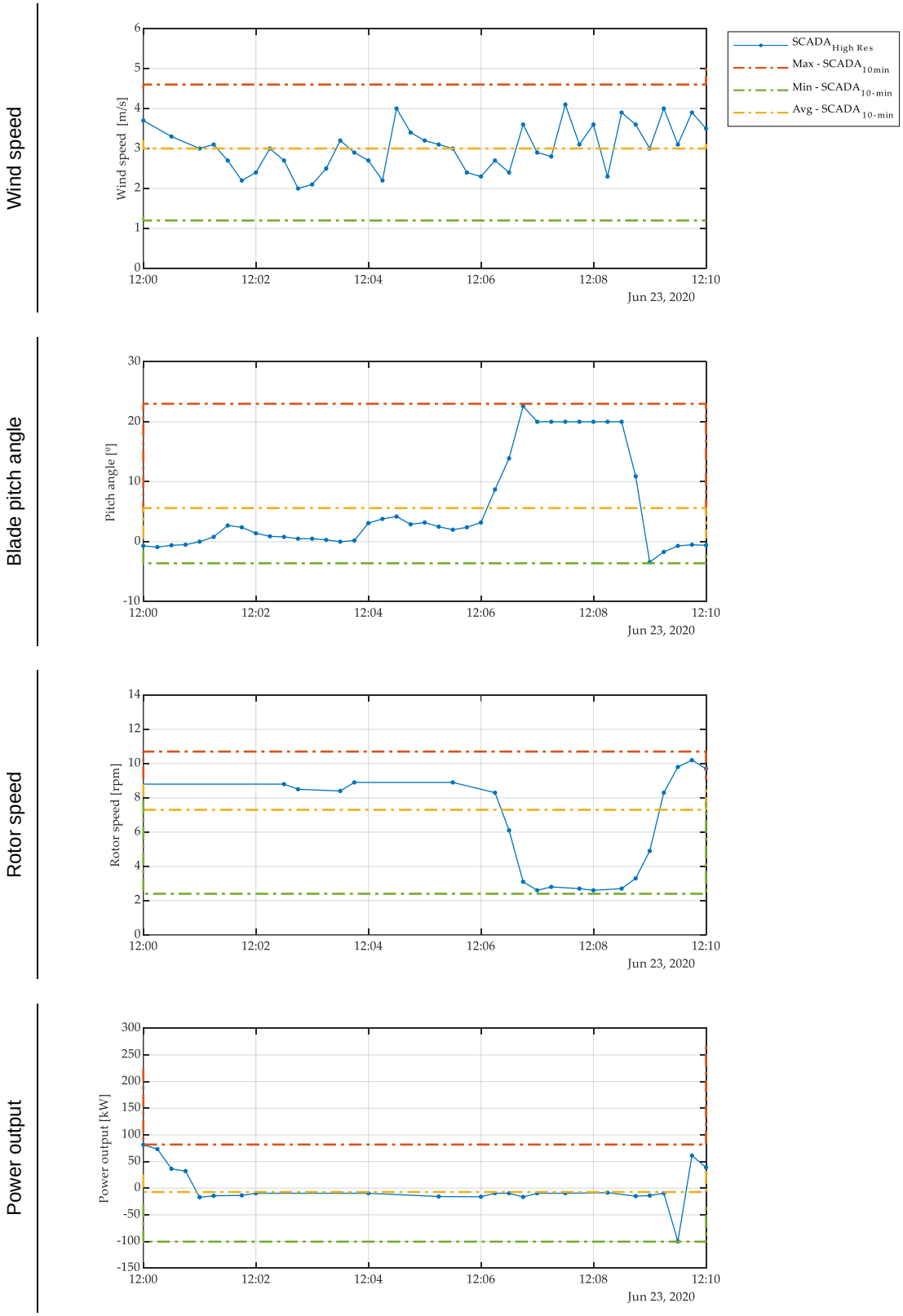


Figure 4.21 – Comparison between SCADA 10-min and SCADA high-resolution at WT1 during a start-up and shutdown event: (a) Wind speed; (b) Blade pitch angle; (c) Rotor speed; (d) Power output.

It is interesting to note that in the initial period (12h01 to 12h06), although the pitch angle and the rotor speed remain within the production range, there is no production (power output < 0 kW) because the wind speed decreases. After that (12:06), the pitch angle increases putting the turbine in idling. The turbine waits for the wind speed to increase in order to avoid continuous start-stop.

As shown in the Table 4.2, the tower monitoring is composed by three independent monitoring systems that adopt different timing protocols. In this way, it is necessary to synchronize all these systems in a common time frame to permit the join processing of different sensors datasets.

Table 4.2 – Tower monitoring systems of WT1 and corresponding timing protocols.

Acquisition system	Sensors type	Timing protocols
KMI	Force-balance accelerometers	Global Positioning System time (GPS)
cRIO	Strain gauges Clinometers Temperature sensors	Internal clock
SCADA	SCADA sensors	Network Time Protocol (NTP)

The Global Positioning System time protocol was chosen as the reference from which all other systems were synchronized, so the force-balance accelerometers system gives the reference time. The synchronization of the cRIO acquisition system was performed by comparing the time series of strains with the time series of accelerations measured by the force-balance sensors, as show in Figure 4.22. The delay between the two systems identified over time is variable due to the limited accuracy of the internal clock of the cRIO system, so the time shift between the two systems is continuously updated. In a second phase, in order to make this synchronization more accurate and easy to automate, a low cost accelerometer placed next to S6 force balance sensor (Figure 4.8) was connected to the cRIO system.

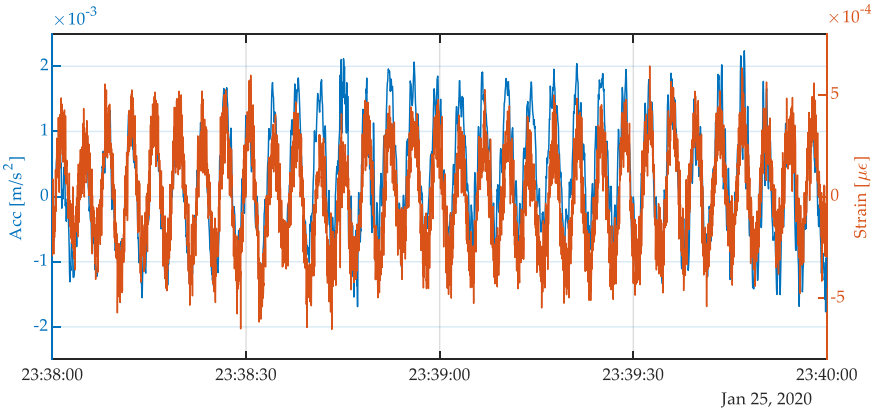


Figure 4.22 – Synchronization of the KMI system (force-balance S3) and cRIO system (strain gauge B).

The synchronization of SCADA data was performed by comparing the evolution of the yaw angle (SCADA high-resolution) with the time series of strains over a full rotation of the nacelle. The eccentricity of the nacelle and rotor mass generates a sinusoidal signal in the strains gauges as shows in Figure 4.23. A constant delay of approximately 50 seconds was observed between the two systems.

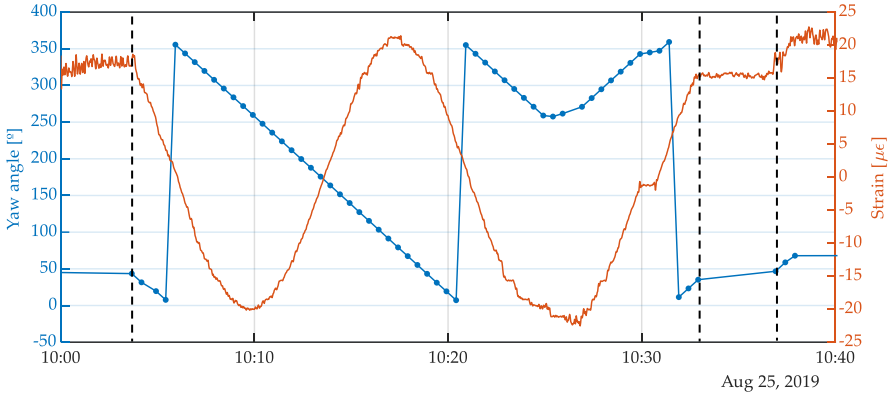


Figure 4.23 – Synchronization of the SCADA data (yaw angle high-resolution) and cRIO system (strain gauge A) (the vertical dashed lines correspond to the singular points used for synchronization).

4.5 FINAL CONSIDERATIONS

This chapter presented the quite extensive monitoring camping that is being conducted in Tocha Wind Farm, described the installation of the monitoring components in operation and presented some preliminary results. The preliminary analyses performed in the frequency domain show that operational modal analysis has the potential to extract useful information from both strain and acceleration measurements performed either in the tower or in the blades.

A deeper processing of the data that is being continuously collected by all the monitoring components will certainly contribute to better understand the in-operation dynamic behaviour of these quite complex structures, to devise processing procedures for effective evaluation of their structure health and to calculate accumulated damage due to fatigue. This step will be instrumental in defining the most effective procedures for assessing structural performance and for estimating accumulated fatigue damage. The analysis of data simultaneously collected in several wind turbines will be very important for understanding the relation between the observed fatigue wear and to devise techniques to extrapolate results from ones to the others.

5
FATIGUE ASSESSMENT OF WIND TURBINE TOWER*

5.1 INTRODUCTION

A significant percentage of the existing wind turbines are reaching their design life (as described in Section 1.1), typically of 20 years. The design of steel tower for onshore wind turbine is most often driven by fatigue calculations. An optimized design aims to match the fatigue life of a particular section of the tower with the intended operational life. However, wind turbines are composed by large flexible structural components and fatigue design is a very complex task. Specially, the definition of the loading scenarios comprehends a considerable uncertainty in their quantification and definition of frequency of occurrence. Consequently, these uncertainties and the approaches used in design may have led to conservative designs and lifetime extension may be possible.

The development of monitoring programs allows acquiring knowledge about the amount of consumed fatigue. Relating the accumulated damage on the structure to the operating conditions (normal production, storms, maintenance and downtime), it is possible to provide inputs to make the projects more optimized (improve design codes), favouring more cost-effective towers. On the other hand, from an operation and maintenance perspective, monitoring may allow the uncovering of structural reserves from conservative designs and update the remaining lifetime expectancy (improve lifetime extrapolation codes).

The present chapter is part of the ongoing research for the development of a fatigue assessment strategy driven purely from in-situ measurements on operating wind turbines. The main goal is to estimate the remaining lifetime of all individual turbines of a wind farm by instrumenting only a subset of the turbines with a load monitoring setup. Results from a two years measurement campaign in Tocha Wind Farm, described in Chapter 4, will be used.

Thus, this chapter is organized as follows: The chapter starts with a brief state of art of fatigue assessment of wind turbine towers (Section 5.2). Section 5.3 gives the background of the procedure for calculation of fatigue damage on onshore wind turbine towers based on strains measurements. Some shortcomings of this approach and alternatives are also presented and discussed. In a first step (Section 5.4), the experimental determination of bending moments at the tower requires the acquired strain raw data to be

* This chapter is based on the papers:
Pacheco, J., Pimenta, F., Cunha, Á., Magalhães, F. (2021) *Experimental Evaluation of Bending Moments at the Tower of an Onshore wind Turbine*. Proceedings of the XI International Conference on Structural Dynamics (EURODYN 2020), 2206-2218. Athens, Greece. https://doi.org/10.47964/1120.9179.19890.

Pacheco, J., Pimenta, F., Magalhães, F., Cunha, Á. (2021) *Use of strain monitoring data for fatigue assessment of wind turbine tower*. Proceedings of the International Conference on Structural Health Monitoring of Intelligent Infrastructure (SHMII-10), 1221-1227. Porto, Portugal.

pre-processed to obtain the actual deformation. Thus, special attention is given to strain signals processing, which includes temperature effects compensation and signal calibration according to IEC 61400-13. Advanced numerical models of the wind turbine are also being developed in FAST. The experimental tower bending moments reported in this contribution are compared with their numerical counterparts. Afterwards, fatigue assessment based on rainflow counting and the Palmgren-Miner rule can be performed. An estimation of the damage accumulated over the monitoring period is obtained. The sensitivity of the calculated fatigue damage to several parameters (window length of strain time series, rainflow histogram resolution, S-N curve parameters and strain signal sampling frequency) is evaluated (Section 5.5).

Section 5.6 aims to extend the damage calculated in the previous section to time periods before the monitoring period, based on the available data from the SCADA system. The realistic short-term damage (10-min) calculated at the instrumented cross-section of the tower are clustered into various load cases and the individual effect of each load case is evaluated. Considering only power production load cases, the short-term damage values are stored in a database that is then used to estimate the endured damage according to previous environmental and operational parameters.

The installation of strain gauges for fatigue assessment of all wind turbines is too time consuming and expensive. For farm-wide fatigue assessment, the obtained damage at an instrumented wind turbine is extrapolated towards the other turbines based on the Fleet Leader Concept. This approach is applied and validated for all wind turbines of the farm under analysis in Section 5.6.5 and the uncertainty of the results is evaluated. It should be noted that the damage extrapolation based on the monitoring time period can only be sufficiently accurate if there are no significant changes of the turbines operation conditions over the lifetime.

It is important to mention that in this contribution only the accumulated fatigue damage in the instrumented cross-section of the tower is evaluated (bottom section at Figure 4.12). In fact, this section might not be the most critical location of the tower (the fatigue design-driving location). However, this is not essential in the context of this research work, since the focus is placed on the methodologies to be applied and not on the analysis of the design. On the other hand, the two tower sections of the wind turbine 1 instrumented with strain gauges are relatively close (≈1.2 m) which does not allow validating the fatigue damage extrapolation techniques along the tower height. These techniques will be applied and validated in another experimental campaign (Serra del Rei Wind Farm) developed within the same research group (Sobrinho et al., 2021). In this monitoring layout, two sections of the tower are instrumented with strain gauges, 23 m apart. Still, the theoretical background to reconstruct strain histories without the need for an actual sensor at the critical section is brief introduce in Section 5.3.2.2.

Finally, in order to experimentally validate the concept of a fleet leader extrapolation, the fatigue damage should be measured in some of the remaining wind turbines on the farm in addition to the fleet leader turbine. However, it was not yet possible to instrument the tower of other wind turbines in the Tocha Wind Farm. Nevertheless, the expansion of the ongoing experimental campaign is being evaluated together with the wind farm owner to further validate the methodology proposed in this document.

5.2 BRIEF STATE OF THE ART

Fatigue is defined as a physical phenomenon where a material cracks after bearing a certain number of load cycles, whereas a single load of the same magnitude would not have caused a failure (Schijve, 2003). This is a common cause of failure in structures and components subjected to time-variable loadings, such as wind turbines.

Fatigue design of wind turbines is actually a very complex task. On the one hand, wind turbines are composed of large structural components designed with several materials, leading to different properties and assessment procedures (Sutherland, 2000). On the other hand, the definition of the loading scenarios is a difficult and extensive task. It is important to note that, apart from quasi-static loads, wind loads have a considerable uncertainty in their quantification, due to their dynamic and non-deterministic nature.

In general, two distinct approaches in fatigue analysis can be followed (Ma et al., 2019): a) use the cumulative fatigue damage to predict fatigue life, assuming that a failure occurs after a number of loading cycles at a particular tension/stress range; b) examine the fracture behaviour of mechanical elements under dynamic loads and consider that a failure occurs if the remaining strength of the component is insufficient due to cracks grown to a critical length. Although the second approach is usually more accurate for fatigue life prediction, it is not so commonly used for fatigue analyses in the wind turbine industry.

In a very simple way, following the first approach, fatigue assessment consists of determination of the loading history, the identification of the damage cycles and the estimation of the total fatigue damage by aggregating the damage contributions of each damage cycle. In time domain analysis, the structure response is expressed as a stress or strain time history and fatigue damage occurs as a result of stress/strain variation over time (so-called cycles). The damage is estimated according to the hypothesis of linear damage accumulation, so-called Palmgren-Miner rule (Miner, 1945). A simple description of how fatigue damage accumulates in a structural component is provided in (Wöhler, 1860). According to Wöhler, each cycle with a given stress range causes a certain amount of damage, and that damage increases linearly with the number of stress cycles applied, until the material breaks. The parameters that may influence fatigue strength are the stress range and the average stress associated with each cycle. A complete description of this procedure is presented in Section 5.3.4 of this work.

Alternatively, frequency-domain methods might be applied. As mentioned above, wind turbines are exposed to random loads that translate into an equally random response. In reality, these response stress and input loading can be viewed as the realization of a random Gaussian process that can be described in the frequency-domain by a power spectral density function (PSD). The PSD represents the distribution of the signal energy at different frequencies and it can be obtained with the application of Fast Fourier Transforms to the time signals. These transformations of loading time histories between time and frequency-domain is subject to certain requirements, as the signal must be stationary and Gaussian (normal probability distribution).

The frequency-domain methods for fatigue assessment offer a direct connection between the PSD and damage or the cycle distribution of the loading. These methods can be divided into narrow-band and wide-band processes. A description of the fundamental theories of random vibration and of the methods to predict fatigue damage from a PSD of stress response are introduced (LEE, 2005). In a general way, for a narrow-band process it is reasonable to assume that every peak of the PSD is coincident with a cycle and that the cycle amplitudes are Rayleigh-distributed. Although, for a wide-band process the relation of the peak distribution and cycle amplitudes is much more complex and several empirical solutions have been proposed (N. W. M. Bishop, 1988; Turan Dirlik, 1985; Zhao & Baker, 1992).

Frequency-domain methods for dynamic and fatigue analysis have been widely used in the offshore oil and gas-engineering field. In (J. van der Tempel, 2006), a fatigue assessment with the frequency-domain approach of a bottom fixed monopile turbine was performed. Acceptable accuracy compared to time-domain numerical simulations and full-scale measurements was found. Other studies applying frequency-domain analysis for wind turbines have been reported in (Bulder et al., 2002; Lee, 2005).

Regarding the classical approach combining S-N curves and a rainflow counting algorithm, it is important to mention some limitations of this method (Adedipe et al., 2016). As a result of improved manufacturing processes, the steel currently used in the construction of the towers has more advanced properties than the material used in the tests on which the S-N curves are based. On the other hand, this method does not allow considering the sequential effect of the stress history. It is verified that the crack opening speed is related to the chronological order of the load cycles, which cannot be done with linear damage accumulation. Finally, this method neglects the material's ability to regenerate, since cracks may have the ability to heal when subjected to compressive stresses.

Despite the limitations of the classic approach, the combination of rainflow counting and Palmgren–Miner rule has been tried and tested thoroughly and is generally accepted as one of the best time-domain methods for a fatigue-life estimation. The main standards and guidelines of wind turbines, including IEC 61400-3 (International Electrotechnical Commission, 2009), IEC 61400-1 (International Electrotechnical Commission, 2014), DNV-2011 (Det Norske Veritas (DNV), 2011), GL-2010 (Germanischer Lloyd (GL), 2010) and GL-2012 (Germanischer Lloyd (GL), 2012), suggest the application of the linear accumulation of damage for fatigue analysis of the support structure.

One of the first examples of fatigue assessment of a wind turbine tower based on the measurement of strains is described in (Söker, 1996). The experimental campaign lasted nine months and included the installation of four sensors in a 500 kW rated power onshore wind turbine. The collected data was processed with the application of the rain-flow counting algorithm. This work intended to optimize the design of these structures.

Within the scope of the “High-strength steel tower for wind turbines” project, a 2.1 MW wind turbine located in Portugal was instrumented with 96 strain channels (Rebelo et al., 2012). The main goal of the project was to improve competitiveness of steel towers used to support multi mega-watt wind turbines.

Pollino and Huckelbridge (Pollino & Huckelbridge, 2012) monitored a 100 kW wind turbine with strain gauges during approximately one year and concluded that the fatigue life of the principal structural details of the tower was significantly higher than 20 years.

In order to study in detail the connection between the steel tower and the concrete foundation a monitoring system based on accelerometers and strain measurements was deployed in a wind turbine located in south Germany (Botz et al., 2016).

More recently, Weijtens (Weijtens et al., 2016) describes an experimental campaign carried out in the North Sea under the Northwind offshore wind project. The Northwind farm comprises 72 Vestas V112-3MW offshore wind turbines (monopile foundations) with a 216 MW capacity and started operation in 2014. This work present the fleet leader concept, in which a limited number of representative wind turbines are instrumented with strain gauges and accelerometers (two wind turbines were instrumented in this case). The fatigue damage on the two wind turbines are quantified having in mind the prediction of the fatigue life progression in the entire wind farm.

A long term monitoring system for structural and fatigue verification of wind turbine support structures is presented in (C. T. Loraux, 2018). The monitoring system is installed on a Vestas V90-2.0 MW wind turbine situated in the biggest wind farm of Switzerland (Mont-Crosin, BE). The results of this work

demonstrated that the wind turbine tower service duration could be extended safely beyond 20 years using simple monitoring systems.

All these works prove the relevance of fatigue assessment of wind turbines with dynamic monitoring systems based on strains measurement.

5.3 PROCESSING STEPS FOR FATIGUE ASSESSMENT FROM STRAINS GAUGES MEASUREMENTS

The fatigue damage calculation procedure based on strain measurements involves a significant number of processing steps. An overview of this procedure is given in Figure 5.1. All the steps involved are described in this section and most of them are illustrated in a case study.

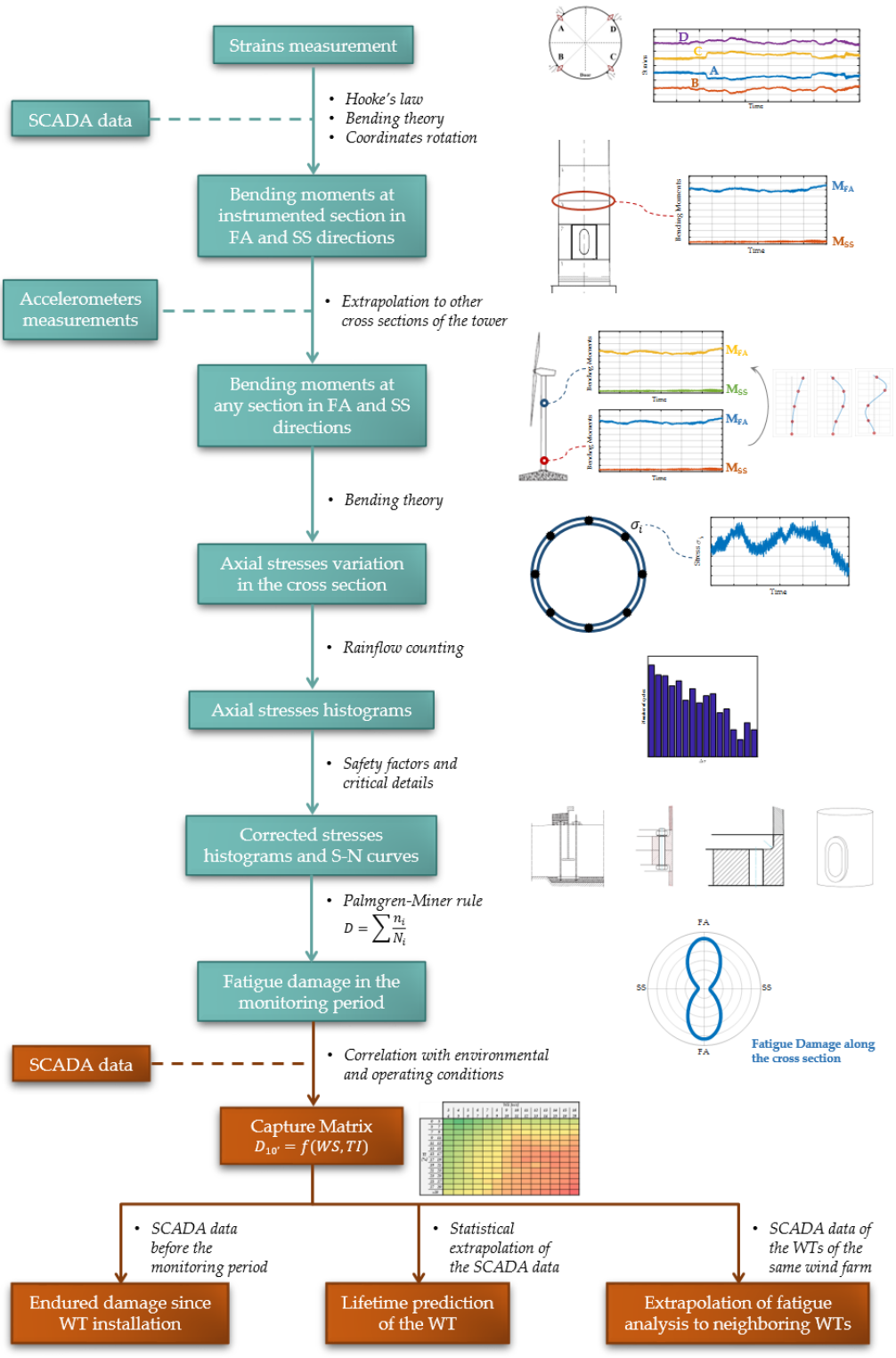


Figure 5.1 – Fatigue Assessment procedure based on strains measurements.

5.3.1 BENDING MOMENTS AT INSTRUMENTED SECTION

The longitudinal strain signals (ε_z) are the input of this procedure. According to the theory of linear elasticity (Hooke's law) for isotropic materials, the longitudinal stress in the tower (σ_z) is given by:

$$\sigma_z = E \cdot \varepsilon_z \tag{5.1}$$

Where, E is the Young's modulus of the steel. It is important to note that the previous equation is valid since the radial deformations caused by the drag force are negligible when compared to the longitudinal deformations, considering the small thickness of the tower cross-sections.

The calculated stress at any sensor installed in the cross-section results from the combination of two bending moments in two perpendicular directions (M_x and M_y) and the normal force (F_N), according the following equation:

$$\sigma_z(\theta_i) = \frac{M_x}{W} \cdot cos(\theta_i) - \frac{M_y}{W} \cdot sin(\theta_i) + \frac{F_N}{A}, \qquad i = \{1, 2, 3, \dots\} \tag{5.2}$$

Where θ_i is the angle of the i-th sensor from the x-axis aligned with the door and A and W are the cross-section area and the elastic section modulus, respectively. In order to calculate the normal force and the two bending moments installed in the cross-section, it is required to measure the longitudinal stress at, at least, three different locations. As the strain sensors only provide the variation from the initial stress state of the structure, the normal force resulting from the tower, nacelle and rotor weight cannot be measured. Still, this can be easily estimated if all the supported masses are known.

In fact, the relevance of mean stress in fatigue analysis in the standards and guidelines depends on the structural detail under analysis. For the fatigue analysis of concrete elements (i.e. foundations and grouted joints) or pre-loaded bolted joints the knowledge of the mean stress is required (John Dalsgaard Sørensen & Sørensen, 2011). For the analysis of the steel elements of the support structure, some standards and guidelines present a correction coefficient to consider the mean stress effect. However, it is usually disregarded, because its consideration introduces a positive effect when the stress range is in the compression side. Thus, it is conservative to neglect this coefficient and, consequently, the mean stress effect.

The nacelle orientation defines the fore-aft (FA) and the perpendicular side-to-side (SS) direction. Subsequently, the bending moment with a vector perpendicular to the rotor axis (M_{FA}) and the perpendicular direction moment (M_{SS}) are obtained by projecting the M_x and M_y bending moments using the yaw angle provided by the SCADA system.

5.3.2 EXTRAPOLATION OF THE BENDING MOMENTS

5.3.2.1 Critical construction details

Due to its geometry and construction process, the wind turbine structures have several details that need to be verified against fatigue damage. Considering only the support structure of onshore wind turbine (tower and foundation), there are mainly five spots of interest: the flange connection between tower segments (including the bolts), the vertical and horizontal welded connections between the tower

cylindrical sheets, the welded connections between the tower cylindrical sheets and the flange, the stress concentration due to the door opening and the connection between the tower and the foundation.

The flanged connection between the tower segments results in an eccentrically loaded bolted connection. In this way, a fast bolt fatigue failure can occur when the external loads are high relative to the bolt preload, because the eccentricity of the connection results in a non-linear relationship between the tensile forces in the bolt and the load applied to the structure.

Some bolted connection designs are describe in (Veljkovic et al., 2011) and different models to estimate the load transferred into bolts can be found in the guideline (Verein Deutscher Ingenieure, 2015). Pedersen (Pedersen, 2017) concludes that the bolted connections can be optimized by placing the bolts as close as possible to the tower wall (in order to reduce the eccentricity) and also demonstrated that an increase in the flange thickness can reduce the stresses in the bolts.

Although, it is important to note that during normal operation of the wind turbine, the stress variation inside the pre-stressed bolts is low and the opening of the joints is not expected (Rebelo et al., 2012). A correct maintenance program for this type of connections makes it possible to correct pre-stressing losses and prevent possible damage to the structure.

Damage in onshore wind turbine support structures is usually related to foundation problems and the connection between the tower and the foundation is a sensitive location for fatigue (Currie et al., 2015). Some problems of excessive levels of vibration have been observed due the cracking and/or gaps in the concrete around the steel ring embedded in the foundation (Pelayo et al., 2011).

For offshore bottom fixed turbines, decreased foundation stiffness due to scour problems is related to decreasing of the expected fatigue life of the structure (S. Sørensen & Ibsen, 2013). Other locations are very sensitive for fatigue damage: in mono-piles the grouted connection of the transition piece is particularly sensitive and foundations models like tripod and jacket present complex geometries with high number of joints with high stresses concentration.

5.3.2.2 Extrapolation of the Bending Moments to any Section

For the complete evaluation of the fatigue damage, it is essential to known the distribution of stresses or strains along the structure, in particular at critical positions identified in the previous section. However, at many critical details, or cross-sections close to critical details, direct measurements of strains is not feasible. It might be impossible due to difficulties to access these cross-sections and also because the instrumentation of all critical spots is not economically feasible.

Thus, when direct measurements of strains are not available, the fatigue assessment of a wind turbine spot can be performed: a) through estimation of the dynamic loads applied to the structure or b) through model-based extrapolation of a limited set of available response measurements.

The first method allows the reconstruction of the dynamic loads applied to the structure. Many algorithms for force identification can be found on the literature (Jacquelin et al., 2003; Jayalakshmi et al., 2018; R. & S., 2006) which already had practical applications in wind turbines. Fritzen in his works adopted a robust observer technique for estimating the wind loads on a 5 MW wind turbine (M .Klinkov & Fritzen, 2010).

Alternatively, response estimation techniques can be used to estimate the strains at any fatigue location without the necessity of prior sensor installation on these locations. From the obtained stress histories, the consumed fatigue can be assessed. This so-called virtual sensing concept utilizes a limited set of

response measurements, as accelerations, strains or SCADA data, to reconstruct the full-field response of the structure.

Various approaches for the estimation of stresses and strains using response estimation techniques are presented in the literature. These virtual sensing techniques can be divided in: the model-based robust observers (Erazo & Hernandez, 2014; Fritzen et al., 2011), the Kalman filter-based techniques, the joint input-state filtering techniques and model decomposition and expansion technique (briefly introduced next). The joint-state input estimation was proposed by Gillijns and Moor (Gillijns & De Moor, 2007) and further developed by Lourens et al. (Lourens et al., 2012). This method estimates the loads and states of the structural model based on filtering. Posteriorly, this algorithm was extended to be applied when accelerations are measured (Maes, Smyth, et al., 2016). Similarly, Kalman filter-based techniques estimate states based on a limited number of responses measurements. This approach was introduced to be applied to structural dynamics by Papadimitriou et al (Papadimitriou et al., 2011). The Kalman filters have proven effective on the simultaneous integration of multiple types of measurements (e.g. accelerations and strains measurements) (Palanisamy et al., 2015; Smyth & Wu, 2007). Alternatively, model decomposition and expansion technique assumes the structural response as a linear combination of the mode shape vectors (Hjelm et al., 2005). Modal expansion algorithms can be applied both in a time and frequency domain (Avitabile & Pingle, 2012; Iliopoulos et al., 2016; M. López Aenlle et al., 2013).

A comparison on the applicability in offshore monopile wind turbines of the Kalman filter, joint input-state filter and modal expansion is carried out in (Maes, Iliopoulos, et al., 2016), that concludes on an acceptable performance in the prediction of accelerations responses in offshore wind turbines foundations.

The fatigue condition in an arbitrary position of the wind turbines structure can be obtained as the sum of the contribution of two components: quasi-static and dynamic. The quasi-static component corresponds to the stress conditions associated with the lower frequency range of the spectrum, generally related to the quasi-static component of the wind action, while the dynamic fatigue component corresponds to the stress conditions associated with higher frequencies of the structure response, which includes the contribution of sinusoidal excitations and vibration modes.

In a simplified way, the quasi-static component of fatigue can be determined by knowing the configuration of the global deformation of the structure and the quasi-static condition at a reference point. The deformed shape of the structure can be estimated based on its stiffness matrix and knowing the most common loading configuration. The quasi-static reference condition can be a bending moment (measured with strain gauges), the evolution of a displacement (measured with GPS) or curvature (measured with inclinometers) over time in an appropriate section of the structure. Assuming the deformed configuration of the structure and a known reference condition, the bending moment of the quasi-static component, and consequently the stresses, can be extrapolated for the entire structure.

Estimating the dynamic contribution to fatigue is a more complex task. In the works (Hjelm et al., 2005; Gustavo Oliveira, 2016) a possible strategy is presented and exemplified. From the modal analysis carried out in the damage detection module, it is possible to determine the modal accelerations of the structure. Adopting a double integration process, the corresponding modal displacements can be determined. Knowing the displacement field for each vibration mode, it is possible to calculate the equivalent forces that impose the same modal deformation. Thus, the bending moment at any point in the structure is then obtained by summing the bending moment contribution of each mode of vibration, once the partial contribution of each mode to the response of the structure is known.

5.3.3 Axial Stress Variation in the Cross-Section

Considering only the stress variation along the FA and SS directions to determine the accumulated fatigue damage in the tower cross-sections is a conservative approach usually adopted in design, since it adopts a single dominant wind direction. In order to optimize the material capacity, the damage can be estimated over the section of the tower using the stress signals calculated along the perimeter of the cross-section (for example, every 10°).

In this way, the cross-section is divided in segments and the stresses at each central point are calculated knowing the geometric characteristics of the section and the FA and SS bending moments.

5.3.4 Rainflow Counting

The rainflow cycle-counting algorithm translates the hysteresis loops experienced by the material during the loading history into a stress histogram. It gives the number of experimental cycles (n_i) for a certain stress range of the i-th bin ($\Delta\sigma_i$) of the factored stress spectrum.

The most common cycle counting methods are level crossing (Rice, 1988), peak cycle (Veers et al., 1989) and rainflow cycle counting method (Dowling, 1972). The last method is indicated by Eurocode 3 for evaluation the stress history and in (Frendahl & Rychlik, 1993) it is considered as the most accurate method among the other common methods.

The rainflow counting algorithm was developed by Matsuishi and Endo (Matsuishi & Endo, 1968) and later Rychlik (Rychlik, 1987) gave a mathematical definition for the rainflow counting method. A number of variations of this original scheme have been published for various applications (Amzallag et al., 1994; Glinka & Kam, 1987). The biggest advantage of this method is that it accounts for all the peaks without doubling, thus there is not any more drop-out in the calculation in terms of uncounted small amplitudes, which leads to less conservative estimation of the fatigue damage. Another major advantage of this method is that it allows the direct application of the Miner's rule to assess the fatigue life of a structure being subjected to a complex loading record.

The rainflow cycle counting of the stress is performed for both directions (FA and SS directions). The number of required stress bins must be preliminary evaluated for each application. In IEC 61400-13 (International Electrotechnical Commission, 2015), it is indicated that in order to achieve sufficient resolution, the number of divisions of the load range shall be at least 100. However, in DNV GL AS (DNV GL AS, 2016) it is recommended that the number of bins should be large enough to ensure reasonable accuracy, and should not be less than 20.

5.3.5 Fatigue Damage During the Monitoring Period

Before calculating the fatigue damage on the structure, it is important to note that the nominal stresses obtained at the interested position are associated with some uncertainty. In order to take into account the uncertainties about material properties and loads, the consequences of failure and to get a representative value for the concentrated stresses at specific details, the standards and guidelines also define partial safety factors.

For example, Eurocode 3 defines a partial factor for equivalent constant amplitude stress range (γ_{Ff}) which must be multiplied by the stress differences ($\Delta\sigma_i$) obtained from a load spectrum and the stress strength ($\Delta\sigma_c$) is divided by the partial factor for fatigue strength (γ_{Mf}). These partial safety factors are applied separately to loads and resistances to obtain the required safety level. On the other hand, (Det

Norske Veritas (DNV), 2010) indicates an overall safety factor (SF) obtained multiplying several sub-factors, such as stress concentration factor, size effect correction and material safety factor.

Still other factors must be considered for each practical application. In (Weijtjens et al., 2016), two types of adhesions for the strain gauges were compared: strain gauges were glued to the turbine wall or welded to the steel. In this study fibre Bragg gratings (FBGs) were used. A 10% reduction in sensitivity was observed for the welded strain gauges compared to the glued strain gauges.

In the last step, the damage calculation is based on the assumption of linear damage accumulation of each stress cycle, according to the Palmgren-Miner rule. The total fatigue damage (D_{total}) is given by:

$$D_{total} = \sum_{j} \sum_{i=1}^{n_\sigma} \frac{n_{ij}}{N_i} \tag{5.3}$$

Where indices i and j correspond to the i-th stress bin of the j-th time series. The n_{ij} is the number of cycles associated with the stress range $\Delta\sigma_i$ and N_j represents the number of cycles to failure at a constant stress range σ_i , which it is obtained from the corresponding S-N curve.

The S-N curves represent the fatigue resistance of a given detail and are determined from series of fatigue tests on laboratory specimens. Typically, these curves are associated with a given survival probability and level of confidence. For the design of steel support structures, all the standards and guidelines define similar S-N curve equations for fatigue analysis. For example, for components predominantly loaded by normal stress, the guideline GL-2010 (Germanischer Lloyd (GL), 2010) recommends the same bilinear S-N curves as define in Eurocode 3, but disregards the threshold value of fatigue strength. The GL-2010 (Germanischer Lloyd (GL), 2010) do not recommend the use of an endurance limit. The Figure 5.2 represents the S-N curves provides by the two references for a particular detail.

It is important to note that, Eurocode 3 define partial safety factors to be applied to the fatigue strength curves according to the accessibility of the component during periodic inspection and maintenance, and the consequences of failure. A full description of the S-N curves of the different codes and a comparative study of these curves can be found in (Im & Choung, 2021).

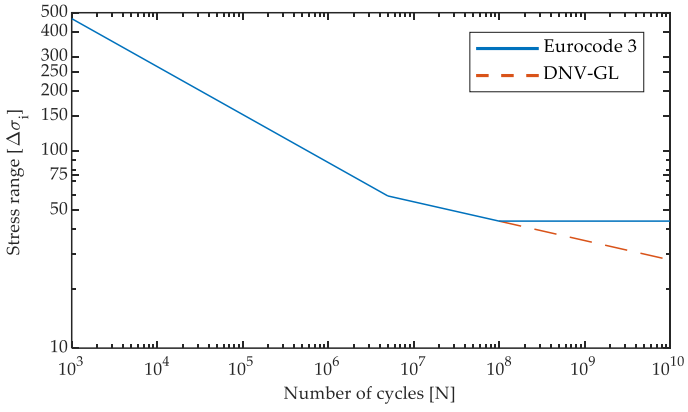


Figure 5.2 – S-N curves defines in GL-2010 and Eurocode 3 (category detail 80 MPa).

In conclusion, the calculated damage refers to the degree of damage of the material under cyclic loading and it is represented by a dimensionless parameter D. For $D = 0$ the material is considered intact and if $D > 1$ the material has reached its fatigue life.

5.3.6 EXTRAPOLATION OF THE FATIGUE DAMAGE IN TIME

Direct measurement of strains at the wind turbine tower allows to estimate the accumulated fatigue damage with good accuracy over the monitoring period. This is an important source information that can be used to estimate the damage prior to and after the monitoring period. The main goal is to estimate the damage at a given angle of the tower section based on a few data from SCADA system: wind speed, turbulence intensity and yaw angle (nacelle orientation).

The presented strategy combines a period of measurements with strains, with long term SCADA data. The experimentally estimated damage (e.g. 10-min damage values) are firstly clustered into several load cases (e.g. power production, parked/idling and emergency shut-down). Based on the approach described in IEC 61400-13 (International Electrotechnical Commission, 2015), the damage values are stored in a database according to the corresponding wind speed and turbulence intensity, the so-called capture matrix. If the wind turbine is directly in the wake of neighbouring wind turbines along the main wind direction, the IEC 61400-13 recommends to classify the damage according to the turbulence intensity and the wind sector. This is illustrated by Weijtens et al. (Weijtens et al., 2016), which performed the damage estimation of an offshore wind turbine taking in account the variation of the turbulence intensity with respect to the wind sector.

For each 10-min time series, a damage value ($D_{10'}$) is picked from the capture matrix bin according the wind speed (WS) and turbulence intensity (TI) given by de SCADA system before the monitoring period. The sum of all individual damage results in the endured damage ($D_{endured}$) over the cross-section of the tower for the period with available SCADA data:

$$D_{endured} = \sum D_{10'}(WS, TI) \cdot rot(Yaw) \tag{5.4}$$

with:

$rot(Yaw)$	Rotating matrix taking in account the wind direction

Note that the endured damage is calculated over the cross-section of the tower. In the previous equation, the term "$rot(Yaw)$" aims to take into account the nacelle orientation (yaw angle) and the referential defined for the strains gauges.

The total endure damage may then be used to estimate the remaining useful lifetime (RUL) of the structure. In a direct way, considering the past period (with available SCADA data) as representative of the whole period of life, the RUL is obtained as:

$$RUL = \frac{T_{operating}}{D_{endured}} - T_{operation} \tag{5.5}$$

with:

$T_{operation}$	Number of years since the wind turbine started operation (assuming SCADA data is always available)

It is important to note that this extrapolation assumes that the monitored period is representative of the loading scenarios from the whole period of operation of the wind turbine. Usually, one year is considered as the minimum monitoring period. Hübler suggests that strain measurements of about 9 to 10 months

lead to a relatively representative and unbiased data set for fatigue damage extrapolation on offshore wind turbines, referring that higher time periods reduce the occurring errors only slightly (Hübler et al., 2018). Although, a more complex approach, based on the probability distribution of environmental and operational conditions, can be followed as shown in (J. van der Tempel, 2006).

Finally, considering that similar wind turbines (same model, controller system and similar loadings) have the same behaviour in the wind farm, the damage capture matrix obtained for the instrumented wind turbine can be used for the others wind turbines in the same wind farm, adopting fleet leader concept, as described in (Weijtens et al., 2016).

5.4 EXPERIMENTAL EVALUATION OF BENDING MOMENTS AT THE TOWER

As a first step in the development of tools to assess the fatigue condition of wind turbine towers, this section describes the data processing needed to obtain an accurate experimental estimation of the bending moments applied in the tower of the fully instrumented wind turbine (WT1) of Tocha Wind Farm and the validation of the obtained results using complementary monitoring components.

5.4.1 PROCESSING METHODOLOGY

Strain gauges are very sensitive sensors and many factors can easily preclude accurate measurements. All potential sources of errors need to be identified and it is necessary to implement a methodology for the signal processing according to the precision of the intended results. Thus, the experimental determination of bending moments in the tower requires the acquired raw data to be pre-processed to obtain the real deformation. In the present application, the methodology adopted consists in the following three steps:

1. Compensation of temperature effect on strain gauges;
2. Signal correction based on the signal average of diametrically opposed sensors;
3. Calibration check according to the guideline IEC 61400-13 (International Electrotechnical Commission, 2015).

Many factors can easily distort strain measurements, but temperature is the most frequent source of errors. Temperature can influence the measurement of strains in two ways: thermal output and non-linear temperature gradient. It should be noted that in the installation under analysis the strain gauges are connected to the acquisition system using a ¼-bridge configuration with three wires in order to avoid the effects of temperature on the cables.

Thermal output is caused by variation of the electrical resistivity of the grid conductor with temperature and the differential thermal expansion between the grid conductor and the steel of the tower. This effect is minimized using the thermal output compensation curve provided by the manufacturer and the temperature measured on the steel surface. The local heating of the sun can also influence the measured strains, as the temperature gradient may become non-linear. This parasite strains are minimized by averaging the two signals provided by the gauge couple installed at 180°.

In order to demonstrate in a practical example the influence of the temperature on the strain measurements, Figure 5.3a represents four strain signals measured at the tower bottom section, after being zeroed during the nacelle full rotation (procedure explained later) performed at around 07:00 (without compensation of the temperature effects). The same signals but with temperature effects minimized is shows at Figure 5.3b). Comparing the figures, it is observed that in the first one the signals provided by the gauge couple installed at 180° are not perfectly symmetric, whereas in the second there is a perfect symmetry with respect to the x-axis.

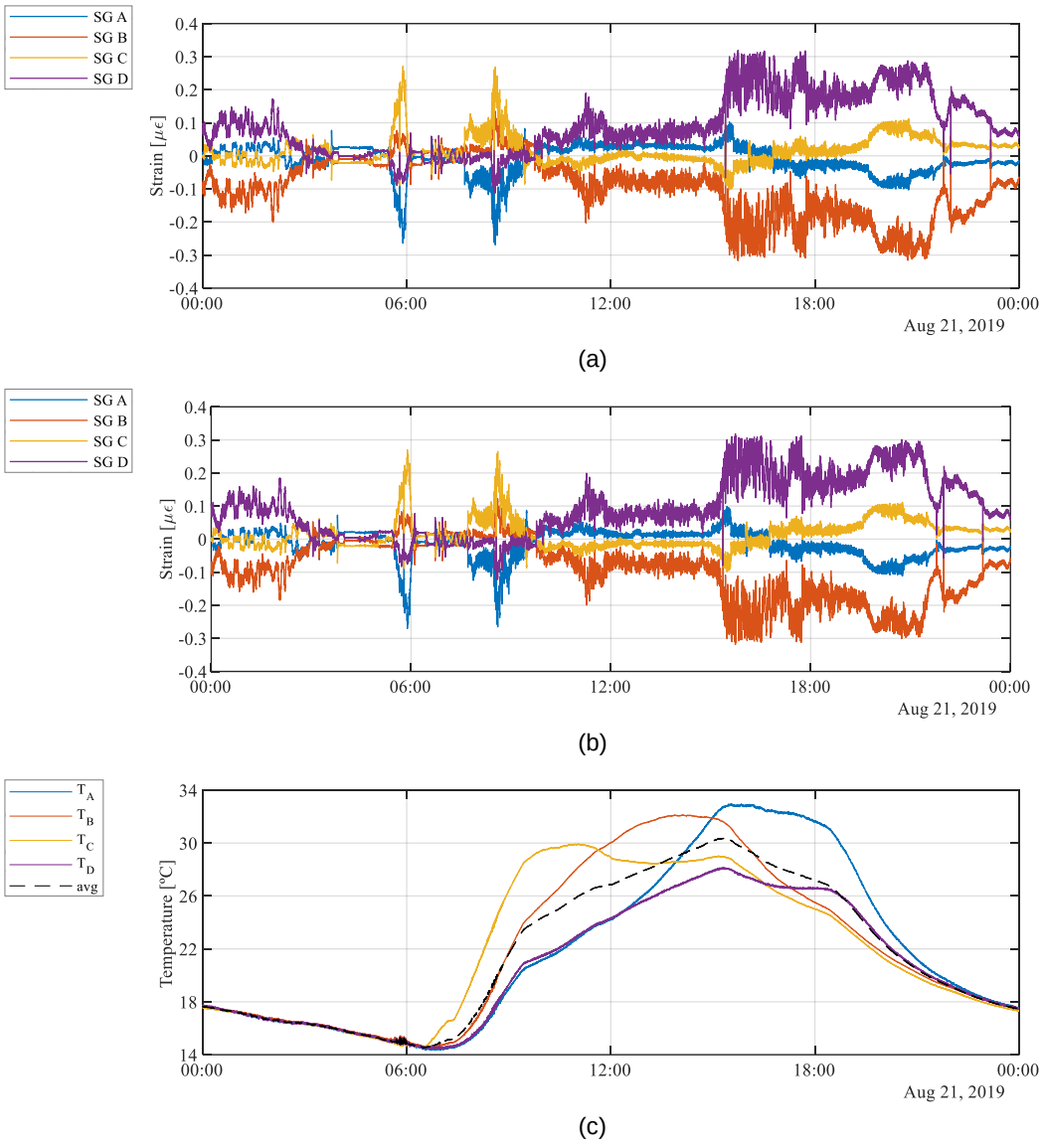


Figure 5.3 – Daily temperature effects on strains measurements at the bottom section: (a) Strains signals zeroed during the nacelle rotation; (b) Strains signals zeroed during the nacelle rotation with compensation of the temperature effects; (c) Temperature measurements.

A significant drift is observed on the strains signals over time (Hoffmann, 2012). The correction of this drift is based on the procedure defined by the IEC 61400-13 called calibration check. This procedure requires yawing the nacelle 360° below cut-in wind speed, as shown in Figure 5.4a. The full rotation of the nacelle generates a sinusoidal signal due to eccentricity of the nacelle and rotor mass, as shown in Figure 5.4b. If the effect of the axial force is disregarded, the mean of this signal represents the zero point. Please note that the strains presented in this figure were previously pre-processed to have zero mean.

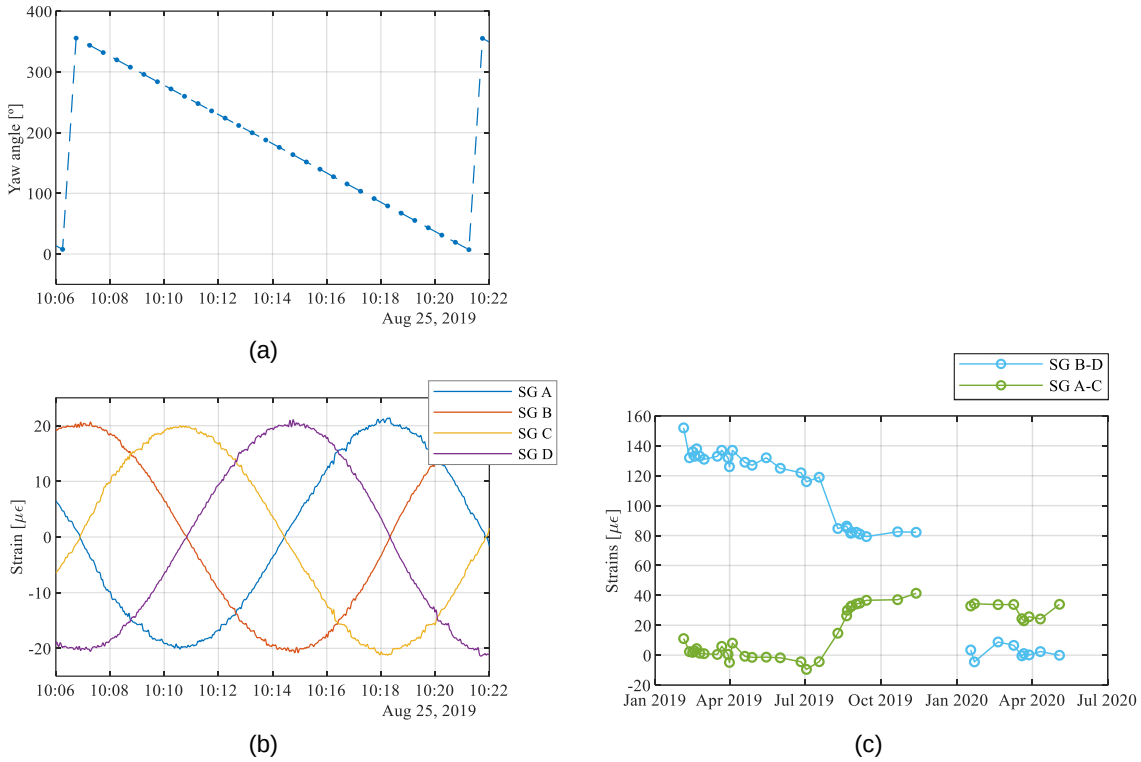


Figure 5.4 – Strain-gauge calibration check: (a) Yaw angle nacelle; (b) Strain signals; (c) Mean value of the full rotation signals observed from Frebuary-2019 to April-2020 (see sensor positions in Figure 4.12).

This procedure is also important to determine the exact position of the sensors in the instrumented section of the tower (despite the care used in the sensor gluing there are always inaccuracies in sensor position). The value of the yaw angle for which the minimum value of the strain signals occurs is assumed to correspond to the radial position of each sensor. The nacelle angle defines the fore-aft and site-side axis for which the bending moments will be estimated.

A total of 38 full rotation of the nacelle, that met all the requirements, were observed in the period between February 1, 2019 and April 30, 2020 and were used for calibration (Figure 5.4c). In December 2019 there was a need to replace some components in the acquisition system that explains the sudden drift variation for the couple B-D. In the following months, the drift remains approximately constant.

5.4.2 Bending Moments Validation

In order to verify whether the values of the strains obtained based on the procedure described in the previous section correspond to real deformation of the structure due to the applied loads, some validation tests were performed.

In this sense, the average values of strains observed in all 10-min time series recorded (a total of 53384 time series were collected in the monitoring period) are shown in the Figure 5.5 as a function of the yaw angle. These values are compared with the theoretical strain curve that is obtained for the maximum thrust force applied at the rotor level (represent by the black curves). This theoretical curve was computed from the drag coefficients presented in (Morrison Hershfield Limited, 2012).

All the obtained experimental results (the cloud of points which almost completely fill the sinusoids) are well framed by the theoretical curves. However, it should be noted that the maximum strain values

are not obtained for all wind directions. This is because prevailing conditions of wind action exist. These results are also important to futher validate the sensors position.

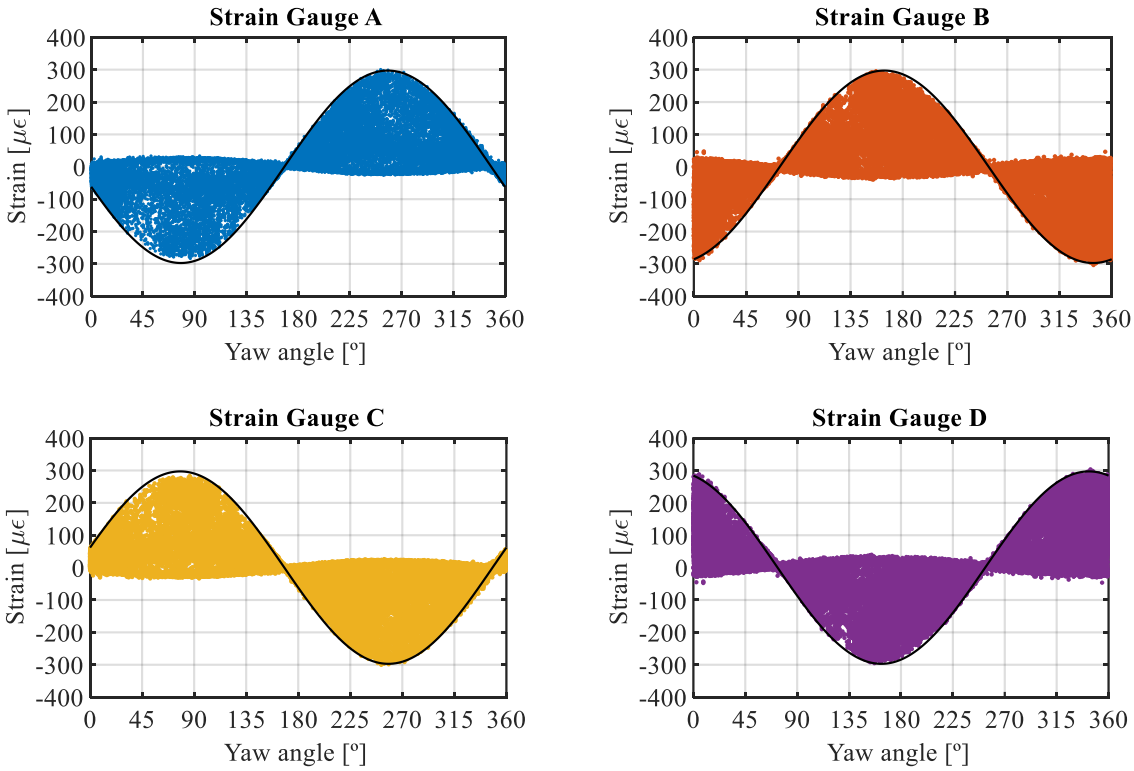


Figure 5.5 – 10-min average strains signal of strain gauges A to D (see sensor positions in Figure 4.12).

In a second verification, the bending moments estimated from the measurement of strains were also compared with those that can be obtained from the measurement of accelerations. Considering a rotor stop event (in which only the first vibration mode of the tower explains the structure's response) the displacement of the tower at the top level was determined by double integration of the acceleration time series. Using a stiffness matrix provided by a simple numerical model develop in the structural analysis software Robot (Autodesk, 2016), it was possible to determine the equivalent modal force applied at the top level of the tower and the associated bending moment at the section instrumented with strain gages. The method followed to determine the response of structure in displacement from the measurement of accelerations is further developed in (Hjelm et al., 2005; G Oliveira et al., 2017).

The variation of the bending moments with respect to the mean value at the base of the tower estimated from accelerations and strains are compared in Figure 5.6. There is an excellent similarity between the bending moments estimated with the two methods. The error is less than 10% and might be explained by the difficulty in accounting for the exact stiffness of the tower.

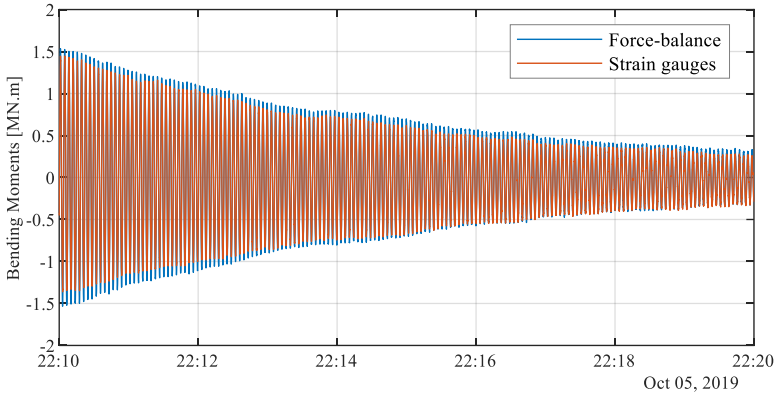


Figure 5.6 – Bending moments variations at the base of the tower estimated from accelerations and strains time series during a rotor stop event.

Finally, considering two alternative turbine operation scenarios, the experimental results are compared with numerical counterparts, obtained from a model developed in FAST (Sprague et al., 2015) and calibrated using the methodology described in (Pimenta et al., 2019). As shown in Figure 5.7, it is possible to verify a good agreement between the numerical and experimental results. It should be noted that the simulated wind loads respect the mean and standard deviations observeds in the field measurements, but the time series are different. In both analysed situations, the mean values and scatter of the FA bending moments are very similar.

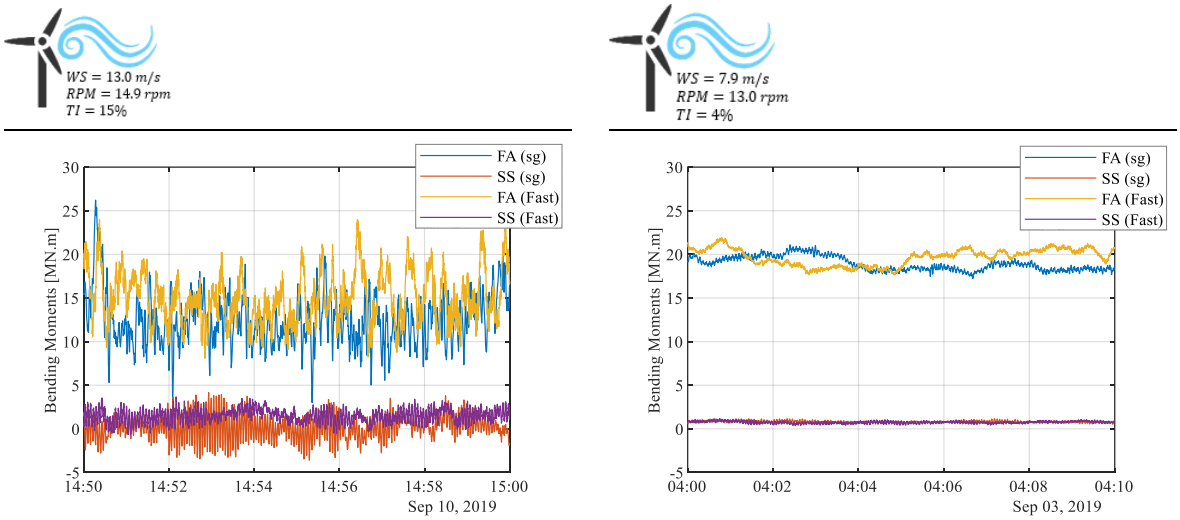


Figure 5.7 – Experimental and numerical bending moments time series for FA and SS directions in the bottom instrumented section of the tower considering two different operating conditions.

5.4.3 BENDING MOMENTS VS OPERATING CONDITIONS

In this section the estimated bending moments are analysed against SCADA data, considering 10-min time series. Figure 5.8a shows the 10-min average bending moment at the tower instrumented section for the fore-aft direction versus the 10-min average wind speed provided by the SCADA system during normal operation, considering variable levels of turbulence intensity. This figure shows that the drag force acting on the rotor (responsible for the deflection of the tower) increases with the wind speed until the reaching of the rated rotor rotation speed. Due to the activation of the pitch control to keep the lift force and the rotor speed constant, the value of the drag force reduces as the wind speed increases. It is important to note that for the same values of wind speed, different values of bending moments are obtained due to the effect of turbulence. In fact, the maximum moment decreases as the intensity of the turbulence increases. This behaviour is explained by the impact of the wind turbine control algorithms, in particular the pitch control system.

The 10-min average bending moment at the tower instrumented section for the side-to-side direction is represented in Figure 5.8b as a function of the 10-min average wind speed and of the turbulence intensity. As expected, the bending moments in this direction are significantly lower than the values obtained for the perpendicular direction. The average bending moments increase as the wind speed increases, especially after activation of the pitch control system. Again, for the same wind speed, the bending moment values are higher when the turbulence intensity is lower.

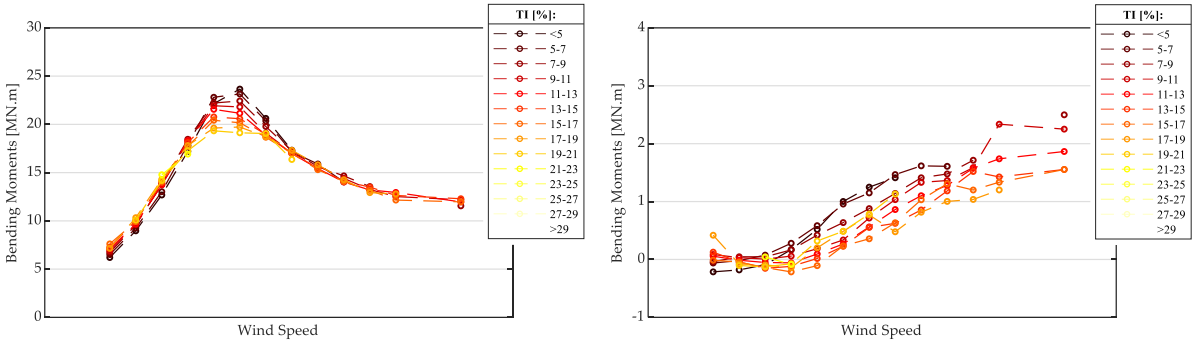


Figure 5.8 – Variation of 10-min average bending moments at the tower base as a function of the wind speed and turbulence intensity, considering normal power production: (a) Fore-aft direction; (b) Side-to-side direction (x scale omitted due to confidentiality agreements).

The average 10-min power output of the wind turbine is shown in Figure 5.9Figure 5.8 as a function 10-min average bending moment for the fore-aft direction and the turbulence intensity. Once again the effect of turbulence is demonstrated. Considering the power production between 0.8 and 1.7 MW, the fore-aft bending moment at the tower tends to decrease for higher turbulence intensities.

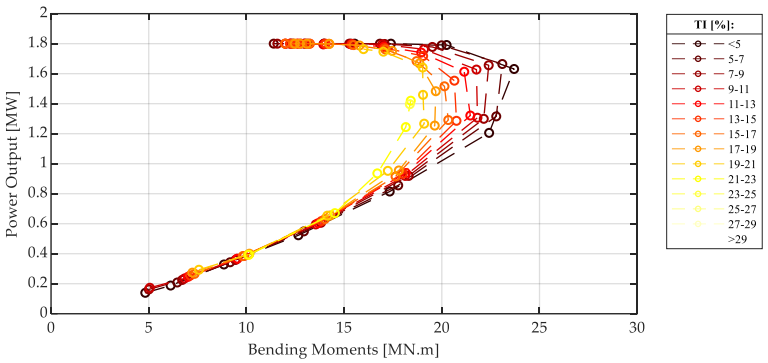


Figure 5.9 – Variation of 10-min average power output during normal power production, as a function of the FA bending moment at the tower and turbulence intensity.

The following figures represent different fore-aft and side-to-side bending moments at the instrumented section for specific type of operating conditions. In every case, the blue signal correspond to the fore-aft bending moment and the orange signal to the side-to-side bending moment. The environmental and operational conditions are given by the SCADA high-resolution.

Considering normal power production, Figure 5.10 shows the bending moment's variation for three average wind speeds, below (7 m/s and 9 m/s) and above (14 m/s) the rated speed, and different turbulence intensities. The results obtained allow a better understanding of the curves presented in Figure 5.8a. Due to the pitch control system activation for the wind speed above the rated speed, the fore-aft bending moment is lower than the equivalent moment obtained for the wind speed of 7 m/s. On the other hand, considering the average wind speed of 9 m/s, the average value of the fore-aft bending moment is higher for the lowest turbulence intensity. Comparing the behaviour of the pitch control system in the two cases, it is possible to see that the pitch angle values are higher for the average turbulence equal to 15%.

Considering the side-to-side bending moments, the average wind speed slightly influence the mean bending moment. On the other hand, turbulence intensity effects the standard deviation and the bending moment amplitude. As mentioned for Figure 5.8b, the side-to-side bending moment increases after activation of the pitch control system.

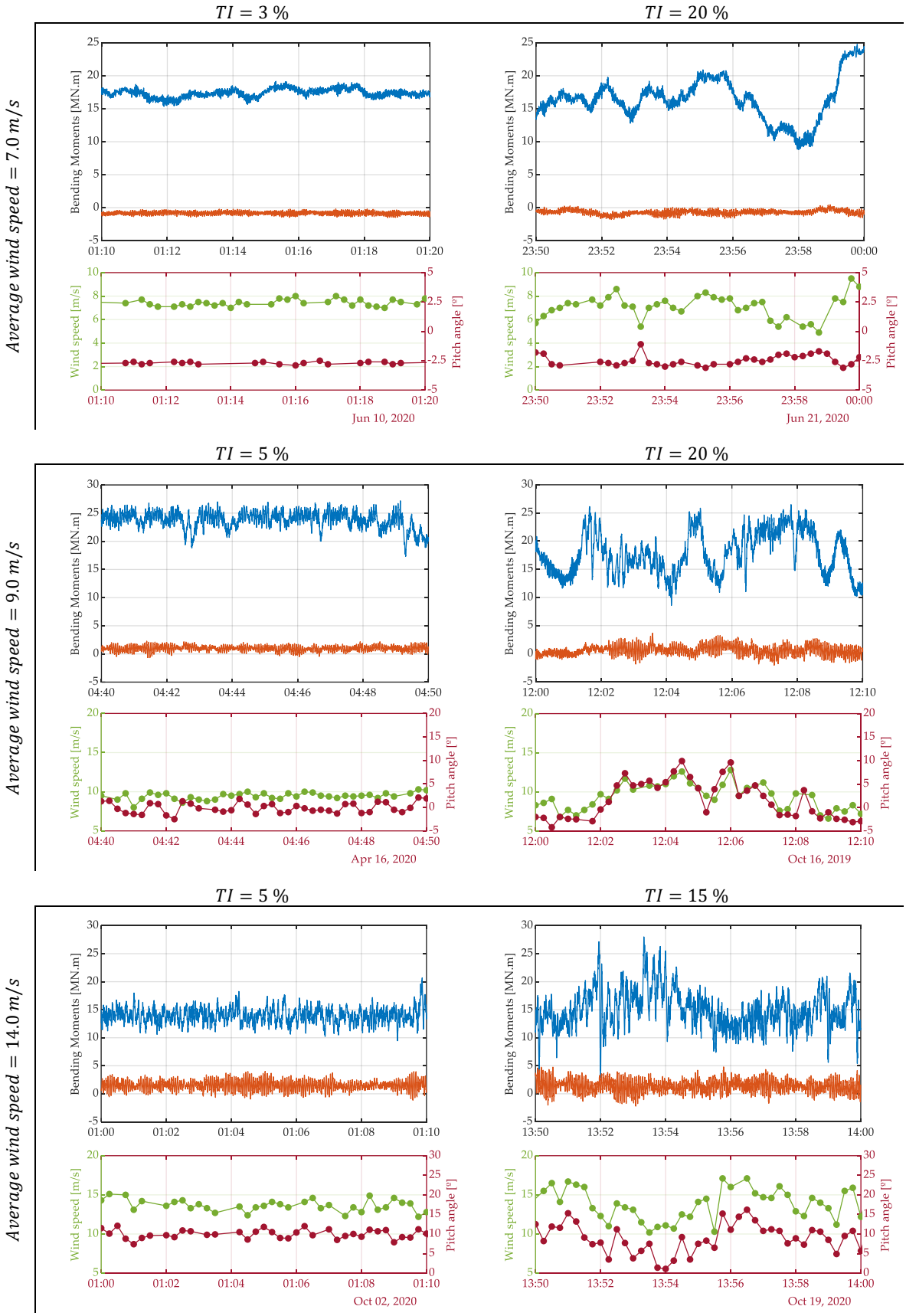
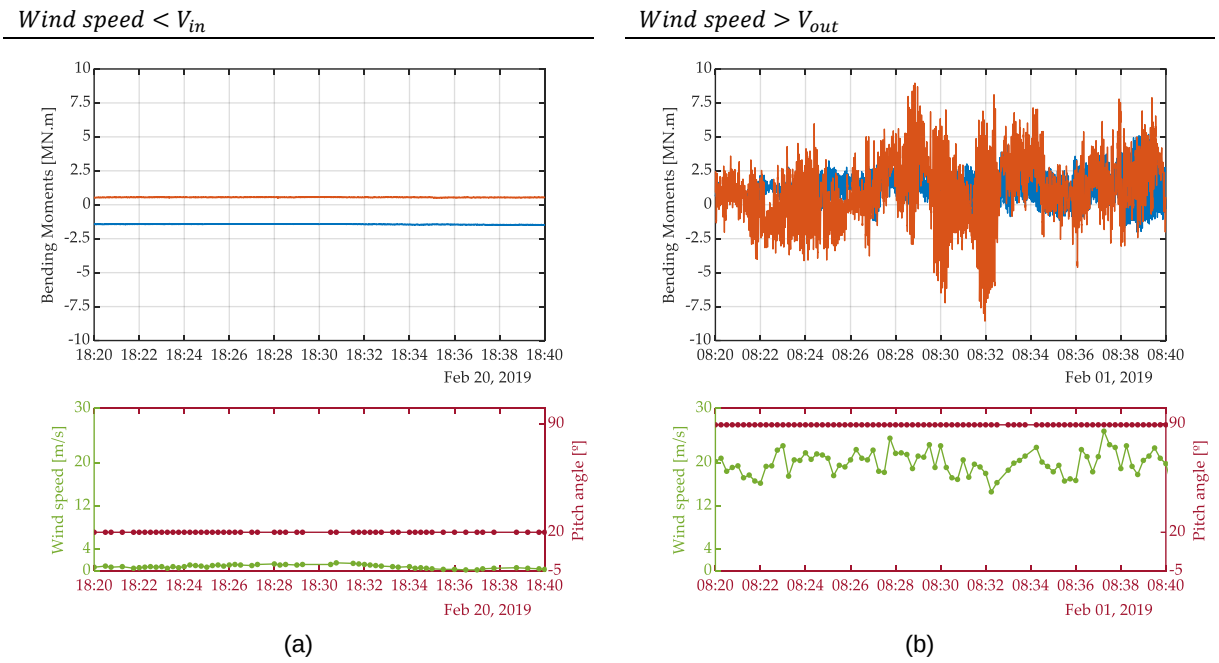


Figure 5.10 – Bending moments measured at tower base during normal power production, considering different wind speed and turbulence intensities. Wind speed and blade pitch angle provided by SCADA high resolution.

Focusing on non-operation events, Figure 5.11 represent 20-min time series of the bending moments during parking/idling conditions. When the wind speed is below the cut-in wind speed (average wind speed below 2 m/s in Figure 5.11a), the blade pitch angle is approximately 20° and the bending moments essentially result from the nacelle eccentric mass. Figure 5.11b represents time series measured during a storm, when the wind speed exceeds 20 m/s. The control system parked the turbine, fixed the yaw angle and the blades are pitched at the maximum value. The values of bending moments are conditioned by the wind gusts.



(a) (b)

Figure 5.11 – Bending moments measured at tower base and wind speed and blade pitch angle time series during parked/idling condition for: (a) Wind speed below the cut-in speed; (b) During a storm.

An example of shutdown procedure is show in Figure 5.12, activated when the wind speed exceed the cut-off of the wind turbine. The blades are pitched at the maximum value and, consequently, the fore-aft bending moment rapidly decreases, leaving the tower in free vibration.

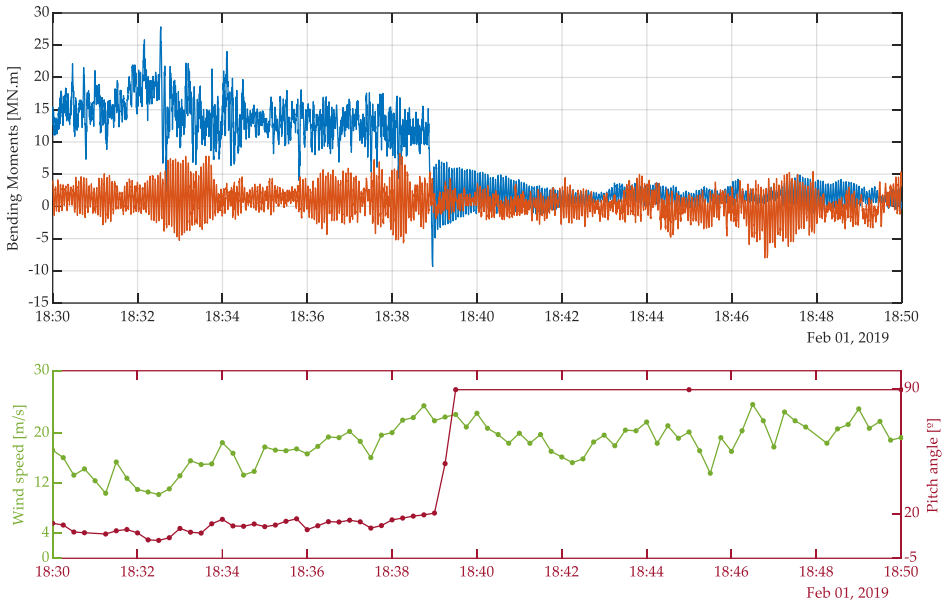


Figure 5.12 – Bending moments measured at tower base and wind speed and blade pitch angle time series during an emergency shutdown event.

Figure 5.13 shows 40-min time series of bending moments measured at low wind speed, when the average wind speed is around 3.5 m/s (very close to the cut-in speed). Initially, the turbine is in idling state with the blades pitched at 20°. Then, the wind speed increases and the turbine starts operation that lasted less than 10-min. During the full plotted period, the turbine started-up operation five times, and shut-down four times. It should be noted that, for this wind speeds increasing the pitch angle to approximately 5° is enough to decrease the lift force and stop the turbine.

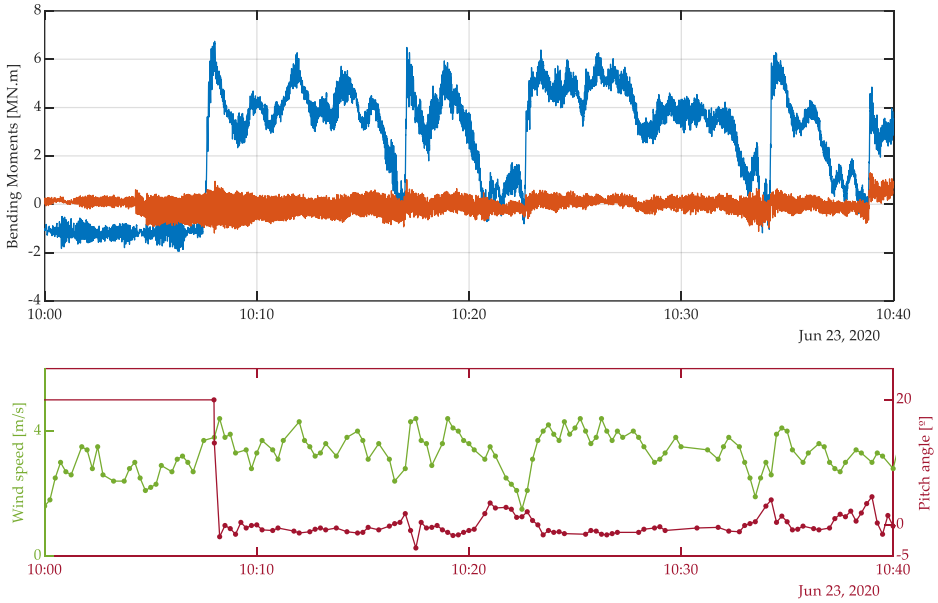


Figure 5.13 – Bending moments measured at tower base and wind speed and blade pitch angle time series during the start-stop of the turbine around the cut-in wind speed.

Once the bending moments installed in the instrumental section of the tower are known, it is possible to estimate the average drag force applied at the rotor level for several operating conditions. Figure 5.14 shows the fore-aft and side-to-side hub forces for power production and parked periods as a function of the wind speed.

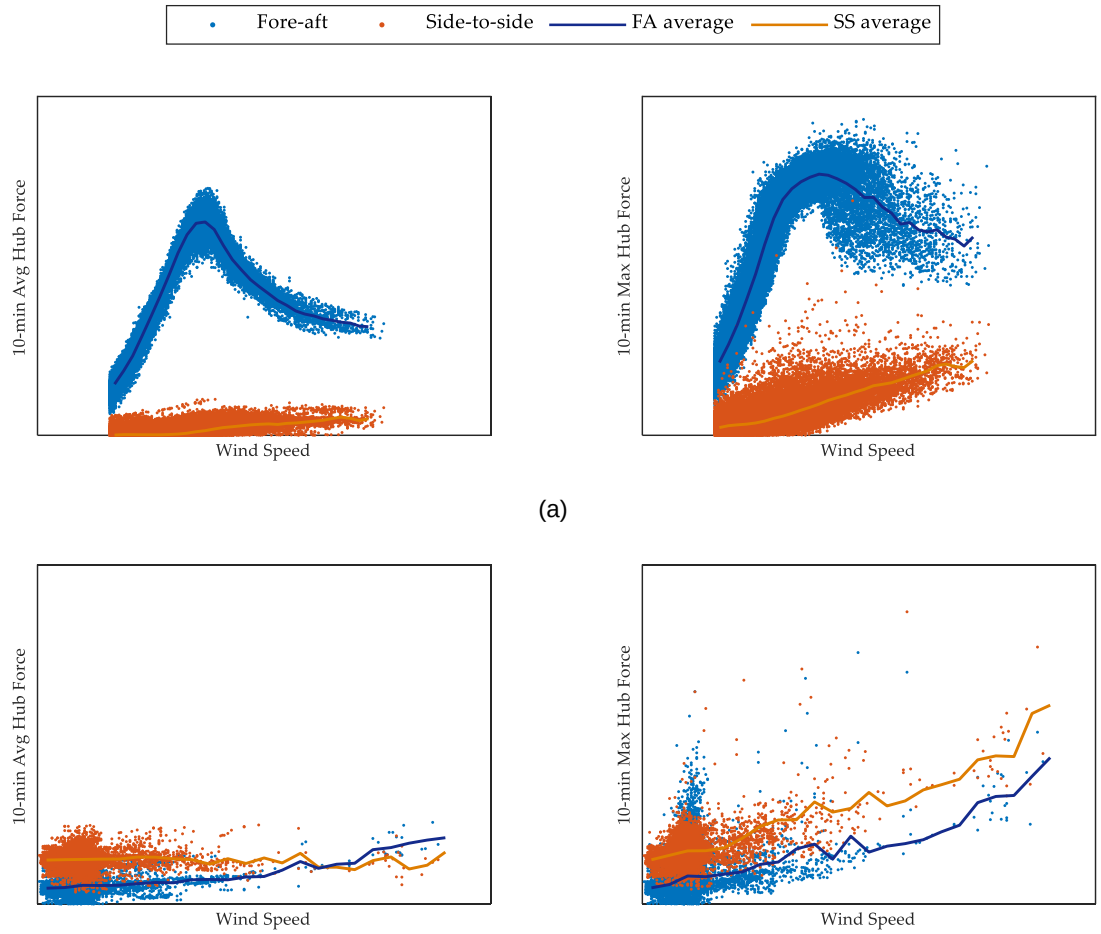


Figure 5.14 – 10-min average (left) and maximum (right) thrust loads as a function of 10-min average wind speed, considering: (a) Power production conditions; (b) Parked periods.

During power production, the 10-min average fore-aft hub force increases gradually up to the rated speed and decreases when the pitch control system of the turbine is activated. On the other hand, the 10-min maximum forces are directly resulting from high wind speeds and increase with it following a bi-linear curve. Side-to-side forces are relatively small compared to the fore-aft force. For parking periods, the hub force is extremely small and only the residual force is actually the force equivalent to the bending moment resulting from the eccentric mass of the rotor.

5.5 FATIGUE ASSESSMENT OF WIND TURBINE TOWER

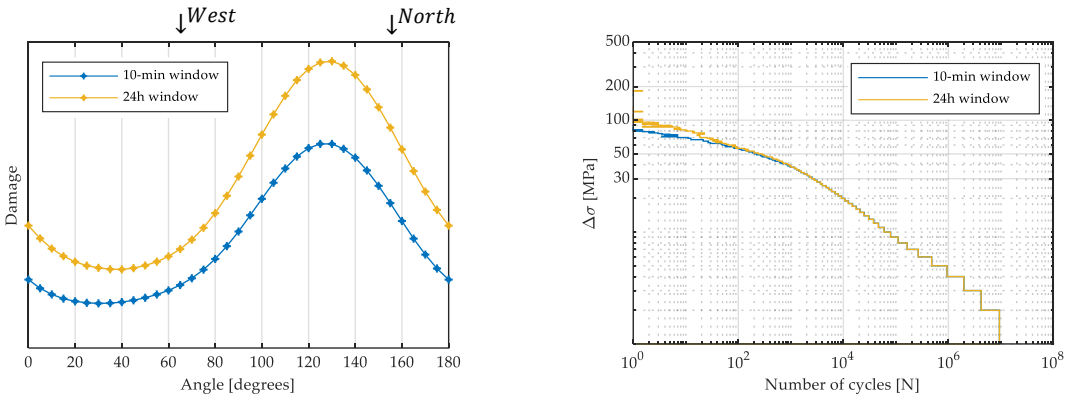
In order to demonstrate the practical applicability of the methodology for the fatigue assessment of wind turbine towers based on strain measurements (described in Section 5.3), the database acquired in the experimental campaign in the Tocha Wind Farm (introduced in Chapter 4) was processed according to this methodology. The results presented in this section are based on experimental data obtained between February 2019 and April 2020 (15 months).

In this first analysis, only the damage accumulated during the monitoring period was calculated and at the precise strain measurement position. The instrumented cross-section is close to a horizontal welding, so this detail was used for the selection of the S-N curve. Since the main goal of this work is the presentation of the processing strategy, it was not assured that this is one of the most critical sections of the tower in terms of fatigue design.

As mentioned above, before applying the methodology for fatigue assessment, it is necessary to previously define several parameters such as those that influence the S-N curves or the processing associated with the algorithm used for counting stress cycles. In order to understand the influence of some relevant parameters on the calculated damage, the following variables will be evaluated independently.

- Window length;
- Rainflow histogram resolution (number of stress bins and stress range);
- S-N curve parameters;
- Strains signal sampling frequency.

The first parameter is window length of the strains time series used to estimate the stress cycles. The damage was estimated over one half of the instrumented cross-section using 10-min and 24-hours long time series, recorded during 15 months and according the S-N curve provided in Eurocode 3. Figure 5.15a shows the damage calculated from 0° to 180° with 5° intervals considering the two window lengths. The damage obtained with 10-min time series was found to be 11% lower than the damage calculated with 24-hour time series. It is verified that the maximum damage in the section occurs for an angle close to the prevailing wind orientation, as demonstrated in Figure 4.1c.

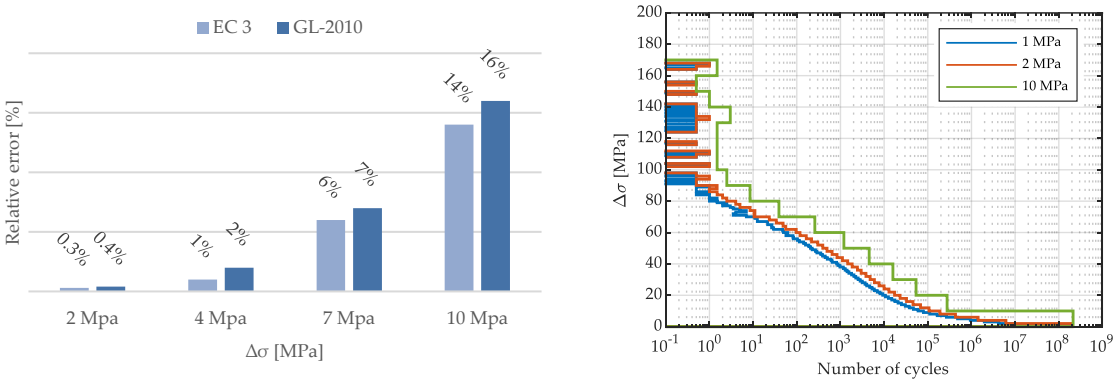


(a) (b)

Figure 5.15 – Influence of the window length: (a) Damage distribution over the half of the section (y scale omitted due to confidentiality agreements); (b) Histogram of the stress cycles.

Figure 5.15b shows the histogram of the stress cycles obtained for the two window lengths. As show in the histogram, a relevant difference can be seen between the two curves for the largest stress cycles, starting from 50 MPa. The largest cycles that can result from changes of wind direction or start-stop events are only detected when the rainflow counting algorithm is performed on full days. Thus, 10-min windows underestimate the cycles with stress variations above 50 MPa.

In order to obtain the number of cycles per stress level, the 10-min strain time series were processed with the rainflow cycle counting method (Dowling, 1972). The mean stress was disregarded for the reasons presented in Section 5.3.1. The number of stress bins and the stress range which are used in the algorithm, directly influence the calculated damage. Thus, the stress histogram was computed for a stress range of 0 to 500 MPa and considering bins with the amplitude of 1 MPa (500 bins), 2 MPa (250 bins), 4 MPa (125 bins), 7 MPa (71 bins) and 10 MPa (50 bins). Figure 5.16a shows the relative difference of the calculated damage in the cross-section, considering the 1 MPa bin amplitude as the reference. Figure 5.16b represent the stress histogram for 1 MPa, 2 MPa and 10 MPa amplitudes bin.



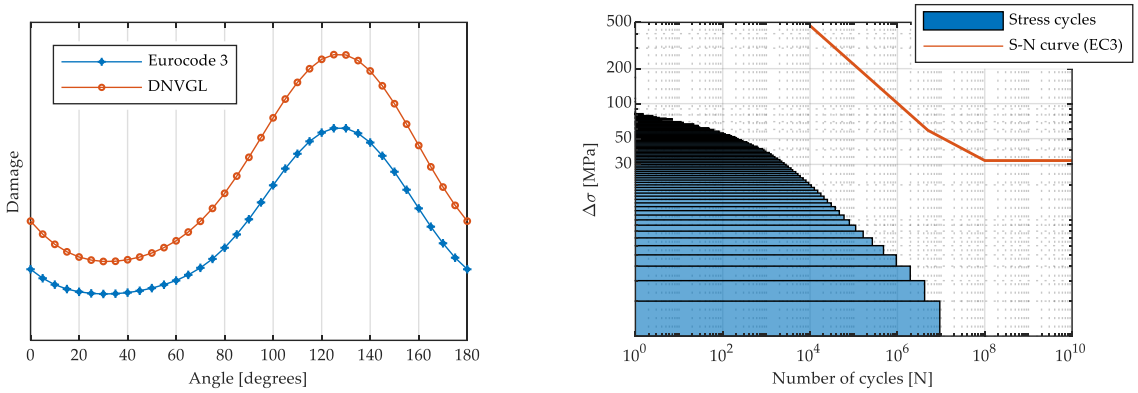
(a) (b)

Figure 5.16 – Influence of the rainflow histogram resolution: (a) Relative difference of the calculated damage (the 1 MPa bin amplitude is the reference); (b) Stress cycles histogram.

As shown in the figures, there is an increase in accumulated damage as the bin amplitude increases. This is due to the loss of resolution of the stress histogram for the cycles associated with higher stress variation, as show in Figure 5.16b. In all the remaining analyses a bin amplitude of 1 MPa was adopted.

Another important analysis is the influence of the S-N curve parameters on the calculated damage. Figure 5.17a shows the damage from the 10-min time series along half of the section based on two alternative S-N curves represented in Figure 5.2 (with and without endurance limit).

It is possible to verify that the damage calculated with the S-N curve provided in Eurocode 3 (considering endurance limit) is significantly lower (approx. 30%) than the damage calculated with bilinear S-N curve without considering endurance limit. The large percentage of low amplitude stress cycles in the monitored data, as shown in Figure 5.17b, justifies these results. In fact, this figure shows that 99% of the total identified cycles are below the endurance limit (44 MPa for category details of 80 MPa).



(a) (b)

Figure 5.17 – Influence of the S-N curve parameters: (a) Damage distribution over the section (y scale omitted due to confidentiality agreements); (b) Histogram of the stress cycles and S-N curve provided by Eurocode 3.

Finally, the influence of the sampling frequency of the acquired strains signal is evaluated. As previously mentioned, this acquisition system is programmed with a sampling frequency of 50 Hz. In an attempt to reduce the calculation time with the application of the rainflow algorithm, the acquired signal was decimated to 25 Hz and 12.5 Hz.

Three alternatives were followed to decrease the signal sampling frequency. Fist, the Matlab "decimate" function was directly applied to the signal. In the second alternative, the signal was resampled without the prior application of a low-pass filter (assuming no relevant frequency content in frequencies above one-half of the sampling frequency). Alternatively, the signal was filtered (Chebyshev Type I and Butterworth filters were applied independently) and then resampled to the desired sampling frequency. The basics of low-pass filtering are discussed in (M. T. Thompson, 2014). The Figure 5.18 compares the stresses cycles as a function of the accumulated damage associated with the four tested alternative pre-processing with the one given by original signal. The damage was estimated based on the bilinear S-N curve provided in GL-2010.

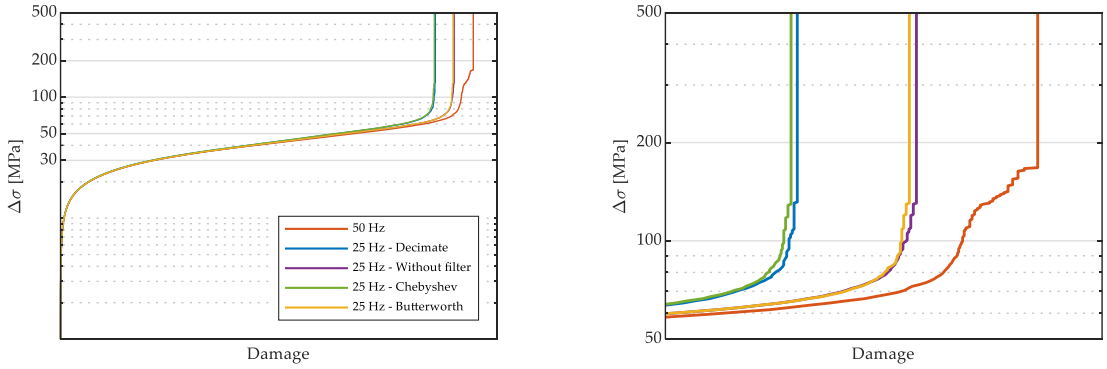


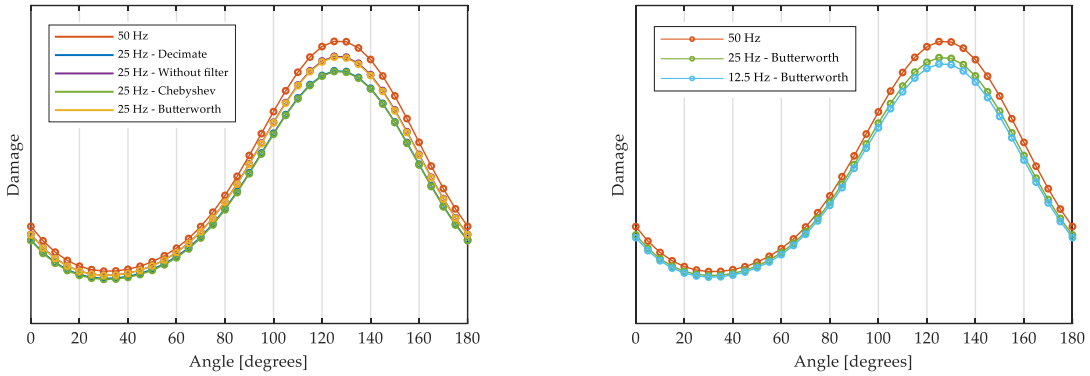
Figure 5.18 – Influence of signal sampling frequency. Stress cycles amplitude as a function of the accumulated damage for a sampling frequency of 25 Hz (with zoom) (x scale omitted due to confidentiality agreements).

The previous figures allow to understand the importance of the procedure to be adopted in the resampling of the signal. As shown, the selected method can have a great influence on the total calculated damage. The “decimate” function of the matlab uses the Chebyshev Type I filter to decimate the signal. For that reason, the results between these two methods are so close.

The application of the Butterworth low-pass filters shown less impact on the estimated damage. These results reflect the importance of the low-pass filter selection. The figures also show the resampling of the signal will always led to a reduction in the estimated accumulated damage.

The damage distributions over half of the section obtained from all the tested pre-processing methods are presented in Figure 5.19a. The purple curve is overlapped with the yellow curve and the blue curve with the green curve.

Comparing with the damage calculated from the original signal, it is possible to observe a difference of -4.6% for the alternative without filter, and -9.4% and -4.8% considering the Chebyshev Type I and Butterworth filters, respectively.



(a) (b)

Figure 5.19 – Influence of signal sampling frequency: (a) Damage distribution over the section considering 4 methods ($f_s = 25\ Hz$); (b) Damage distribution over the section for all sampling frequency (Butterworth filter) (y scale omitted due to confidentiality agreements).

Figure 5.19b represent the damage distribution over half of the section calculated according the bilinear S-N curve provided in GL-2010, adopting a Butterworth filter with 2 alternative re-sampling rates. The damage calculated with signals with a sampling frequency of 25 Hz and 12.5 Hz were found to be 4.8% and 6.6% lower than the damage calculated with the original signal (cumulative damage calculated for the critical angle of the section).

Table 5.1 shows the relative differences between the accumulated damage at the critical angle of the cross-section of the tower, considering the different sampling methods and sampling frequencies.

Table 5.1 – Relative differences of accumulated damage at the critical angle of the cross-section of the tower considering the different sampling methods and sampling frequencies.

Method	$f_s = 25\ Hz$	$f_s = 12.5\ Hz$
Matlab “decimate” function	-8.8	-10.5
Without low-pass filter	-4.6	-6.4
Chebyshev Type I filter	-9.4	-11.0
Butterworth filter	-4.8	-6.6

5.6 EVALUATION OF FATIGUE LIFE CONSUMPTION WITHIN THE WIND FARM

5.6.1 INTRODUCTION

The first standard for lifetime extension of wind turbines is based on a combination of inspections and fatigue damage simulations considering a design model (DNV GL AS, 2016). These fatigue damage simulations can be significantly improved if the load conditions are known. However, the data currently measured at wind turbines is insufficient to support turbine lifetime assessment. The installation of additional sensors, such strain gauges, allows overcoming this limitation. However, the installation of strain gauges is still not well accepted by operators. The cost of installation, the need for experienced professionals to install, the need to stop operation during installation and the need to prepare the tower surface (including paint removal) might be the main reasons.

In order to support the operators, an accurate fatigue assessment is needed for all wind turbines in the wind farm. An interesting approach is to assess the lifetime of the entire farm based on the extrapolation of the experimental results from few instrumented turbines with additional sensors to the other wind turbines. The concept of extrapolating measurements from instrumented to non-instrumented turbines was introduced for blade loading by (Braam et al., 2012) as the "Fleet Leader Concept". This cost-effective monitoring tool is very useful for operators as it allows, for the long term, to support decisions when approaching design lifetime (can the operation be extended or what is the remaining value of our assets) and adjust wind farm control (balance power production and fatigue life consumption). On the other hand, for the short term, this tool allows to improve knowledge, identifying the operating conditions that cause more damage (e.g. for turbines with high fatigue loads in blades it is better to park than idle) and to plan major component replacements (predictive maintenance avoids long unexpected downtimes).

The first works on lifetime estimation based on strain measurement were conducted about 30 years ago (Söker, 1995, 1996). However, in the last years, due to the increasing relevance of lifetime extensions, this topic has become a research focus again (C. Loraux & Brühwiler, 2016; Weijtens et al., 2016). Since experimental data is always limited, the main challenge of this procedure lies on how to extrapolate short-term damage to lifetime damage (C. Loraux & Brühwiler, 2016; Söker, 1996; Weijtens et al., 2016). The reliability of state-of-art extrapolations techniques is still not precisely known (Häfele et al., 2018; Zwick & Muskulus, 2015).

This work aims to implement a measurement driven fatigue monitoring concept to measure and assess the progression of fatigue in an entire wind farm. A limited number of wind turbines, called fleet leaders, are instrumented to measure the load history of the support structure. The methodology is based on calculation of the real damage accumulated during each 10-min time series by applying rainflow counting and Miner's rule on measured bending moments applied to the tower. The recorded load histories allow determining the consumed lifetime of the turbine and calculating the remaining useful life. Considering that similar wind turbines (same model, controller system and similar loadings) have the same behaviour in the wind farm, the damage capture matrix obtained for the instrumented wind turbine can be used for the others wind turbines in the same wind farm. In this way, the results of the fleet leader will be extrapolated to other turbines using only environmental conditions, in particular wind conditions. The extrapolation process of tower fatigue damage and the inherent uncertainty is investigated, considering different alternative methods. The strain measurements obtained from the experimental campaign at Tocha Wind Farm are utilised.

5.6.2 FLEET LEADER CONCEPT

An overview of the extrapolation method based on the fleet leader concept is given in Figure 5.20. As shows in the figure, this method consists of two main parts: i) Construction of the damage capture matrix of the fleet leader (blue arrow); ii) Damage extrapolation to non-monitoring periods and towards another turbines (brown arrow). All steps are explained in more detail in the following sections.

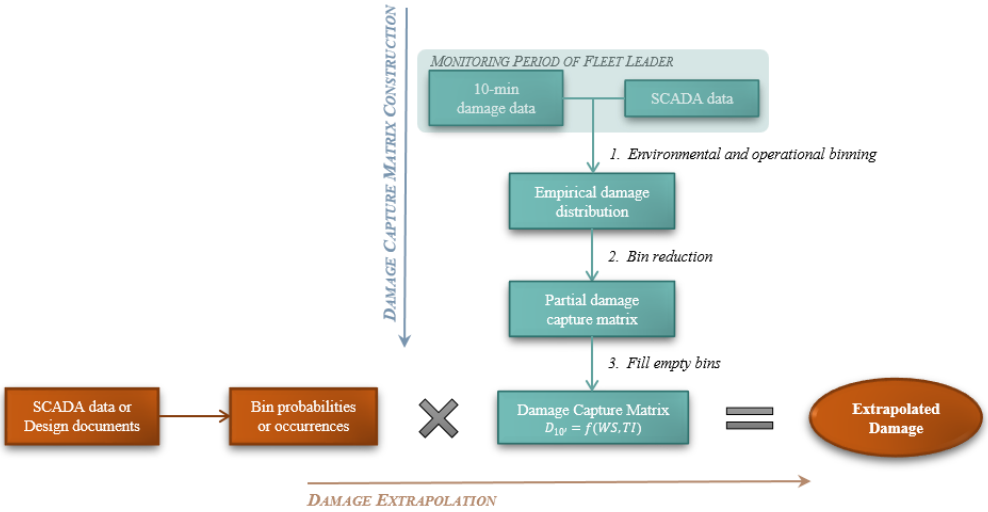


Figure 5.20 – Overview of damage extrapolation method form the fleet leader to the entire wind farm.

As will be shown later, throughout the various steps of the extrapolation method, several parameters must be defined and might influence the results significantly. For this section, choices are made based on experience and existing bibliography. Some shortcomings and alternatives are also presented and discussed.

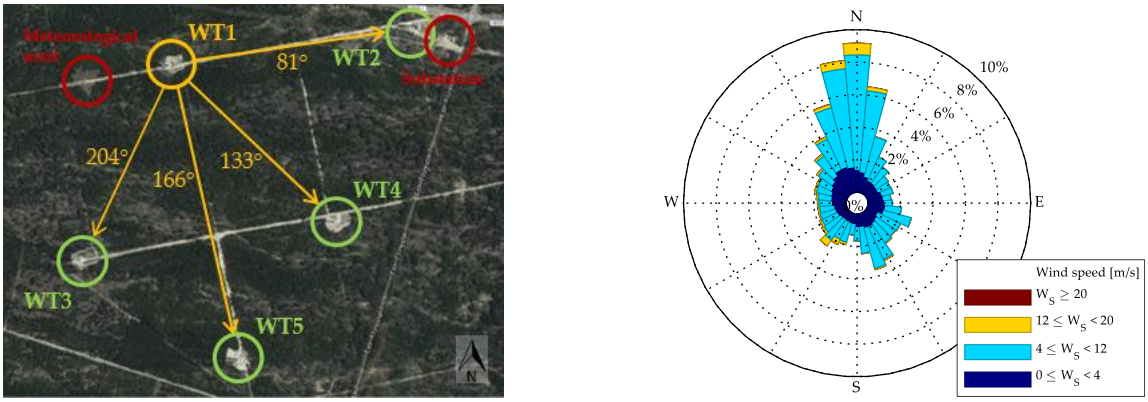
The methodology proposed in this work will be validated with the experimental data collected at Tocha Wind Farm, described in Chapter 4, between February 2019 and February 2021. In this work, the fatigue assessment is associated with a detail located about 6.0 m above the tower foundation, very close to the instrumented bottom section (Figure 4.12). The measured strains signal was divided into 10-min intervals and the accumulated damage was calculated based on the classic approach using rainflow counting and Miner's rule, according the procedure introduced in Section 5.3.2. The resulting stress ranges were distributed over 500 predefined bins spaced 1.0 MPa, for every 10-min interval separately. It was adopted the S-N curve provide by GL-2010. Due to confidentiality issues, only normalized values can be presented.

The tower strain monitoring system, described in Section 4.4.2, is complemented by the environmental and operational parameters provided by the SCADA system. 10-min time series for which the required meteorological measurements are not available are excluded from the calculations. It should be noted that some studies indicate than wind turbine anemometer does not provide reliable to accurately determine wind speeds and turbulence intensity (N Noppe et al., 2015). However, it should be noted that: (1) the adopted values, delivered by an anemometer placed on the top of the nacelle, are corrected to minimize the disturbances motivated by the rotor; (2) in the context of the present analysis, it is not relevant to have accurate values of wind speed and turbulence, but instead, two parameters, always estimated in the same way, which are correlated with the endured fatigue damage.

The first step of the methodology is the selection of the wind turbine(s) that will be the fleet leaders of the wind farm. In this case study, two criteria were used. The first criterion was the size of the wind

farm. Taking into account that Tocha Wind Farm is a small farm, only one wind turbine was selected as the fleet leader. Then, in order to directly measure the impact of turbulent air on fatigue loads and thus be able to draw conclusions for other wind turbines in the same farm, it is essential that fleet leaders are subjected to both clean non-turbulent wind as well as turbulent air flows influenced by the wakes of the other turbines.

Thus, WT1 was selected based on its position on the farm and prevailing wind conditions. As shown in Figure 5.21, WT1 is loaded by a steady flow (for north winds), but for southeast winds (second most frequent direction), it is in the wake of turbine WT5. Figure 5.21b also represents the wind directions for which WT1 is in the wake of the remaining wind turbines.



(a) (b)

Figure 5.21 – Tocha Wind Farm: (a) Layout of the wind farm and identification of the fleet leader and its wake directions; (c) Characterization of the wind conditions.

The orography of the farm implantation area is also a criterion to take into account when selecting the fleet leader. Terrain complexity can lead to different loading contributions between the turbines and, consequently, different structural behaviour. Due the location of this farm in a coastal area with very soft orography, this criterion is not relevant at Tocha Wind Farm. However, this premise will be addressed and justified later in this work.

5.6.3 Damage Capture Matrix Construction

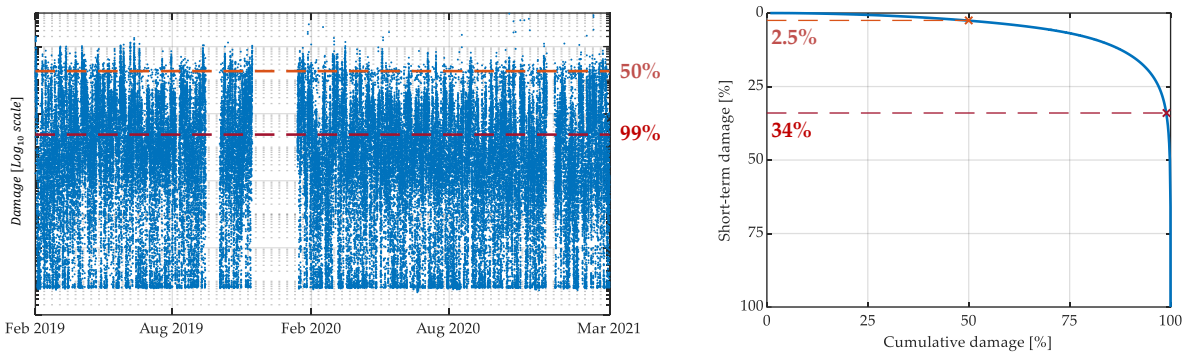
The damage capture matrix is a key element in the extrapolation process. For a correct estimate of the fatigue damage evolution over the farm's operating time, it is essential that the damage matrix is representative of all turbines and that it realistically relates the damage accumulated in the structure with specific environmental and operating conditions. This first part of the extrapolation method is divided into three steps that are described next.

5.6.3.1 Damage Binning

For the farm wide assessment, the extrapolation of the fatigue results from the fleet leader to the entire wind farm should take into account the differences between performances of each wind turbine. In fact, several parameters can influence damage accumulation in the structure.

The evolution of the 10-min damage over the monitoring period, in the weld connection that is close to the instrumented section, for the FA (fore-aft direction) is presented in Figure 5.22a. As shown, each short-term damage can have a wide range of impact on the total fatigue damage. Figure 5.22b represent

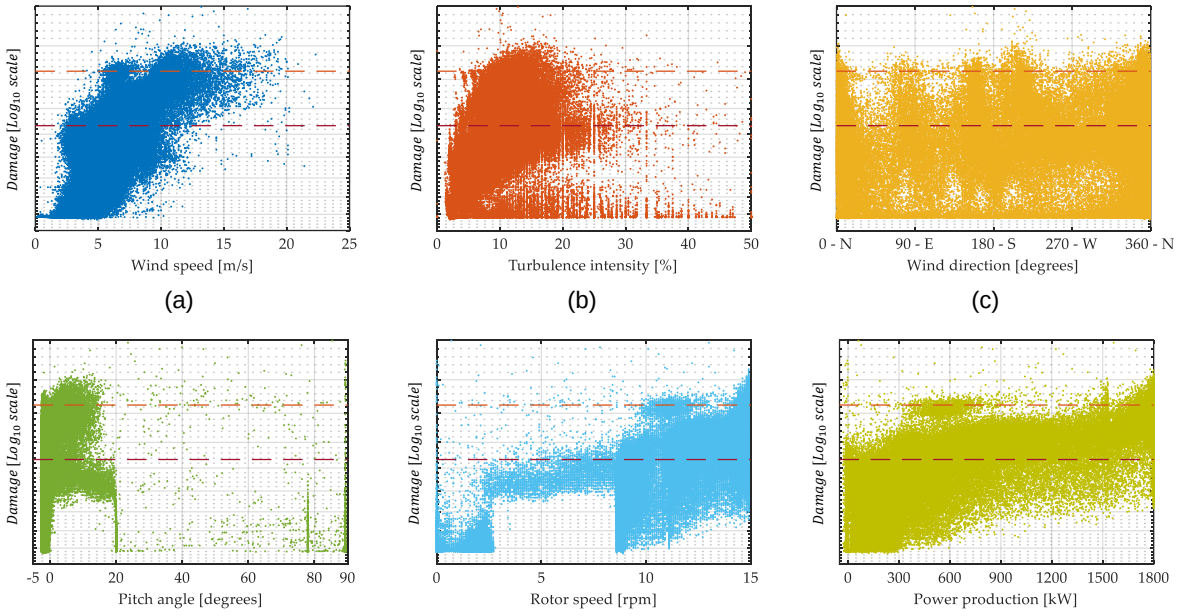
the accumulated damage considering the short-term damage sorted in descending order of associated damage value. These figures allow to conclude that only 2.5% of the short-term damage are responsible for 50% of the total accumulated damage in the monitoring period (the points above the orange dashed line) whereas 99% of the total cumulated damage is caused by 34% of the monitoring period (red dashed line).



(a) (b)

Figure 5.22 – Short-term damage for FA direction: (a) Time evolution over the monitoring period; (b) Cumulative damage distribution.

In Figure 5.23, the 10-min damage for the FA direction is represented as a function of the environmental parameters (average wind speed, turbulence intensity and wind direction) and operational parameters (pitch angle, rotor speed and power output). The points above the orange and red dashed lines represent, respectively, the 50% and 99% of the accumulated damage over de monitoring period.



(a) (b) (c)

(d) (e) (f)

Figure 5.23 – Short-term damage for FA direction as a function of: (a) Wind speed; (b) Turbulence intensity; (c) Wind direction; (d) Pitch angle; (e) Rotor speed; (f) Power output.

Effectively, Figure 5.23a shows that wind speed plays a relevant role in the fatigue life progression of wind turbines. The time series associated with higher wind speeds represent the most significant impact on fatigue damage. Almost 50% of the damage occurs exclusively for wind speed above 10 m/s (when

the blades pitch control is active). There is also greater damage associated with increasing turbulence intensity. In the plot with the wind direction, it is possible to identify orientations with greater damage, which are associated with the main wind directions and wake interactions with the remaining turbines (further discussed in the next sections).

Figure 5.16d indicates that the damage is higher for blade pitch angle values between 3° and 20° which are typical pitch values for wind speeds above the turbine rated speed (when the pitch control is active). The points close to 90° and above the orange dashed line indicates storms (parked conditions and extreme wind speed). On the other hand, shutdowns are associated with the few points above the orange dashed line and pitch higher than 20°. Finally, rotor speed and power production plots lead to similar conclusions. There is a direct relationship between these parameters and the short-term damage.

These results prove the influence of environmental and operational parameters on damage accumulation. In order to link short-term fatigue damage with the specific operating conditions of the wind turbine, the 10-min damage were clustered into six different load cases:

- Normal power production ($WS < V_{rated} = 12\ m/s$);
- Normal power production ($WS \geq V_{rated}$);
- Power production with fault;
- Start/Stop;
- Parked or idling;
- Shutdown ($WS > V_{out}$).

The inputs of this clustering method are environmental parameters (wind speed and turbulence intensity) and operational parameters (rotor speed, power output and pitch angle) provided by the SCADA system. To take into account the influence of pitch angle and consider out-of-range production, as power production with fault, the power production was divided into three load cases. The clustering method makes a first scan on the SCADA data to identify all the 10-min that do not generate power, and a second one to classify power production situations. The measured data was coupled with operational and environmental data in order to consider the variations of these parameters for a safe and reliable estimation of the service duration of the wind turbine tower. Figure 5.24 summarize the individual effect of each load case on the accumulated fatigue damage at the tower section under analysis as a function of the wind speed.

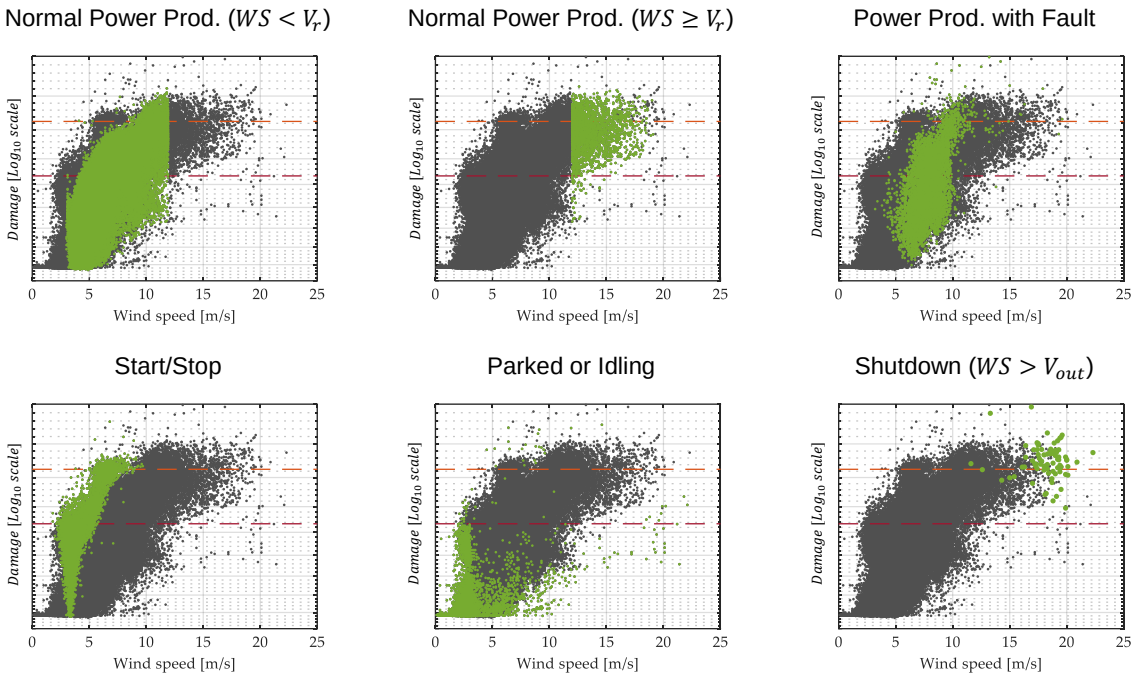


Figure 5.24 – Short-term damage for FA direction as a function of the wind speed for the six load cases.

Figure 5.25 represents for each load case the contribution to the total accumulated damage, the relative damage (calculated as the ratio of associated damage and a percentage of the associated operating time) and percentage of operating time over the monitoring period. As shown in the figure, an important percentage of damage occurs during power production. The wind turbine produced energy in 72% of the total monitoring time, which is associated with 85% of the total accumulated damage.

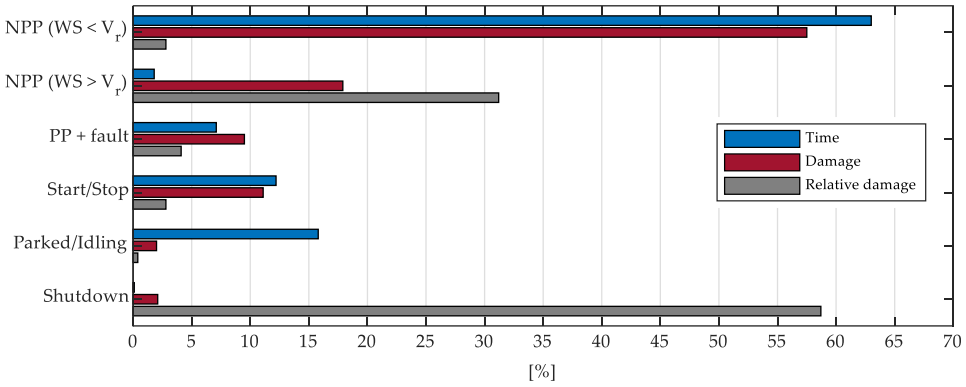


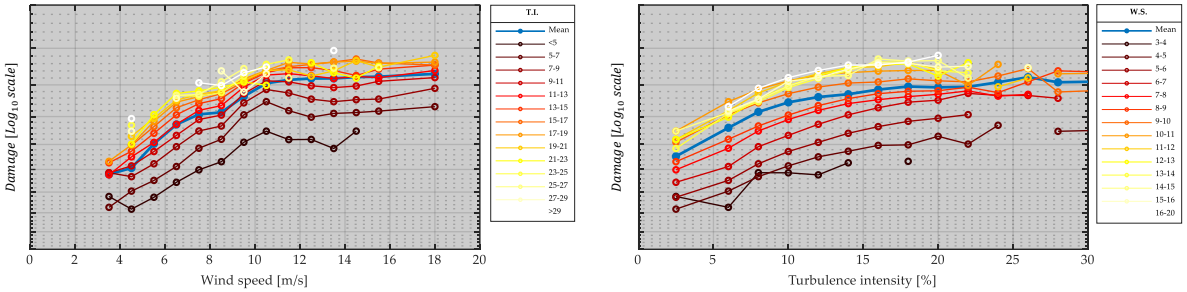
Figure 5.25 – Accumulated and relative damage and total time for different load cases.

It is important to highlight that shutdowns and normal production having the pitch control system activated (wind speed above 12 m/s) are the most aggressive operating conditions, with higher relative damage. On the other hand, parked and idling load cases have a minimal impact on fatigue damage.

In the following analysis, only the short-term damage classified as power production (10-min time intervals during which the turbine produced power) are considered, as these represent the highest percentage of damage. The remaining loading categories, given their specificity, will be analysed in future works.

At this point, it is important to define which parameters are of interest to bin the damage data. Based on a similar approach described in IEC 61400-13 for power production load cases, the calculated short-term damage are classified according to the wind speed and turbulence intensity. The operational parameters are not considered as they are conditioned by the environmental parameters through the turbine control mechanisms.

The influence of wind speed and turbulence intensity on accumulated damage is shown in Figure 5.26. This damage is calculated along the nacelle direction (FA direction). A clear trend is visible as the fatigue damage increases for increasing levels of wind speed and the turbulence intensity.



(a) (b)

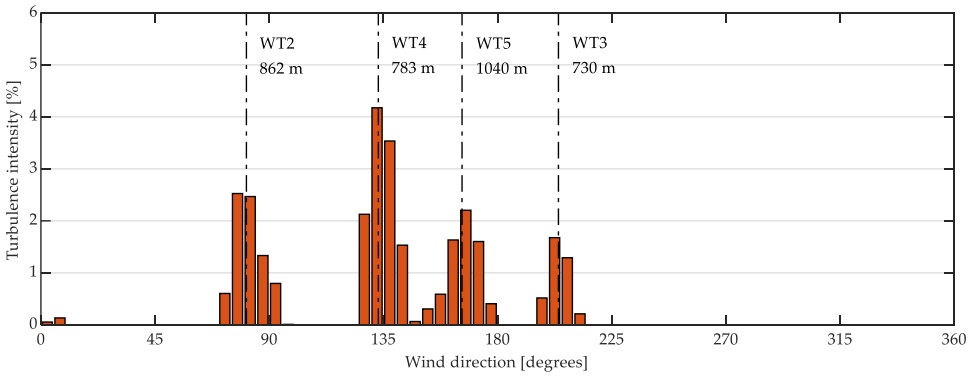
Figure 5.26 – Average 10-min damage for power production, binned based on: (a) Wind speed; (b) Turbulence intensity.

Finally, it is important to take into account the influence of neighbouring wind turbines wakes on the 10-min damage calculated for the fleet leader. In fact, in the foundation fatigue assessment of an offshore wind turbine (monopile), Weijtens obtained DEL (damage equivalent load) values twice as high when the instrumented wind turbine is behind other turbines, compared to unperturbed air conditions (Weijtens et al., 2016).

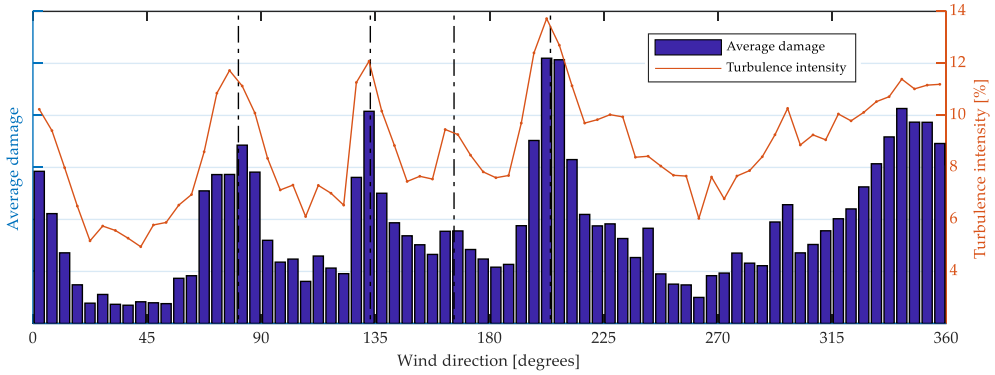
In order to evaluate the influence of the neighbouring turbines wakes on the accumulated damage in WT1, Figure 5.27a shows the difference between the turbulence intensity at WT1 and the average turbulence intensity in the five turbines of the farm, as a function of the wind direction. The distributions were calculated considering the 10-min average values provided by SCADA data between 2012 and 2021. Only the 10-min intervals in which all turbines are in production were considered. The figure also identifies the distances between the turbines and the wind directions for which WT1 is behind the other turbines (see Figure 5.21).

Of particular interest are the peaks where the difference in turbulence intensity is greater. These wind sectors match very well with the wind direction for which WT1 is behind the other turbines.

Since 10 minutes average are used, in this analysis the time interval that the air mass takes to travel between the turbine rotors was neglected. This simplification is valid considering the small dimensions of the farm.



(a)



(b)

Figure 5.27 – Turbulence intensity and average damage for different wind sectors: (a) Difference between the turbulence intensity measured at WT1 and the average turbulence intensity in the five turbines of the farm; (b) Average damage and turbulence intensity at WT1 for wind speed bin of 7-9 m/s.

In order to associate the accumulated damage with the position of the wakes identified above, Figure 5.27b represents, for WT1, the variation of average damage and turbulence intensity for different wind sectors. In order to reduce the influence of wind speed in the calculated damage, only wind speeds in the interval 7-9 m/s are considered. There is an excellent correlation between turbulence intensity and average damage. Comparing the damage to the wake orientations, it is curious to see that the average damage is greater when the distance to the fleet leader's rotor is smaller (the maximum average damage occurs when WT1 is behind WT3 and is minimal when it is behind WT5).

It is also possible to identify a second orientation for which the average damage is considerably high, which corresponds to the main wind direction at the site (Figure 5.21b).

Based on these results, two wind sectors were defined. The first sector corresponds to the wind direction for which the turbine does not receive turbulent wind and the second sector contains the angles for which the turbine is behind the other turbines. For each sector, the respective damage capture matrices were calculated and compared. The differences between the matrices are minimal. The effect of the wakes seems to be reasonably reproduced by the increased turbulence. Thus, in the remaining analyses, the division of the wind direction into sectors will not be considered.

5.6.3.2 Bin Reduction

The final damage matrix typically used in the extrapolation methods is composed of a single representative damage value in each bin. This damage value represents the damage accumulated by the wind turbine in service in these environmental conditions during a specific time interval (in this case 10-min). The metric usually recommended is the mean value of damage measurements in each bin. If conservative approximations are needed other statistical metrics can be used, as the 75th and 90th percentile. On the other hand, if the quality of the measurements data are limited (bins with limited number of 10-min time series) the mean values tend to underestimate the real damage, as these rare events are not sufficiently covered. In these cases, high percentiles should be applied to be conservative (Hübler et al., 2018).

In this work, considering the high number of available records, a normal distribution is fitted to the damage indexes included in each bin. In this way, for each 10-min time series, a damage value and its probability distribution are picked from the damage matrix bin according to the wind speed and turbulence intensity.

In order to ensure the good representativeness of the damage matrix, it is important to analyse the probabilistic distributions of the damage within each bin. Thus, the damage histograms for two different environmental combinations are present in Figure 5.28. Despite some differences, a normal distribution can be fitted to the observations of both matrix bins, since these contain a sufficient amount of recorded data.

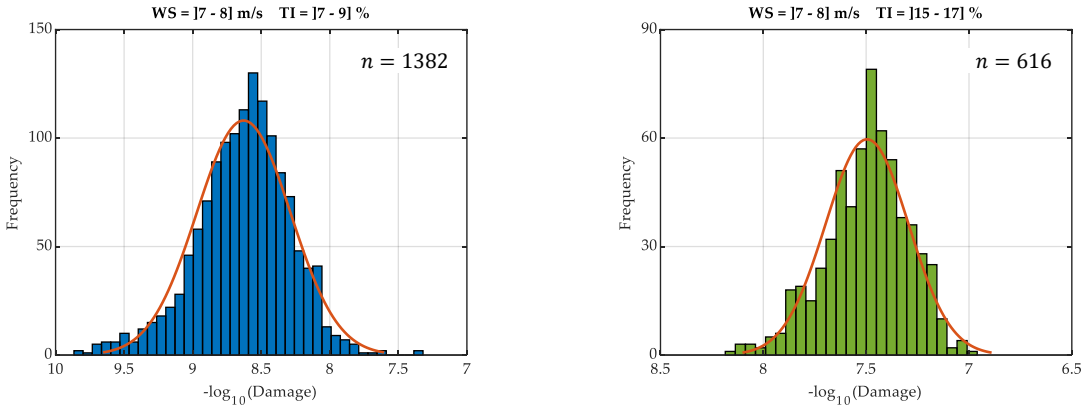


Figure 5.28 – Damage distribution within two wind speed and turbulence intensity bins (histogram) fitted with a normal distribution (orange curve).

Note that for an accurate probabilistic distribution of the damage within each bin it is important to have a sufficiently large amount of data. However, as shown in Figure 5.30 (which will be further discussed later), the amount of available damage data is limited for some bins associated with higher wind speeds. Consequently, fitted probabilistic functions are quite uncertain and the damage metrics can lead to biased extrapolated damage calculations.

To overcome this limitation, the statistical bootstrapping resample method (Efron, 1979) is proposed in (Nymfa Noppe et al., 2020). The advantages of bootstrapping are that it is a straightforward way to derive the estimates of a probabilistic distribution (standard errors, confidence intervals and mean) based on limited known samples. As an example, bootstrapping was already used to analyse limited wind data in (Gass et al., 2011).

In this case, bootstrapping can be used to estimate the unknown empirical damage distribution in each bin based on available damage values. Bootstrapping involves drawing a series of random samples from

the available damage values many times, with replacement (the same measurement can be picked more than once). The average damage is then calculated for each of the bootstrap samples. The resulting distribution of the calculated values then provides an estimate of the sampling distribution of the average damage for that bin.

As an example, this procedure is repeated $N_b = 20000$ times for four bins, with 6, 16, 20 and 39 short-term damage values (Figure 5.30). The comparison of damage value distributions before (orange dashed curve) and after (orange curve) applying the bootstrapping method is shown in Figure 5.29.

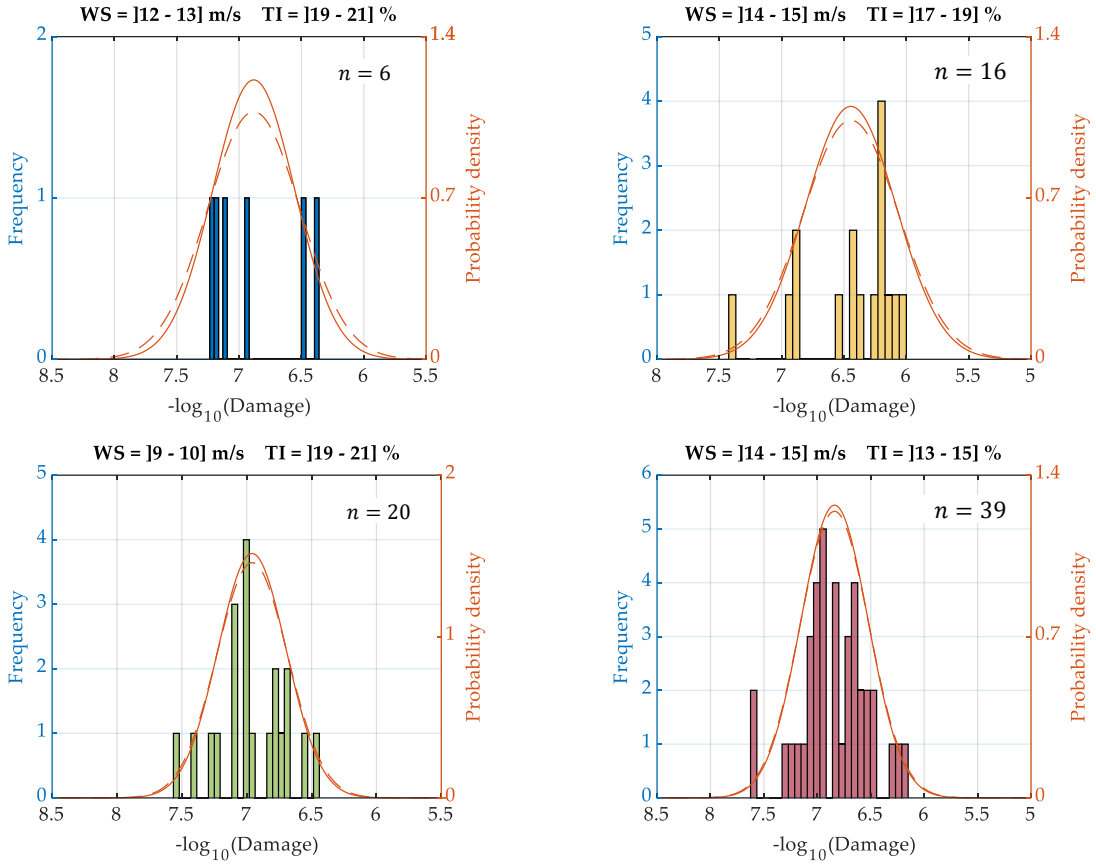


Figure 5.29 – Damage distribution within four wind speed and turbulence intensity bins (histogram) fitted with a normal distribution before (orange dashed distribution) and after (orange distribution) applying bootstrapping.

As shown in the figures, the probability distributions became similar to each other as the number of observations in each bin increases. It is essential to ensure that the mean damage value is the same before and after applying the bootstrapping method.

5.6.3.3 Fill up Empty Bins

As already explained, the extrapolation method presented here assumes that the monitored period is representative of the loading scenarios for the entire service life of the wind turbine. However, the damage capture matrix is composed by the combination of environmental parameters and it is possible, and very likely, that some of these combinations are rare or do not occur during the measurement period. Figure 5.30 shows the number of 10 minutes time series recorded for each combination of wind speed and turbulence intensity bin of the damage capture matrix.

TI [%]	WS [m/s] 3 4	4 5	5 6	6 7	7 8	8 9	9 10	10 11	11 12	12 13	13 14	14 15	15 16	16 20	
0 5	6	1540	1452	1916	1204	1135	800	435	126	33	2	3			8652
5 7	1	845	1409	997	1372	801	754	399	176	78	44	21	15	23	6935
7 9	6	758	1511	1468	1382	1347	1262	677	333	162	83	44	41	34	9108
9 11	7	640	1636	1648	1777	1682	1149	733	383	212	123	89	44	59	10182
11 13	2	479	1785	1780	1793	1195	699	555	301	200	132	81	42	51	9095
13 15	1	210	1249	1506	1111	659	357	225	168	126	69	39	31	33	5784
15 17		64	603	591	616	196	123	80	86	74	47	25	17	13	2535
17 19	1	17	124	256	187	74	39	34	25	19	13	16	9	5	819
19 21		7	28	71	51	34	20	8	13	6	2	4	3	1	248
21 23		3	5	21	24	5	5	2		2	3	1	2		73
23 25		2		4	4	4	5	3	1						23
25 27				2	2	4	2		1		2		1		14
27 29		1		1		1	2	2							7
> 29		2			3	2	4	2			1				14
	24	4568	9802	10261	9526	7139	5221	3155	1613	912	521	323	205	219	

Figure 5.30 – Matrix with the number of recorded 10 minutes time series during power production in the monitoring period.

As shown in the figure, most of the recorded time series occur for winds below the rated wind speed (12 m/s) and for turbulence intensities below 17%. As expected, despite the long monitoring period (two years in this work), some of bins remain empty. On the other hand, some bins contain a reduced number of records, lower than recommended in IEC 61400-13.

Thus, two alternatives can be considered: (1) disregard the empty bins in the fatigue damage extrapolation method or (2) adopt a well-justified method to fill the empty bins. As might be expected, the first method leads to an underestimation of the extrapolated damage. Still, the empty bins during the monitoring period correspond to environmental conditions with a reduced probability of occurrence during the turbine lifetime. Anyway, these bins should not be neglected, as these are commonly associated with higher damage values (higher wind speeds and turbulence intensity). But, fill up the empty bins will increase the uncertainty of the extrapolated damage. Considering the pros and cons, option (2) was chosen in this work.

The empty bins should be filled with a well-considered value. In that sense, depending on the available information, several methods can be followed. This can be based on load case tables provided by design documents. However, this information is not always available and may be difficult to access. Furthermore, simulations carried out in the design phase are usually too conservative. Alternatively, each empty bin can be filled with the maximum value found in the neighbouring bins. Despite being a very simple method, it proved to be acceptable in the study reported in (Nymfa Noppe et al., 2020). It should be noted that, using the highest damage value to fill empty bins does not always lead to conservative results. Considering that the monitoring period is limited, it is very likely that environmental conditions will occur that lead to higher damage values. In a third possibility, the empty bins can be filled considering a damage capture matrix obtained from numerical simulations. In this approach, it is important to ensure that numerically estimated damage matrix has damage values equivalent to those obtained with experimental data for the already filled bins, in order to guarantee correct filling of the empty bins of the experimental damage matrix. This is not easy to achieve.

In this work, an different strategy was followed. The empty bins were filled with an extrapolation method based on the measured damage values. For this purpose, two alternative methods were tested. First, a three-dimensional surface was fitted to the damage, assuming the fatigue damage (D) is a function of the wind speed (WS) and turbulence intensity (TI) and using quadratic terms:

$$\langle D_{i,j} \rangle = p_1 + p_2 \cdot WS_i + p_3 \cdot TI_j + p_4 \cdot WS_i^2 + p_5 \cdot WS_i \cdot TI_j + p_6 \cdot TI_j^2 \quad (5.6)$$

with:

$\langle D_{i,j} \rangle$	Estimated damage for bin i,j
p_k	Parameters obtained by fitting the available data ($k = \{1, 2, \dots, 6\}$)
WS_i	Wind speed for i-th wind speed bin ($i = \{1, 2, \dots, 14\}$)
TI_j	Turbulence intensity for j-th turbulence intensity bin ($j = \{1, 2, \dots, 14\}$)

Assuming Gaussian errors propagation, the uncertainty in the estimated fatigue damage (σ_D) is given by:

$$\sigma_D^2 = \sum_k^{N=6} \left(\frac{\partial D}{\partial p_k} \sigma_{p_k} \right)^2 = \sigma_1^2 + \sigma_2^2 \cdot WS_i^2 + \sigma_3^2 \cdot TI_j^2 + \sigma_4^2 \cdot WS_i^4 + \sigma_5^2 \cdot WS_i^2 \cdot TI_j^2 + \sigma_6^2 \cdot TI_j^4 \quad (5.7)$$

with:

σ_k	Uncertainty associated with the parameters p_k

As a second approach, for each wind speed bin, a function was fitted to describe the damage variation with the turbulence intensity. After testing several alternatives for the function to be used, it was concluded that good fittings were obtained with a $log10$ function. Therefore, it is assumed that the fatigue damage (D_i), for a given wind speed bin, is given by:

$$\langle D_i \rangle = \langle a_i \rangle \cdot \log_{10}(TI_j) + \langle b_i \rangle \quad (5.8)$$

with:

$\langle a_i \rangle$, $\langle b_i \rangle$	Constants obtained by fitting the available data

The estimated value statistical properties, assuming Gaussian errors propagation, will be given as:

$$\sigma_{D_i}^2 = \left(\frac{\partial D}{\partial a} \sigma_{a_i} \right)^2 + \left(\frac{\partial D}{\partial b} \sigma_{b_i} \right)^2 = \left[\sigma_{a_i} \cdot \log_{10}(TI_j) \right]^2 + \sigma_{b_i}^2 \quad (5.9)$$

with:

σ_{a_i}, σ_{b_i}	Uncertainty associated with the parameter a_i and b_i

In both methods, the fitting was based on the experimental results of bins with more than 20 samples. The minimum short-term damage recorded in each bin was selected based on the recommendations provided by IEC 61400-13 for power production measurements, corroborated by the analysis of the probability distribution presented in Section 5.6.3.2.

Based on this methodology, a total of 96 bins were filled (50% of the damage capture matrix). The proposed extrapolation method to fill up the empty bins of the damage capture matrix is schematically represented in the Figure 5.31.

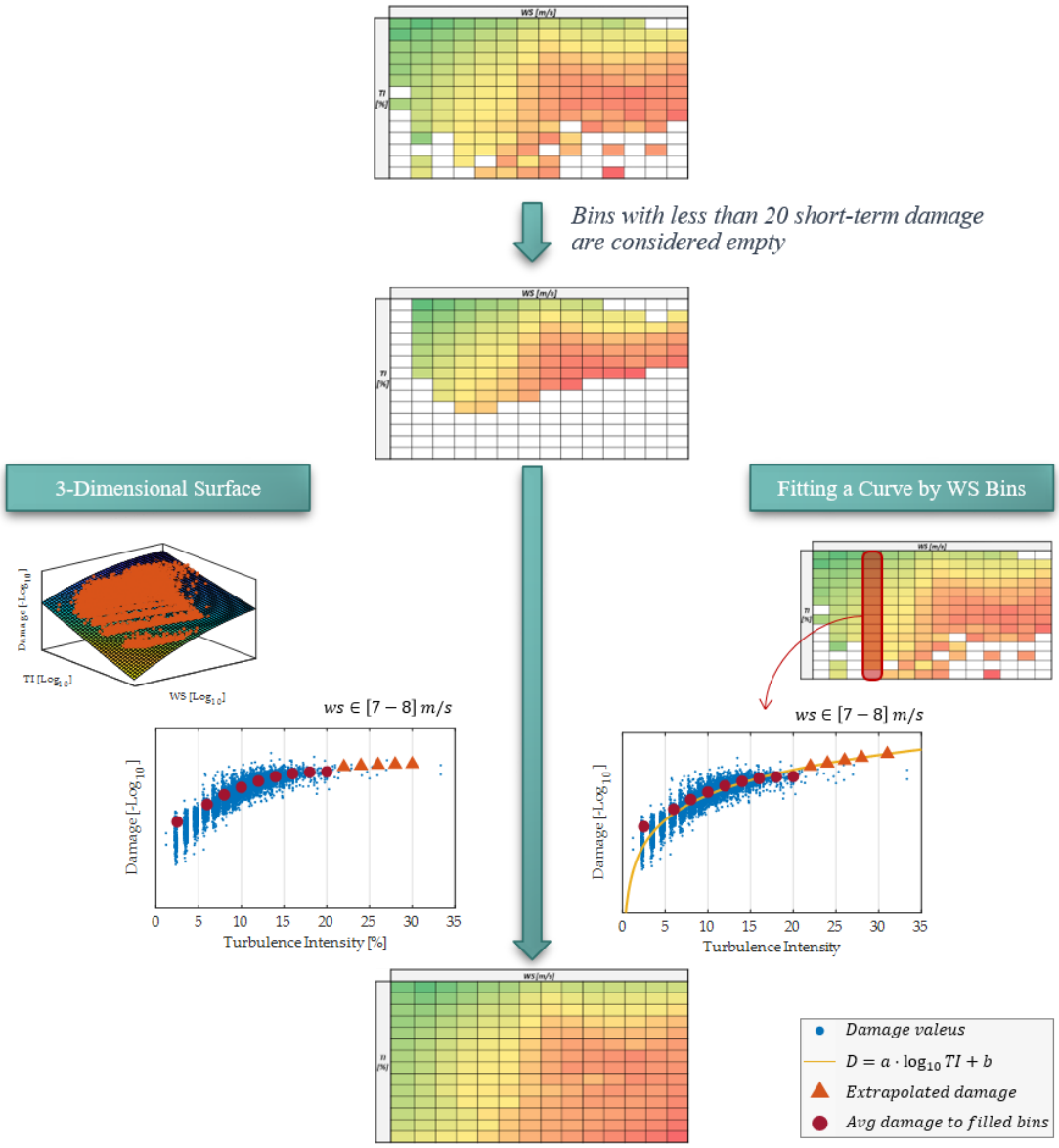


Figure 5.31 – Two alternative approaches followed to fill up the empty bins of the capture damage matrix (red rectangles in the matrices represents higher damage).

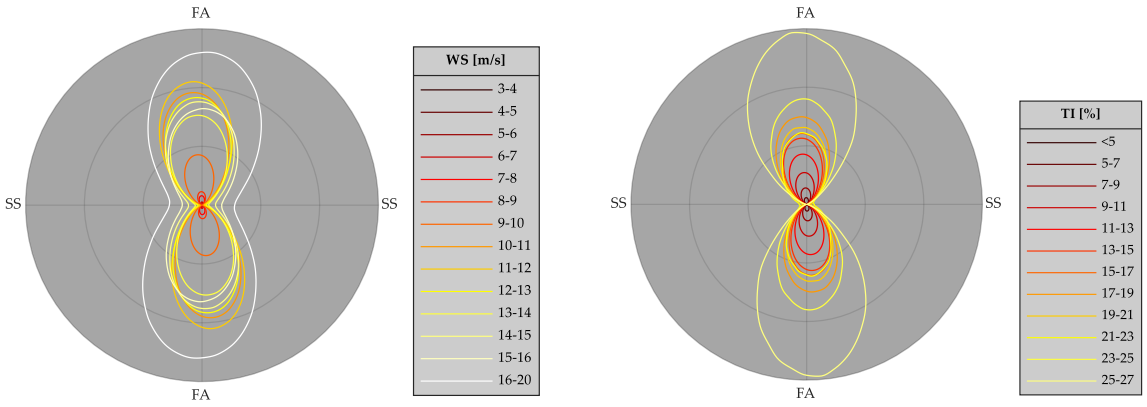
The first method is more robust because it allows considering, in the same equation, the real values of wind speed and turbulence intensity associated with each measured fatigue value. In this way, it is possible to capture simultaneously the variation of damage as a function of wind speed and turbulence intensity. However, the second method is more flexible as more parameters are adjusted.

It should be noted that the two plots shown in the previous figure (damage value as a function of turbulence intensity) allow to verify that the extrapolated average damage seems to be overestimated for the higher turbulence intensity values in both methods (safety side). Extrapolated damage values are highest for the second method. In the next section, the influence on the total accumulated damage will be evaluated.

At this point, a damage capture matrix is obtained for the fleet leader and the first step of the extrapolation method, outlined in Figure 5.20, is completed. The damage matrix obtained is schematically represented in Figure 5.31. The colour of the cells of the matrix is a function of the short-term average damage (negative logarithm base 10), for each wind speed and turbulence intensity bins, calculated along the nacelle direction. It is clear that fatigue damage is directly related to the wind speed and the turbulence intensity.

The damage presented at the previous capture matrix is computed along the nacelle direction, independently of the wind orientation. However, to not overestimate the damage at a specific location of the cross-section and take into account the variation of the wind direction, the damage matrix was calculated along the entire perimeter of the cross-section. For each 10-min period, the cross-section was discretised into segments with 1° of length. For each point, the variation of the normal stress and the respective load cycles were determined using the experimentally determined bending moment and the fatigue damage was calculated.

Figure 5.32a shows the average damage distribution along the cross-section, considering the influence of wind speed for a turbulence intensity between 11% and 13%, and Figure 5.32b shows the influence of the turbulence intensity for wind speeds between 7 and 8 m/s.



(a) (b)

Figure 5.32 – Distribution of the damage over the tower cross-section as a function of: (a) Wind speed for $TI \in [11 - 13[$ %; (b) Turbulence intensity for $WS \in [9 - 10[\ m/s$.

As shown in the figures, the maximum damage does not always occurs in the nacelle direction. In fact, due to the lateral vibration of the tower, maximum damage occurs with a small deviation from the FA direction. On the other hand, the minimum damage is perpendicular to the nacelle direction and for low wind speeds, it is close to zero.

Finally, due to the lack of experimental data, the damage variation along the cross-section of the tower is not considered for bins classified as empty and filled according to the described methodology. The estimated damage for the empty bins is only extrapolated for the nacelle orientation and considered constant throughout the entire section. In this way, the final damage obtained with the fleet leader concept will be overestimated throughout the section, except for the critical point where the damage is maximum.

5.6.4 DAMAGE EXTRAPOLATION IN THE INSTRUMENTED WIND TURBINE

The final goal is to estimate the damage at one wind turbine of the farm, instrumented or non-instrumented, based on damage measurements in the fleet leader and knowing the environmental and operational conditions of the turbine in consideration.

To find the estimated damage for any turbine (D^{ET}), each term of the damage capture matrix, as calculated for the fleet leader (D_i^{FL}), is multiplied by the bin probability of occurrence of the extrapolated turbine (P_i^{ET}). By summing the result, the extrapolated damage is obtained, as shown in the equation:

$$D^{ET} = \sum_{i \in bins} D_i^{FL} \cdot P_i^{ET} \tag{5.10}$$

As describe in Figure 5.20, the bin probabilities of occurrence can be obtained from design documents or from in situ measured data, such as SCADA data. The second approach allows accurately represent the conditions at the particular site of the wind turbine. However, this approach is only recommended if sufficient data is available, at least one year.

In this work, the SCADA data is available from the beginning of farm production, for all wind turbines. The number of occurrences of each bin for the extrapolated wind turbines are obtained binning the available SCADA data for each turbine in the same way the damage data of the fleet leader was binned.

The next sub-sections are focused on the fatigue damage extrapolation results for the instrumented wind turbine, whereas Section 5.6.5 is dedicated to the extrapolation of results to the remaining wind turbines of the farm.

5.6.4.1 Damage Capture Matrix Validation

The first analysis is performed during the two years monitoring period and using both monitoring and SCADA data. In Figure 5.33, the damage accumulated in the instrumented cross-section of the tower over the monitoring period is compared with the damage estimated with the combination of the capture matrix and the SCADA data for the same period. The estimated damage is based on the three alternatives of the damage capture matrix, taking into account the method used to fill the empty bins and the ones assumed empty due to the low number of observations:

- D_{3D}: Extrapolation based on a 3-dimensional surface;
- D_{Log}: Extrapolation based on logarithmic function;
- D_{Max}: Extrapolation with the maximum value found in the neighboring bins.

It is still considered a fourth alternative ($D_{Bootstrp}$) where the damage distribution of the bins with less than 20 short-term damage is obtained from the statistical bootstrapping resample method. This is just a control alternative as it does not allow filling empty bins and perform extrapolation of results to non-observed conditions.

The shaded area in the figure represents the uncertainty of the estimated cumulative damage (95% confidence interval).

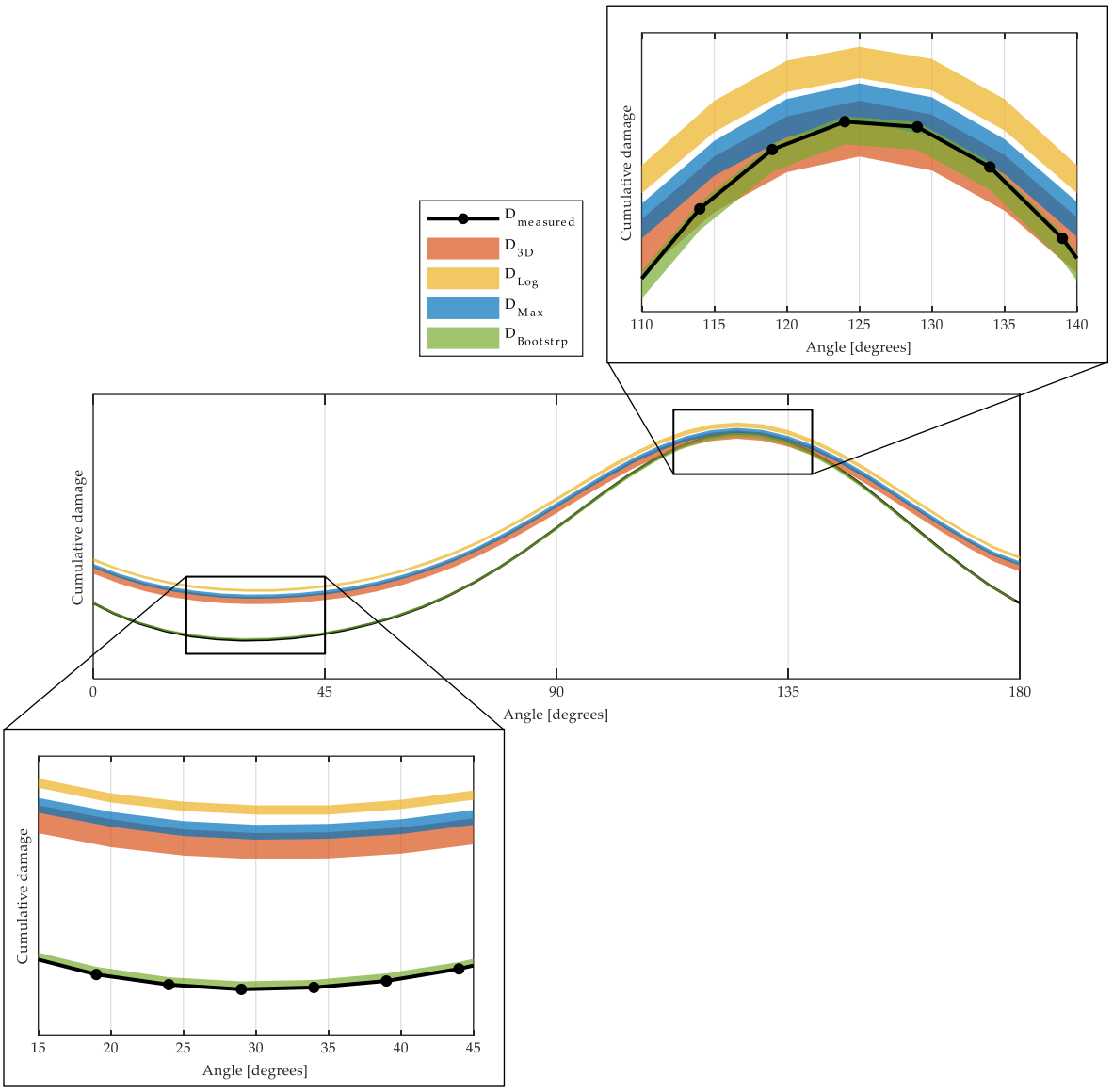


Figure 5.33 – Comparison of real and extrapolated fatigue damage over the instrumented tower cross-section considering the monitoring period.

Looking closer to the results, one can observe, as expected, a high similarity between damage estimated with the bootstrapping method ($D_{Bootstrp}$) and the measured damage, since the green shading and the black line are very close to each other throughout the entire section.

Observing the critical point of the cross-section, where fatigue damage is maximum, the extrapolation methods allow to obtain extrapolated damage close to the actual measured damage, with differences between the mean value of the extrapolated damage distribution and actual damage (ΔD) below 3% ($\Delta D_{3D} = -0.4\%$, $\Delta D_{Log} = 3.3\%$, $\Delta D_{Max} = 1.0\%$). As mentioned in the previous section, the application of the logarithmic function to fill the damage matrix leads to an overestimation of the mean damage values and, consequently, of the accumulated damage.

It is important to note that, for the section angles where the accumulated fatigue damage is smaller, the estimated damage is overestimated due to the contribution of the empty bins of the damage matrix, which were filled assuming the damage value corresponding to the FA direction, without considering the damage distribution over the section.

In order to quantify the contribution of the empty bins of the damage matrix to the estimated value of the cumulated damage, the damage from the experimentally characterized bins and the extrapolated bins were quantified. The results are shown in the Table 5.2.

Table 5.2 – Cumulative damage obtained from the experimentally characterized and extrapolated bins for the critical angle [%].

Estimated Damage	Experimental bins	Extrapolated bins
D_{3D}	92.3	7.7
D_{Log}	90.0	10.0
D_{Max}	91.4	8.6

Although the number of 10-min time series associated with the capture matrix's empty bins represents only 1% of the total number considered on the extrapolation procedure, the cumulative damage from these bins represents at least 8%. The contribution of these bins should increase with the length of period of time for which the damage is extrapolated.

In a next step, the two-year monitoring period is split into two different periods: Period A based on data from February 2019 to January 2020 and Period B based on data from February 2020 to February 2021. Note that the definition of these models is usually performed considering a period of data large enough to include all the relevant variations of the predictors. In that sense, a period of one year is usually enough to define these models. In this way, the models based on each monitoring period are used to estimate the damage in the other period. The procedure for damage matrices construction, introduced in Section 5.6.3, is applied separately for each period. Only the damage capture matrix in which the empty bins were filled based on 3-dimensional surface is considered (D_{3D}), as it presented better results in the previous analysis.

The results for the critical point of the cross-section under analysis are present in Figure 5.34. The black line represents the actual damage in the monitoring period. The blue and orange line/distribution represents the mean value/uncertainty of the extrapolated damage based on Period A and Period B, respectively.

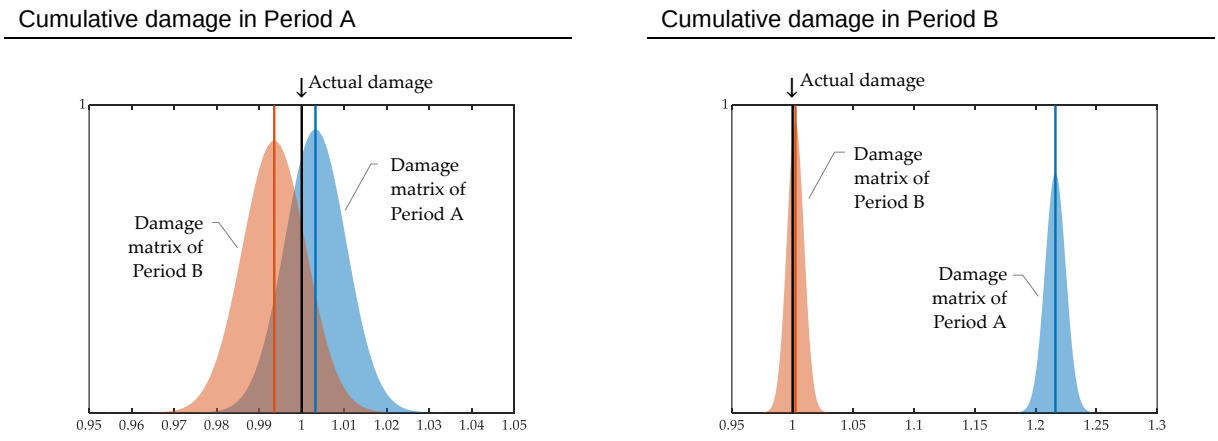


Figure 5.34 – Extrapolated damage at the critical point of the instrumented cross-section for each combination of monitoring and extrapolation periods, normalized to the actual damage measured in the respective monitoring period.

As expected, the results show that the extrapolated damage is very close to the real damage when the monitoring and extrapolation periods are coincident (blue line/distribution for cumulative damage at Period A and orange line/distribution for cumulative damage at Period B).

Considering the real cumulative damage at Period A, the extrapolated damage based on Period B also provided a very good estimation. On the other hand, the extrapolated damage for period B, based on Period A, presents a considerable bias. Still, a conservative value is obtained. The difference between the results obtained based on period A and B is due to the representativeness of the damage matrices obtained with each monitoring period. In fact, during period A there were gaps in the SCADA data recording in the months of September, December and January (Figure 5.22a). Consequently, the number of 10-min datasets available to build the damage matrix corresponding to period A (N_A) is significantly lower than the number of datasets used to build matrix B (N_B): $N_A/N_B = 0.74$. The greater number of bins filled based on the extrapolation process (overestimated as referred to in Section 5.6.3.3) justifies the overestimated accumulated damage in period B based on the data monitored in period A (Figure 5.34).

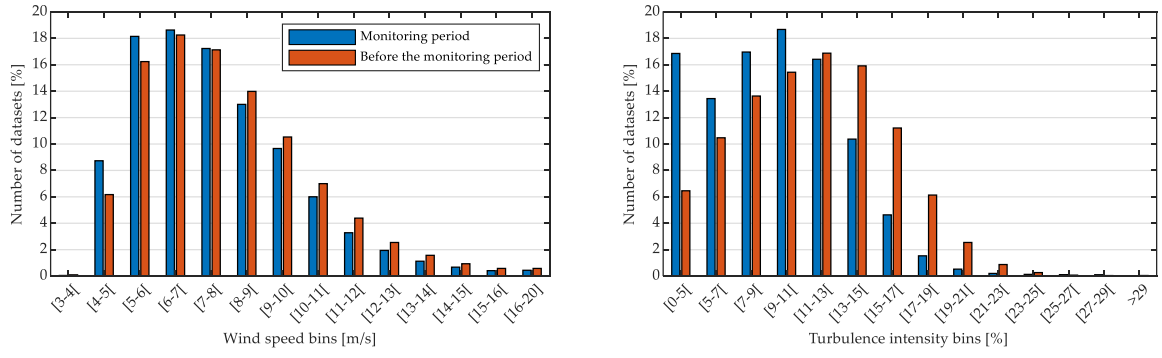
It should be noted that the uncertainties associated with the estimated damage (distributions shown in the figure) only reflect the uncertainty of the measured damage values and of the extrapolation methods to fill the empty bins, which is also based on the uncertainty of the measured damage values. These characterize the uncertain ty of the procedure and not the error with regard to the real value.

In conclusion, it is very important to have a relevant monitoring period covering diverse operating conditions.

5.6.4.2 Total Endured Damage of the Instrumented Wind Turbine

After validating the procedure for extrapolating the damage to non-monitoring periods, it is possible the reconstruction of the total endured damage, based on the two-years monitoring period. SCADA data available for WT1 since January 2013 has been binned according to the procedure presented in Section 5.6.3.1, considering only power production 10-min periods.

In order to check the validity of the extrapolation of the endured damage of WT1, it was investigated whether the monitoring period is representative of the environmental conditions recorded on the wind farm since the beginning of operation. Figure 5.35 compares the distribution of the percentage of 10-min periods, measured before and in the monitoring period, according the turbulence intensity and wind speed bins.



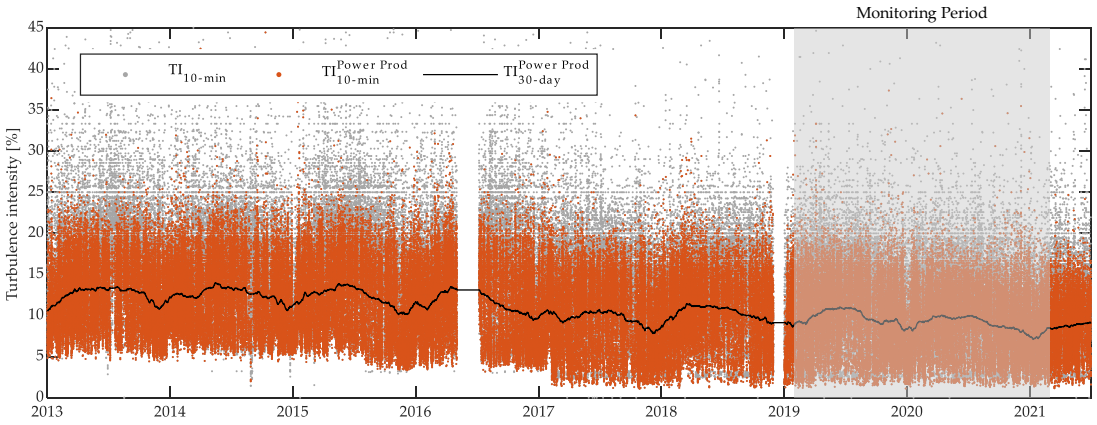
(a) (b)

Figure 5.35 – Distribution of the number of 10-min periods measured by SCADA system at WT1, before and in the monitoring period according the: (a) Wind speed bins; (b) Turbulence intensity bins.

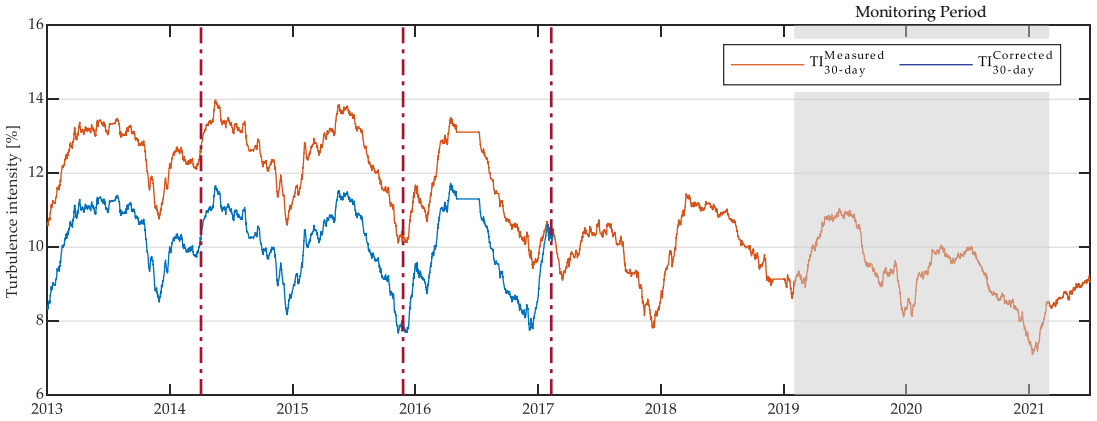
Figure 5.35a demonstrated a similar distribution for the wind speed bins, with slightly higher wind speeds in the non-monitored period. However, for the period prior to the start of the experimental campaign, there is a higher percentage of records for bins associated with higher turbulence intensities, as represented in Figure 5.35b. The differences identified can be justified, by the change in environmental conditions (for example, the decrease in the turbulence of the wind flow due to the reduction of trees in the surroundings of the farm); or by the change the model for calculating the intensity of turbulence using the data measured by the nacelle anemometer. As mentioned in Section 5.6.2, the anemometer situated at the top of the nacelle is subjected to a strong interference of the rotor that is minimized by the application of calibrated transfer functions.

The SCADA data history was evaluated in order to understand the change in turbulence intensity behavior between the two periods. The 10-min average turbulence intensity provided by the wind turbine anemometer until June 2021 is presented in Figure 5.36a. Orange points correspond to 10-min power production time series and the black curve represents the correspondent 30-day moving average. The grey points represent all 10-min average turbulence intensity recorded by the SCADA system and the shaded area identifies the monitoring period.

Based on the information provided by the wind farm owner, it was possible to conclude that the mentioned differences in the turbulence intensity values are mainly due to updates of the wind turbine control software provided by the manufacturer. Since 2013, there have been three software updates that have changed the wind flow turbulence calculation model, identified by the dashed vertical lines in the Figure 5.36b.



(a)



(b)

Figure 5.36 – Turbulence intensity measured at WT1 (Jan-2013 to Jun-2021): (a) Turbulence intensity variation (10-min and 30-day moving average); (b) 30-day moving average of measured and corrected turbulence intensity.

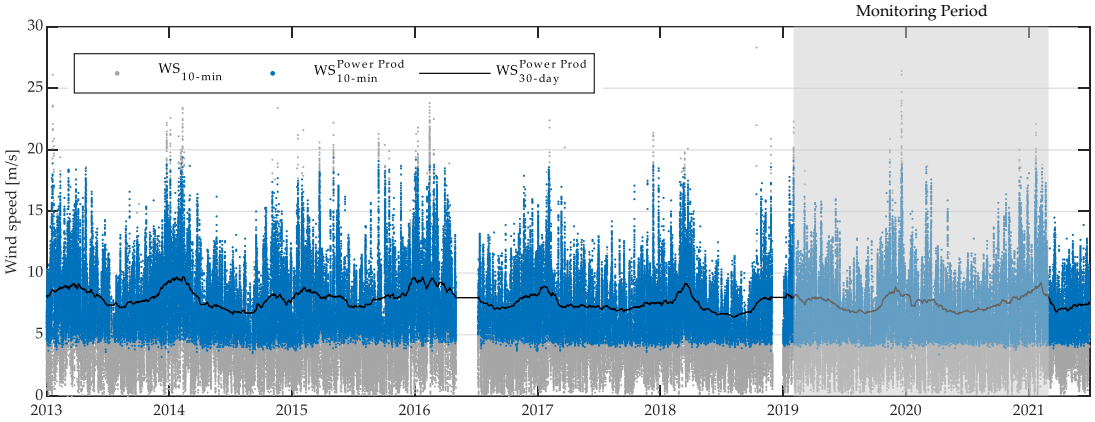
Looking closer to the results, it is possible to correlate the wind turbine software updates with the change in the envelope of points in Figure 5.36a and with the changes in the trend of the respective 30-day moving average (orange line in Figure 5.36b). This precludes the direct use of the SCADA data before the last software update. In fact, this is an important limitation of the caption matrix concept to estimate the damage accumulated in the tower since its installation. Changes to the control software that affect the behavior and operation of the turbine, or that change the evaluation of environmental and operational parameters may invalidate the application of this methodology.

After an exhaustive analysis of all the available information, it was possible to conclude that the updating of the model for calculating the intensity of turbulence is the only obstacle to the application of the concept presented here. In order to circumvent this problem, it was necessary to develop a procedure to correct the turbulence data recorded before January 2017. The procedure developed was based on the annual relationship of the turbulence intensity in the monitoring period (reference period) between the several wind turbines on the farm (explained with more detail in the following section). The relationships obtained were then used to correct the average value and annual dispersion of turbulence in the remaining periods (periods with different software versions). It should be noted that the turbulence intensity values obtained after correction may not accurately represent the real values observed on the farm. This correction only intends to obtain a dataset that allows the application and demonstration of the procedure developed in this work. In this context, it is not very important to have a realistic estimation of the turbulence intensity, but it is crucial to have a variable correlated with the turbulence intensity that is calculated in a consistent way during the full operating life of the wind turbine.

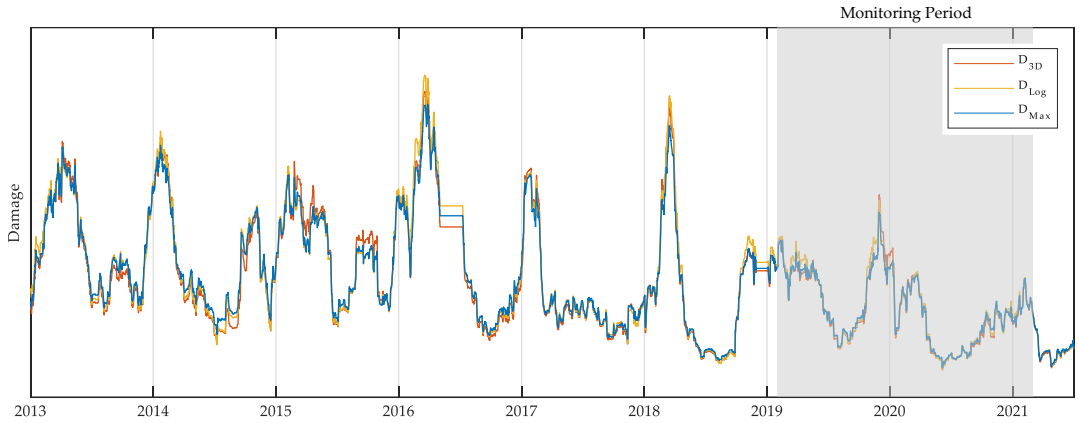
It is important to mention that there is a decreasing trend in the values of the intensity of the turbulence within the monitoring period (without any change on the wind turbine software), which might be explained by a forest fire and subsequent deforestation.

The 10-min average wind speed provided by SCADA system until June 2021 is presented in Figure 5.37a (grey points). The blue points correspond to 10-min power production time series and the black curve is the correspondent 30-day moving average. In contrast to that observed for the turbulence intensity, the wind speed does not appear to be affected by the software updates.

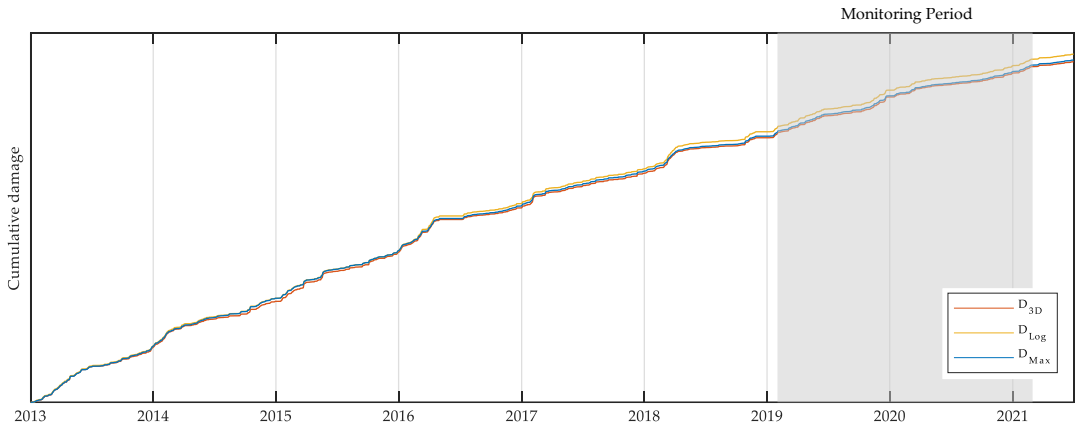
Using the three alternatives of the damage capture matrix (D_{3D}, D_{Log}, and D_{Max}), the 30-day damage moving average is presented in Figure 5.37b for the critical point of the instrumented cross-section. Figure 5.37c presents the accumulated estimated damage based on the SCADA data. More than 300 thousand of 10-min datasets were considered as SCADA data input, taking into account wind speed, turbulence intensity and wind direction.



(a)



(b)



(c)

Figure 5.37 – Reconstructed fatigue damage for the critical angle of the cross-section (May 2012 to June 2021): (a) Wind speed variation (10-min and 30-day average) over the wind turbine lifetime; (b) 10-min damage values and 30-day moving average damage; (c) Cumulative damage.

These figures clearly show the seasonal effects on the endure damage. The recording of events with strong winds on the monitoring period is very important. Within the monitoring period, the windiest months were December 2019 and January 2021, being recorded winds with maximum speeds in accordance with the previous winters.

The estimated damage based on the three types of damage matrix adopted in this work lead to very similar results. As show in Figure 5.38, the difference between the estimated final accumulated damage for the critical point of the cross-section is less than 5%.

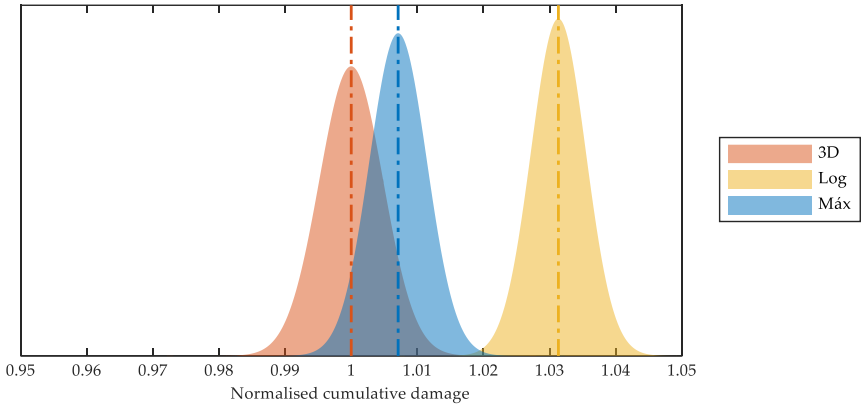


Figure 5.38 – Distribution of the extrapolated endured damage at the critical point of the tower instrumented cross-section based on the three alternatives of the damage capture matrix, normalized to the D_{3D} (the vertical dash lines shows the damage mean values normalized to the D_{3D} mean value).

The weight of extrapolated bins for the final cumulative damage is approximately 11%, similar to the values obtained in Table 5.2. These results demonstrate the good representativeness of the monitoring period for the entire operating life of the structure. On the other hand, it allows validating the correction of the turbulence intensity values, since in this way the environmental conditions are similar before and during the monitoring period. On the other hand, not correcting the turbulence intensity values would lead to a 30% higher cumulative damage for the critical angle of the cross-section, with 17.5% of the total damage coming from extrapolated bins

Finally, in order to assess the impact of increased wind speed and turbulence intensity on the accumulated damage, two scenarios were compared with the original case: increase of 10% of the average wind speed and the turbulence intensity. The original data was modified by artificially increasing the two parameters over the entire period, separately. The cumulative estimated damage for the three scenarios is shown in Figure 5.39 (normalized cumulative damage). Only the damage capture matrix in which the empty bins were filled based on 3-dimensional surface is considered (D_{3D}).

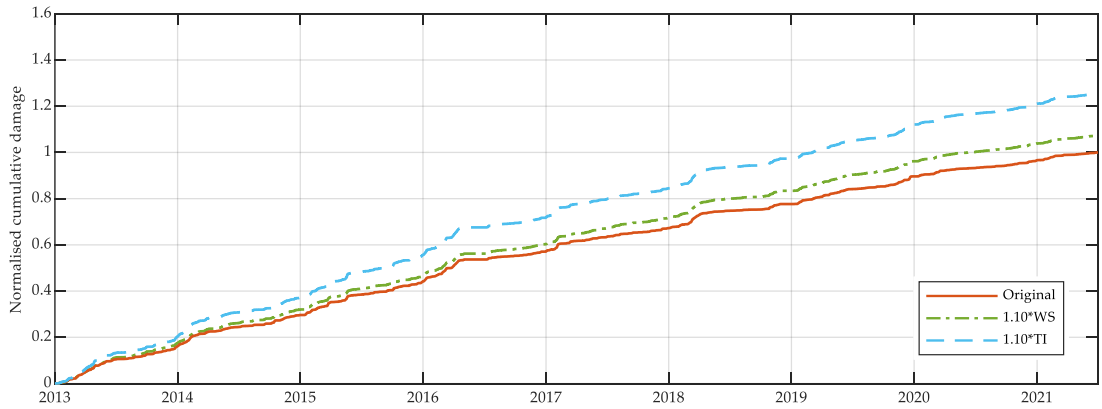


Figure 5.39 – Distribution of the extrapolated endured damage at critical point of the tower cross-section under alternative operating conditions.

With the increase of 10% of the average wind speed, the estimated damage increases 7%. On the other hand, with the increase of 10% of the turbulence intensity, the estimated damage increases 25%. These results demonstrate a greater preponderance of the turbulence intensity in the accumulated damage. These results are especially important for the analysis of wind turbines that are in the wake of other turbines in the farm, so exposed to additional turbulence.

5.6.5 FATIGUE DAMAGE EXTRAPOLATION WITHIN THE FARM

The procedures developed and validated throughout this chapter make it possible to determine the accumulated fatigue damage in an instrumented section of the tower during the monitoring period and, subsequently, the extrapolation of these results to non-instrumented periods. The final step concerns the extrapolation of the fatigue results obtained for the fleet leader to the remaining non-instrumented wind turbines in the same wind farm. As explained, this procedure is based on the assumption that similar wind turbines (same model, controller system and similar loadings) have the same behaviour in the wind farm.

Based on the damage extrapolation method represented in Figure 5.20, the bins occurrences of the damage capture matrix are given by the SCADA data recorded in each wind turbine since 2013. However, as mentioned for WT1 in the previous section, updates to the control software of the wind turbines with impact on the turbulence intensity estimation were identified. Figure 5.40b represents the different software versions of the control for each wind turbine (consequently, different models for calculating the turbulence intensity). Each colour represents a version of the software installed in that period. It is important to mention that since the beginning of the experimental campaign, there were no updates and all turbines operated with the same software version.

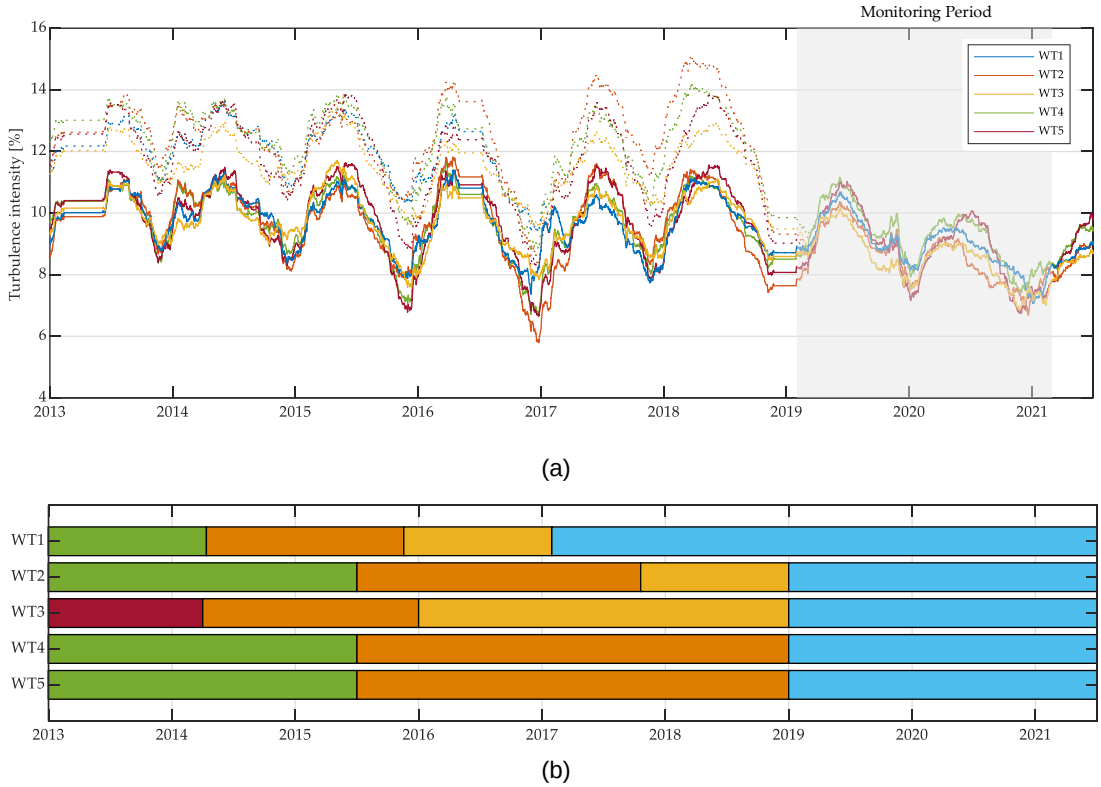


Figure 5.40 – Turbulence intensity correction (Jan-2013 to Jun-2021): (a) 30-day moving average of measured and corrected turbulence intensity for all wind turbines; (b) Control software version of each wind turbine.

The procedure used to correct the turbulence intensity values for WT1 was applied to other wind turbines. Essentially, it is assumed that the relation between annual averages of the turbulence intensity of the five wind turbines is kept over time. As the software update of all turbines was not done simultaneously, with these relations it is possible to undo the changes introduced by each software update. Figure 5.40a compares the 30-day moving average turbulence intensity before (dashed line) and after (solid line) these corrections for all wind turbines on the wind farm. In this figure, only 10-min

average values of SCADA data are considered, in which all wind turbines in the farm are in power production. The results allow to understand the impact of the models used to estimate the intensity of the turbulence. Considering the turbulence intensity data without prior correction would certainly lead to an overestimation of the damage accumulated in the structure.

Before applying the fleet-leader procedure, an analysis of the environmental and operational conditions of each wind turbine in the period from Jan-2013 to Jun-2021 was performed, extending the preliminary wake analysis presented in Section 5.6.3.1. This is based on 10-min average values provided by SCADA system. Figure 5.41 represents the difference between the wind speed measured in WT1 and WT5 and the average wind speed measured in the remaining turbines as a function of the wind sector. Equivalent results for the turbulence intensity are also shown. In order to avoid any differences in environmental conditions during the analysed period due to different removed data points, only 10-min instances where all five turbines have proper data and are in power production are used. In the same figures, the distribution of operating time as a function of wind direction is also represented for each wind turbine (orange histogram). The dashed vertical lines identify the wind directions for which the turbine under analysis is in the wake of the other turbines.

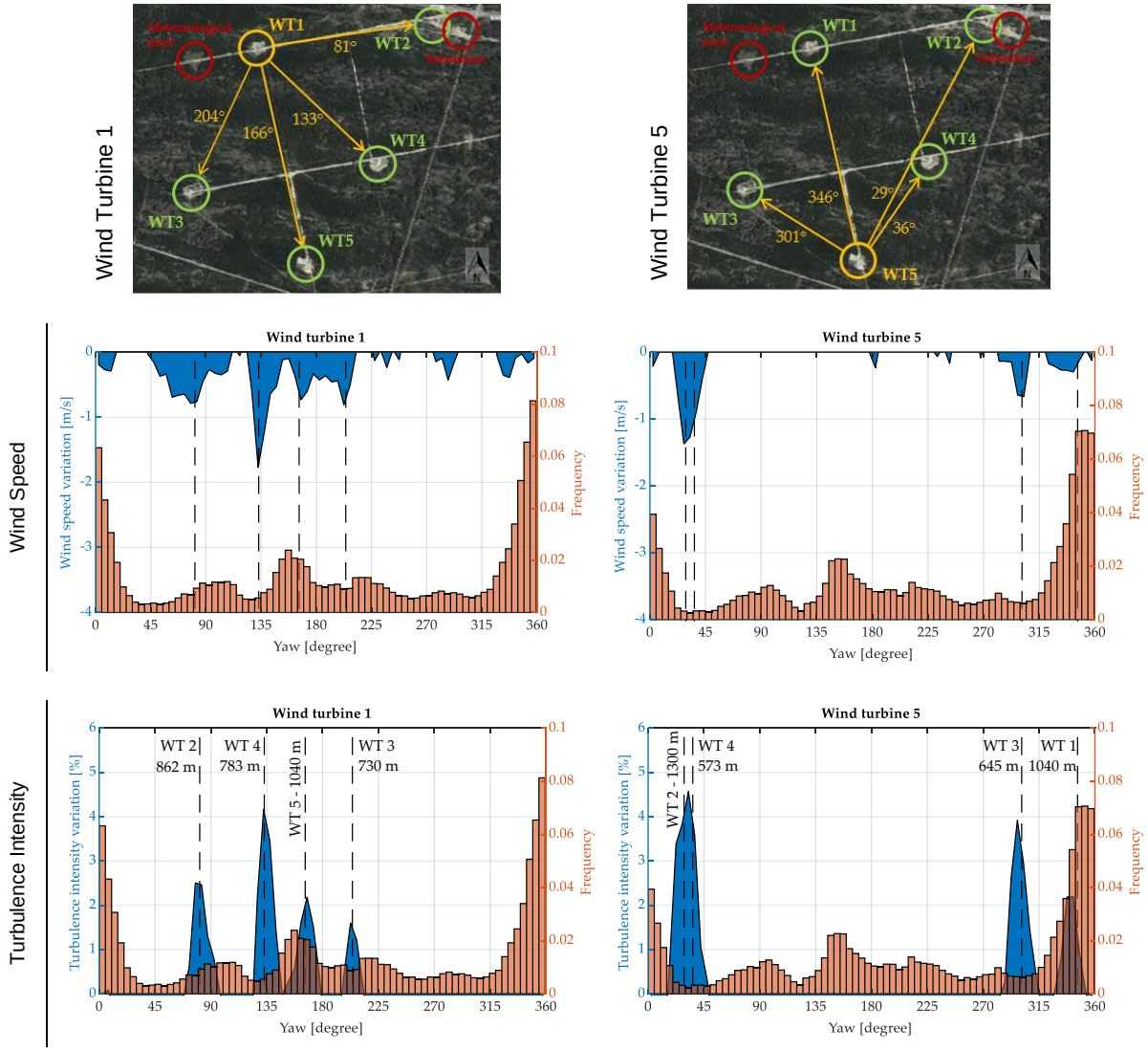


Figure 5.41 – Identification of the wakes and difference between the wind speed/turbulence intensity measured at WT1 and WT5 and the respective average values in the five turbines of the farm, from Jan-2013 to Jun-2021.

As explained for Figure 5.27, in this analysis the time interval that the air mass takes to travel between the turbine rotors was neglected. This simplification is valid considering the use of 10 minutes means and the small dimensions of the farm. Equivalent analyses were performed for the remaining wind turbines of the farm. The results for WT2, WT3 and WT4 are shown in Figure 5.42, where the wakes direction are identified through colours.

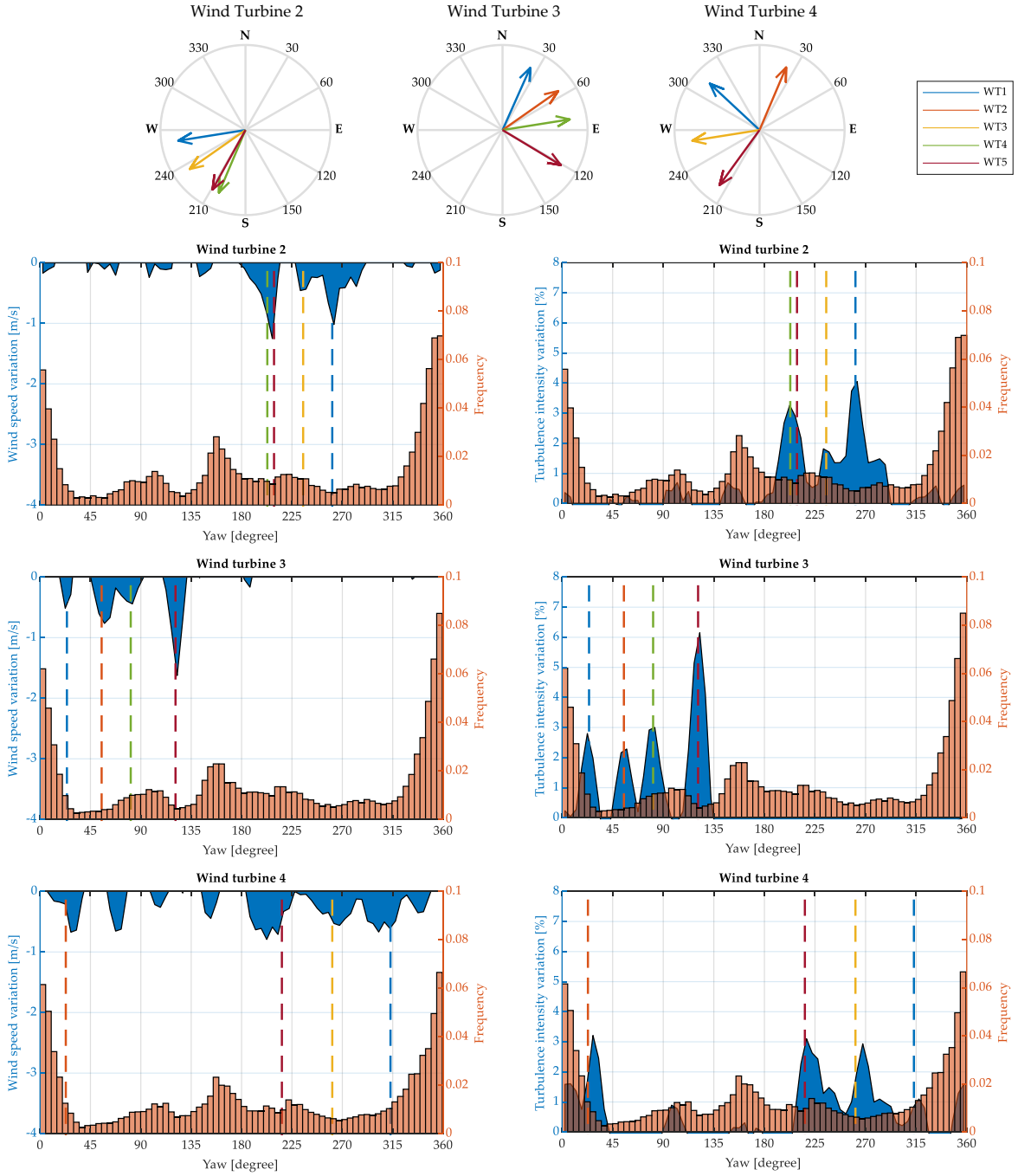


Figure 5.42 – Identification of the wakes and difference between the wind speed/turbulence intensity measured at WT2, WT3 and WT5 and the respective average values in the others five turbines (Jan-2013 to Jun-2021).

For all wind turbines, there is an excellent correspondence between the variation in the wind speed/ turbulence intensity and the orientation of the wakes of the other turbines on the farm. The wind flow in the wakes is characterized by lower wind speed but greater turbulence intensity. This variation tends to

increase with the proximity of the rotors. The good results achieved in the wakes identification are certainly due to the flat orography of the site where the farm is located.

In general, variations in the turbulence intensity between 2% and 6% are identified, while the variation in wind speed values is less than -2 m/s. In this way, also taking into account the last results of the previous section, it is possible to conclude that the wind turbines in the wakes of neighbouring turbines will have greater cumulative damage when in operation.

Looking closer to the results of Figure 5.41 and Figure 5.42, it is clear that WT5 has a significant part of its operating time in the wake of WT1. In fact, considering that the more frequent wind direction is north, wind turbines 5 and 4 are more loaded by wakes, while the other three are more loaded by less turbulent winds.

The damage capture matrix (D_{3D}) obtained for the fleet leader was used to estimate the damage accumulated in each of the wind turbines in the farm. The normalised cumulative damage for WT1 is shown in the Figure 5.43, for the critical point of the tower cross-section under analysis in each turbine.

It is possible to highlight three distinct behaviors. WT5 is the one with the greatest accumulated damage, very similar to WT4. As anticipated by the previous analyses. On the opposite side, WT1 and WT2 have less fatigue life consumed due to their position on the wind farm. Finally, WT3 presents an intermediate behavior between the two previous cases. The reduced distance to the WT1, WT4 and WT5 may explain the results.

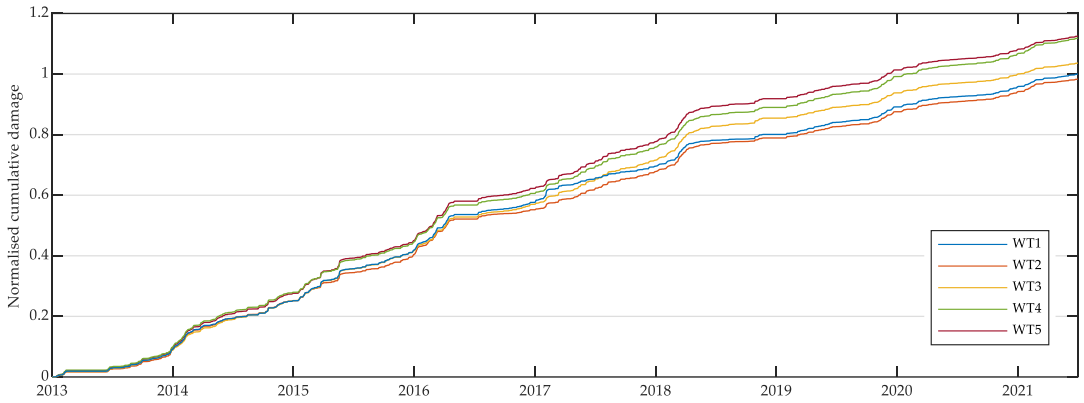


Figure 5.43 – Cumulative estimated damage (D_{3D}) for the critical angle of each wind turbine of the wind farm.

The distribution of the extrapolated endured damage at critical point of the tower cross-section under analysis for all wind turbines of the wind farm and normalized to the WT1 damage, is represented in Figure 5.44. For each resulting damage distribution, a vertical dash line shows the mean value. The figure demonstrates that the procedure developed throughout this work makes it possible to estimate meaningful estimates for the damage accumulated in each structure.

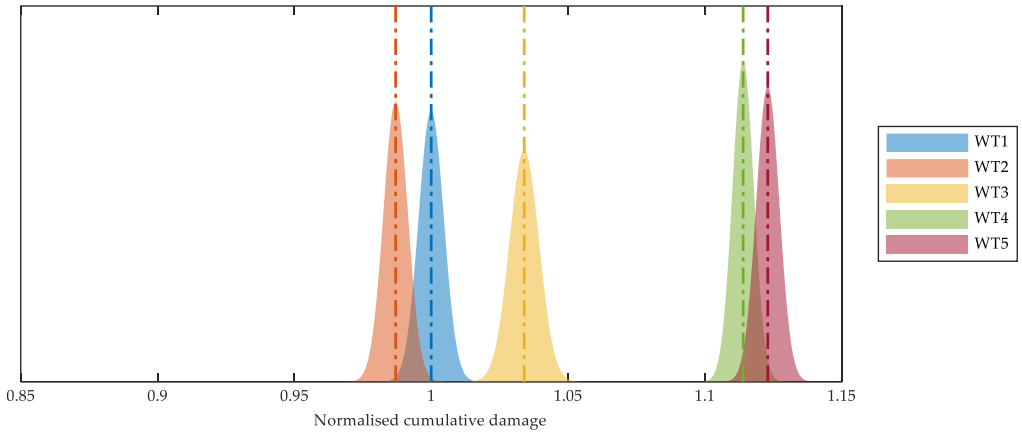


Figure 5.44 – Distribution of the extrapolated endured damage at critical angle of the tower cross-section for all wind turbines of the wind farm and normalized to the WT1 (vertical dash line shows the mean value).

The distributions represented in Figure 5.44 have different uncertainty values. In fact, the uncertainty of each distribution is dependent on the relative weight of bins with experimental data. The contribution of the extrapolated bins of the damage matrix to the estimated values of the accumulated damage is shown in the Table 5.3. Comparing Table 5.3 and Figure 5.44, it can be seen that the larger the contribution of the extrapolated bins is to the total damage, the greater is the dispersion associated with the damage distribution. It is important to mention that for wind turbines with greater accumulated damage (WT4 and WT5) the percentage of extrapolated bins is lower than in the other cases, making the damage estimates more reliable.

Table 5.3 – Extrapolated endured mean damage obtained from the real and extrapolated bins of the damage capture matrix for the critical angle [%].

Estimated Damage	Real bins	Extrapolated bins
WT1	90.5	9.5
WT2	91.0	9.0
WT3	89.9	10.1
WT4	93.5	6.5
WT5	92.6	7.4

The values presented in the Table 5.3 also demonstrate a good representativeness of the environmental and operational conditions of the fleet leader during the monitoring period for all turbines on the farm. In this way, selecting only WT1 as fleet leader seems to be a good choice in this case study.

5.7 FINAL CONSIDERATIONS

Fatigue is a design driver for many wind turbine support structures and a concern to the operators. The fatigue monitoring strategy discussed in this chapter was developed to assess the structural integrity of the entire wind farm using 10-min SCADA data of all wind turbines and strain measurements at the tower of a limited group of turbines (fleet leaders). The chapter starts with a review of the short-term damage calculation procedures based on strain measurements. The text is then progressively oriented towards more detailed aspects of the implementation of the fleet leader concept.

After a general introduction to fatigue damage calculation and extrapolation within an instrumented structural element, this chapter presents the methodology followed for the experimental evaluation of bending moments at the tower of a wind turbine. Special attention is given to the signal processing of strain gauges measurements, taking into account that temperature is known to be the major cause of signal perturbation. In this way, it is presented a procedure to minimize de daily temperature effects and also the long-term effects on the strain gauges recordings. The post-processed strain signal and the for-aft and side-to-side bending moments obtained are validated with theoretical values and other experimental results (tower accelerations monitoring system).

The procedure for fatigue assessment based on a time domain analysis is illustrated with a case study. It is demonstrated that the definition of the type of S-N curves, the window length of the strains time series used to estimate the stress cycles as well as the rain-flow histogram resolution and strains signal sampling frequency have a relevant influence on the calculated damage.

The following conclusions can be drawn from the first part of this chapter (Sections 5.3 to 5.5):

- A monitoring layout for measurements of tower mechanical loads was validated over a period of two years. This monitoring system shown a great robustness;
- The temperature and long-term effects on the strain gauges sensors was quantified for this application and a pre-processing procedure was implemented for their minimization;
- The SCADA data, available with low and high frequency, provides a very useful and complementary information regarding the environmental and operational parameters of the instrumented wind turbine. The combination of the SCADA data with a strain monitoring system was very effective for the calculation of the mechanical loads and as well as fatigue wear;
- The more precise operational data provided by the SCADA system with high frequency allows to detect the short events responsible for the overloading of the structure and the yawing nacelle events, fundamental for strains sensors calibration;
- Direct strain monitoring allows to record short events as well as seasonal variations that can be used to understand the complex wind turbine behaviour under a large variety of operating conditions. This results are very useful to validate numerical estimates obtained with complex aero-elastic simulation tools, such as FAST;
- Automatic data processing can provide owners with a real estimation of the fatigue consumption, since the strain measurements allowed to accurately estimate fatigue damage over the monitoring period for the instrumented tower cross-section.
- The influence of all the used-defined parameters to be adopted in the processing of experimental data for fatigue assessment was quantified.

The presented literature review on the processing of experimental data for fatigue assessment of wind turbine towers and the illustration of the most relevant processing step in a case study will certainly contribute to widespread the application of these experimental tools on the management of wind turbine assets.

In the second part, the challenges for a farm wide fatigue assessment are discussed. The adopted approach is based on the fleet leader concept, in which a limited number of representative turbines are instrumented with accelerometers and strain gauges. Suggestions and recommendations regarding the number and location of fleet leaders on the farm are presented and discussed.

The 10-min damage obtained from direct measurement over the monitoring period were coupled with operational and environmental conditions. The algorithm developed for the clustering of 10-min damage estimations allowed to characterize the influence of the environmental and operational parameters on the accumulated fatigue damage. In particular, it was observed that:

- Selected short-term damage can have a wide range of impact on the total fatigue damage (only 2.5% of the 10-min damage are responsible for 50% of the total accumulated damage in the monitoring period);
- Shutdown is the most damaging load case, but the low frequency of occurrence (0.1%) makes it less significant (2.1% of the total damage);
- Normal operation is responsible for the majority of the accumulated damage (84.8%), and represent the most common load case (71.8%);
- Normal operation above the rated wind speed is responsible for 17.9% of the damage on the monitoring period, despite representing less than 5% of the time;
- Parked and idling load cases have reduced impact on fatigue damage (2.0% of the total damage);
- For normal power production, although the maximum bending moment installed at the tower base occurs for wind speeds close to the rated speed, fatigue damage increases continuously with wind speed.

For extrapolation of the experimental fatigue results to non-monitored periods and non-monitored wind turbines, only short-term damage during normal operation was considered. However, for a realistic indication of actual accumulated damage, all operational conditions should be accounted for. The damage is accumulated differently during normal operation, parked conditions and rotor stop events. The proposed methodology would be applied separately on each load case data.

Based on an approach described in IEC 61400-13 for power production load cases, the calculated short-term damage were classified according to the wind speed and turbulence intensity. Special attention was given to the damage capture matrix construction, in order to obtain accurate damage extrapolations. The following conclusions can be drawn from the matrix construction step:

- This bin filling can introduce a bias, that should be minimized and preferably forced to be in the safe side;
- The occurrence probabilities of the bins should be based on measurement data, if a sufficient amount of data is available, in order to be representative for the full lifetime of the turbine;
- In each bin, a mean damage should be used together with a probability distribution;
- For the bins with a limited amount of available data, especially for some rare bins associated with high wind speed/turbulence intensity, the empirical damage distribution is uncertain, and therefore, the deduced damage metrics (the mean damage in this work) are uncertain as well;

- In this cases, statistics tools (sample-based bootstrapping) can be used to estimate the unknown empirical damage distribution in each bin by only using the available damage values;
- The fleet leader, due its location on the wind farm, can be directly in the wake of the neighbouring turbines. In this case, the variation of the turbulence intensity with respect to the wind sector must be analysed (especially for large wind farms).

It is important to note that, these results/recommendations should be further validated in future investigations using other wind farms.

The obtained damage capture matrix is then used to develop a model for the reconstruction of the fatigue damage endured by the instrumented wind turbine (WT1). This model was first validated considering the monitoring period. Then, it was used to estimate the accumulated damage based on SCADA data recorded during 8.5 years. This study allows drawing the following conclusions:

- Based on the clustering of the operating conditions, the damage endured by the instrumented wind turbine is estimated with adequate accuracy even with a limited number of parameters (wind direction/speed and turbulence intensity);
- Accumulated damage during missing periods of strain measurements at the fleet leaders can be estimated as well;
- The annual average wind speed and turbulence intensity strongly affects the total endured damage by the turbine support structure;
- A minimum measurement length is required in order to guarantee representative measurement data for reliable lifetime estimations. The importance of measuring in windy periods, when the majority of the damage occurs, was demonstrated;
- The uncertainties decrease with the measurement duration to construct the damage capture matrix, and increases with the number of extrapolated bins considered on the extrapolations;
- Simulations demonstrated that turbulence intensity has greater impact on increased damage than the wind speed;

Nevertheless, one of the most important conclusions is related to the validity and applicability of the data processing strategy implemented and tested. If there are no significant changes of the turbine or of the environmental conditions over the lifetime, damage extrapolations based on sufficiently long monitoring period present adequate accuracy. As explained, changes in the models for turbulence intensity estimation does not allow respecting the aforementioned premise. In this way, it is essential that the owners of the farms ensure that the environmental and operational data are recorded in a consistent way over time. Otherwise, several monitoring periods may be necessary.

Finally, the developed method was extended to the neighbouring wind turbines considering the available SCADA data since 2013. Based on the results from the ongoing monitoring campaign that is being conducted in Tocha Wind Farm, the following additional conclusions can be drawn:

- Interesting results on the fatigue progression in wind farm have been deduced, including the characterization of wakes (wind flow with lower speed but greater turbulence intensity than unperturbed air);
- Site specific environmental and operational conditions will play an important role in farm wide fatigue assessment;

- The combination of SCADA data with a well-designed monitoring system in operation during an adequate time period permits to significantly improve farm wide fatigue estimates;
- It is important that the operation/control system implemented in the wind turbines is homogeneous throughout the farm to guarantee the validity of the developed method;
- The size of the farm and the relative position of the turbines are two parameters that, despite being simple, proved to be sufficient for the choice of fleet leaders (for a flat terrain).

6
ANALYSIS OF WIND TURBINE BLADES EXPERIMENTAL DATA

6.1 INTRODUCTION

The blades are key components of a wind turbine, converting the kinetic energy of the wind flow to mechanical energy. The structural design of wind turbine blades is particularly challenging. Blades are large and complex components designed with several materials, leading to different properties and manufacturing procedures (H. J. Sutherland, 2000). As the size of turbines has grown over the past two decades, wind turbine blades continue to be the target of technological improvements by the use of better designs, materials, manufacturing, analysis and testing.

This chapter seeks, in the first place, to provide knowledge about the instrumentation of wind turbine blades, filling an important gap in the available bibliography on this topic. Procedures and best practices are described to obtain good results with the instrumentation of wind turbine blades. The challenge is to develop a robust low-cost monitoring system that provides incontrovertible evidence of an improved exploitation of the structural asset. The structural health monitoring of the blades includes acquiring and analysing data from sensors and evaluation of the integrity and health of a structure. The instrumentation of the rotors of two wind turbines at Tocha Wind Farm are the basis to describe thermal compensations effects on Fiber Bragg Grating (FBG) sensors and a procedure for sensors calibration. Then, it is introduced a method to analyse root bending moments on the blades of the wind turbines instrumented with axial strain sensors at the blade roots. SCADA data from these turbines is also available and used in this analysis. Finally, the strains measured are used in a first attempt to estimate fatigue damage at blade roots. The influence of wakes on blade fatigue damage is considered comparing the damage estimated for the blades of two wind turbine rotors aligned with the main wind direction at the farm under analysis.

This first section introduces the main topics concerning wind turbine blades and composite materials. Although the theory of aerodynamics of a wind turbine rotor was briefly presented in Chapter 2, this section introduces the main loads acting on blades. One focus of this review is on the failure mechanisms of wind turbine blades. These are important topics to interpret the methodologies and the results obtained in the next sections. Finally, the operation and maintenance costs of a wind turbine cannot be ignored. One effective way to reduce the life cycle costs and to extend the life of the wind turbine structure is by the application of SHM. This is also further justified in this first section.

6.1.1 Blade Structure and Composite Materials

On a global scale, blades have to be sufficiently light, stiff and strong, in order to not contribute with enormous gravitational loads (for the blade itself and for the tower), to not deflect too much (avoiding collision with the tower) and to resist to a very high number of cycles during their lifetime. Hau (Hau, 2006) expected of around 10^7 to 10^8 of loading-unloading cycles and Mandell (Mandell & Reed, 1992) has estimated that number to be around 10^8 to10^9 in a given life of 20 years. At the same time, blades have to be locally stiff enough to ensure that the shape of the aerodynamic profiles (the airfoils) is kept as stable as possible, to avoid losses of efficiency. In order to accomplish all these prerequisites, fibre reinforced polymer composite materials are typically used in blades of wind turbines.

A wind turbine blade consists of two outer shells that ensure the blade aerodynamic profile, jointed together and stiffened by one or several internal webs or by a main spar, as show in Figure 6.1. Usually, the spar and aerodynamic shells are manufactured separately and then bonded together. In a simple way, the blade manufacturing process consists of four phases:

- Manufacturing of the spar: the inner part of the blade is made of composite materials, fibreglass and carbon pre-coated with epoxy resin (a thermostable polymer that hardens when mixed with a catalyst agent);
- Manufacturing of the shells: these cover the spar and are made of composite sandwich laminates painted on the outside surface;
- Assembly and curing: the spar and the two aerodynamic shells are bonded together in order to obtained a single firm and strong structure;
- Finishing: the structure undergoes an inspection prior to the blade being moved to its destination wind farm;

It is important to note that alternately blade-manufacturing process were developed, where the entire blade is manufactured in one piece. As the material properties of a composite are highly dependent on the manufacturing process, new manufacturing technologies were developed and implemented (Mishnaevsky et al., 2017; Veers et al., 2003). Note also that manufacturing processes may introduce defects that can lead to complex failure behaviour.

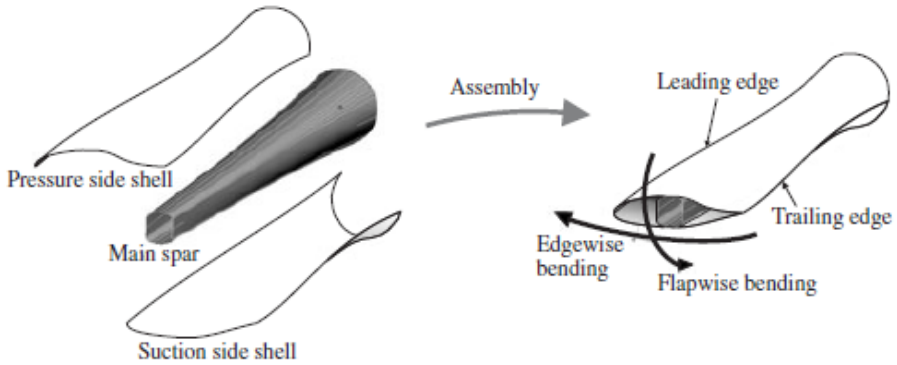


Figure 6.1 – Schema of the components of a wind turbine blade (adapted from (Lund & Stegmann, 2005)).

Wind turbine blade loads act in two orthogonal directions, flapwise and edgewise service load as defined in Figure 6.1. The flapwise load is essentially caused by the wind action (aerodynamic loads) acting perpendicularly on the rotor plane, when the turbine is in power production. These loads present high variability in both amplitude and mean, thereby inducing high scatter in load history data. On the other hand, edgewise loads essentially consist of gravitational forces from the blade's weight and torque loads

driving the turbine. This loading is more deterministic and changes direction twice during each rotor revolution. The loads frequency distribution contains two peaks, corresponding to the wind loading and blade self-weight gravitational load (H. Sutherland, 1996).

The loading environment described above is associated with distinctive structural characteristics of wind turbine blades. As shown in Figure 6.2, different locations at the blade have different cycling loading histories. The spar or internal webs resist the flapwise bending moments. The main laminates in the main spar of the pressure side (blade side where the wind hits) is subjected to cyclic tension-tension loads while the suction side is subjected to cyclic compression-compression loads. The edges of the profile carry the edgewise bending moments. The laminates at the leading and trailing edges that carry the bending moments associated with the gravitation loads are subjected to tension-compression loads. Finally, the airfoils shells are made of sandwich structures, which are primarily designed against elastic buckling.

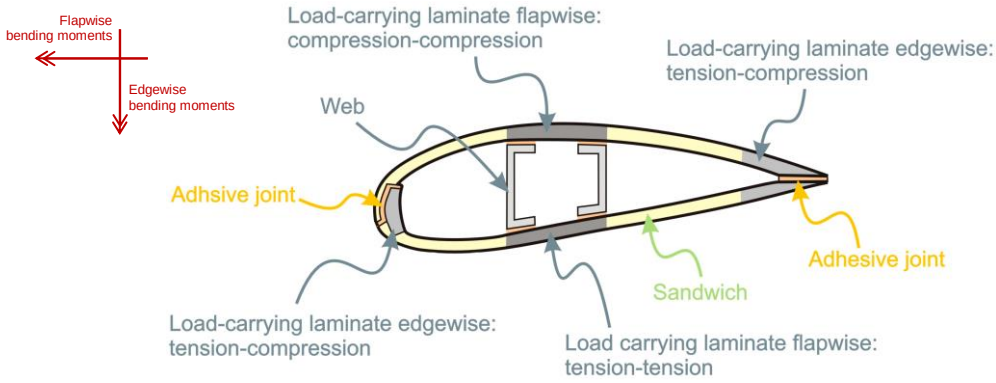


Figure 6.2 – Schema of section of wind turbine blade with two internal webs and definition of load cycles (adapted from (Mishnaevsky et al., 2017)).

The blades are mainly subjected to edgewise and flapwise bending and shear loads, thus performing like a beam, transferring the loads to the wind turbine hub. As loading and stresses increase toward the rotor hub, wind turbine blades tend to increase in thickness toward the blade root, and gain in slenderness toward the tips. In fact, wind turbine blades can be considered slender bodies, with a thickness that results from a compromise between ideal slenderness for aerodynamic efficiency and ideal thickness for structural integrity. Usually, wind turbine blades are divided into three main areas, classified by aerodynamic and structural function, as show in the Figure 6.3.

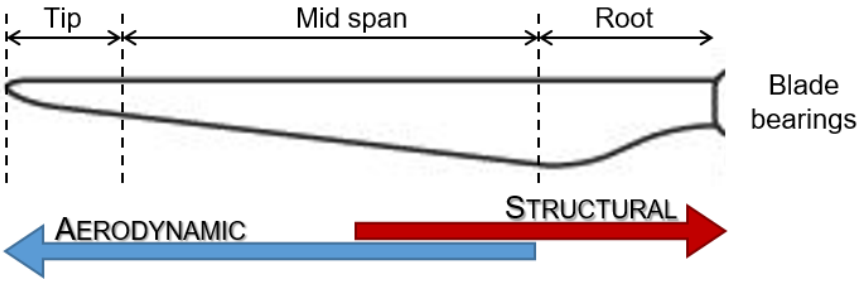


Figure 6.3 – Classification of the three areas of the wind turbine blades.

The blade root represent the transition between the circular mount and the first aerofoil profile. This section carries the highest loads. So the blade root typically consists of thick aerofoil profiles to improve structural integrity with low aerodynamic efficiency. The mid span mainly play an aerodynamic role,

where the lift to drag ratio is maximised without compromising structural integrity. Finally, the tip only has an aerodynamic function. These aerofoils are design to reduce the noise and losses.

Another important feature in the design and production of the wind turbines blades is the blade materials. Over the years, there has been a great development of materials and manufacturing processes, from wood to metals (steel and aluminium) and to nowadays composites (Brøndsted & Nijssen, 2013; Hau, 2006). Composite materials results from a combination of fibres and a matrix, where different combinations and mixing ratios are possible. In a simple way, stiffness of the fibres, fibre volume fraction and the orientation of the fibres are the parameters that largely drive the composite properties. As the volume fraction of fibres increases in unidirectional composites, the stiffness, tensile, and compression strength increase proportionally (Roger, 2006). Nonetheless, fatigue performance can be reduced by high fibre volume fraction, above 65%, consequence of poor resin distribution. The matrix and the interface established between the fibres and matrix are also important parameters (Mishnaevsky, 2012).

The most commonly used fibres have been the glass fibres, especially E-glass fibres are used as the main reinforcements in composites. Although, with the balance between stiffness and weight for large wind turbine blades there is a clear growing tendency towards incorporating carbon fibres (hybrid glass/carbon composites). Carbon fibres ensure higher stiffness and lower weight while their disadvantages are higher cost, lower compressive strength and high sensitivity to local defects (Barbero, 2017). The combination of carbon and E-glass fibres allows to achieve the combination of higher stiffness with limited cost increase. Other alternatives are high strength glasses (S-glass), basalt and aramid fibres. With regard to resin matrix, epoxy matrices have become the primary material in blade production. These provide better fatigue performance and are more durable in comparison with other solutions like polyester (Mishnaevsky, 2012).

In conclusion, fibre reinforced plastic materials have become the most used blade material as they combine high stiffness to maintain optimal aerodynamic performance, low density to reduce gravity forces and long fatigue life to reduce material degradation (Brøndsted et al., 2005). However, these materials continue to present several challenges regarding their properties and behaviour (generally anisotropic in nature). An more deep overview of composite materials for wind turbine applications is presented in (Mishnaevsky et al., 2017).

6.1.2 Loads and Damage Mechanisms

In addition to the geometric, structural and material complexity, wind turbine blades are subject to a large variety of dynamic loads contributing to the fatigue wear of the structure. The definition of the loading scenarios is a difficult and extensive task. Environmental loads acting on the wind turbines show a dynamic, non-deterministic nature, leading to a considerable uncertainty in their quantification and frequency of occurrence. The fatigue loads have been identified as one of the key sources of damage, with delamination as the main cause for the failure of the turbine blades (Ciang et al., 2008). Focusing on onshore wind turbine, there are mainly three sources of fatigue loads for wind turbines blades: aerodynamic loads, gravity and inertia loads and loads from turbine operation.

Wind loading is the primary external source of excitation of wind turbines. Usually, time varying wind speed time series are assumed as the sum of two components: a mean wind speed and a turbulent component. The turbulent component is responsible for the dynamic excitation of the blade. It is considered a non-deterministic variable and, for that reason, it is usually defined by statistical means, as turbulence intensity. As opposed to aerodynamic loads, gravity and inertia loads are relatively simple to

calculate and can be divided into gravitational loads, centrifugal loads and gyroscopic loads. The rotor operation generates cyclic tension and compression loads along the blade. Particularly, large edgewise bending moments are generated, leading to variable tension-compression forces at the leading and trailing edge. Together with wind turbulence, the gravitational loads have a dominating influence on the fatigue strength of a wind turbine blade. On the other hand, centrifugal and gyroscopic loads have a reduced impact on fatigue assessment of the blades due the relatively low rotor speed. Finally, loads from transient events (starting and stopping of the turbine) or due to pitch angle variation can contribute to fatigue damage. These loads are moderate during normal operation, but can become large enough for an emergency-shutdown.

Although wind turbine blades are designed for 20 years, structural monitoring, maintenance and repair procedures are essential to ensure their integrity. The blades are damaged due to mechanical loads (static and fatigue) and environmental conditions (temperature and humidity) as well as manufacturing defects (wrinkles, fibre misalignment, dry spots, disbands, voids) (Katnam et al., 2015). The failure behaviour depends not only on inherent heterogeneity and anisotropy but also on possible failure modes and their interactions (Orifici et al., 2008). Mechanical properties and environmental conditions are important parameters that driven the failure behaviour. In the analysis of composite structures, different length scales can be considered (intra-lamina, inter-lamina, laminate, and component levels) (Mishnaevsky, 2012). Figure 6.4 represents the main structural damage mechanisms of wind turbine blades. Further details on damage mechanism and main failures in wind turbine blades can be found in (Brøndsted et al., 2005; Ciang et al., 2008; McGugan & Mishnaevsky, 2020).

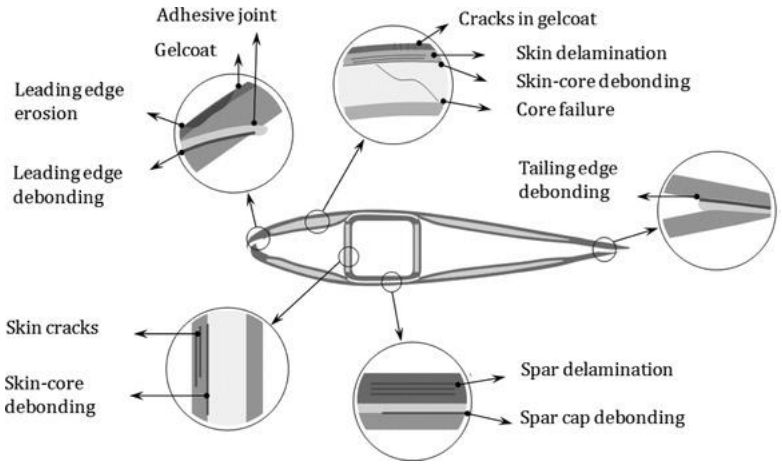


Figure 6.4 – Main structural damage mechanisms of wind turbine blades (adapted from (Katnam et al., 2015)).

6.1.3 Structural Health Monitoring

Typically, wind turbine blades require repair after 2 to 5 years after installation, creating a permanent factor of costs increase for wind energy industry (Bech et al., 2018). In fact, blades are the fifth biggest contributor to wind turbine failure with a contribution of 6.2%, after pitch and hydraulic system, auxiliary components, generator and gearbox (Carroll et al., 2016). Blades show 0.456 minor repairs, 0.010 major repairs, and 0.001 major replacement per wind turbine per year (Mishnaevsky Jr., 2019). Structural repair costs are in average twelve times higher than minor repairs, with proportional increased downtime costs. The total downtimes are 55.8 h/year for minor repair and 23.1 h/year for major repair (Carroll et al., 2016). Wind turbine blade damage can be classified according to (Mishnaevsky, 2019). With the increase of offshore market, larger operational and maintenance costs are expected. The failure

rate for blades and hub per turbine per year is four times higher for offshore than for onshore wind turbines (Dao et al., 2019).

Incorporating SHM techniques in many applications provides significant advantages that include minimizing operation and maintenance costs as well as the ability to collect information and data for future design and optimisation of blades. Although the application of structural health monitoring methods to wind turbines is a well-studied topic, the practical application of these methods to wind turbines blades presents several challenges. As described in Chapter 2, condition monitoring is an important tool for ensuring the integrity of wind turbines components (Oliveira et al., 2016) and allows to reduce operation and maintenance costs (Tchakoua et al., 2014). Focusing on the blades, structural health monitoring methods include vibration monitoring, strain measuring, acoustic emissions, impedance techniques, ultrasonic waves, smart paint, laser vibrometry, impedance tomography, thermography, and nanosensors (McGugan & Mishnaevsky, 2020; Rolfes et al., 2014). The main goals of these techniques involve ice detection, damage detection, load monitoring, pitch angle monitoring and rotor imbalances. A more deep overview of health monitoring of wind turbine blades can be found in (McGugan & Mishnaevsky, 2020). The two most commonly investigated sensor technologies for permanent on-line monitoring are described below.

Vibration monitoring techniques are the most common methods to monitor blades condition (Coronado & Fischer, 2015).These methods allows to detect changes to the structure of the blades (possible damage) based on the analysis of their modal properties (OMA methods). An active vibration-based SHM system based on electromagnetic actuator and a number of accelerometers is proposed in (Tcherniak & Mølgaard, 2017). Numerical simulations of accelerometer signals along the tower and blades were used to o carry out SHM of floating offshore wind turbines in (H.-C. Kim et al., 2019). However, as referred in Chapter 2 OMA of wind turbine blades requires supplementary methods to take into account the time-variance of the structure, due the rotation of the rotor.

Structural health monitoring methods using strain measurements on the blades are also common, being typically used for load monitoring (Coronado & Fischer, 2015). Strain measurements can be carried out using electric strain gauge or fibre optic sensors. Load monitoring can provide important knowledge for control strategies to minimize extreme loading on the blades and other components of the wind turbine and can be used by operators to make maintenance decisions for turbines (Liao et al., 2019). On the other hand, structural health monitoring methods using dynamic strain measurements can be used for the fatigue life assessment of blades (Schroeder et al., 2006). This topic will be discussed later in this chapter.

Additionally, one of the emerging problems of the wind market is the end-of-life management of wind turbine components. Many parts of wind turbines can be recycled. However, this is hardly ever the case for the composite wind blades. Due to their structural and material complexity, blades are composed of various materials elements that are extremely difficult to separate into recyclable parts. Consequently, composite fibreglass in blades is the most difficult, and the most expensive part of turbines to recycle (Rani et al., 2021). The blade waste provides from three types of sources: manufacturing waste, service waste and end-of-life waste. Considering all these sources, a total of 43 million tons of blade waste will be accumulated worldwide by 2050, where Europe represent 25% of the waste (China – 40%, USA – 16% and the rest of the world 19%) (Pu Liu & Barlow, 2017). Composites account for more than 90% of the weight of wind turbine blades (P Liu & Barlow, 2016).

Different strategies of end-of-life management of wind turbine blades can be adopted, from disposal (landfilling and incineration), via life extension, reuse and recycling, to the development of new generation of blade materials (smart, bio-based and biodegradable materials) (Mishnaevsky, 2021).

There exist several options to increase the service time of wind turbine blades, among them, using more durable materials, ensure better maintenance, repair and reuse. The development of new extra-durable wind blades can only be implemented in the following years with the new wind turbines. The reactive options to increase the service time of already installed blades require improving maintenance and repair. This includes health monitoring, damage reporting and identification (inspection and non-destructive tests) and repair procedures. The condition-based maintenance is a very promising approach to identify damage at an early stage, define repair strategies and extend blade lifetime. This will provide a transitional solution for coming years, until the new recycling technologies and new generation of wind turbine blade materials come to the market (Mishnaevsky, 2021).

6.2 STRAIN MEASUREMENTS WITH FIBER BRAGG GRANTING SENSORS

6.2.1 EXPERIMENTAL APPLICATION AT TOCHA WIND FARM

As described in Chapter 4, the V100-1.8 MW wind turbines of the Tocha Wind Farm are equipped with a 100 m rotor with three blades. The energy input from the wind is adjusted by pitching the blades according to the control strategy based on prevailing wind conditions. The pitch system also works as the primary brake system by pitching the blades out of the wind (rotor idle). Double-row four-point contact ball bearings are used to connect the blades to the hub. Each 49 m blade is made with fibreglass reinforced epoxy and carbon fibres based on the *Prepreg* blade manufacturing process (Hindersmann, 2019). As described in Section 6.1.1 the blades consists of two airfoil shells bonded to a supporting beam.

The strain measurement systems can be costly (Hameed et al., 2009; Ovenden et al., 2019). There are several challenges such as intrusive installation (need to remove the protective layer), installation carried out by specialized technicians, need to calibrate sensors after installation, power availability and installing an interrogator unit for data processing, typically inside de hub (Bouzid et al., 2015). Therefore, methods to improve the cost-effectiveness of strain measurement for condition monitoring systems for blades would be valuable (Yang et al., 2010).

Furthermore, the standard strain gauge techniques in wind turbines measurements are susceptible to significant errors. The main error sources are inaccurate location of the strain gauges, their bonding and protection method, misalignment errors and transverse sensitivity, temperature effects, gauge reinforcement effects and errors associated with the performance of the monitoring system (installation/equipment). Some of these errors become significant for measurements on composite materials as in the case of wind turbine blades. Anisotropic materials exhibited directional sensitivity of the stiffness matrix that depends on the manufacturing procedure and varies between instrumented points on the same blade. Consequently, thermal expansion coefficients and thermal conductivity of these materials also demonstrate anisotropy. On the other hand, composites are still less subject to standardization in their properties than other materials, as metals. Humidity is also an important factor, as these are also moisture absorbers. Finally, it is important to take in account that the anisotropic behaviour of composites, leads to coupling between shear stress and normal strain.

These errors can be minimized taking into account recommendations present in guidelines and best-practice procedures. Focusing on selecting sensor positions at the blade, IEC 61400-13 mention that is important to choose a location which:

- Has a high strain per unit load level
- Provides a linear relationship between stress and load;
- A region of uniform stress (is not subject to stress gradients or stress concentration);
- Has space to apply sensors and allows temperature compensation;
- Measurement devices can be easily fixed.

As presented on Chapter 4, in the Tocha Wind Farm case study, two wind turbine rotor were instrumented at the 3 blade roots. Figure 6.5 represents the variation of the flapwise and edgewise stiffness and of the drag and lift coefficients along the Vestas V100-1.8MW blade length. Near the root, the blade cross-section changes from a wing profile to a circular profile and the higher internal forces are verified. Furthermore, this section performs a purely structural function. For these reasons, the blade root was chosen as the section to be instrumented. In order to avoid the stress concentration/gradient

created by the connection of the blade to the hub, the instrumented section is approximately 2 m away from the blade end.

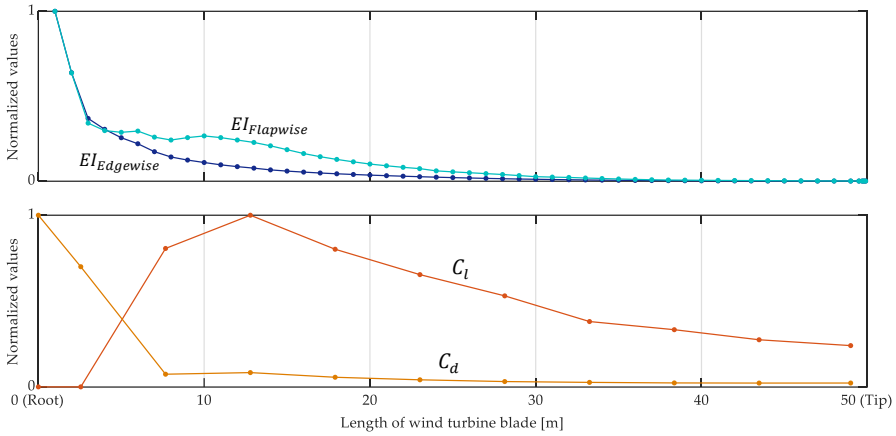


Figure 6.5 – Variation of flapwise ($EI_{flapwise}$) and edgewise ($EI_{edgewise}$) stiffness and drag (C_d) and lift (C_l) coefficients along the blade (normalized values).

Another important step involves the selection of instrumentation devices. In order to avoid risks of damage in the occurrence thunderstorms, fiber optic systems are preferred with regard to electrical based sensors. The following requirements must be taken into account:

- Measurement range: The operating range of the sensors must be compatible with the strains experienced in the instrumental section of the blade;
- Mounting type: For composite materials, the two options are gluing or embedding;
- Robustness: The sensors are bounded inside the blade to protect them from environmental conditions, and to prevent damage of the synthetic coating of the blade. However, they must be moisture resistant;
- Operating temperature: Within wind turbines blades, temperature conditions can have a wide range, but within temperature range of the most common sensors;
- Temperature compensation needs: strain sensors are sensitive to temperature changes, and correction is advised (procedure described in Section 6.2.2);
- Controlling optical losses: Modern sensors are compatible to link very long distances without important signal degradation. However, type of connections, fiber type and cable bending radius and length should also be considered.

As described in Section 4.4.4, in the case study under analysis the HBM – FiberSensing WindMETER (complete monitoring solution for wind turbine blades) was used. It consists of a low-power measurement unit and FBG strain sensors with corresponding temperature sensors. The specifications defined for the sensors were a measuring range of $\pm 5000\ \mu\varepsilon$, $1\ \mu\varepsilon$ resolution and temperature range from $-20°\ \mathrm{C}$ to $80°\ \mathrm{C}$. Figure 6.6 schematically represents the strain blade monitoring system adopted, together with the photos of the sensors and acquisition system (located inside the hub).

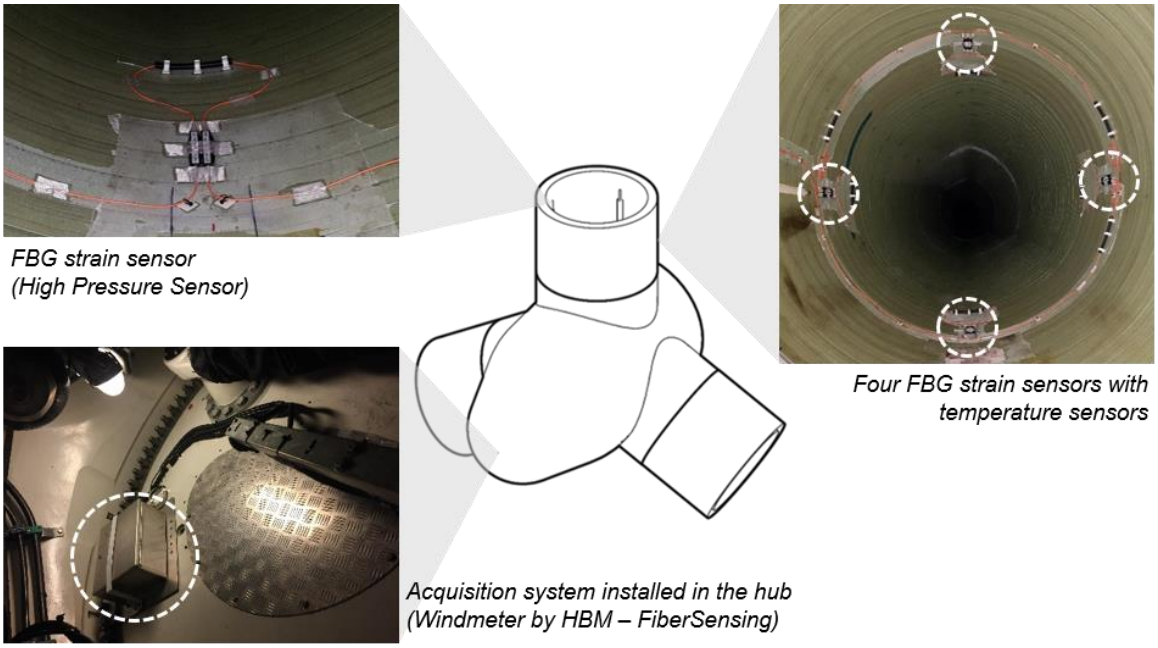


Figure 6.6 – FBG monitoring system adopted within the framework of Tocha Wind Farm monitoring project.

For the installation of the sensors, it is important to prepare blade surface (remove protective coatings and avoid irregularities) in order to be sure that the sensor will get directly in contact with the fiberglass material. The sensors are positioned in four evenly spaced locations (LP: Low Pressure, HP: High Pressure, LE: Leading Edge and TE: Trailing Edge) at each blade root, where the blade cross-section is circular, as schematically depicted in Figure 6.7. The sensors were named based on the pressure distribution due to wind flow on the blades' airfoil.

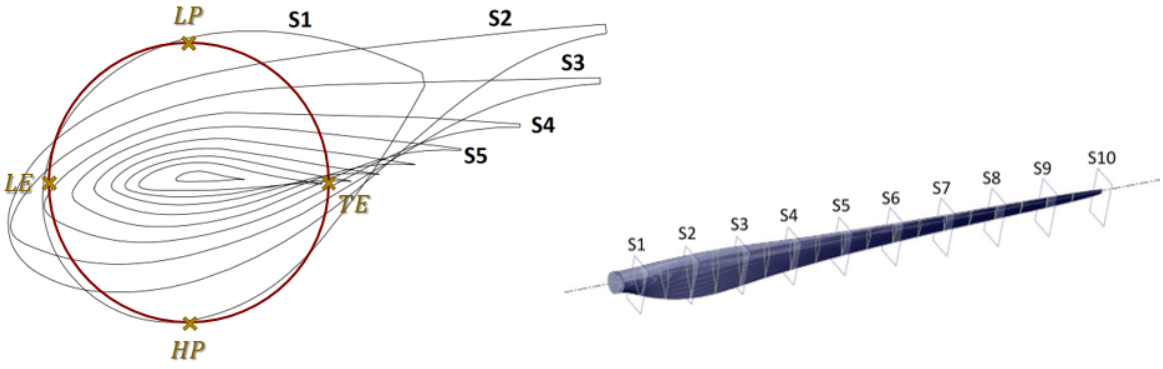


Figure 6.7 – FBG sensor location at blade root (instrumented blade cross-section in line).

6.2.2 Fiber Bragg Granting Strain Sensors

The technological progress of fiber optic communication has stimulated the development of the fiber optic sensors (Yin & Yu, 2002). Due to the increased sensitivity and form factor versatility, fiber optic sensors have been exploited to replace traditional sensors in a wide range of civil monitoring applications including strain, vibration, acceleration, rotation, pressure, temperature measurements, and many others. These sensors exhibit dielectric property, which allows them to be applied in harsh environmental conditions such as high temperature, electro-magnetic interferences or in the presence of

corrosive materials. In addition, these sensors are compatible with communication systems and are able to perform remote sensing (Campanella et al., 2018).

Optic sensors based on Fiber Bragg Gratings have acquired a large market share, especially on the strain measurements field. In addition to the advantages mentioned above, these type of optic sensors allow a direct physical correlation between the measured Bragg wavelength and strain, recalibration is not necessary, the wavelength-encoded sensor signal cannot be disturbed by influences on the transmission lines (Campanella et al., 2018).

A Fiber Bragg grating is an optical device obtained through introducing a modulation of the refractive index (grating) of the fiber core by a manufacturing process called “inscription” or “writing”. The inscription can be implemented with different interferometric methods, as describe in (Cusano et al., 2011; Joe et al., 2018; Mihailov, 2012).

In a simple way, the bare fiber, cladding and protective coating mainly form the Bragg sensor. A dielectric material, called cladding, coats the fiber core. In order to ensure the internal reflection in the core section, the reflective index of the cladding is slightly lower than the fiber core. The protective coating provides mechanical strength to the fiber and protects the fiber from damage and moisture absorption.

Figure 6.8 represents a simple FBG where the perturbation is periodic, equally spaced and modulation strength is only positive. As show, the light propagating in forward direction through the core of an optical fibre is reflected due to the discontinuity at the layer interfaces, while the remaining part passes over. Thus, the beam is divided in two components that travel in opposites directions. In this way, FBG sensors measure the changes in reflective signal from the grating when it is subjected to mechanical or thermal deformation.

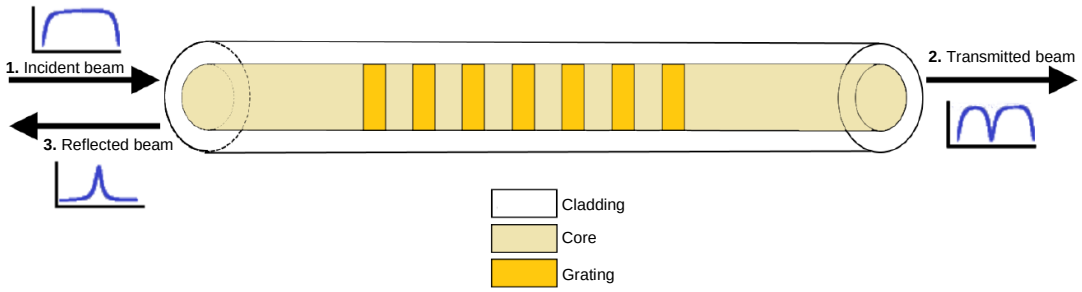


Figure 6.8 – FBG index profile and the spectrum of the incident, reflected and transmitted beams (adapted from (Campanella et al., 2018)).

The Bragg wavelength (λ_B) reflected by the sensor is given by:

$$\lambda_B = 2 * n_{eff} * \Lambda \tag{6.1}$$

with:

n_{eff}	Effective refractive index
Λ	Grating pitch (or grating period)

A very important source of error is the temperature effect that induces a wavelength shift that can be misinterpreted as deformation. The wavelength of a FBG strain sensor changes with strain and temperature according to:

$$\frac{\Delta\lambda}{\lambda_0} = k * \varepsilon + \alpha_\delta * \Delta T \tag{6.2}$$

with:

$\Delta\lambda$	Wavelength shift
λ_0	Wavelength of the sensor at the zero moment
ε	Strain due to structure deformation
k	Gauge factor
α_δ	Change of the refraction index
ΔT	Temperature shift from the zero moment

In the previous equation, ε describes the strain due to loading (ε_{Load}), which is to be calculated, and the deformation of the structure due to temperature effects ($\varepsilon_{Structure}^{Temp}$). The second expression ($\alpha_\delta * \Delta T$) describes the change of the glass refraction index (n) caused only by temperature (ε_{FBG}^{Temp}).

$$\varepsilon = \varepsilon_{Load} + \varepsilon_{Structure}^{Temp} \tag{6.3}$$

$$\alpha_\delta * \Delta T = \varepsilon_{FBG}^{Temp} \tag{6.4}$$

As demonstrated, the temperature effect induces a wavelength shift that can be misinterpreted as deformation. This means that in order to determine the actual deformation of the structure due to loading, it is necessary to know the effect of temperature on the FBG sensor and take into account the thermal expansion of the base material where the sensor is attached.

Thus, the behaviour of a FBG sensor under the effect of strain and temperature is given by:

$$\frac{\Delta\lambda}{\lambda_0} = k * (\varepsilon_{Load} + \alpha_{sp} * \Delta T) + \alpha_\delta * \Delta T \tag{6.5}$$

with:

α_{sp}	Expansion coefficient of the structure material ($\varepsilon_{Structure}^{Temp} = \alpha_{sp} * \Delta T$)

Because temperature has a very strong impact on the FBG sensor signals, precise strain measuring results can only be achieved with proper temperature compensation. There are four different alternatives that implies an additional sensing element.

The most common solution, which was applied in this work, involves a temperature FBG sensor placed under the same temperature as the sensor to compensate. In this way, the strain measurement can be corrected knowing the temperature on the same location of the strain sensor, the thermal cross-sensitivity

of the sensor provided by the sensor manufacture (on the data and calibration sheets) and the thermal expansion coefficient of the structure material.

Secondly, it is possible to measure the temperature impact on strain measurements using a temperature compensation FBG sensor. The more simple solution is based on an optical strain gauge that is applied to the same material and subjected to equal temperature conditions, but not subjected to strain due to load (ε_{Load}). However, it is not always possible to find a position without strain on the structure to fix the compensation FBG.

The third alternative is based on an optical compensation element, for example, an FBG sensor with a known behaviour with temperature. Finally, considering sensors operating in this push-pull configuration (tension-compression configuration), the effect of temperature can be nulled by combining both strain measurements. In this way, an optical strain gauge installed on the opposite surface of the specimen is required.

It should be noted that there are sensor solutions on the market that cancel the intrinsic effect of temperature changes on the FBG wavelength, but not on the thermal expansion of the instrumented structure material (HBM-FiberSensing, 2015). By selecting two of these sensors, operating in a push pull configuration, there is no need for an extra sensor for temperature compensation of the measurement.

Considering the first mentioned method, using a temperature FBG sensor that is not stressed, the wavelength of the temperature FBG sensor only changes with temperature, according to equation:

$$\frac{\Delta\lambda}{\lambda_0} = \left(k * \alpha_{glass} + \alpha_\delta\right) * \Delta T \tag{6.6}$$

with:

α_{glass}	Thermal expansion coefficient of the fiber (usually, $\alpha_{glass} = 0.55 * 10^{-6}/°C$)

Thus, the temperature shift from the zero moment is given by:

$$\Delta T = \frac{1}{k * \alpha_{glass} + \alpha_\delta} * \frac{\Delta\lambda}{\lambda_0} \tag{6.7}$$

When a fiber is fixed to the structure, the FBG sensor signal changes with the strain due to loading (ε_{Load}) and the deformation of the structure due to temperature effects ($\varepsilon_{Structure}^{Temp}$):

$$\frac{\Delta\lambda}{\lambda_0} = k * \varepsilon_{Load} + \left(k * \alpha_{sp} + \alpha_\delta\right) * \Delta T \tag{6.8}$$

The strain measured by the FBG sensor is obtained by:

$$\varepsilon_{Load} = \frac{\Delta\lambda}{k * \lambda_0} - \left(\alpha_{sp} + \frac{\alpha_\delta}{k}\right) * \Delta T \tag{6.9}$$

Finally, the strain caused by loading can then be computed as:

$$\varepsilon_{Load} = \frac{1}{k} * \left[\frac{\lambda_m - \lambda_{0m}}{\lambda_{0m}} - \frac{\lambda_T - \lambda_{0T}}{\lambda_{0T}} * \left(\frac{k * \alpha_{sp}}{\alpha_\delta} + 1\right)\right] \tag{6.10}$$

with:

λ_m	Measured wavelength on strain-measuring FBG sensor
λ_{0m}	Wavelength of the strain-measuring FBG sensor at the zero moment
λ_T	Measured wavelength on temperature-measuring FBG sensor
λ_{0T}	Wavelength of the temperature-measuring FBG sensor at the zero moment

6.2.3 CALIBRATION OF STRAIN GAUGES

The temperature compensated strain data provided by the High Pressure, Low Pressure, Leading Edge, and Trailing Edge sensors can be directly used to determine the flapwise and edgewise bending moments at blade roots. This procedure requires an initial calibration process that is describe in IEC 61400-13. In a simple way, calibration is the process through which it is established a physical relationship between the measured signal output and the mechanical load input acting on the structure. Usually, it is expressed mathematically by the coefficients of the calibration line.

In this way, each pair of diametrically opposed sensors has to be calibrated based on a known reference input moment, in order to establish a relationship between their output and input load. However, this approach is particularly complex to be applied to large wind turbines, due to their large dimensions and to the large magnitude of the loads necessary to cover the expected range in operation. In addition, the sometimes hostile and time-varying environmental conditions (temperature and wind) may affect the calibration process.

The standard IEC61400-13 assumes linear calibration and defines three suitable calibration methods: use of gravity, analytical or model based calibration and application of external loads. For the calibration of blade bending moments, the analytical procedure is not feasible, since the material properties are not currently well known. On the other hand, the application of external loads along the blades is difficult to execute and implies high costs in terms of resources and losses due to non-operation time of the wind turbine.

Gravity calibration is the most commonly adopted method. This uses the self-weight of the blade in low wind conditions. It requires knowledge of the blade mass and centre of gravity to calculate the bending moment at the instrumented cross-section and it is achieved by exposing the sensors to a well-defined moment caused by gravity in flapwise direction and after in edgewise direction, separately. This can be done by fixing the blade in a horizontal position and pitching the blade to different pitch angles (0°, 90°,

180°, 270°). The dependencies of the signals on the bending moments are determined by linear regression of the signals and the moments, given by:

$$\begin{bmatrix}\varepsilon_F \\ \varepsilon_E\end{bmatrix} = \begin{bmatrix}A_1 & A_2 \\ A_3 & A_4\end{bmatrix} * \begin{bmatrix}M_F \\ M_E\end{bmatrix} \tag{6.11}$$

with:

ε_F	Signal of diametrically opposed strain gauges in flatwise direction $\varepsilon_F = \varepsilon_{HP} - \varepsilon_{LP}$
ε_E	Signal of diametrically opposed strain gauges in edgewise direction $\varepsilon_E = \varepsilon_{LE} - \varepsilon_{TE}$
M_F	Flapwise bending moment motivated by the blade self-weight
M_E	Edgewise bending moment motivated by the blade self-weight
A_i	Calibration coefficients ($i = 1, \dots, 4$)

The coefficients A_2 and A_4 are caused by crosstalk effect of the edgewise bending moment on the flapwise signal and the crosstalk effect of the flapwise bending moment on the edgewise signal, respectively. In the ideal case, only a single calibration coefficient is required in the main loading direction and crosstalk effects can be neglected ($A_2 = A_4 = 0$). However, in most cases, the perpendicular moment is not zero and the crosstalk sensitivity terms need to be considered.

It is important to note that equation (6.11) is based on simultaneous consideration of diametrically opposed sensors or readings of ½ bridges installations. Consequently, this results in a single calculation of moments for a given cross-section incorporating all strain data. Alternatively, ε_F and ε_E can be single strain gauges reading using a ¼ bridge installations. In this case, it is possible to evaluate moments for several possibilities of strain gauge pairs: $\{\varepsilon_{LE}, \varepsilon_{HP}\}$, $\{\varepsilon_{LE}, \varepsilon_{LP}\}$, $\{\varepsilon_{TE}, \varepsilon_{HP}\}$, $\{\varepsilon_{TE}, \varepsilon_{LP}\}$. In this way, four separate calculations of moments can be achieved. Although, each pair may result in different values for the moment, sometimes separated by several percentage points.

Post in (Post, 2016) demonstrated that it is possible to improve significantly the calculation of the bending moments with inclusion of crosstalk effects. On the other hand, further improvement is possible when including torsion as a third degree of freedom. Although, this last alternative implies the installation of a rosette strain gauges at low pressure and/or high pressure of the instrumented section of the blade.

It is important to note that every measurement and calibration process has uncertainties associated with it. Strategies for their consideration are described in (International Electrotechnical Commission, 2015). The difficulty to perform a correct load sensor calibration due to the continuing increase of the dimensions of wind turbines is addressed in (Lekou & Mouzakis, 2009).

Alternatively, gravity calibration can be done by idling the rotor at different pitch angles as demonstrated in (Bezziccheri et al., 2017). Due to the imbalance of the mass of the blade, a rotation of 360° of the rotor allows to generate a set of calibration points using the sinusoidal signal generated at the blade root. The main limitation of these methods is that they imply knowledge of the blade weight, its gravity center, the pitch angle, the azimuth angle, precone angle of the blades (angle between the rotor plane and the blade axis) and tilt angle (angle between the horizontal axis and the rotor shaft). These wind turbine characteristics are rarely available or known precisely. Still, this procedure was successfully applied in (Moynihan et al., 2022).

Despite the advantages of calibration based on gravity loads, as it allows periodic recalibration, without the necessity of complex procedures and modifications of the turbine, it is important to note that a calibration based on unbalanced masses will only cover part of the measurement range. In fact, unbalanced masses cause small bending moments relative to those generated by aerodynamic actions during operation.

Finally, these calibration methods assume that only the blade weights are significantly contributing to the bending moments, while lift and drag forces are negligible. In fact, it is recommended not to perform calibration in transient operating conditions or for wind speeds larger than cut-wind speed, due to the inertia of the blade and aerodynamic contributions. But, these conditions might be difficult to fulfil.

6.3 EXPERIMENTAL DETERMINATION OF BENDING MOMENTS

The data available in this work includes four axial strain measurements from the root of each blade at wind turbines 1 and 5. This data is from a period spanning fourteen months of operation from November 2019 to December 2020. SCADA data, which is synchronized with the strain sensor measurements, is available for the same period (average 10-min and high–resolution), as described in Chapter 4.

6.3.1 METHODOLOGY AND DATA PROCESSING

The raw signals provided by the sensors include some outliers. Figure 6.9a shows the original wavelength readings, where some outliers are seen in the signal. In this way, at a first step, the outliers were removed and replaced using a cubic spline interpolation. Figure 6.9b shows the cleaned signals for blade 1 of the wind turbine 1. The procedure applied to remove the outliers was programmed and applied automatically to all the measured signals, as a pre-processing before temperature compensation.

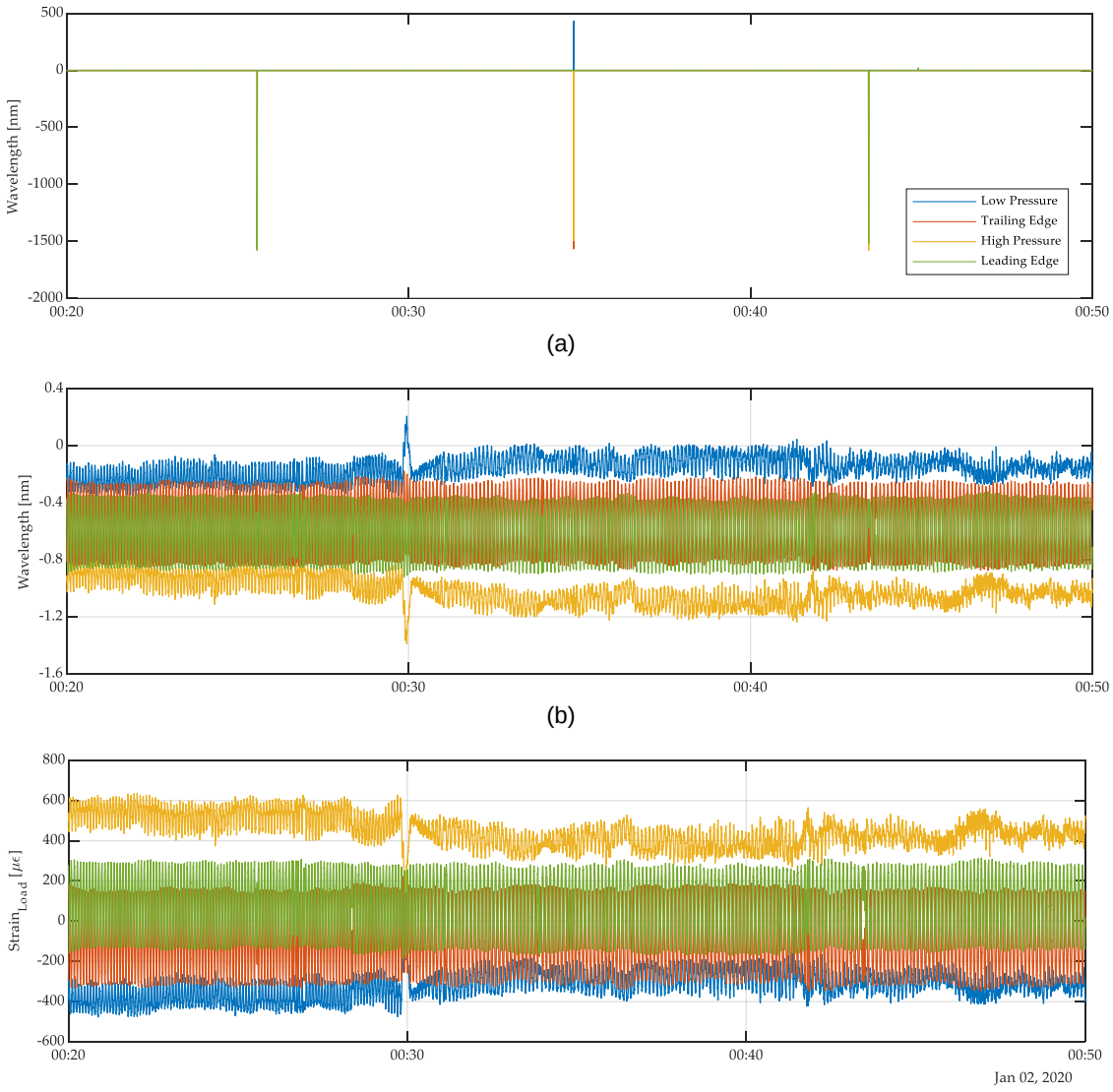
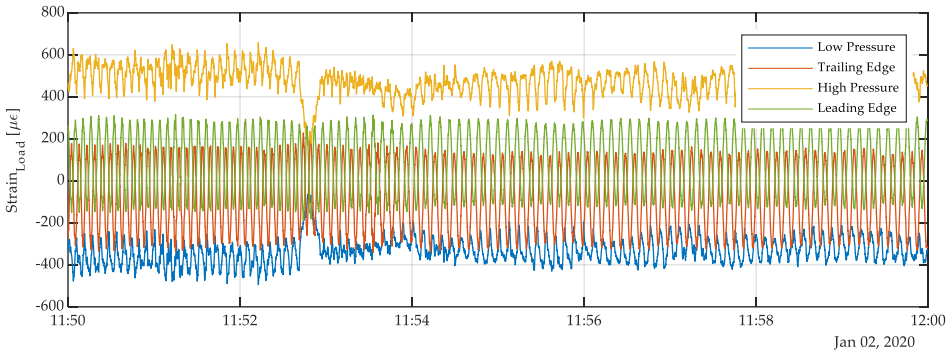


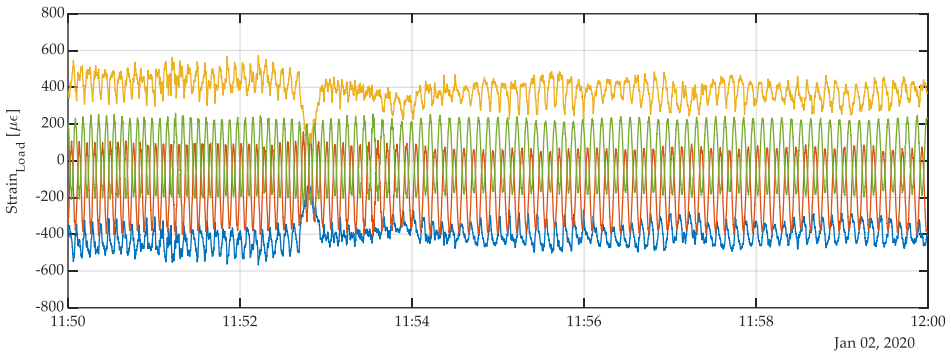
Figure 6.9 – Signal pre-processing of strain gauges: (a) Raw signal; (b) Cleaned signal; (c) Temperature compensated strain gauge measurements after senor calibration (blade 1 of the WT1).

After, the signals were temperature compensated using the method presented in Section 6.2.2 and the calibration sheets provided by the manufacture. The temperature compensated strain readings, after the sensor calibration, are shown in Figure 6.9c.

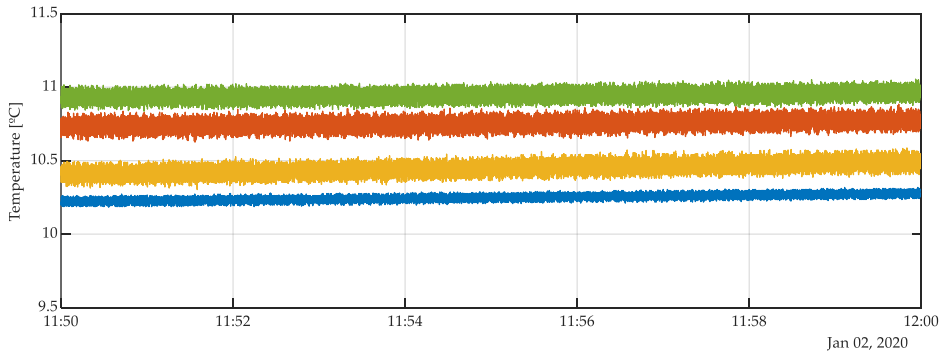
The effect of temperature on the acquired signals is shown in Figure 6.10a and Figure 6.10b, where the time series with and without thermal compensation are compared. A significant signal offset can be observed after the temperature compensation. These are similar for the four signals, since the recorded temperatures are very close. Consequently, the difference from the reference temperature ($T_0 \approx 22\,°C$) is also similar.



(a)



(b)



(c)

Figure 6.10 – Temperature effects on strain gauges signal: (a) Time series without temperature compensation; (b) Time series with temperature compensation; (c) Temperature measurements (blade 1 of the WT1).

Finally, the flapwise and edgewise bending moments at blade roots were calculated directly from the temperature compensated strain data, as suggest on standard IEC61400-13 and describe in Section 6.2.3. The calibration procedure followed for blade B of WT5 is illustrated in Figure 6.11. Each blade was positioned in the three positions represented in the figure, considering the pitch angles at 0° and 90° (indicate in the figure). The blade mass moment at the instrumented cross-section was calculated considering the distribution of the mass along the blades. Knowing that its weight distribution is constant, positioning the blade in well-defined positions, it is possible to correlate the recorded signals output of each sensor pairs (signals at Figure 6.11) with calculated bending moments. This procedure was applied for the 3 blades of wind turbines 1 and 5.

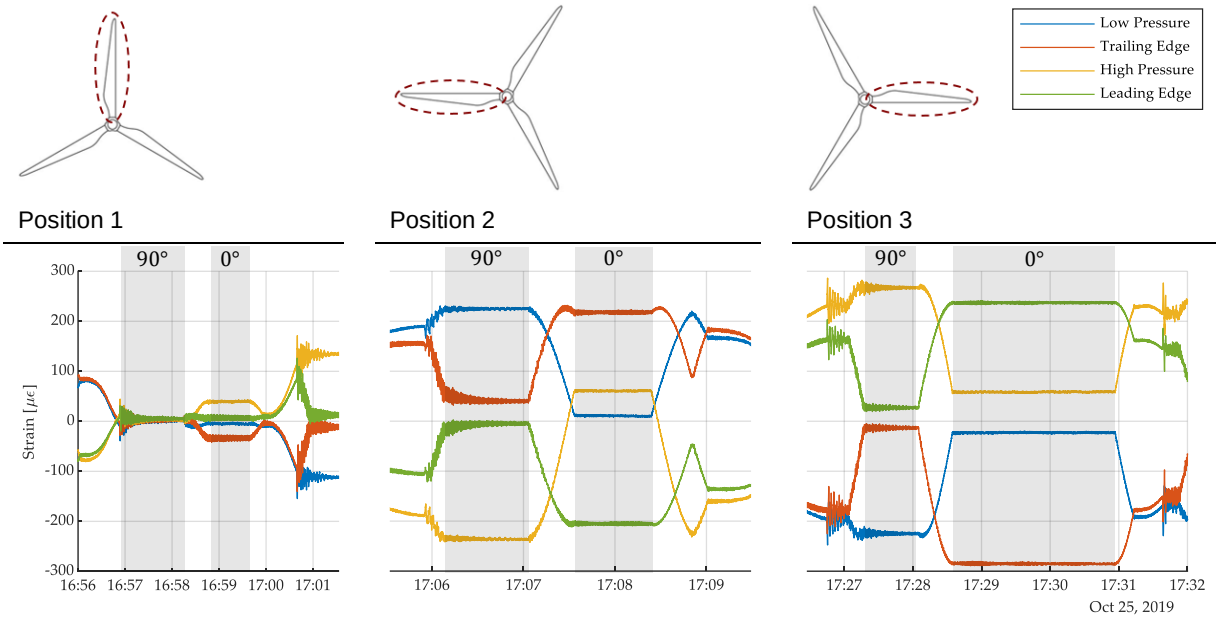


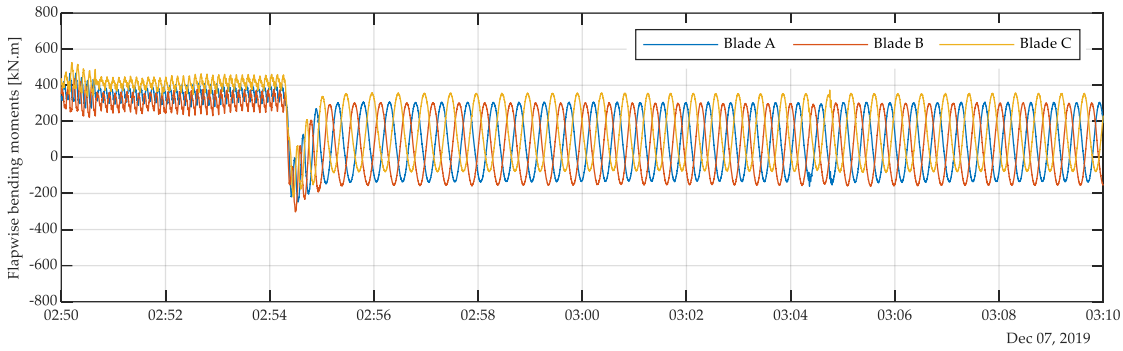
Figure 6.11 – Determination of the calibration coefficients (blade B of the WT5).

As a first step, sensors were zeroed placing the blade at Position 1 and pitched at 90°, in order to reduce the wind action (Figure 6.11 on the left). In fact, when the blade is in vertical upward direction, the weight acts as a compressive load with similar effect in all sensors. However, due to the tilt and precone angles of the rotor (angle between the horizontal axis and the rotor shaft and angle between the rotor plane and the blade axis, respectively), the weight is not perfectly aligned with the longitudinal axis of the blade. However, these angles are generally not rigorously known. Since, the variation of the strains due to the axial action of the weight of the blade is much smaller than the respective variation caused by the bending moment of the weight, the sensors were zeroed, neglecting these conditions.

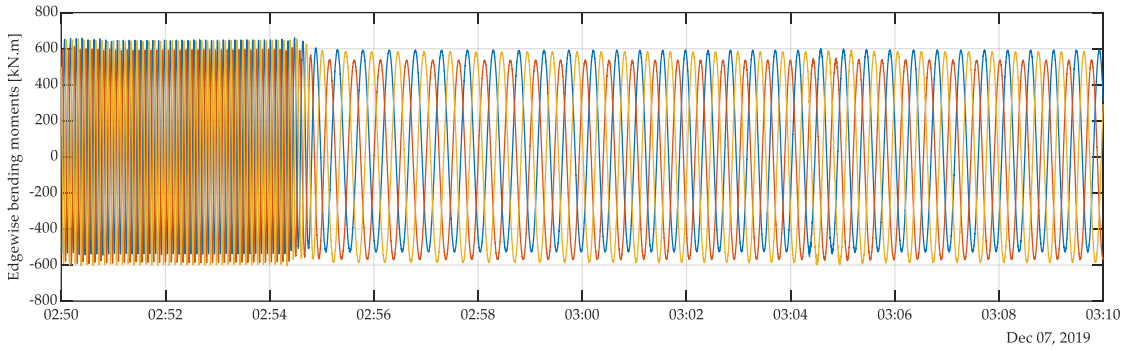
In a forthcoming step, the values of the calibration coefficients A_1 and A_4 (Equation (6.11)) were calculated. In the horizontal position, the weight of the blade motivates a significant bending moment in both positions 2 and 3. In this case, the sensors pairs $\{\varepsilon_{LE}, \varepsilon_{TE}\}$ and $\{\varepsilon_{LP}, \varepsilon_{HP}\}$ should record an inverse variation, considering the pitch angle at 0° and 90°, respectively.

The bending moments were calculated using the difference of diametrically opposed sensors, neglecting eventual crosstalk effects. The comparison of the bending moments obtained, considering or not the crossed effects, allowed to conclude that in this particular case study, the uncertainty of the measurements of the sensors located in the plane perpendicular to the application of the forces translated into less precise estimates of the moments.

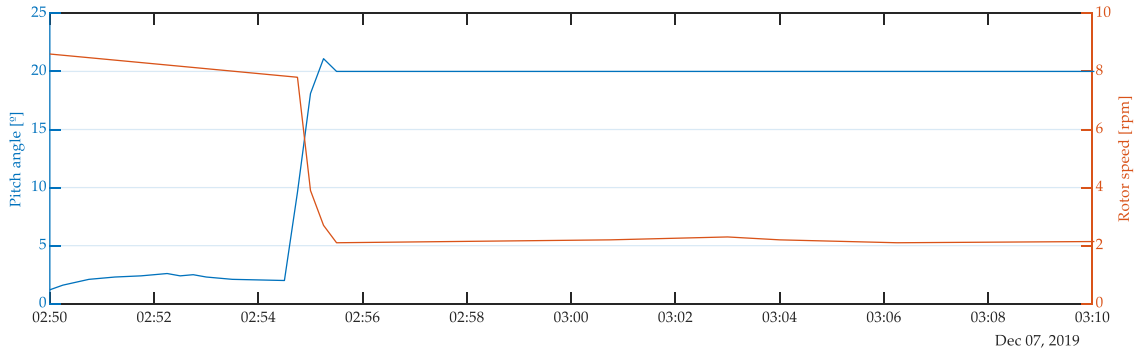
After this calibration the variation of the bending moment over time can be estimated. Figure 6.12 shows the estimated flapwise and edgewise bending moments at blade roots for the three blades of wind turbine 1 during a stop event (wind speed below the cut-in speed of the turbine). The pitch angle and rotor speed, obtained from the SCADA data with high-resolution, are also represented. As the rotor slows down due to a change in pitch angle, the component of weight contributing to the edgewise moment reduces, while the component contributing to the flapwise moment is increased.



(a)



(b)



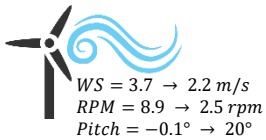
(c)

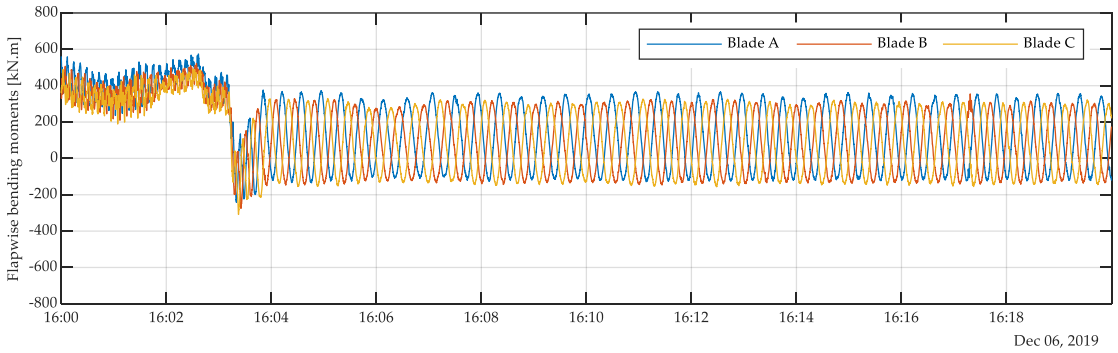
Figure 6.12 – Blade root bending moments of the wind turbine 1 during a stop event: (a) Flapwise bending moments; (b) Edgewise bending moments; (c) Pitch angle (blue line) and rotor speed (orange line).

The bending moments are expected to be of the same magnitude for the 3 blades, when the rotor is in slow rotation (after the transient event). However, the figures indicate some bias in the data. Considering the flapwise direction, the maximum bending moment after the transient event is 308 $kN.m$, 303 $kN.m$ and 373 $kN.m$, for the blades A, B and C, respectively. On the other hand, for the edgewise direction the differences found are less important. The maximum edgewise bending moment for blades A, B and C are, respectively, 600 $kN.m$, 547 $kN.m$ and 590 $kN.m$.

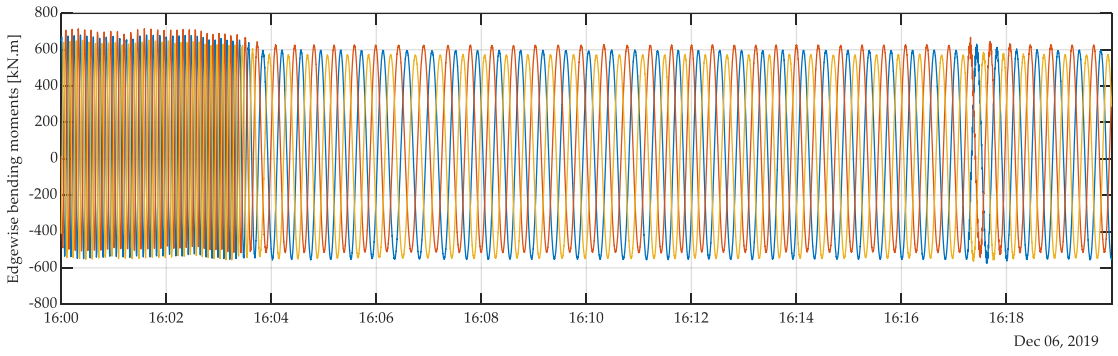
The observed bias is probably caused by sensor calibration, temperature compensation or differences in the sensors' installation. Differences in the mass of the blades or in the behaviour of the blade pitch system are not expected, as the tests carried out showed that the rotor is correctly balanced. Given the uncertainty associated, sensor calibration is the most likely reason. So, improvement of sensor calibration procedures is a relevant research task.

Similar results were obtained for wind turbine 5. Figure 6.13 represents the flapwise and edgewise bending moments during a stop event, when the wind speed is below of the cut-in speed of the turbine. High resolution SCADA data is not available for the WT5, but the operating condition should be very similar to those reported for WT1 in Figure 6.12





(a)



(b)

Figure 6.13 – Blade root bending moments of the wind turbine 5 during a stop event: (a) Flapwise bending moments; (b) Edgewise bending moments.

In this case, flapwise bending moment is similar for the blades B and C, slightly higher for blade A. The maximum value in slow rotation is 356 $kN.m$, 308 $kN.m$ and 313 $kN.m$, for blades A, B and C, respectively. For edgewise direction, the maximum bending moment obtain for blade A, B and C is, respectively, 598 $kN.m$, 623 $kN.m$ and 571 $kN.m$.

Comparing the values of the bending moments obtained for the six blades of the two wind turbines, the dispersion of results is justified by the limitations of the calibration procedure adopted. However, it is assumed these are acceptable and do not affect the quality of the results obtained later on.

6.3.2 BENDING MOMENTS VS OPERATING CONDITIONS

The procedure presented and described in the previous section to estimate the bending moments at the root of the blades was applied to all the dataset collected at the 3 blades of WT1 and WT5. Figure 6.14 represents the power curve of WT5 and the evolution of the blade pitch angle as a function of the wind speed, based on the SCADA data (10-min average values). The colour of the points represents the 10-min average bending moments at the root of blade A for flapwise and edgewise directions.

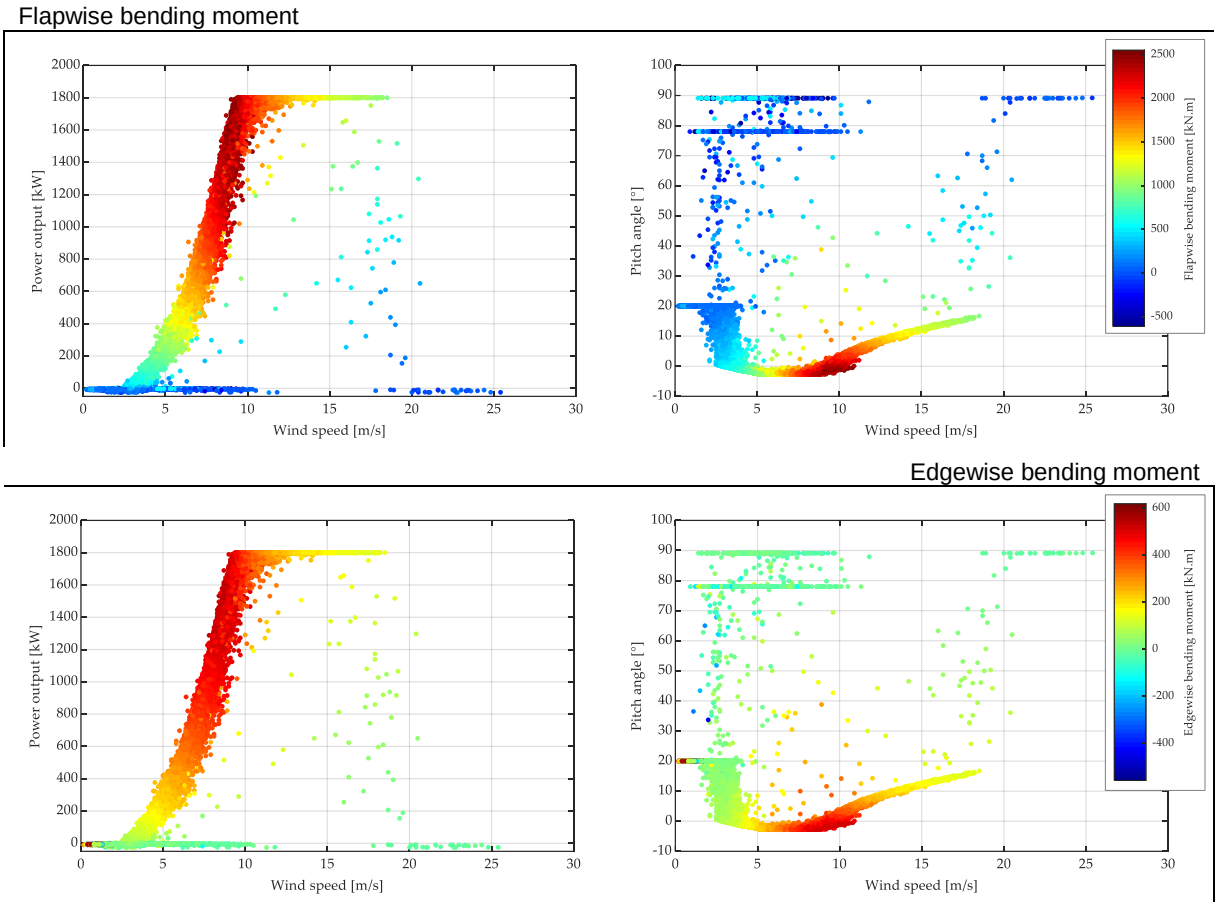


Figure 6.14 – Power curve and variation of the blade pitch angle as a function of the wind speed, considering the flapwise and edgewise bending moments at root of blade A of the WT5.

As shown in the figures, the loads induced on the blades are controlled by wind conditions and the wind turbine control mechanisms. The maximum bending moments occur during power production, for wind speeds close to the rated speed, from which the pitch system control is activated. On the other hand, when the turbine is parked or idling, the installed loads are minimal.

Taking into account the various factors that influence the distribution of loads in the structure, in this section, by combining the strain measurements with the SCADA data and the clustering of the 10-min series into the different operation conditions (described in Section 5.6.3.1), the flapwise and edgewise bending moments at blade roots are characterized considering the six loads cases defined for the tower analysis (Chapter 5).

6.3.2.1 Transient Events

Figure 6.15 represents the 10-min time series of the bending moments at blade roots of WT1 during park/idling conditions. When the wind is below the cut-in wind speed (Figure 6.15a), the variation of the observed bending moments results from the action of the blades weight during the slow rotation of the rotor. Note that the blades are pitched 20°. For this reason, the amplitude of the bending moments is greater in the edgewise direction.

Figure 6.15b shows 10-min bending moment time series during a storm event, with winds speed exceeding 20 m/s. In this case, the blades are pitched to the maximum value. The edgewise bending moments are conditioned by the wind gusts, while the moments in the flapwise direction results from the wind load and the blades' weight due to slow rotor rotation.

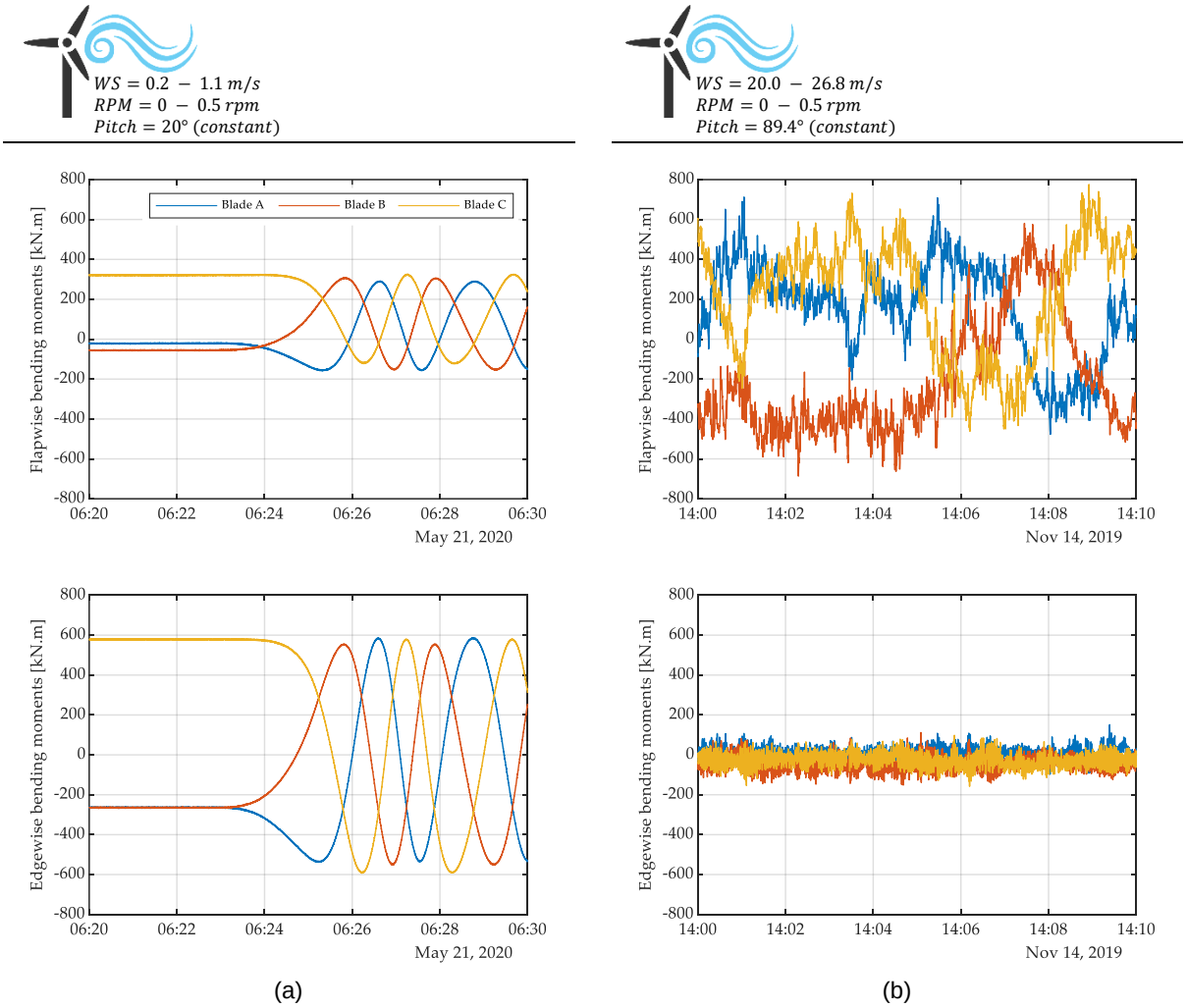
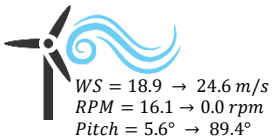


Figure 6.15 – Flapwise and edgewise bending moments at the blade roots of the wind turbine 1, during park/idling conditions: (a) Wind speed below the cut-in speed; (b) During a storm.

The bending moments measured during a shutdown ($WS > 20\ m/s$) event are shown in Figure 6.16. The blades are pitched to 90° (approximately) and, consequently, the bending moments rapidly decreases in both directions and assume a behaviour similar to the one represent in the Figure 6.15b.



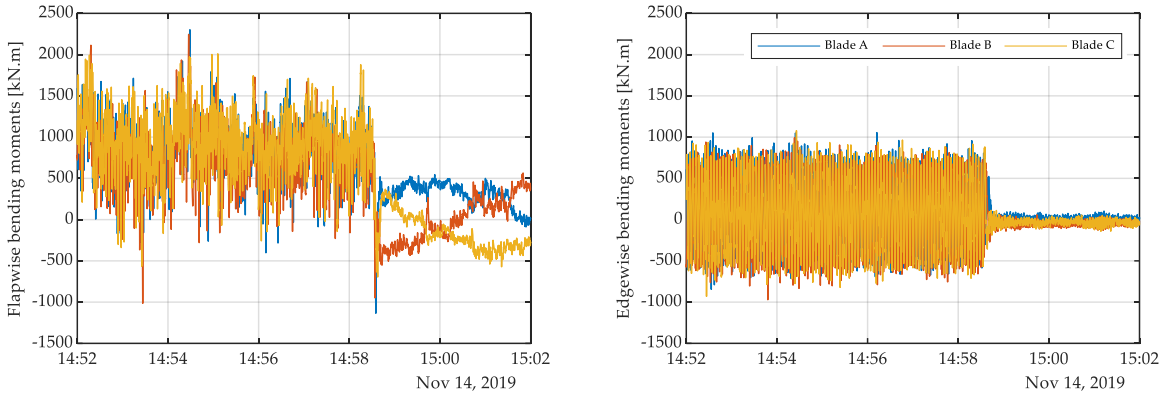
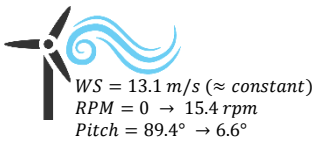


Figure 6.16 – Flapwise and edgewise bending moments at the blade roots of the wind turbine 1, during a shutdown event (wind speed above the cut-out speed).

Figure 6.17 represents the 10-min evolution of flapwise and edgewise bending moments at the blade roots of WT1 at a start-up event. Typically, during a maintenance operation, the wind turbine is parked with a wind speed higher than cut-in speed. When the turbine is commanded to start operation, the pitch angle decreases to typical operating values, and the rotor speed rapidly increases.



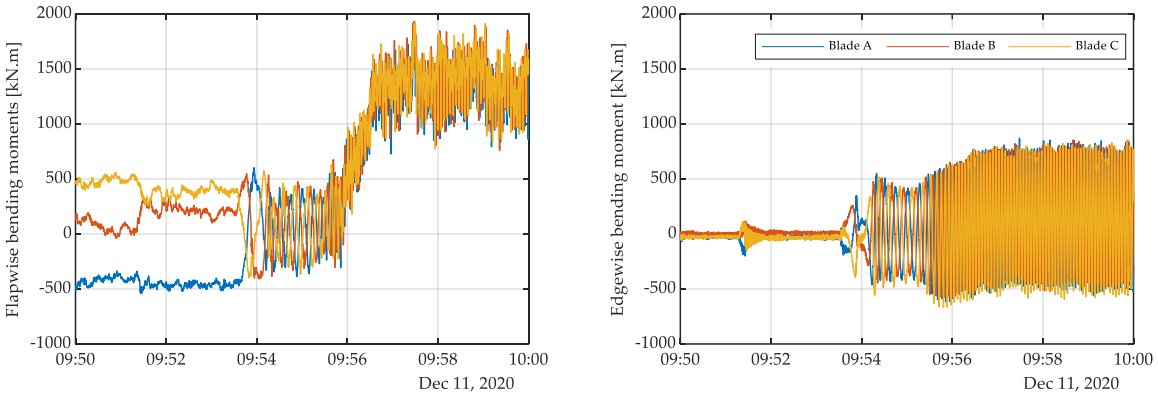


Figure 6.17 – Flapwise and edgewise bending moments at the blade roots of the wind turbine 1, during a start-up event after a maintenance operation (wind speed above the cut-in speed).

The same time period used to represent the bending moments at the base of the tower for repeated starts and stops of production of the wind turbine (Figure 5.13), is now represented for the bending moments measured at the root of the blades of WT1 (Figure 6.18). The starts and stops represent greater variations in moments in the flapwise direction than in the edgewise direction. This observation is justified by the fact that the rotor speed and the pitch angle remain practically constant, while the wind speed has the greatest variations.

$WS = 1.5\ to\ 4.7\ m/s$
$RPM = 1.8\ to\ 10\ rpm$
$Pitch = -3.6°\ to\ 20°$

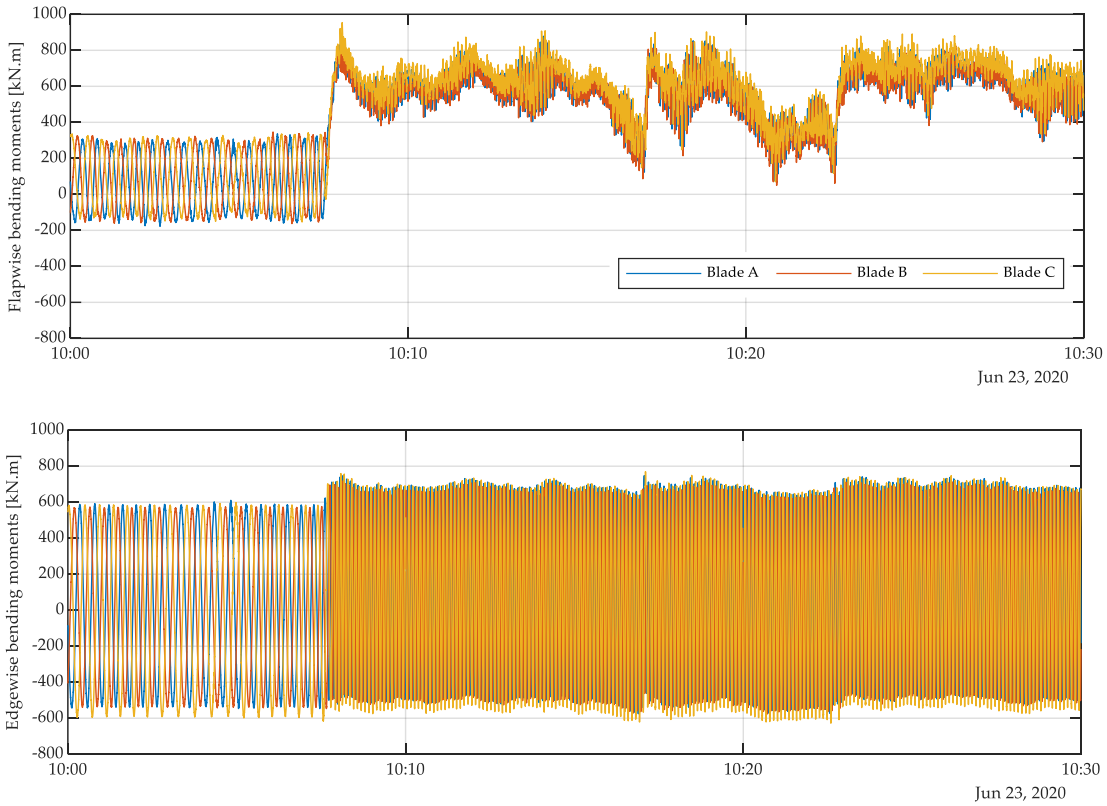


Figure 6.18 – Flapwise and edgewise bending moments at the blade roots of the wind turbine 1 during the start and stop of the turbine around the cut-in wind speed.

6.3.2.2 Power Production

Focusing on the 10-min time series classified as power production, the bending moments measured at blade roots were binned based on the same procedure applied on the tower analyses (described in Section 5.6.3.1). Figure 6.19 shows the 10-min average flapwise bending moment at the blade roots of wind turbines 1 and 5 versus the 10-min average wind speed provided by the SCADA system, considering variable levels of turbulence intensity.

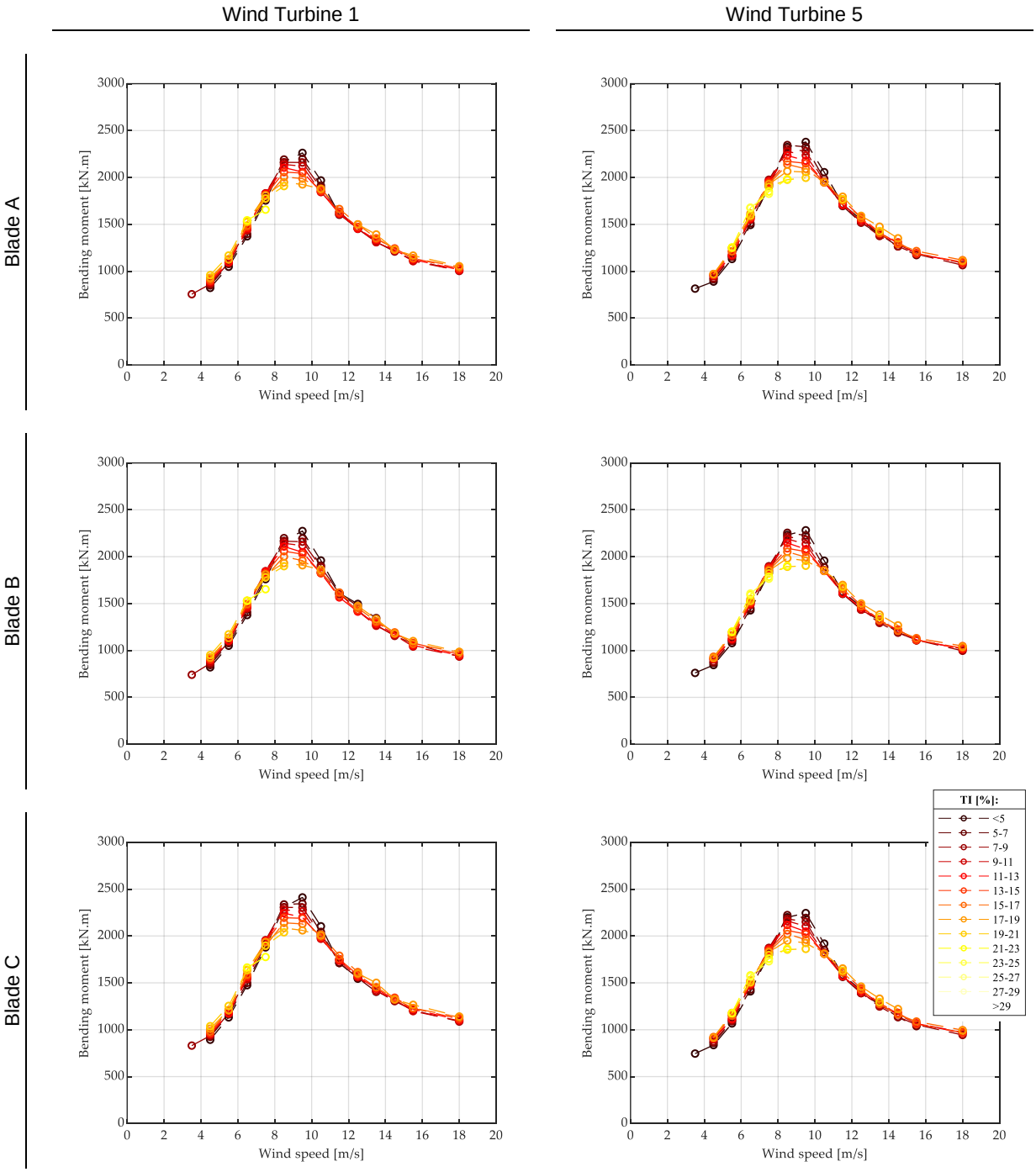


Figure 6.19 – Variation of 10-min average flapwise bending moments at the root of blades A, B and C of the wind turbines 1 and 5 as function of the 10-min average wind speed provided by the SCADA system, considering variable levels of turbulence intensity, during power production.

The obtained curves are very consistent for the 6 analysed blades. The shape of the curves is also similar to one obtained for the variation of the bending moments at the base of the tower for the FA direction (Figure 5.8a) and, in fact, analogous conclusions can be draw. The drag force acting on the blades increases with the wind speed until reaching the rated speed of the turbine. The activation of the pitch control allows to keep the lift force and the rotor speed constant. In this way, the average flapwise bending moment on the blades decreases with the wind speed increase and the associated pitch angle increase. Again, due to the wind turbine control algorithms, the maximum bending moment decreases as the intensity of the turbulence increases.

Comparing the results obtained for the various blades, it appears that blade C of WT1 and blade A of WT5 present slightly higher values. These differences are considered acceptable and are probably explained by inaccuracies in the sensor calibration procedure.

In order to further interpret the results obtained in Figure 6.19, Figure 6.20 represents the time series of flapwise bending moments of three specific bins of the power production regime for blade A of the wind turbine 1.

Considering the wind speed bin where the flapwise bending moment is maximum ($WS =]9 - 10]\ m/s$), two time series associated with different values of turbulence intensity are compared (Figure 6.20a). As shown, the average flapwise bending moment is higher for the lowest turbulence intensity. Although the 10-min average wind speed is similar for both cases, the pitch angle varies between -1.9° and 1.7° (mean -0.6°) for the lower turbulence intensity, and between -3.2° and 7.4° (mean 0.3°) for the larger turbulence. Note that greater average bending moments does not mean greater fatigue damage.

Figure 6.20c represents two time series of flapwise bending moments associated to the same turbulence intensity bin ($TI =]7 - 9]$ %) but with different mean wind speeds. Due to the activation of the pitch angle control, the 10-min average moment is very similar for both cases, although the wind speed is very different. As shown, for wind speeds above the rated speed, the blades are subjected to greater bending moment variations and, probably, larger fatigue consumption.

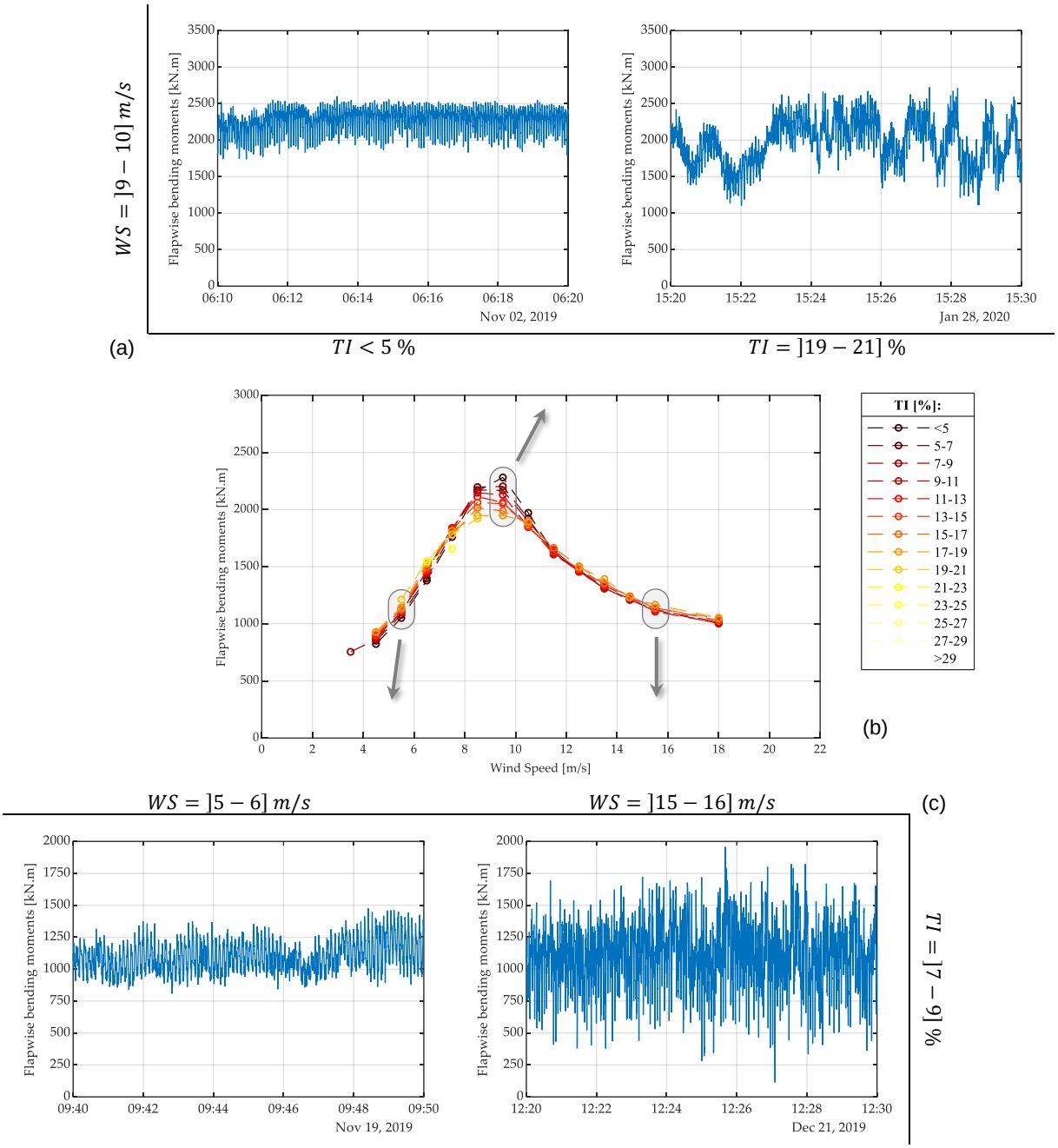


Figure 6.20 – Flapwise bending moments at the root of blade A (WT1) during power production: (a) Bending moment time series for the $]9 - 10]\ m/s$ wind speed bin; (b) Variation of 10-min average flapwise bending moment with the 10-min average wind speed and turbulence intensity; (c) Bending moment time series for the $]7 - 9]$ % turbulence intensity bin.

Figure 6.21 shows the 10-min average edgewise bending moment at the blade roots of wind turbines 1 and 5 versus the 10-min average wind speed provided by the SCADA system during power production and considering variable levels of turbulence intensity.

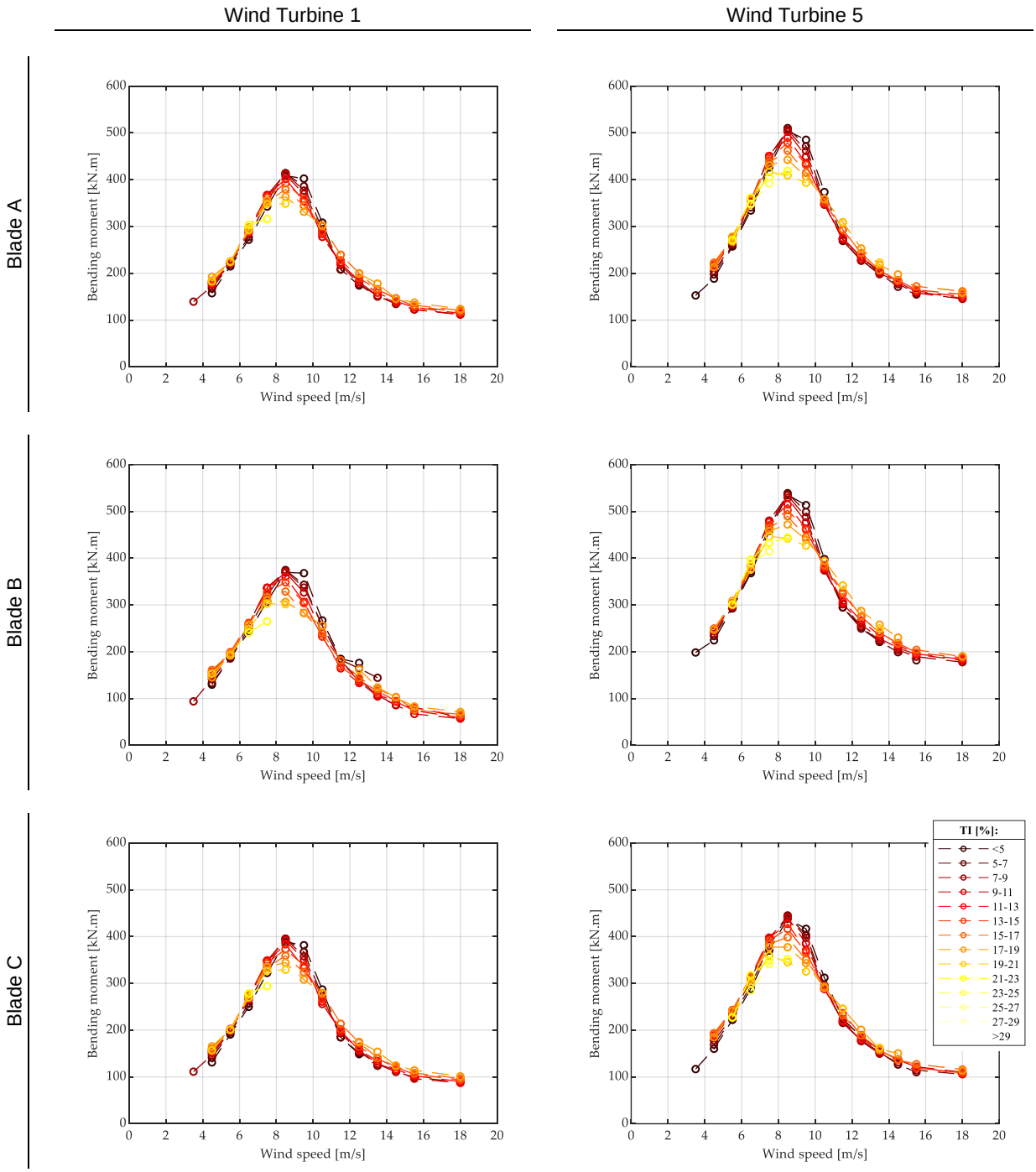


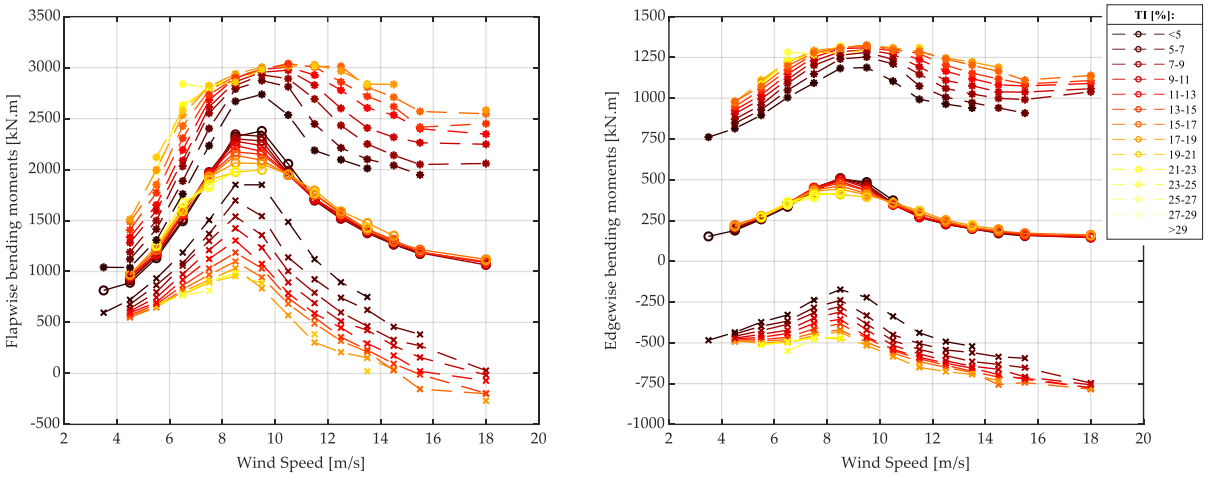
Figure 6.21 – Variation of 10-min average edgewise bending moments at the root of blades A, B and C of the wind turbines 1 and 5 as function of the 10-min average wind speed provided by the SCADA system, considering variable levels of turbulence intensity, during power production.

Comparing the results obtained for the several instrumented blades, it is possible to identify some differences between them. Above all, it appears that the moments obtained for the WT5 blades are slightly higher than those found for the WT1. Again, the calibration procedure may explain these deviations. In fact, sensors calibration can influence the vertical position of the curves presented for different turbines. Despite the installation being carried out by the same team of technicians, the

calibration procedure was performed with different environmental conditions (different days) and the lift and drag forces acting on the blades impacts the calibration accuracy.

The configuration of the curves here presented is very similar to that obtained for the variation of bending moments for the flapwise direction (Figure 6.19). Although, the mean bending moments obtained for the edgewise direction have a smaller amplitude. Since, when the turbine is in production, for small values of pitch angles, the wind action acts approximately in the perpendicular direction. In fact, in production, the edgewise moments are mainly due to the action of the blade's weight. The mean moment increases as the wind speed and the rotor speed increases. When the wind speed exceeds the rated speed, the pitch angle control is activated and the bending moments decreases.

At this point is important to mention that the curves obtained for the mean bending moments in the edgewise direction (Figure 6.21) are not representative of the real moments installed in the instrumented cross-section. Figure 6.22 shows the 10-min mean, maximum and minimum values of the bending moment for flapwise and edgewise directions at root of the blade B of WT5, versus the 10-min average wind speed provided by the SCADA system, during power production and considering variable levels of turbulence intensity.



(a) (b)

Figure 6.22 – Variation of the 10-min bending moments at the root of blade B of the WT5 during power production ('o': mean, '∗': maximum and '×': minimum values): (a) Flapwise direction; (b) Edgewise direction.

As show in Figure 6.22b, wide range of values are observed for edgewise direction between the maximum and minimum values. As mentioned, due the rotor rotation, the load provided by blade weight changes direction twice during each rotor revolution.

On the other hand, in the flapwise direction, the difference between the maximum and minimum values is reduced for lower wind speeds and increases significantly for higher winds. As shown in Figure 6.20c, the dispersion is mainly due to the activation of the pitch angle.

Note that for both directions, as expected, the dispersion of the bending moment increases with the turbulence intensity (the distance between the maximum and minimum moment lines increases for lighter curves).

As it was possible to understand from the results presented so far, the variation of the bending moments at the root of the blades is largely dependent on the variation of the pitch angle and, consequently, of the rotor speed. Figure 6.23 represents de variation of the 10-min average of bending moments at blade B

of WT5 for flapwise and edgewise directions, as a function of 10-min average of rotor speed and pitch angle. The colour of the points indicate the wind speed provide by the SCADA system.

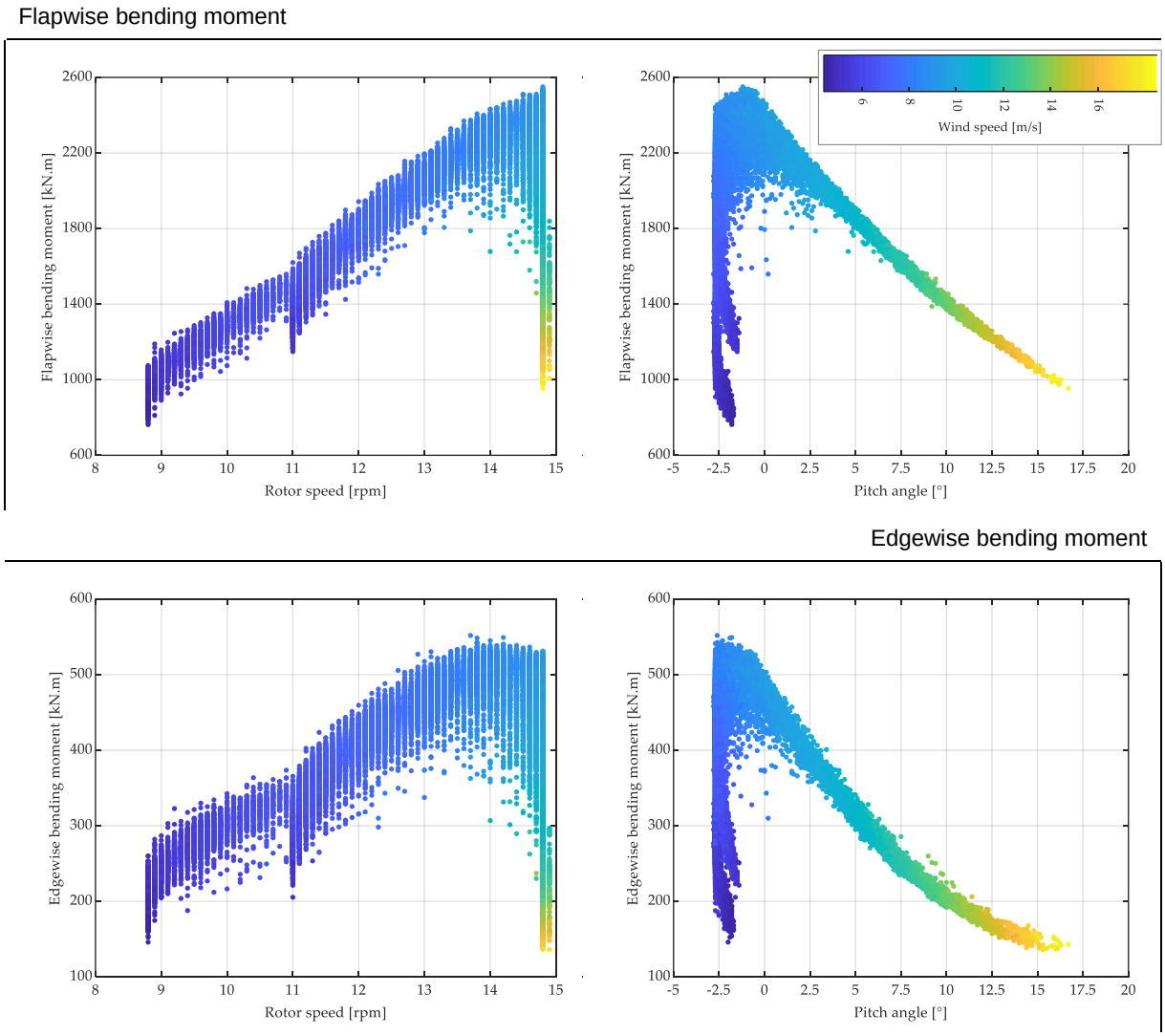


Figure 6.23 – Variation of the 10-min flapwise and edgewise bending moments at the root of blade B of the WT5 during power production, as a function of rotor speed and pitch angle, where the colour of the points indicate the 10-min average wind speed.

The figures show that for lower wind speeds, the pitch angle varies around its minimum value. As the wind increases, the rotor speed and the moments installed in the blades increase. When the maximum of speed of the rotor and bending moments is reached, the pitch angle control is activated. After that, as the wind speed increases, the pitch angle also increases, allowing to keep the rotor speed constant and at its maximum level, while the bending moments decrease.

6.4 PRELIMINARY FATIGUE ANALYSIS

6.4.1 FATIGUE MODELLING OF COMPOSITE WIND TURBINE BLADES

The attractive mechanical properties of composite materials justify their growing use in wind turbine applications. However, considering the current level of knowledge and shortcomings of existing models, characterization of fatigue behaviour of these materials is a very complex task. Furthermore, the generalization and extrapolation of the knowledge acquired with homogeneous and isotropic materials to composite materials (inhomogeneous and anisotropic) is not simple and very limiting in certain aspects. The main difficulty is associated with the fact that a variety of damage phenomena can occur (fibre fracture, fibre buckling, matrix cracking, delamination), each one with their specific growth rates and laws of interaction (Kaminski et al., 2015). Consequently, damage evolution response of composites is very different from the one observed in steel specimens. Figure 6.24a graphically schematizes the difference in damage accumulation evolution between composite materials and homogenous materials (metals). From a certain point of view, fatigue in composites and fatigue in metals are similar. Both begin with damage initiation, followed by damage propagation, and end in ultimate failure. The main difference is in the relative time spent in each phase.

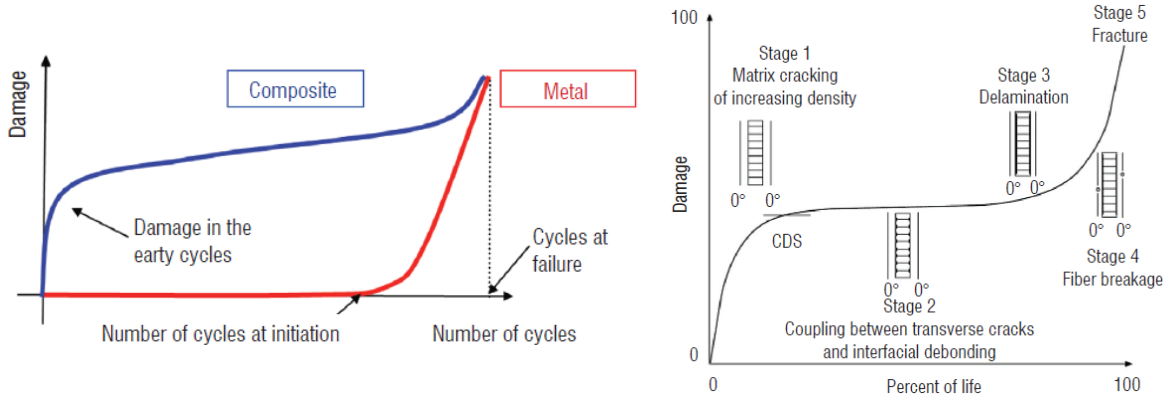


Figure 6.24 – Fatigue damage evolution: (a) Damage as a function of the number of cycles for composites and metals; (b) Stages of damage modes development in composite materials. Adapted from (Kaminski et al., 2015).

For metals, a significant portion of the fatigue process is spent propagating a single crack. As a crack attempts to propagate through the metal, plasticity occurs at the crack tip causing crack blunting and strain hardening. This process can be repeated for many thousands of cycles. In this way, metals present gradual and invisible deterioration during most of their entire lifetime (stiffness remains quasi-constant) and no degradation of material properties is observed during the course of fatigue progress. At the end of the material's life, small macroscopically observable cracks develop across the material, along which they grow until the final fracture (Degrieck & Van Paepegem, 2001). With constant stiffness, the linear relation between stress and strain remains constant throughout the fatigue process.

In the case of composites, strain hardening is negligible. The damage starts very early and the extent of damage zones grows steadily. As show in Figure 6.24b, the type of damage in these zones can change, for example, small matrix cracks can lead to larger delamination (Degrieck & Van Paepegem, 2001). Gradual deterioration, in stiffness and strength, leads to a continuous redistribution of stresses and a relative reduction of the amplitude of stress concentrations within the section studied. In this way, methodologies derived for metals (elastic analysis and linear fracture mechanics) are mostly unsuitable for composites. The fatigue process in a fibre-reinforced composite requires the simulation of the complete sequence of damage states and growth of damage inside the component.

Another important particularity of composite materials is that they often fail catastrophically without any warning, leaving less or no time for repair and maintenance. However, hybrid composites offer pseudo ductility (Zuo et al., 2021). In this way, catastrophic fatigue failure can be avoided by hybridization. But, increasing fibre resistance or matrix toughness, or even improving fibre/matrix bonding, does not always result in an improved fatigue performance (longer fatigue life and higher fatigue ratio) (Kaminski et al., 2015).

Fatigue modelling is still a very recent concern and significant efforts have been made to establish new concepts. Taking into account the particularities presented for composite materials, different fatigue models were developed, which can be divided into three categories: life-based failure criterion models, residual property calculation models and progressive damage models (Degrieck & Van Paepegem, 2001). In this work, only the first method will be applied, because it is widely used in engineering applications. A brief reference to the remaining methods is presented next. A complete literature review of the most notable models that are relevant for the evaluation of the fatigue response of composite wind turbine blades can be found in (Rubiella et al., 2018).

Phenomenological residual properties models represent the first type of progressive damage evolution modelling approach developed. These are based on the phenomenological analysis of residual material properties, proceed by analysing residual properties, as stiffness and strength. These models intended to expresses the growth rate of damage as a function of macroscopically observable properties (D'Amore & Grassia, 2019; van Kuik et al., 2016). However, due to the experimental cost of the Phenomenological models their popularity in research is decreasing in favour of progressive damage models.

Progressive damage models are among the most promising models (Degrieck & Van Paepegem, 2001). The state of deterioration of the studied composite component are described by one or more damage variables. These type of model takes a micro-mechanical approach and is based on the actual damage mechanisms. Loading histories remain a concern given their strong influence on composite failure modes, notably depending on the loading evolution. This approach require a sound physical modelling of the underlying mechanisms of damage. Some examples of fatigue life prediction of composite materials using these models can be found in (Bhattacharya & Ellingwood, 1998; Chaboche, 1988; Diel & Huber, 2017).

6.4.1.1 Constant Amplitude Fatigue Models

In order to study fatigue damage and its effect on the material response, a basic terminology can be defined by analysing a constant amplitude cycle load and assuming the state of the material in terms of stresses, as represented in Figure 6.25a.

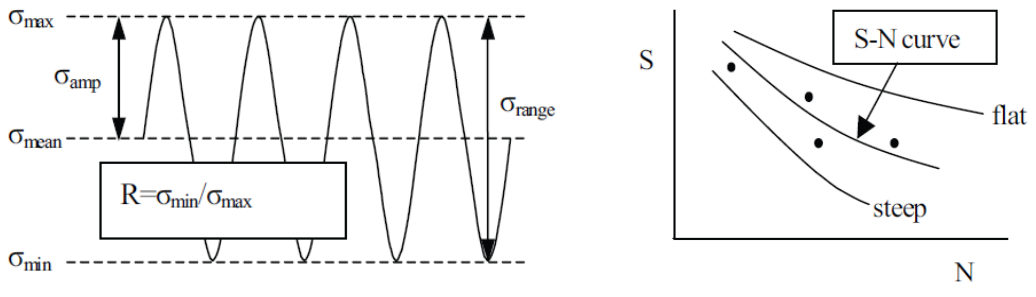


Figure 6.25 – Constant amplitude fatigue models: (a) Basic fatigue terminology; (b) Typical S-N curve trends for composite materials (adapted from (Roger, 2006)).

Considering a constant amplitude stress cycle, in each cycle, the stress varies between a maximum stress (σ_{max}), and a minimum stress (σ_{min}). Based on these two parameters, the variation of the stress over time can be defined by the stress amplitude (σ_{amp}), the mean stress (σ_{mean}), the stress range (σ_{range}) and stress ratio (R), which are defined as follow:

$$\sigma_{amp} = \frac{\sigma_{max} - \sigma_{min}}{2} \tag{6.12}$$

$$\sigma_{mean} = \frac{\sigma_{max} + \sigma_{min}}{2} \tag{6.13}$$

$$\sigma_{range} = \sigma_{max} - \sigma_{min} \tag{6.14}$$

$$R = \frac{\sigma_{min}}{\sigma_{max}} \tag{6.15}$$

Results from fatigue experimental characterisation carried out at constant stress ratio (R) are generally plotted in the form of an S-N curve, represented in Figure 6.25b. The S-N curve represents the applied stress S against the number of load cycles to failure N. Note that for S, can be used as stress, load, strain and displacement. Usually, stress is used for homogeneous materials, and otherwise, strain is currently used for composites (so-called $\varepsilon - N$ curves). Classically, the logarithm of constant amplitude fatigue life N is assumed to be linearly dependent on the logarithm of stress/strain S:

$$\log N = A - m * \log S \tag{6.16}$$

with:

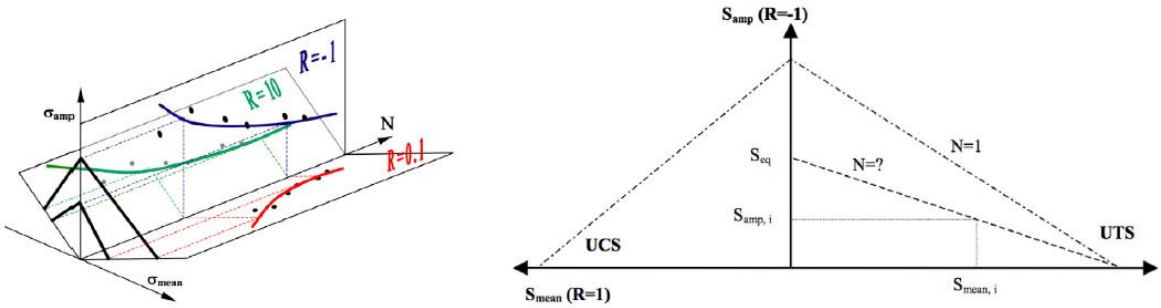
A	Constant which depend on fatigue stress state
m	Slope parameter of the curve

Where A and m are constants which depend on fatigue stress state. It is important to note that each family of S-N curves are associated to a confidence limit, typically 95%. In fatigue experiments, cyclic loads are chosen leading to cycle counts within a limited range. The curves fitted to these experiments need to be extrapolated to higher cycle counts for design purposes. It is possible to observe that fatigue lifetime decreases with increasing stress range. The curve is upper limited by the ultimate strength and below a stress range value no fatigue damage exists.

One limitation of the presented procedure is the disregard of the mean stress on S-N curves. In fact, experiences show that the fatigue lifetime of a component may depend on the mean stress and its amplitude. As explained in Chapter 5, the mean stress can be neglected for homogeneous materials such as steel. However, it is essential to consider the effect of the mean stress and material anisotropy on the fatigue life of composite materials (Park et al., 2014). In the nineteenth century, many approaches were developed to consider the effect of the mean stress. The most common approaches were proposed by Gerber in 1874, Goodman in 1899, by Soderberg in 1930 and by Morrow in the 1960s (Milella, 2013).

The Constant Life Diagram (CLD) is a useful tool to represent the S-N data due its capability to summarize all information on the material's fatigue behaviour. The CLDs aim to consider the differences in the fatigue response of the composite materials under different loading conditions, taking in to account the effect of the mean stress and material anisotropy on the fatigue life of composite

materials. Figure 6.16 represents a schematic of the relation between S-N curves and a constant life diagram. The diagram is the projection of constant amplitude fatigue data on a plane perpendicular to the life axis (N-axis). Constant lifelines in the projections connect points with the same estimated lifetime, as a function of the mean stress and stress amplitude (Roger, 2006). For composites, constant life diagrams are not symmetric, since the composite tensile properties are dominated by fibres and the matrix provides support to fibres when subjected to compressive forces. So, the ultimate tensile strength (UTS) is higher than the ultimate compressive strength (UCS).



(a) (b)

Figure 6.26 – Fatigue life prediction models: (a) Schematic constant life diagram for composites; (b) Linear Goodman Diagram (adapted from (Roger, 2006)).

Linear Goodman diagram, as represented in Figure 6.16b, is the most commonly used diagram for composite materials. An ample discussion on Goodman diagrams data and applications can be found in (Philippidis & Vassilopoulos, 2004). In conclusion, fatigue-life models are simple and straightforward models based on empirical relations that can be easily implemented for the fatigue analysis of wind turbine blades. These are adopted in current standard lifetime prediction methods, as the IEC 61400-1 international standard (International Electrotechnical Commission, 2014) and the DNV GL certification and design guidelines (DNV GL AS, 2015).

6.4.1.2 Variable Amplitude Fatigue Models

The variable amplitude load time history is converted to a series of constant amplitude cycles that can then be analysed with a Goodman diagram using the rainflow counting over range-mean counting. Due to cycling loading, fatigue damage increases in a cumulative way. As explained for homogeneous materials in Chapter 5, the Palmgren-Miner linear damage rule (1945), is one of the most widely recognized linear cumulative damage models for fatigue analysis, and likely among the simplest.

$$D_{Total} = \sum_i \frac{n_i}{N_i} \leq 1 \tag{6.17}$$

Where D_{Total} is the total damage, n_i is the number of load cycles in the fatigue load block i, and N_i is the allowable number of cycles for the load amplitude $S_{k,amp}$ and mean $S_{k,mean}$ in block i. Failure is considered to occur when the value of the accumulated damage (damage sum) is equal to 1.

A shortcoming of Miner's rule is that it fails to predict sequence effects. So, it does not reproduce the observation that depending on the sequence of loading applied to a component, the damage mechanisms undergone by the component may vary. In other words, if cycles with low stress amplitude loads are

applied a few times, these may not be enough to initiate a damage. Although if there is a pre-existing crack, these cycles with low stress amplitude could be enough to propagate the damage already in the component.

Various other damage accumulation models have been proposed since the Palmgren-Miner rule. Owen and Howe (Owen & Bishop, 1974) developed a subsequent, non-linear version of Miner's Rule in order to improve the first damage rule for glass reinforced polymer composites:

$$D_{Total} = \sum_{i} \left[A * \frac{n_i}{N_i} + B * \left(\frac{n_i}{N_i} \right)^q \right] \tag{6.18}$$

Where A and B are data-fitting constant parameters. High cycles fatigue are characterized by high q values that decreases toward unity as the stress increases. Note that Miner's rule is a particular case of this equation, assuming $q = 1$. However, there are some practical problems in the application of these nonlinear methods. These methods require material and shaping constants which must be determined experimentally, and this requires a high number of tests. Furthermore, to take into account the sequence of effects, the number of calculations can become a problem in complicated load histories (H. J. Sutherland, 2000).

6.4.2 FATIGUE RESULTS

Taking into account the particularities mentioned in the previous section about fatigue analysis of composite materials, Figure 6.27 shows an overview of the procedure adopted in this work for fatigue damage estimation based on strain measurements at wind turbine blade roots.

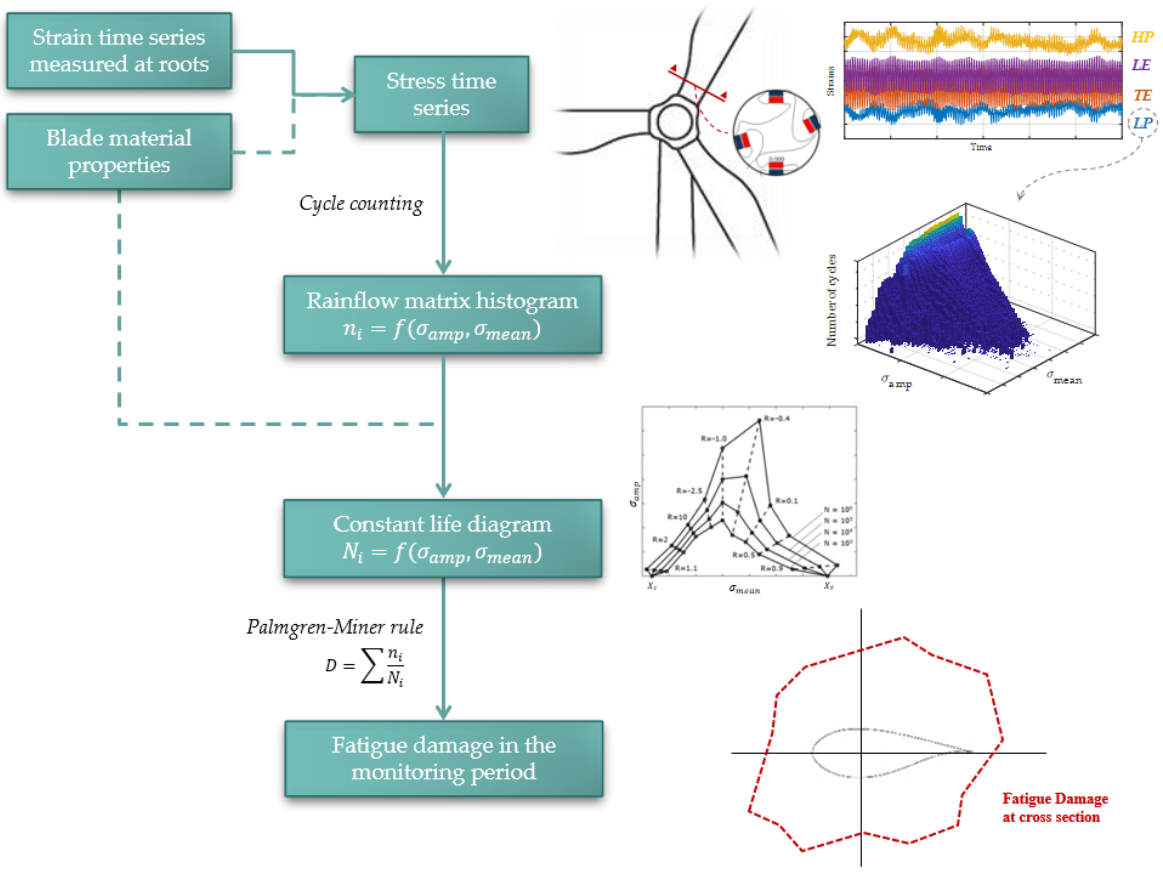


Figure 6.27 – Fatigue assessment of wind turbine blades based on strain measurements.

As mentioned, the growth of damage is a complicated process and the structural degradation is a non-linear and history-dependent process. However, in this work, for a preliminary experimental fatigue evaluation, a simplified approach was used. Similar to the procedure described in Chapter 5 for tower fatigue assessment, fatigue damage is measured by the cumulative damage D_{Total} given by the Palmgren-Miner linear damage rule, as represent in equation 6.17.

The 10-min strain time series measured at the blade roots and pre-processed as described in Section 6.3.1 are the inputs of this procedure. The longitudinal stresses are obtained multiplying the strain signal by the Young's modulus of the blade material (see Table 6.1), according the equation 5.1. Note that, in this work the fatigue analysis was performed on stresses rather than strains, since the S-N curves used later were defined in stresses. Furthermore, since the acquisition system was programmed with a high sampling frequency (100 Hz), the strain signal was filtered (Butterworth filter) and then resampled to 50 Hz, as describe in Section 5.5.

First, detailed time histories of mean stress, amplitudes, and cycles is needed. From the 10-min time series measured, the rainflow method (describe in Section 5.3.4) was used to extract the number of cycles (n_i) for given stress amplitude and mean stress bins.

In order to calculate the permissible number of cycles (N_i) for a given stress state (mean value of the stress $S_{k,M}$ and amplitude of the stress $S_{k,A}$), based on the Goodman method, the following equation, provided by DNVGL-ST-0376 standard (DNV GL AS, 2015), was adopted:

$$N_i = \left[\frac{\frac{R_{k,t} + |R_{k,c}|}{2} - \left| \gamma_{m,short\ term} \cdot S_{k,m} - \left(\frac{R_{k,t} - |R_{k,c}|}{2} \right) \right|}{\gamma_{m,fatigue} \cdot S_{k,A}} \right]^m \quad (6.19)$$

with:

$R_{k,t}$	Characteristic short term structural member resistance in tension
$R_{k,c}$	Characteristic short term structural member resistance in compression
m	Slope parameter of the S-N curve
$\gamma_{m,short\ term}$	Reduction factor γ_m for short-term verification
$\gamma_{m,fatigue}$	Reduction factor γ_m for fatigue verification

At this point, it is important to define the properties of the material that makes up the wind turbine blades. However, this information is not provided by the manufacturer. The search in the main bibliography of the subject allowed to define current characteristics of the material for blades made of fibreglass reinforced epoxy and carbon fibres (Andersen et al., 1996). The assumed properties of the blade material are presented in Table 6.1.

Table 6.1 – Material properties of the wind turbine blades adopted in this work.

Properties of blade material	
Maximum tensile strength [MPa]	670
Maximum compression strength [MPa]	475
Young's modulus [GPa]	29.5
Slope of the S-N diagram	11.5

It should be noted that the purpose of this work is to demonstrate the application of a methodology for experimental fatigue assessment of blades and to analyse relative results obtained for the two instrumented rotors. So, eventual discrepancies between the adopted values and the real values of the blades material properties will not negatively impact the referred goals.

6.4.2.1 Rainflow Matrix Histograms

For fatigue analysis, the stress fluctuations should be specified in terms of mean, amplitude and number of cycles. According to the DNV-OS-J102, a minimum resolution for the discrete values of stress should be defined, and then the detailed time history should be established in discrete form by rainflow analysis (Det Norske Veritas (DNV), 2010).

In this case, the fatigue loads are represented in a matrix form, with one row for each mean strain bin, one column for each strain amplitude bin, and the number of counted cycles as the entry of each matrix element. Based on the analysis of the collected experimental data, the strain amplitude (ε_{amp}) was computed for a strain range from 0 $\mu\varepsilon$ to 2500 $\mu\varepsilon$, divided into 250 bins (bin amplitude of 10 $\mu\varepsilon$). The mean strain (ε_{mean}) was calculated for a strain range of -2000 $\mu\varepsilon$ to 2000 $\mu\varepsilon$, with a bin amplitude of 40 $\mu\varepsilon$ (100 bins).

Figure 6.28 represents the rainflow matrix histogram for edgewise direction (TE and LE sensors) at blade A of the WT1, considering power production. These sensors measure the strain caused by inertial forces (weight of the blade) during each rotation. For low wind speeds and low turbulence, it is expected that this signal was constant amplitude and zero mean. This behaviour is corroborated by the peak of the histogram for mean strains close to zero and amplitudes close to 500 $\mu\varepsilon$.

However, for high wind speeds there is another factor influencing the signal recorded by the sensors, the activation of the pitch angle. With pitch angle activation, sensors TE and LE will measure bending moment time histories with two contributions: blade weight and wind loads on the blade.

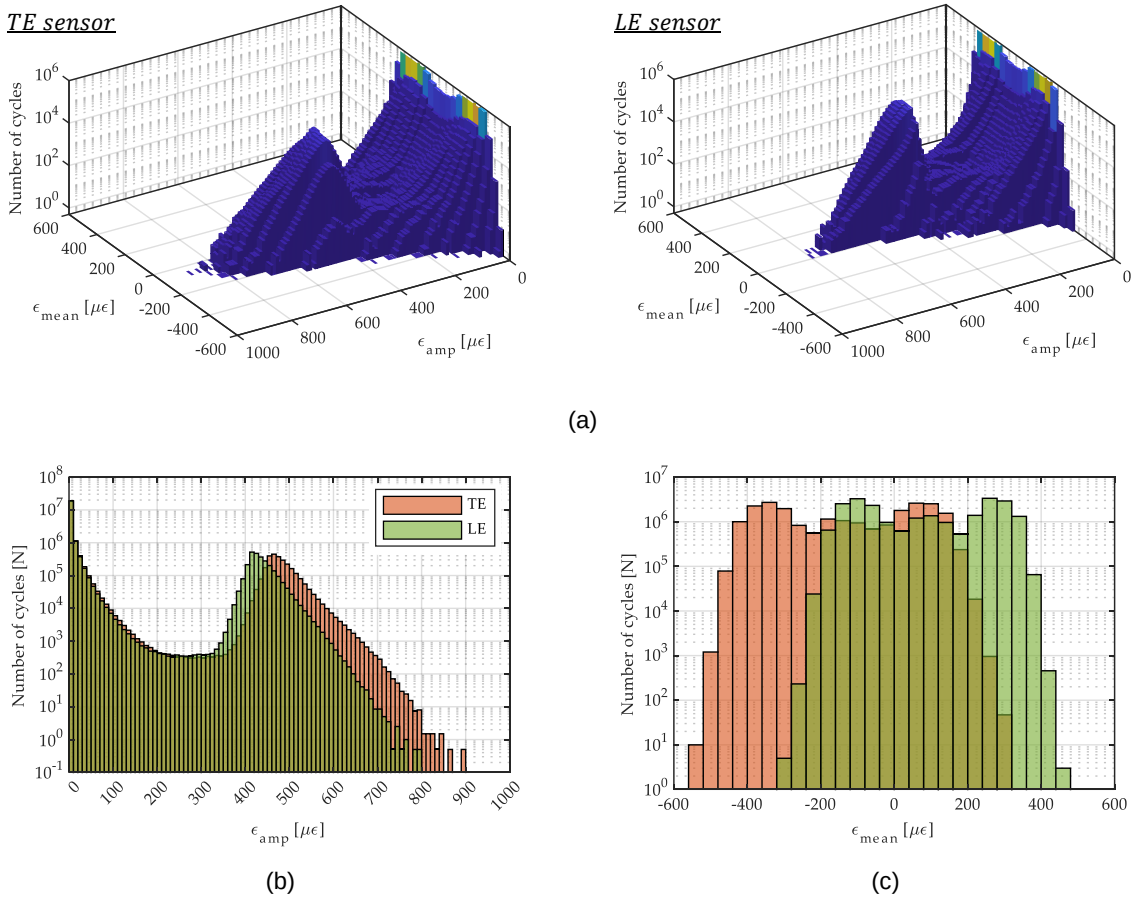


Figure 6.28 – Rainflow counting cycles at root of the blade A of WT1 for edgewise direction: (a) 3D rainflow for TE and LE sensors; (b) Number of cycles as a function of strain amplitude; (c) Number of cycles as a function of mean strain.

Focusing on flapwise direction, HP and LP sensors measure strains essentially induced by the wind loads. When the turbine is in operation, the high-pressure side of the blade is under tension, while the low-pressure side is in compression. This behaviour can be seen in Figure 6.29 which represents the

rainflow matrix histogram for flapwise direction (HP and LP sensors) at blade A of the WT1, considering power production.

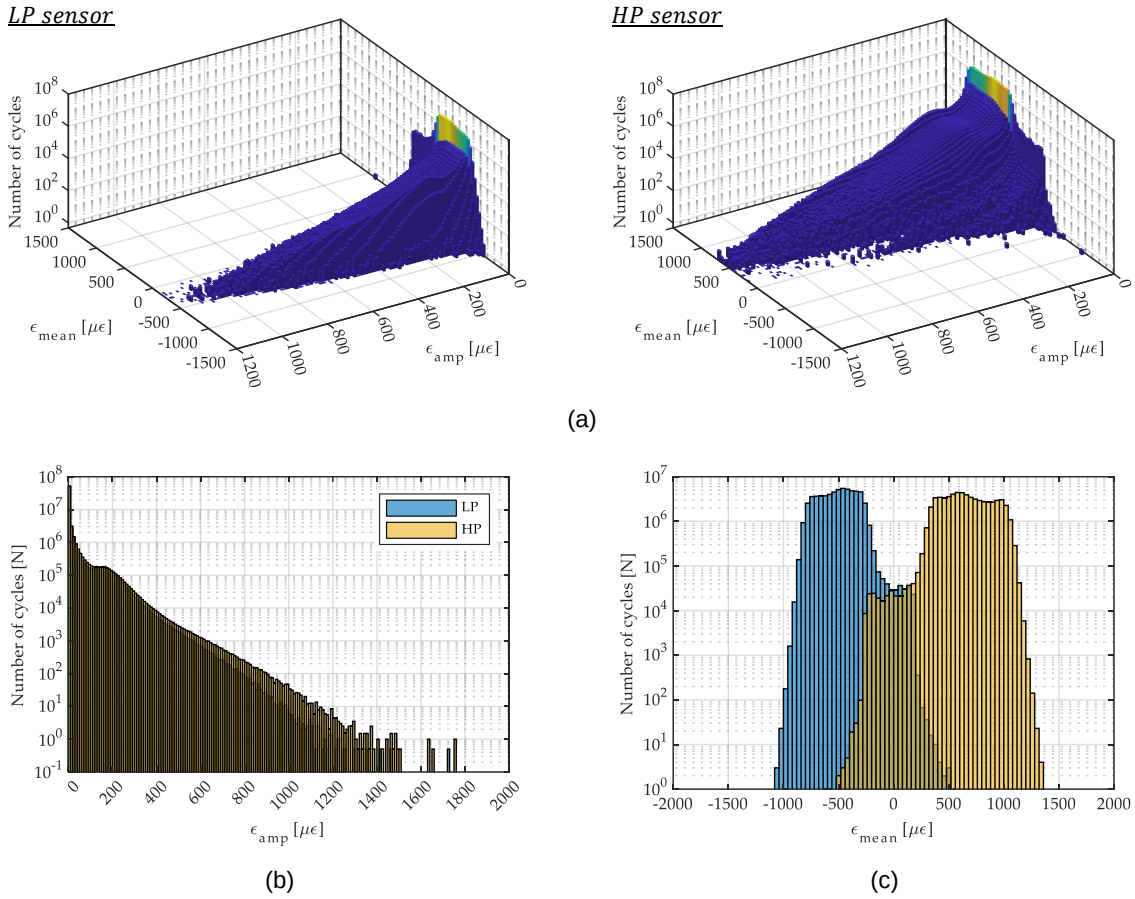


Figure 6.29 – Rainflow counting cycles at root of the blade A of WT1 for flapwise direction: (a) 3D rainflow for LP and HP sensors; (b) Number of cycles as a function of strain amplitude; (c) Number of cycles as a function of mean strain.

Comparing the histograms obtained for the two main directions, it is possible to observe a greater range of strain amplitudes and mean strains for the flapwise direction. On the other hand, the high number of cycles with amplitudes of 500 $\mu\varepsilon$ (resulting from rotor rotation) for the edgewise direction will certainly have a significant impact on accumulated fatigue damage.

It is important to note that this analysis was performed for all rotor blades of wind turbines 1 and 5. Similar results were found considering the strain amplitude and mean strain.

6.4.2.2 Fatigue Damage

The experimental data collected during about one year, from November 2019 to December 2020, was processed according to the procedure described in Section 6.4.2. The time evolution of the 10-min damage calculated at the instrumented points of wind turbines 1 and 5 is presented in Figure 6.30. The gaps observed in these figures are associated with recording problems. The histograms in the figure represent the average relative frequency of the fatigue damage evaluated in each sensor of the three blades of the respective wind turbine. The damage values shown are normalized (due the confidentiality constraints) and the same vertical scale was used in all plots.

In the figures, the points above the orange and red dashed lines represent, respectively, 50% and 99% of the accumulated damage over the monitoring period. As it was observed for tower fatigue analysis (Section 5.6.3.1) the damage mainly occurs during storms and high wind speed periods.

As a result of the wind action mainly in the flapwise direction, there is a greater dispersion of the damage values evaluated by the sensors sensitive to the bending moments in this direction. In the respective histograms it is possible to identify a peak for normalized damage values close to 0.58. This peak corresponds to the turbine idling. The blades are pitched at 20° and the rotor is in slow rotation (typical $<$1 rpm), similar to that described in Figure 6.15a. The variation of the weight component in this direction is responsible for these damage values.

On the other hand, the damage for the edgewise direction show less dispersion. As mentioned, the damage for this direction results mainly from the variation of the blade's own weight load in each rotor revolution (more deterministic action).

Comparing the damage according to each pair of sensors in each direction, it is verified that the values obtained are not exactly the same. The differences found were already justified with the analysis of the respective rainflow histograms. However, in the final evaluation of the damage these differences seem acceptable.

Comparing the data obtained for the two wind turbines analysed in this chapter, in general the damage values are higher for the WT5. The fact that WT5 is located in the wake of WT1, for the main wind direction may explain these results (Figure 5.41). However, this topic will be addressed later.

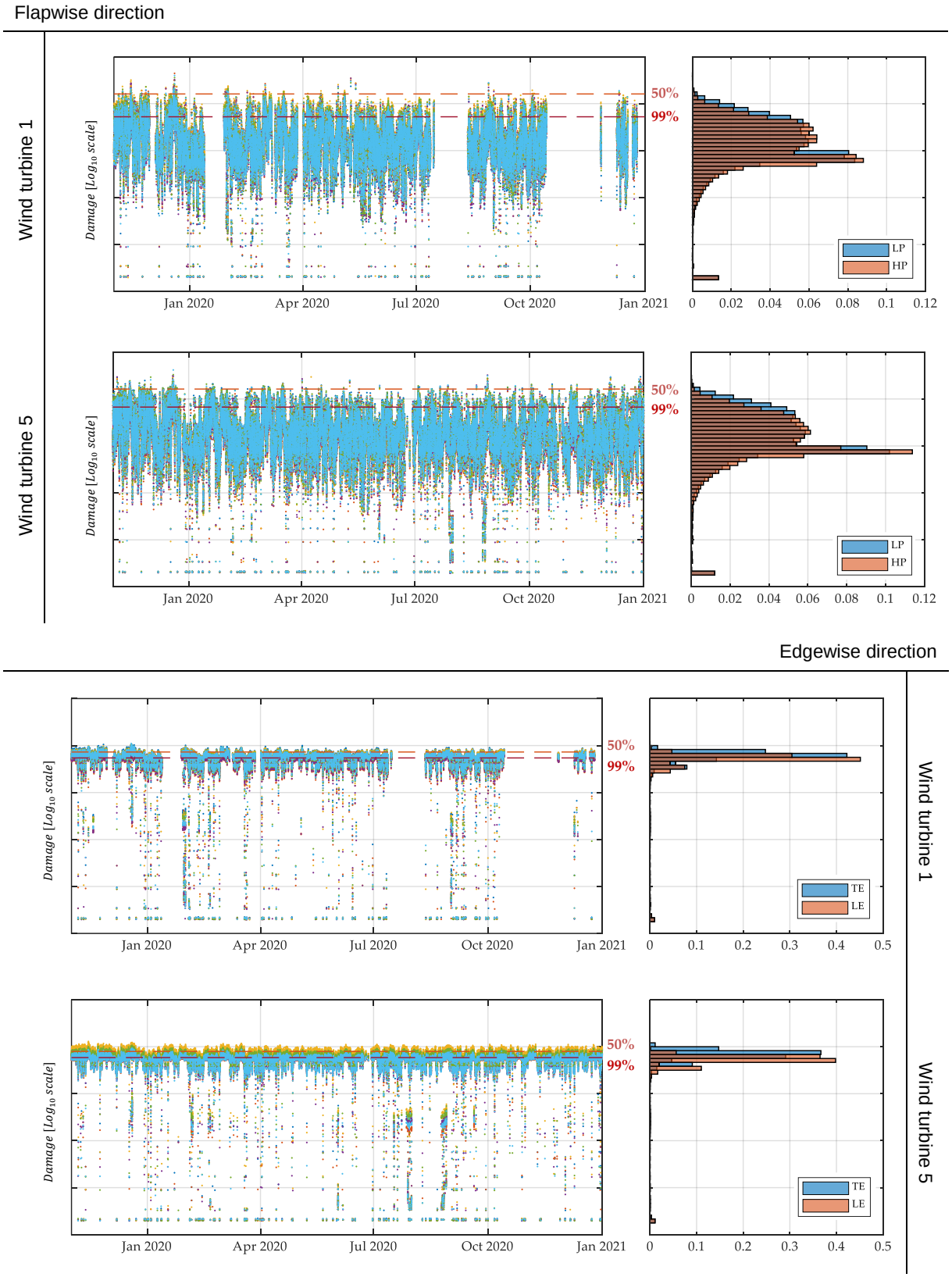


Figure 6.30 – Time variation of the normalized short-term damage for flapwise and edgewise direction for WT1 and WT5 over the monitoring period and corresponding histogram (all figures have the same vertical scale).

In order to demonstrate the influence of environmental and operational parameters on damage accumulation at blade roots, Figure 6.31 represents the 10-min damage for the flapwise and edgewise direction (average values for sensor pairs in each direction at blade A of WT5) as a function of the wind speed, blade pitch angle and rotor speed. The different load cases defined in Section 5.6.3.1 are identified in the figure with different colours. Due to its low representativeness, the "power production with fault" cluster was not included in the figures. The damage values shown are normalized and the same vertical scale was used in all plots.

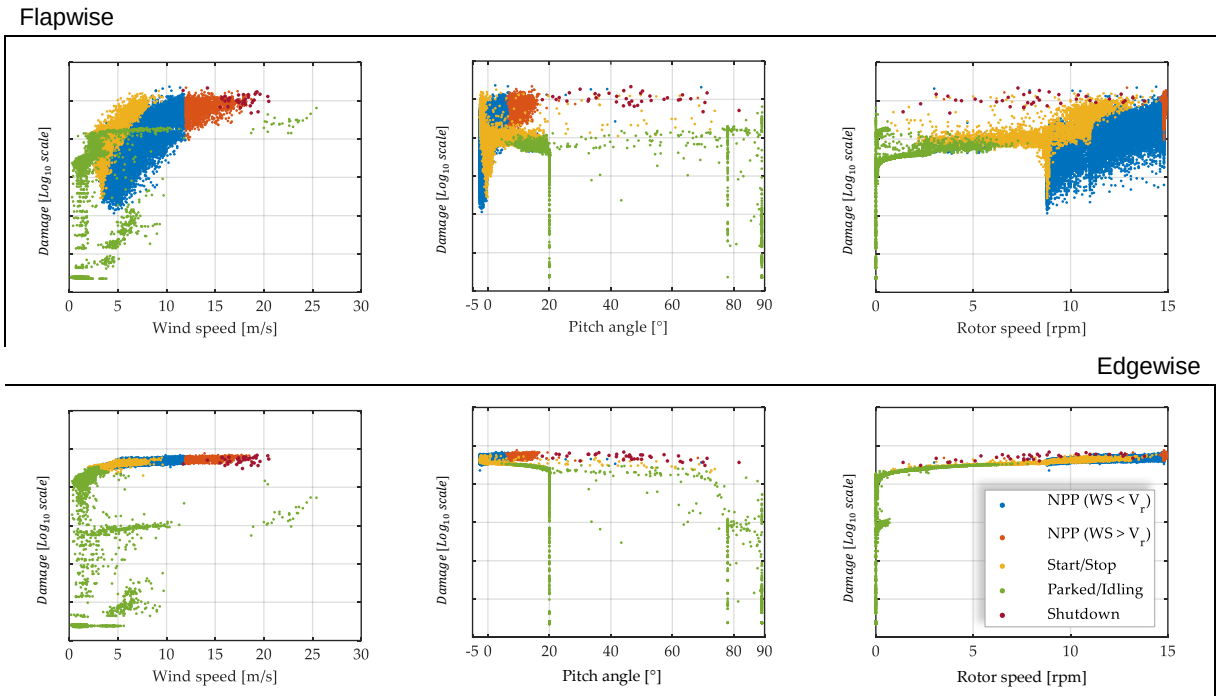


Figure 6.31 – Variation of the average damage at flapwise and edgewise directions (mean values for blade A of WT5) as a function of the environmental and operational parameters considering five load cases (all figures have the same vertical scale).

Once again, there is a greater dispersion of the results for the flapwise direction in relation to the edgewise. Wind speed plays an important role in fatigue life progression of wind turbine blades. In fact, especially in the flapwise direction, the time series associated with higher wind speeds represent the most significant impact on fatigue damage.

As shown in the figures, shutdown events (red points) and normal production having the pitch control system activated (orange points) have the higher normalized damage values. On the other hand, parked and idling load cases (green points) have lower damage values, but still relevant for the edgewise direction These results are in agreement with those shown in Figure 6.32 that represents, for each load case, the percentage of the operating time over the monitoring period, the contribution to the total accumulated damage and the relative damage (calculated as the ratio of the associated damage and the associated operating time). The figure represents the average values for all blades of WT1 and WT5, according to the two main directions.

Despite the record failures observed for WT1, the frequency of each load case is similar for the two wind turbines. Furthermore, the results obtained in terms of relative damage are similar for the two instrumented wind turbines. As shown in the figure, an important percentage of the monitoring period occurs during power production when the wind speed is lower than rated speed (69%), followed by parked/idling (18%) and start/stop (11%).

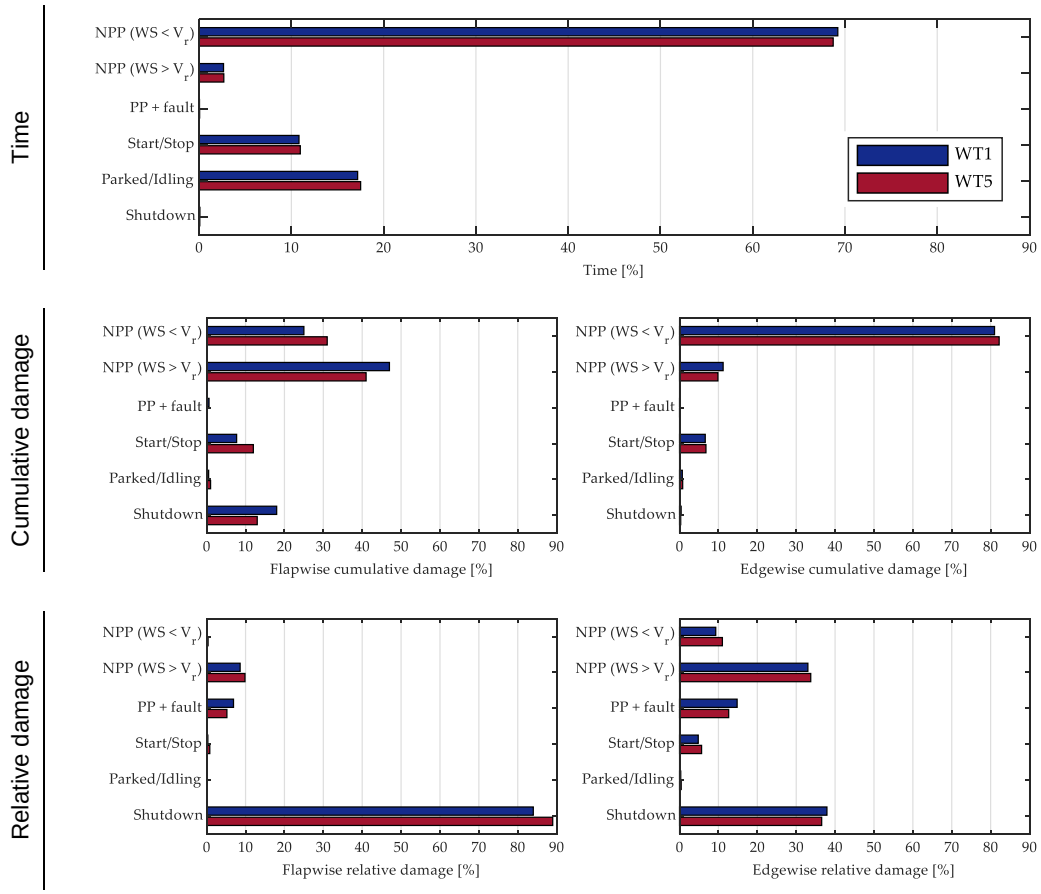


Figure 6.32 – Total time and relative damage at wind turbines 1 and 5 for different load cases (average values for all blades of each wind turbine, according to each damage main direction).

As shown, relative damage has a different distribution for the two main directions. Again, the differences found can be explained based on the main loads acting in each direction. For the flapwise direction, the shutdown events are clearly the most severe load case. It is important to note that although much of the damage accumulates during turbine operation, this does not represent the most critical case of operation. Considering the edgewise direction, there is no load case that stands out so clearly. However, shutdown events and normal operation above rated wind speed represent the most critical cases.

As in the analyses carried out in Chapter 5, only the short-term damage classified as power production (10-min time intervals during which the turbine produces power) is considered in the following analysis. Based on a similar approach described in IEC 61400-13 for power production load cases, the calculated short-term damage values are classified according to the wind speed and turbulence intensity.

Figure 6.33 shows the 10-min average flapwise and edgewise damage at the blade roots of wind turbines 1 and 5 versus the 10-min average wind speed provided by the SCADA system, considering variable levels of turbulence intensity. The damage values shown are normalized and the same vertical scale was used in all plots. A zoom of the results is also presented for the sensors in the edgewise direction.

A clear trend of fatigue damage increase for increasing levels of wind speed and turbulence intensity is observed. However, as already mentioned, the damage variance is less significant for the edgewise direction than for the flapwise direction. In fact, the damage in the edgewise direction is less influenced by operating and environmental conditions. As referred for Figure 6.30, the damage calculated for WT5 is slightly higher than for WT1. This subject will be discussed in detail afterwards.

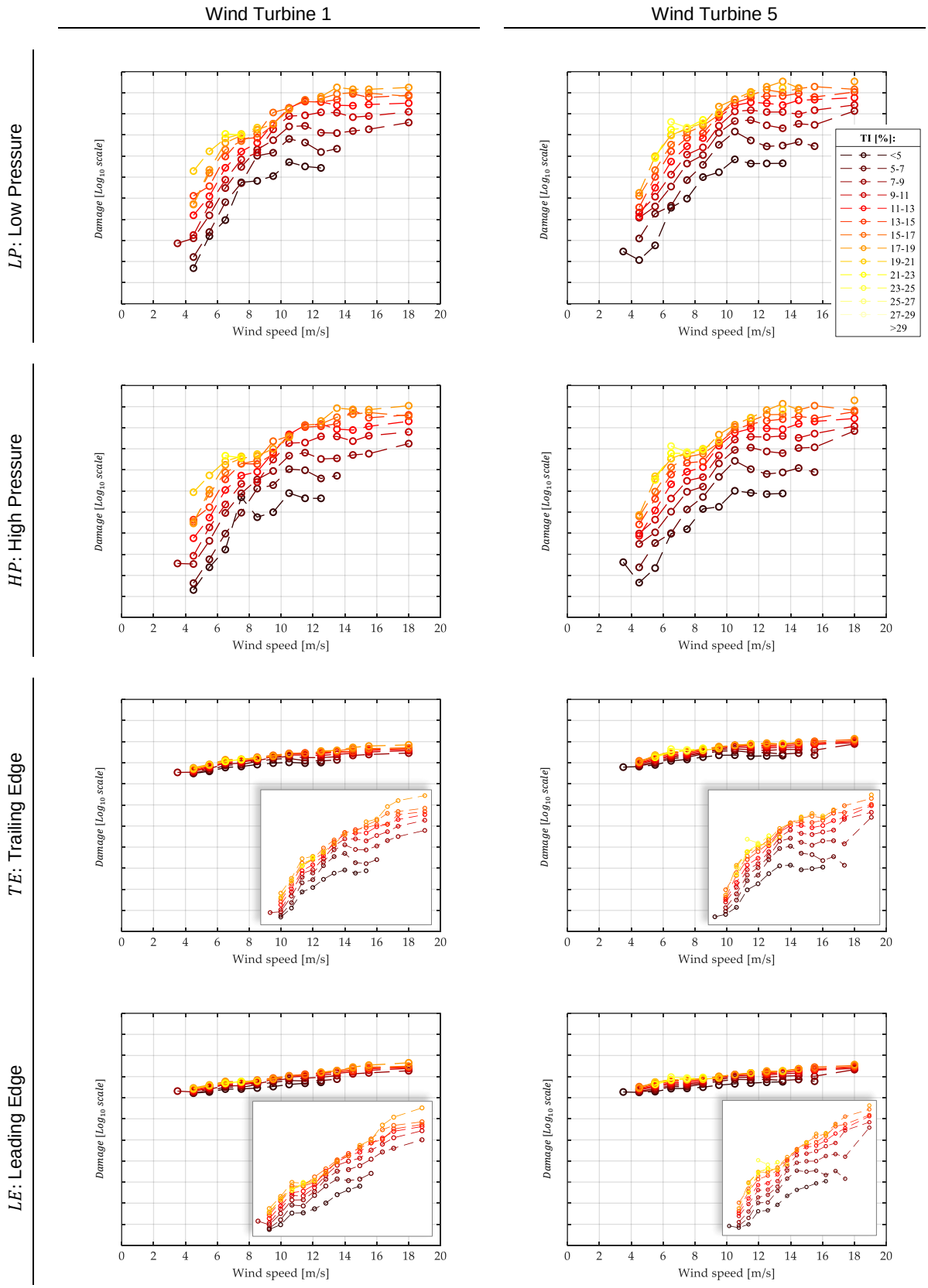


Figure 6.33 – Average 10-min damage at flapwise and edgewise directions at WT1 and WT5 considering power production, as a function of the wind speed and turbulence intensity, with zooms for the edgewise direction.

6.4.2.3 Effect of Wakes in Fatigue Damage of Wind Turbine Blades

It should be noted that the main objective of this chapter is to evaluate the influence of the neighbouring turbines wakes on the accumulated damage. In a wind farm, the upstream wind turbines disturb the upcoming flow field and increase the downstream turbulence (Besnard & Bertling, 2010; Sedaghatizadeh et al., 2018; Sun & Yang, 2018). The wind coming out of a turbine is very turbulent and has lower velocity, so-called wake, as most of its energy was already extracted. Consequently, wake effects increase the fatigue loads on wind turbines in operation. However, the wake flow is considerably different from the traditional boundary layer flow, and poses many challenges in determining the fatigue loads on wind turbines operating in a wake (Vera-Tudela & Kühn, 2017).

As a result, detailed examinations of the wake effects on the fatigue loads and subsequent fatigue damage are needed. The first studies were conducted by Thomsen and Sørensen (Thomsen & Sørensen, 1999). It was found that the most important parameters determining the fatigue load are the turbulence intensity and the length scale of the wind. Posteriorly, the study of wake effects on the fatigue loads allowed to understand that the additional turbulence intensity significantly increases the fatigue loads (S.-H. Kim et al., 2015; Lee et al., 2013). More recently, computer simulations were used to evaluate the dynamic response of a wind turbine under an arbitrary distribution of the flow field, varying in space and time, allowing the estimation of fatigue loads on a downstream wind turbine located at various positions in the wake (Z. Liu et al., 2020). Most of the work developed in this area is based on numerical or analytical analysis. Therefore, the experimental evaluation of wake effects based on experimental data is of great importance.

A distinct division can be made into the near and far wake region. Typically, the near wake region extends from just behind the turbine rotor to approximately one to three rotor diameters downstream. This region is influenced by rotor angular velocity and blade geometry and includes stalled flow, 3D effects and tip vortices. The far wake is the region beyond the near wake, where the main attention is put on turbulence models and topographical effects (Vermeer et al., 2003).

A wind turbine placed within the wake region of an upstream turbine will experience reduced energy production and increased mechanical stresses. As an example, reference (Weipao et al., 2016) states that a second-row turbine located $7D$ downstream of the front row (where D is the rotor diameter) produces 44% less power. The most obvious solution is increasing the space between wind turbines to let the wake recover back to undisturbed free-stream conditions. In this sense, some studies indicate $20D$ as the required recovery length (Ghaisas & Archer, 2016). However, for the most recent wind turbine rotor diameters (currently over 200 m), such large spacing is not practical.

Trying to contribute to this very relevant research filed, in the present work, the fatigue damage was calculated considering three yaw sectors. These sectors were defined considering the difference between the turbulence intensity at WT1 and WT5 and the average turbulence intensity observed in the five turbines of the farm, as a function of the wind direction, as represent in Figure 6.34. For better analysis of these angles, Figure 6.34 should be observed together with Figure 5.41 from Section 5.6.5, which identifies the wakes for WT1 and WT5.

In the first yaw sector, WT5 is in operation in the wake of WT1 ($yaw\ angle = 346° \pm 5°$). The reverse situation is represented with yaw sector 2 ($yaw\ angle = 166° \pm 5°$). Finally, in yaw sector 3 both wind turbines are subject to unperturbed wind flow ($yaw\ angle = 250° \pm 20°$). It should be noted that in the following analyses, only 10-min time periods in which both wind turbines are in production are considered.

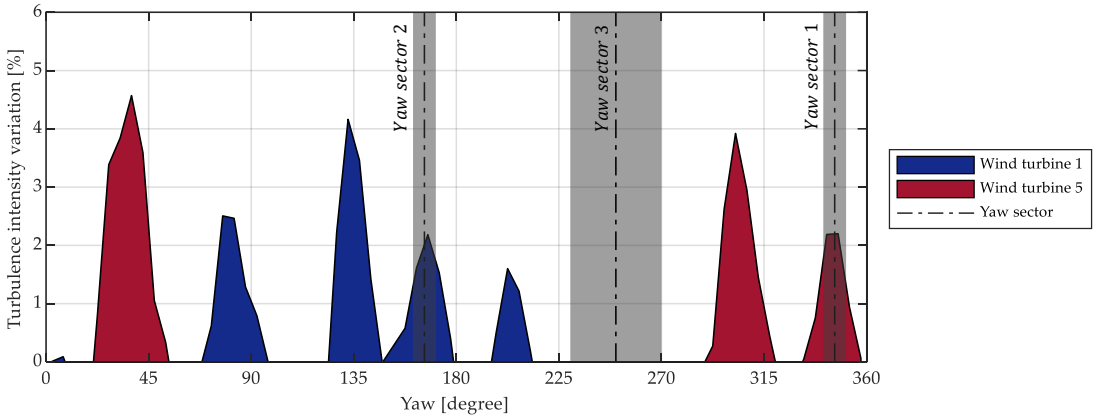


Figure 6.34 – Identification of the analysed yaw sectors and difference between the turbulence intensity measured at WT1 and WT5 and the respective average values in the five turbines of the farm, from Jan-2013 to Jun-2021.

Wind turbine 1 and wind turbine 5 are approximately 1040 m apart (Figure 5.41). Since the rotor diameter is 100 m, the distance between the analysed wind turbines is approximately $10D$. Since $3D < 10D < 20D$, for yaw sectors 1 and 2, the downstream turbine is within the far wake region, where the effects of wake interaction are noteworthy.

In the following analyses, only 10-min time periods in which both wind turbines are in production are considered.

Considering yaw sector 1 (WT5 on the wake), 1046 observations were selected, corresponding to approximately 2.9% of the total monitoring period. For these observations, the relation between the environmental and operational parameters of wind turbines 1 and 5 are represented in Figure 6.35.

As expected, lower wind speed and greater turbulence intensity and, consequently, lower rotor speed and power output are observed in the wind turbine that is located on the wake. It is important to mention that, despite the lower wind speeds in the WT5, it presents lower values of the pitch angle of the blades. As described in Section 6.3.2.2, this behaviour (higher pitch angle) results from the greater turbulence intensity observed due to the wake effect.

In fact, only the nacelle orientation has a wake-independent distribution which indicates that there are no control strategies implemented in the farm that can minimize wake interactions. In particular, yawing of wind turbines in order to increase wind farm power production by deflecting wakes away from downstream turbines is not observed. Although it is a frequently used optimization strategy (Shapiro et al., 2018).

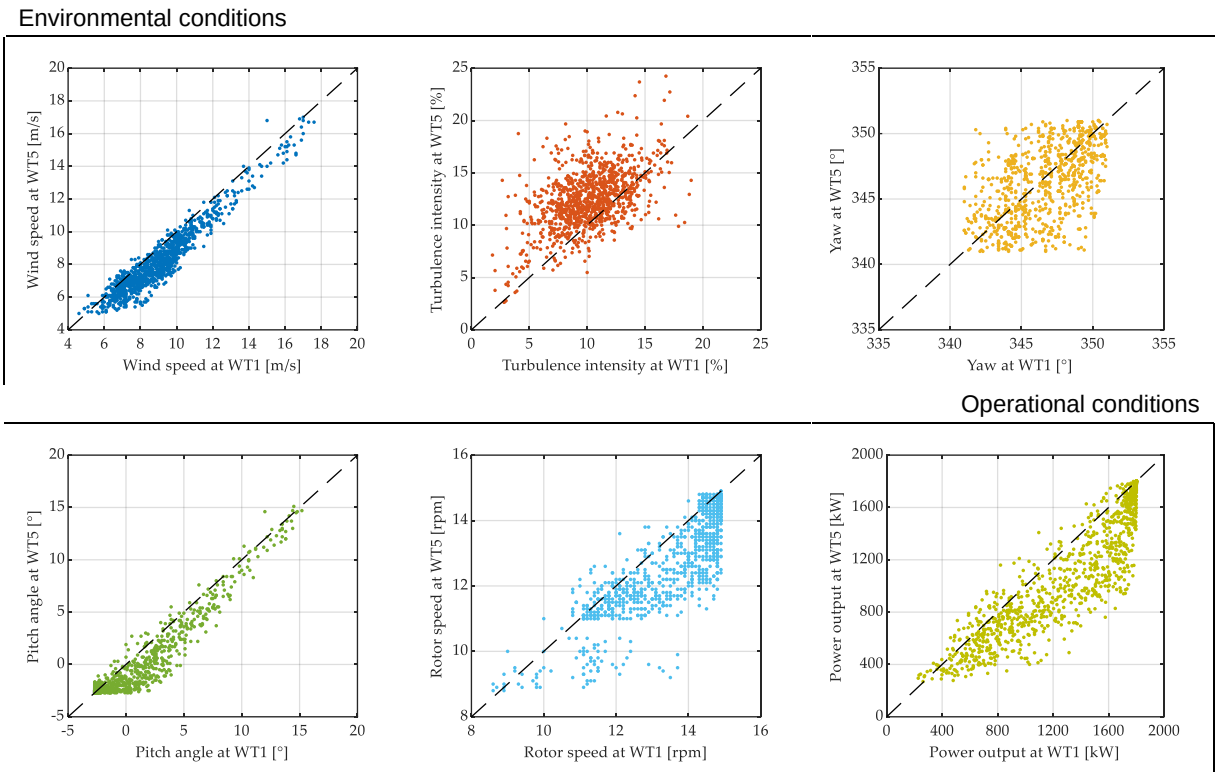


Figure 6.35 – Relation between environmental and operational parameters at WT1 and WT5 considering the yaw sector 1 (WT1: upstream turbine and WT5: downstream turbine).

Considering yaw sector 1, the damage accumulated in the four instrumented points of each blade of the wind turbines 1 and 5 is presented in the Figure 6.36 (the widest bars represent the average value of the three blades).

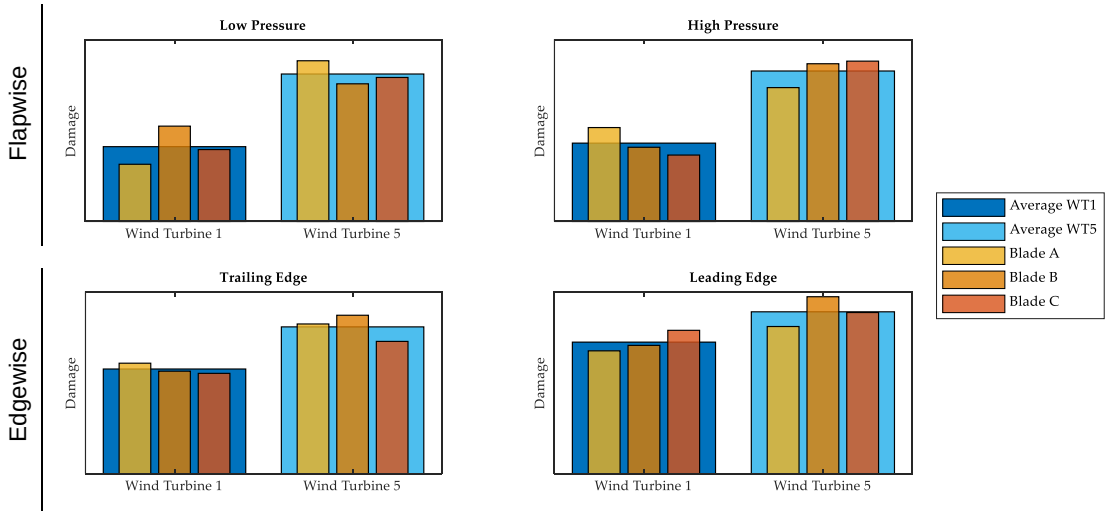


Figure 6.36 – Comparison of accumulated damage on blade roots of the WT1 and WT5 considering the yaw sector 1 (WT1: upstream turbine and WT5: downstream turbine). All plots with the same vertical scale. Vertical scale values not included due to confidentiality constraints.

As expected, it is observed that the damage accumulated at the root of the WT5 blades is higher than that observed in the WT1. As also shown, the difference of the cumulative damage is smaller for edgewise direction.

Considering the reverse case (yaw sector 2), 324 observations were selected, corresponding to approximately 0.9% of the total monitoring period. The relation between the environmental and operational parameters of wind turbines 1 and 5 are represented in Figure 6.37.

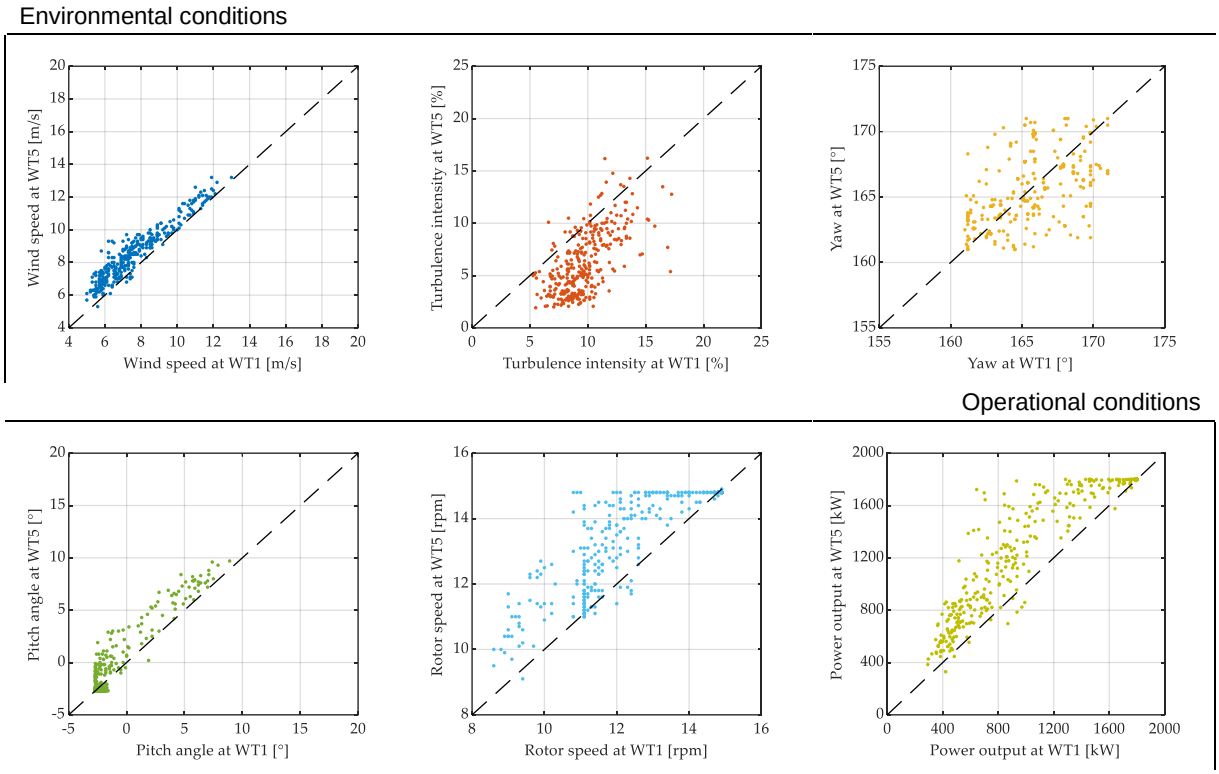


Figure 6.37 – Relation between environmental and operational parameters at WT1 and WT5 considering the yaw sector 2 (WT1: downstream turbine and WT5: upstream turbine).

Despite the lower number of observations recorded for this case (south winds are less frequent at this site), it is possible to identify a similar behaviour to that described in the previous analysis for the relationship between the variables of the two wind turbines.

Comparing the damage accumulated in each blade (Figure 6.38), once again it is higher for the wind turbine that is on the wake. However, in this case, the differences of the average cumulative damage between the two turbines, for both main directions, are smaller than those obtained for yaw sector 1. Despite the reduced number of observations that may contribute to a higher dispersion of the results associated with the blades of the same wind turbine, the differences in the mean values are clear.

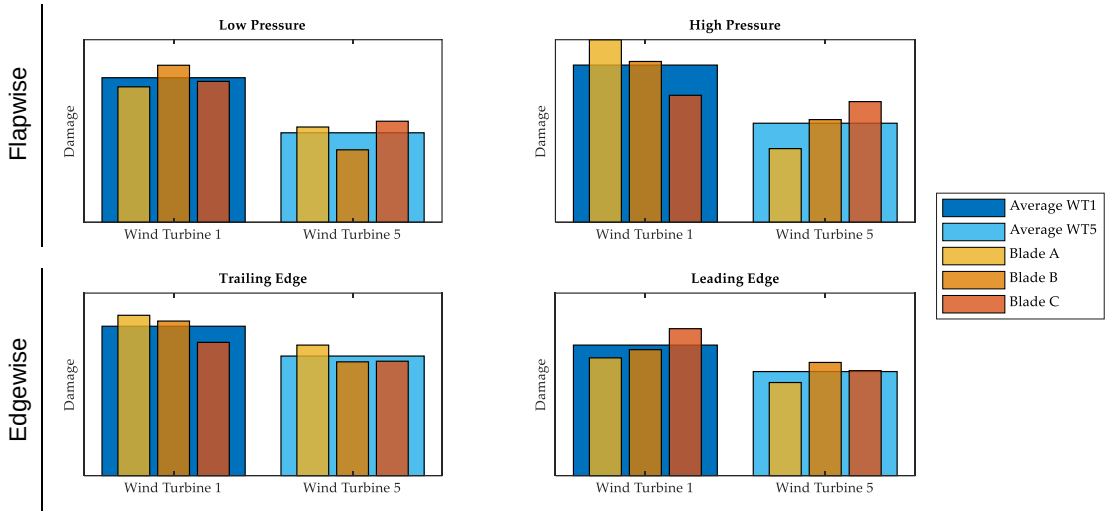


Figure 6.38 – Comparison of accumulated damage on blade roots of the WT1 and WT5 considering the yaw sector 2 (WT1: downstream turbine and WT5: upstream turbine). All plots with the same vertical scale. Vertical scale values not included due to confidentiality constraints.

Finally, considering the situation where both wind turbines receive an undisturbed wind flow (yaw sector 3), 1288 observations were selected, corresponding to approximately 3.5% of the total monitoring period. In Figure 6.39, the relation between the environmental and operational parameters of wind turbines 1 and 5 is presented.

This control case shows that both wind turbines are subject to very similar environmental conditions, presenting also, as expected, similar operating conditions.

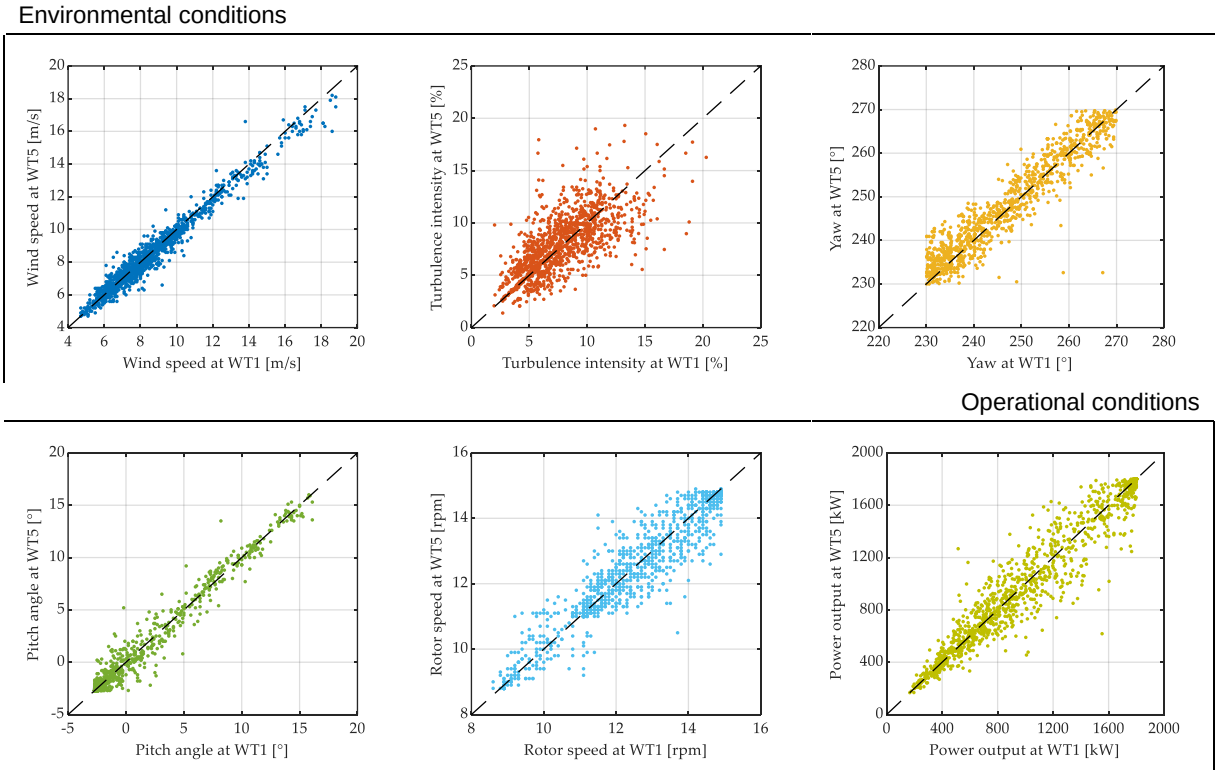


Figure 6.39 – Relation between environmental and operational parameters at WT1 and WT5 when both wind turbines are loaded by an unperturbed flow (yaw sector 3).

As shown in Figure 6.40 the differences in accumulated fatigue damage between WT1 and WT5 differences are much lower than those observed in the presence of wakes.

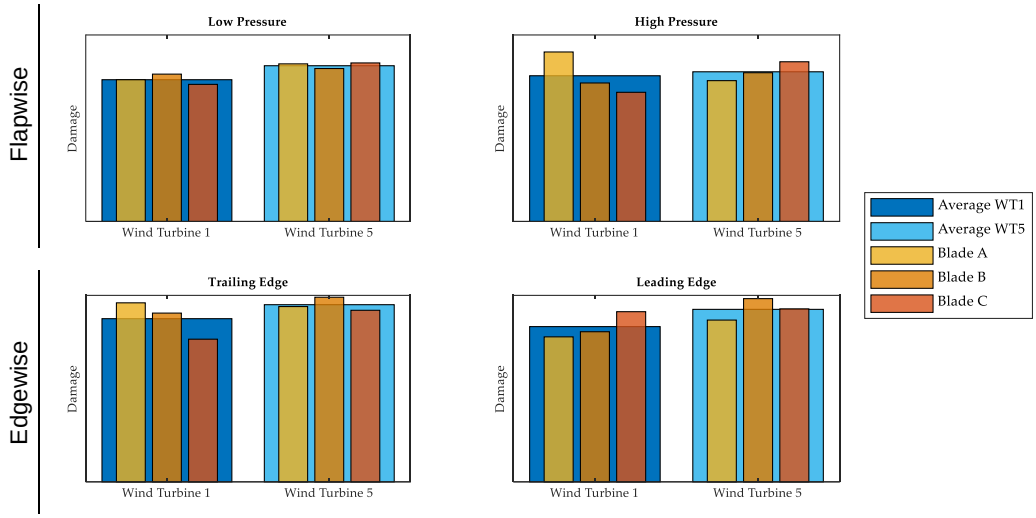


Figure 6.40 – Comparison of accumulated damage on blade roots of the WT1 and WT5 when both wind turbines are loaded by an unperturbed flow (yaw sector 3). All plots with the same vertical scale. Vertical scale values not included due to confidentiality constraints.

Focusing on the damage accumulated at the root of the blades considering each of the defined yaw sectors, the results obtained in this section clearly demonstrate the increase of fatigue loads and the decrease in the power production of wind turbines placed within the wake region.

The small differences in the cumulative damage for flapwise direction found for yaw sectors 1 and 2 might be justified by the uncertainties associated with the calibration procedure. As described in Section 6.4.1, the calculation of fatigue damage in composite materials is dependent on both the amplitude of the cycles and the mean cycle stress. The analysis of the evolution of the bending moments at the root of the blades for the different load cases (Section 6.3.2) made it possible to identify small differences in the moments installed on the various blades. Also considering the results obtained for yaw sector 3, in which both wind turbines are subjected to undisturbed wind flows, the accumulated damage in WT5 is slightly higher. So, damage of WT5 might be a bit overestimated.

Another factor that can influence the relationship between the accumulated damage obtained for each yaw sector is related to the variation of wind flow conditions in each wind direction. The distribution of the number of observations for each yaw sector, considering wind speed and turbulence intensity, is represented in Figure 6.41. As mentioned, the number of observations in each yaw sector is quite different, which influences its representativeness.

On the other hand, the figure demonstrates that the conditions of the wind flow that load the upstream turbine are different in each yaw sector. For example, the unperturbed wind flow in yaw sector 2 is considerably less turbulent than the incident in yaw sector 1. In this way, different fatigue damage is obtained which may lead to different relationships between the fatigue damage for upstream and downstream wind turbines.

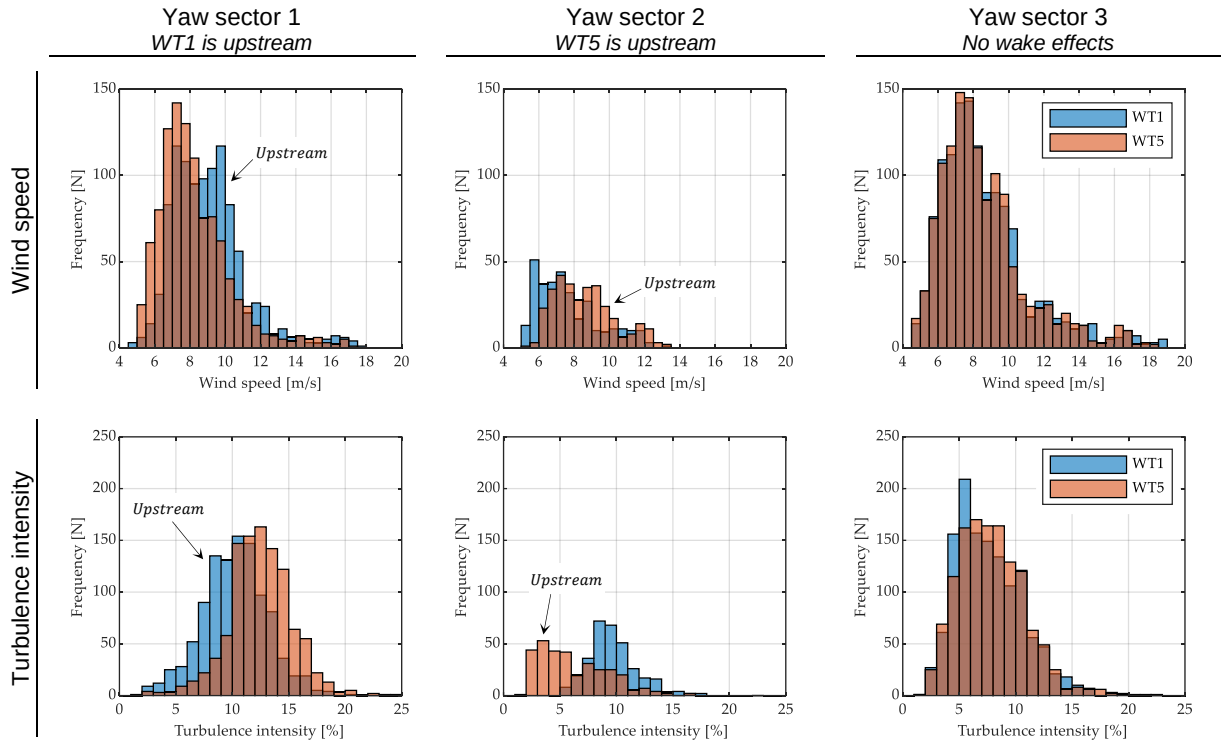


Figure 6.41 – Distribution of the number of observations for each yaw sector, considering wind speed and turbulence intensity.

For the edgewise direction, the differences in the cumulative damage at upstream and downstream wind turbines are less representative. As shown in Figure 6.33 (Section 6.4.2.2), the damage for the edgewise direction shows less variation as a function of wind speed and turbulence intensity.

As conclusion, the results obtained in this section allow to clearly observe the increase in fatigue damage for the wind turbines located on the wake and distanced about $10D$ from the upstream wind turbine. The impact of turbulence on fatigue life should be highlighted. Although the wake wind flow has a lower speed (thus being associated with less damage) the increase in turbulence intensity considerably increases the damage caused to the downstream turbine. In fact, Riziotis et al. (Riziotis & Voutsinas, 2000) identified turbulence intensity as the parameter with the most significant impact on fatigue load contributions. On the other hand, terrain complexity surrounding the wind turbine, due to disturbance of wind flow, could account for about 30% of additional fatigue loading contribution (Mouzakis et al., 1999).

Considering now the wake effect on the productivity of the wind farm, Table 6.2 shows the energy produced by each wind turbine in each defined yaw sector. The results show that the turbine located inside the wake of the upstream wind turbine verifies a reduction of the total energy produced greater than 15%. On the other hand, when both wind turbines are without the influence of wakes, the energy produced is practically the same.

Table 6.2 – Total energy production at upstream and downstream wind turbines and relative variation for each yaw sector over the monitoring period.

Wind direction	Total energy production [MWh]		Relative variation [%]
	WT1	WT5	
Yaw sector 1	226.5	193.7	17.0
Yaw sector 2	53.3	66.2	-19.4
Yaw sector 3	238.7	237.8	0.4

Since wake interactions introduce additional mechanical stresses on wind turbines and reduce the overall energy production of wind farms. Various strategies to minimize the wake effects have been proposed in the last years, including manipulating the direction of rotation of the blades (Vasel-Be-Hagh & Archer, 2017) and optimizing the design of the wind farm (Nash et al., 2021).

For existing wind farms, the wake control can be performed by lessening the strength of the upstream wakes, accelerating the wake recovery and redirecting the upstream wakes away from the downstream wind turbines. In fact, steering the wake imposing a yaw misalignment is a promising strategy (Howland et al., 2016) as proved in the following works (Astolfi et al., 2019; Bromm et al., 2018). A review of several active wake control strategies, including yaw control, pitch control, torque control, tilt control, and precone angle control, can be found in (Nash et al., 2021).

6.5 FINAL CONSIDERATIONS

This chapter addresses the processing and analysis of experimental data collected in wind turbine blades, in particular the strains measured at the blade root. In the first part, the constitution and the structural behaviour of most common blades is briefly described. Special importance is given to the instrumentation of rotors and composite materials, with references to guidelines and suggested procedures, in order to fill the gap of information in this field.

After this general introduction to wind turbine blades, the chapter presents the methodology followed for the experimental evaluation of bending moments at blade roots. This analysis is based on strain measurements and SCADA data from a Vestas V100 onshore wind turbine. The complexity of the calibration of strain gauge readings to obtain mechanical loads in large wind turbines, when direct application of calibration loads is not feasible, is discussed.

The following conclusions can be drawn from the first part of this chapter (Sections 6.2 and 6.3):

- The robustness of the monitoring layout for measurements of blade mechanical loads was validated over a period of one year in two wind turbines;
- Suggestions and recommendations regarding the wind turbine blades instrumentation are presented;
- The temperature on the strain gauges sensors was quantified for this application and a pre-processing procedure was implemented for it minimization;
- The problems associated to calibration of strain gauge sensors used for mechanical load measurements according to the standard IEC-61400-13 is discussed;
- Direct strain monitoring allows to record short events as well as seasonal variations that can be used to understand the complex wind turbine behaviour under a large variety of operating conditions;
- The maximum bending moments occur during power production, for wind speeds close to the rated speed;
- Paying particular attention to the power production load case, it is possible to highlight:
    - The fluctuations of the bending moments are extraordinarily large when the blade pitch is activated;
    - The blades experience smaller mean bending moments for increasing turbulence values;
    - The variation of the bending moments at the root of the blades is largely dependent on the variation of the pitch angle and, consequently, of the rotor speed;
    - Due to the rotor rotation, a wide range of values is observed for the edgewise direction between the maximum and minimum bending moments;
    - In the flapwise direction, the difference between the maximum and minimum values is reduced for lower wind speeds and increases significantly for higher wind speeds;
    - For both directions, the dispersion of the bending moment increases with the turbulence intensity, especially when the blade pitch angle is activated.

In the second part, the challenges for fatigue assessment of composite materials are discussed. Section 6.4 provides a brief literature review of the most notable models relevant to the evaluation of the fatigue response of composite wind turbine blades. The lack of consensus and shortcomings of literature are also discussed.

After that, an approach for damage assessment was implemented using the data acquired with FBGs. This approach is established adopting a life-based failure criterion model. The short-term damage obtained from direct measurement over the monitoring period was coupled with operational and environmental conditions. This study allows drawing the following conclusions:

- Due to the wind action mainly acting in the flapwise direction, there is a greater dispersion of damage values for this direction. On the other hand, the damage for the edgewise direction show less dispersion, as results are mainly driven by the blade's weight, a more deterministic action;
- For the flapwise direction, shutdown is clearly the most severe load case, while shutdown and normal operation represent the most critical cases for the edgewise direction;
- Considering power production, fatigue damage increases for increasing levels of wind speed and turbulence intensity. However:
    - The damage variance is less significant for the edgewise direction than for the flapwise direction;
    - The damage in the edgewise direction is less influenced by operating and environmental conditions.

Based on the developed procedure for wind turbine blade fatigue assessment, the present work analyses the variation of the accumulated fatigue damage at blade roots for wind turbines placed within the wake region of an upstream turbine in a distance of 10 rotor diameters. Based on the results from the ongoing monitoring campaign that is being conducted in Tocha Wind Farm, the following conclusions can be drawn:

- The wake effects have a great impact on the behaviour of wind turbines. In particular, it is worth noting:
    - Relevant reduction in the power production of the inner wind turbines;
    - Increase of the fatigue loads on wind turbines in operation;
- Additional turbulence intensity provided by upstream wind turbines significantly increased the fatigue loads;
- Considering the power production load case, two wind turbines separated by $10D$ and subject to the environmental conditions recorded during the monitoring campaign:
    - For the flapwise direction, the damage accumulated at the root of the blades at downstream wind turbines is significantly higher compared to the wind turbine that receives the undisturbed flow;
    - The damage at the edgewise direction increases for the downstream wind turbine, but less significantly than for the flapwise direction;
    - Total energy output decreases by more than 15% due to wake effects.

7
CONCLUSIONS AND FUTURE RESEARCH

7.1 CONCLUSIONS

This work explored the potential of using wind turbines monitoring systems at the level of wind farms. In this scope, several processing routines were developed and implemented to extract in an automatic way the maximum information that a monitoring system based on the dynamic response of wind turbines can deliver. In this way, the collected data is transformed into useful information for the wind farm owners. The monitoring strategy was designed to be applied in the context of a wind farm and focused on two main goals: detection of stiffness reductions motivated by the appearance of damage and evaluation of the fatigue consumption of the main structural components.

The thesis starts with a description of the main structural elements of the most common wind turbines, with a special emphasis on their structural behaviour and operation. A brief description of the main theories about the aerodynamic performance of wind turbines is also presented, aiming to facilitate the comprehension of the response of the turbine under different operating conditions.

Then, the focus of the thesis is oriented to the development a cost-effective monitoring system aiming the analysis and characterization of the dynamic behaviour of wind turbines. This characterization is helpful to study the applicability of the OMA techniques to wind turbines. Several methodologies developed and implemented in the context of the dynamic monitoring system are also described, as an automated procedure for operational modal analysis and statistical tools for detection of damage. The processing tools were validated analysing the acceleration data collected during a period of one year at a Senvion MM82 wind turbine. The major conclusions drawn from this analysis are:

- Monitoring solutions based on continuous modal identification are adequate to detect structural changes in wind turbines;
- It is possible to effectively optimize the original monitoring system, significantly reducing costs and without impairing performance on an equal scale. Even with a small number of MEMS sensors carefully positioned in the tower, it is possible to detect different types of damage at an early stage;
- It was possible to define the maximum noise level of the sensors, which allows obtaining estimates of the modal properties of current wind turbines;
- Criteria and general guidelines that help in the delineation of an instrumentation architecture for a particular case were established, according to the available budget and the accuracy of the intended results.

The next chapters are focused on the most complete case study of this thesis. It comprises the analysis of different data, provided by several monitoring systems, collected during a period of two years at Tocha Wind Farm. In Chapter 4 the experimental campaign is thoroughly described and the preliminary results are shown. Chapter 5 is essentially dedicated to the processing of strain gauge measurement at the tower. The following achievements were obtained with this analysis:

- Direct monitoring of wind turbines provides accurate data for the evaluation of wind loading effects, since the effects to temperature and long-term sensor drifts can be excluded;
- Development of a clustering algorithm for classification of 10-min time series according the operating condition (based on the data provided by SCADA system);
- Realistic examination of the fatigue damage of the wind turbine tower, linked with environmental and operational parameters allows to characterize the influence of the operating conditions on the accumulated fatigue damage;
- Construction of a damage capture matrix for power production conditions, considering only two environmental parameters: wind speed and turbulence intensity. Different methodologies were recommended to fill the empty bins of the matrix;
- Development of a model for the reconstruction of the fatigue damage endured by the instrumented wind turbine, with limited number of parameters (wind direction/speed and turbulence intensity). This includes the quantification of the uncertainty associated with each estimation;
- Implementation of an approach for farm wide fatigue assessment (so called fleet leader concept). The fatigue results obtained from a limited number of representative turbines (instrumented with accelerometers and strain gauges) are extrapolated to the entire farm using an empirical formula (considering only power production condition);
- Definition of rules and recommendations for the fleet leaders choice at a given wind farm;
- Characterization of the influence of the wind turbulence motivated by the neighbouring rotors in the accumulate fatigue damage of the tower.

Lastly, Chapter 6 comprises de analysis of strain data measured at blade roots at two wind turbines at Tocha Wind Farm. The experimental data considered in this chapter was collected during twelve months of operation. With this study, some important outputs should be referred:

- Calculation of the blade-root moments based on strain measurements after careful pre-processing and calibration;
- Quantification of the wind loads and characterization of the blades dynamic response considering different loading scenarios;
- An approach for damage assessment was developed using the data acquired with FBG sensors, considering wind turbines loaded by winds with different velocities and turbulence intensities;
- Characterization of the interaction between neighbouring wind turbines and its effect on fatigue life consumption of the blades and energy production.

7.2 FUTURE RESEARCH

The work presented in this thesis contains useful contributions for the development and implementation of new methodologies for structural monitoring of wind farms. Notwithstanding, some future research is still needed to benefit from all the potential that a dynamic monitoring system can provide. The experimental data collected at the Tocha Wind Farm, with great scientific value, should be further analysed in future research works in order to complement the methodologies developed in this work. Some interesting topics are presented in the following paragraphs.

A damage detection module of the monitoring system was developed, optimized and applied to the Senvion MM82 wind turbine at Torrão Wind Farm (Chapter 3). In a next step, this module should be tested and implemented considering the extensive experimental campaign at Tocha Wind Farm (describe in Chapter 4). The following topics should be addressed in order to improve this module:

- Improvement of the existing methods to automatically track the time evolution of the modal properties (natural frequencies, modal damping ratios, mode shapes and modal curvatures) to be applied to acceleration and strain time series measured in the tower and blades;
- Quantification of the uncertainty associated with the estimated modal properties, the estimation of the modal contribution of each mode and better strategies to deal with the non-stationarity motivated by the nacelle rotation, the harmonics motivated by the rotor rotation and the rotation of the sensors instated in the blades;
- Development of statistical tools to minimize the environmental and operational factors (temperature, wind, nacelle position, rotor speed, blades pitch) on the tracked modal parameters and detect frequency shifts that might be associated with damage, taking into account the uncertainty of the modal parameters estimates;
- Testing the MEMS based system developed at FEUP. These sensors with different costs, and so with different noise levels, should be further tested. In this way, real more noise acceleration time series can be obtain, replacing the artificial accelerations time series (obtained in Chapter 3 by adding band-limited white noise time series with different amplitudes to the originally measured acceleration);

Fatigue monitoring of the support structure of the wind turbines requires further developments. Some topics are referred in the following paragraphs:

- Apply the fatigue extrapolation algorithms for non-instrumented periods to all turbine operating conditions (power production and transient events);
- Expand the experimental campaign in the Tocha Wind Farm and instrument at least one more wind turbine tower with a strain monitoring system (preferably the WT5) in order to validated the algorithms developed for fatigue damage extrapolation within the farm (Section 5.6.5);
- Implementation of new algorithms to evaluate stress cycles in non-instrumented points of the tower using the automatically identified modal parameters, Kalman filters to decompose the measured responses on modal contributions, the measurements of the strains or rotations (important for the quasi-static components) and simple numerical models of the tower and blades (just introduced in Section 5.3.2.2);
- Having in mind the evaluation of the static bending moment diagrams along the tower and validation of the algorithms described in the previous paragraph, a new section of the WT1 tower could be instrumented with additional strain gauges. The new-instrumented section should be far enough away from the previously instrumented section;

- Evaluate whether clinometers are able to provide accurate estimates of the bending moment by comparison with the results delivered by the strain gages. The installation of the clinometers is less intrusive than the installation of strain gauges. They allow to measure the rotation at the base of the tower and to alternatively estimate the bending moment from curvatures derived from the measurement of rotations in two close sections;
- Test of new techniques in the measurement of wind field near the wind turbine, such as drone-mounted LIDAR systems, in order to provide much more reliable data at higher frequency, to study wind-structure integration;
- Propose an optimized (in terms of cost) monitoring system for fatigue assessment considering alternative monitoring layouts. Since, the fatigue analysis also depends on the acceleration measurements this analysis is interconnected with the one described in the previous paragraphs (damage detection module). Furthermore, should be defined the minimum number of strain gages and/or clinometers and the minimum monitoring period to perform accurate extrapolations to non-measured periods;
- Develop a set of rules for the design of a farm wide optimized monitoring system;

The preliminary work development on blades monitoring raised several research topics, issues and additional objectives that were not addressed. In this context, some topics requiring further analysis are referred in the following paragraphs:

- Development of a new methodology that allows automatic calibration of FBG sensors during normal turbine operation.
- Development and application of new fatigue calculation models, such as progressive damage models;

Finally, advanced numerical models of the wind turbine are currently being developed in FAST. The experimental results reported in this thesis are being used for calibration of these numerical models and then the model might be useful for a better understating of the experimental data. The comparison of numerical and experimental results will be presented in future works.

REFERENCES

A

Adams, D., White, J., Rumsey, M., & Farrar, C. (2011). Structural health monitoring of wind turbines: method and application to a HAWT. Wind Energy, 14(4), 603–623. https://doi.org/https://doi.org/10.1002/we.437

Adedipe, O., Brennan, F., & Kolios, A. (2016). Review of corrosion fatigue in offshore structures: Present status and challenges in the offshore wind sector. Renewable and Sustainable Energy Reviews, 61, 141–154. https://doi.org/https://doi.org/10.1016/j.rser.2016.02.017

Ahmad, R. and Kamaruddin, S. (2012) 'An overview of time-based and condition-based maintenance in industrial application', Comput. Ind. Eng., 63, pp. 135–149.

Allen, M. S., Sracic, M. W., Chauhan, S., & Hansen, M. H. (2011). Output-only modal analysis of linear time-periodic systems with application to wind turbine simulation data. Mechanical Systems and Signal Processing, 25(4), 1174–1191. https://doi.org/https://doi.org/10.1016/j.ymssp.2010.12.018

Amzallag, C., Gerey, J. P., Robert, J. L., & Bahuaud, J. (1994). Standardization of the rainflow counting method for fatigue analysis. International Journal of Fatigue, 16(4), 287–293. https://doi.org/https://doi.org/10.1016/0142-1123(94)90343-3

Andersen, S. I., Bach, P. W., Bonnee, W. J. A., Kensche, C. W., Lilholt, H., Lystrup, A., & Sys, W. (1996). Fatigue of materials and components for wind turbine rotor blades. https://doi.org/CG-NA-16-684-EN-C

APREN (2021) Anuário 2021 APREN. Lisbon, Portugal.

Astolfi, D., Castellani, F., & Natili, F. (2019). Wind Turbine Yaw Control Optimization and Its Impact on Performance. In Machines (Vol. 7, Issue 2). https://doi.org/10.3390/machines7020041

Autodesk. (2016). Robot Structural Analysis Professional (Version 29.0.05650(x64)).

Avitabile, P., & Pingle, P. (2012). Prediction of Full Field Dynamic Strain from Limited Sets of Measured Data. Shock and Vibration, 19, 408919. https://doi.org/10.3233/SAV-2012-0686

B

Bangalore, P., & Patriksson, M. (2018). Analysis of SCADA data for early fault detection, with application to the maintenance management of wind turbines. Renewable Energy, 115, 521–532. https://doi.org/https://doi.org/10.1016/j.renene.2017.08.073

Barbero, E. (2017). Introduction to Composite Materials Design, Third Edition. CRC Press. https://doi.org/10.1201/9781315296494

Bech, J. I., Hasager, C. B., & Bak, C. (2018). Extending the life of wind turbine blade leading edges by reducing the tip speed during extreme precipitation events. Wind Energy Science, 3(2), 729–748. https://doi.org/10.5194/wes-3-729-2018

Besnard, F., & Bertling, L. (2010). An Approach for Condition-Based Maintenance Optimization Applied to Wind Turbine Blades. IEEE Transactions on Sustainable Energy, 1(2), 77–83. https://doi.org/10.1109/TSTE.2010.2049452

Bezziccheri, M., Castellini, P., Evangelisti, P., Santolini, C., & Paone, N. (2017). Measurement of mechanical loads in large wind turbines: Problems on calibration of strain gage bridges and analysis of uncertainty. Wind Energy, 20(12), 1997–2010. https://doi.org/https://doi.org/10.1002/we.2136

Bhattacharya, B., & Ellingwood, B. (1998). Continuum damage mechanics analysis of fatigue crack initiation. International Journal of Fatigue, 20(9), 631–639. https://doi.org/https://doi.org/10.1016/S0142-1123(98)00032-2

Boller, C., Chang, F.-K., & Fujino, Y. (2009). Encyclopedia of Structural Health Monitoring. John Wiley & Sons. https://doi.org/10.1002/9780470061626

Botz, M., Oberländer, S., Raith, M., & Grosse, C. (2016). Monitoring of Wind Turbine Structures with Concrete-steel Hybrid-tower Design.

Bouzid, O. M., Tian, G. Y., Cumanan, K., & Moore, D. (2015). Structural Health Monitoring of Wind Turbine Blades: Acoustic Source Localization Using Wireless Sensor Networks. Journal of Sensors, 2015, 139695. https://doi.org/10.1155/2015/139695

Braam, H., Obdam, T., & Verbruggen, T. (2012). Low cost load monitoring for offshore wind farms. Conference on Noise and Vibration Engineering 2012.

Bromm, M., Rott, A., Beck, H., Vollmer, L., Steinfeld, G., & Kühn, M. (2018). Field investigation on the influence of yaw misalignment on the propagation of wind turbine wakes. Wind Energy, 21(11), 1011–1028. https://doi.org/10.1002/we.2210

Brøndsted, P., & Nijssen, R. P. L. (2013). Advances in Wind Turbine Blade Design and Materials. Woodhead Publishing Limited.

Brøndsted, P., Lilholt, H., & Lystrup, A. (2005). COMPOSITE MATERIALS FOR WIND POWER TURBINE BLADES. Annual Review of Materials Research, 35(1), 505–538. https://doi.org/10.1146/annurev.matsci.35.100303.110641

BSI. (2017). BS EN13306: Maintenance - Maintenance terminology.

Bulder, B. H., van Hees, M. T., Henderson, A., Huijsmans, R. H. M., Pierik, J. T. G., Snijders, E. J. B., Wijnants, G. H., & Wolf, M. J. (2002). Study to Feasibility of and Boundary Conditions for Floating Offshore Wind Turbines. https://doi.org/Technical Report No. 2002-CMC-R43

Burton, T., Jenkins, N., Sharpe, D., & Bossanyi, E. (2011). Wind Energy Handbook (2nd ed.). John Wiley & Sons. https://doi.org/10.1002/9781119992714

C

Campanella, C. E., Cuccovillo, A., Campanella, C., Yurt, A., & Passaro, V. M. N. (2018). Fibre Bragg Grating Based Strain Sensors: Review of Technology and Applications. In Sensors (Vol. 18, Issue 9). https://doi.org/10.3390/s18093115

Carden, E. P., & Fanning, P. (2004). Vibration Based Condition Monitoring: A Review. Structural Health Monitoring, 3(4), 355–377. https://doi.org/10.1177/1475921704047500

Carroll, J., McDonald, A., & McMillan, D. (2016). Failure rate, repair time and unscheduled O&M cost analysis of offshore wind turbines. Wind Energy, 19(6), 1107–1119. https://doi.org/https://doi.org/10.1002/we.1887

Chaboche, J. L. (1988). Continuum Damage Mechanics: Part II—Damage Growth, Crack Initiation, and Crack Growth. Journal of Applied Mechanics, 55(1), 65–72. https://doi.org/10.1115/1.3173662

Ciang, C. C., Lee, J.-R., & Bang, H.-J. (2008). Structural health monitoring for a wind turbine system: a review of damage detection methods. Measurement Science and Technology, 19(12), 122001. https://doi.org/10.1088/0957-0233/19/12/122001

Commission, E., Innovation, D.-G. for R. and, Veljkovic, M., Husson, W., & Heistermann, C. (2012). High-strength tower in steel for wind turbines (Histwin). Publications Office.

Coronado, D., & Fischer, K. (2015). Condition monitoring of wind turbines: State of the art, user experience and recommendations. Fraunhofer IWES.

Crabtree, C. J., Zappalá, D., & Tavner, P. J. (2014). Survey of commercially available condition monitoring systems for wind turbines.

Cruz, J., & Atcheson, M. (2016). Floating Offshore Wind Energy (1st ed.). Springer, Cham. https://doi.org/https://doi.org/10.1007/978-3-319-29398-1

Currie, M., Saafi, M., Tachtatzis, C., & Quail, F. (2015). Structural integrity monitoring of onshore wind turbine concrete foundations. Renewable Energy, 83, 1131–1138. https://doi.org/https://doi.org/10.1016/j.renene.2015.05.006

Cusano, A., Cutolo, A., & Albert, J. (2011). Fiber Bragg Grating Sensors: Recent Advancements, Industrial Applications and Market Exploitation. Bentham Science Publisher. https://doi.org/http://dx.doi.org/10.2174/97816080508401110101

D

D'Amore, A., & Grassia, L. (2019). Comparative Study of Phenomenological Residual Strength Models for Composite Materials Subjected to Fatigue: Predictions at Constant Amplitude (CA) Loading. Materials (Basel, Switzerland), 12(20), 3398. https://doi.org/10.3390/ma12203398

Dai, J., Yang, W., Cao, J., Liu, D., & Long, X. (2018). Ageing assessment of a wind turbine over time by interpreting wind farm SCADA data. Renewable Energy, 116, 199–208. https://doi.org/https://doi.org/10.1016/j.renene.2017.03.097

Dao, C., Kazemtabrizi, B. and Crabtree, C. (2019) 'Wind turbine reliability data review and impacts on levelised cost of energy', Wind Energy, 22(12), pp. 1848–1871. doi: https://doi.org/10.1002/we.2404.

Degrieck, J., & Van Paepegem, W. (2001). Fatigue damage modeling of fibre-reinforced composite materials: Review. Applied Mechanics Reviews, 54(4), 279–300. https://doi.org/10.1115/1.1381395

Det Norske Veritas (DNV). (2010). DNV-OS-J102 - Design and Manufacture of Wind Turbine Blades, Offshore and Onshore Wind Turbines.

Det Norske Veritas (DNV). (2010). DNV-RP-C203 - Fatigue Design of Offshore Steel Structures.

Det Norske Veritas (DNV). (2011). DNV-OS-J101 - Design of Offshore Wind Turbine Structures.

Devriendt, C. et al. (2014) 'Structural health monitoring of offshore wind turbines using automated operational modal analysis', Structural Health Monitoring, 13(6), pp. 644–659. doi: 10.1177/1475921714556568.

Diel, S., & Huber, O. (2017). A Continuum Damage Mechanics Model for the Static and Cyclic Fatigue of Cellular Composites. Materials, 10(8). https://doi.org/10.3390/ma10080951

DNV GL AS. (2015). DNVGL-ST-0376 - Rotor Blades for Wind Turbines.

DNV GL AS. (2016). DNVGL-ST-0262 - Lifetime Extension of Wind Turbines.

Dowling, N. (1972). Fatigue Failure Predictions for Complicated Stress-Strain Histories (J. of Materials (ed.); J. of Mate).

E

EC (2008) 'Waste Framework Directive (2008/98/EC)'. Available at: http://data.europa.eu/eli/dir/2008/98/oj.

ECN. (2007). Condition Monitoring for Offshore Wind Farms.

Efron, B. (1979). Bootstrap Methods: Another Look at the Jackknife. The Annals of Statistics, 7(1), 1–26. https://doi.org/10.1214/aos/1176344552

Erazo, K., & Hernandez, E. M. (2014). A model-based observer for state and stress estimation in structural and mechanical systems: Experimental validation. Mechanical Systems and Signal Processing, 43(1), 141–152. https://doi.org/https://doi.org/10.1016/j.ymssp.2013.10.011

EU (2009) 'Directive 2009/28/EC of the European Parliament and of the Council of 23 April 2009 on the promotion of the use of energy from renewable sources and amending and subsequently repealing Directives 2001/77/EC and 2003/30/EC.' Available at: http://data.europa.eu/eli/dir/2009/28/oj.

EU (2018) 'Directive (EU) 2018/2001 of the European Parliament and of the Council of 11 December 2018 on the promotion of the use of energy from renewable sources'. Available at: http://data.europa.eu/eli/dir/2018/2001/oj.

Evans, J. R. et al. (2014) 'Performance of Several Low-Cost Accelerometers', Seismological Research Letters, 85(1), pp. 147–158. doi: 10.1785/0220130091.

F

Farrar, C. R., & Worden, K. (2007). An introduction to structural health monitoring. Philosophical Transactions of the Royal Society A: Mathematical, Physical and Engineering Sciences, 365(1851), 303–315. https://doi.org/10.1098/rsta.2006.1928

Farrar, C. R., Doebling, S. W., & Nix, D. A. (2001). Vibration–based structural damage identification. Philosophical Transactions of the Royal Society of London. Series A: Mathematical, Physical and Engineering Sciences, 359(1778), 131–149. https://doi.org/10.1098/rsta.2000.0717

Frankfurt School-UNPE (2018) Global Trends in Renewable Energy Investment 2018. Frankfurt, Germany.

Frendahl, M., & Rychlik, I. (1993). Rainflow analysis: Markov method. International Journal of Fatigue, 15(4), 265–272. https://doi.org/https://doi.org/10.1016/0142-1123(93)90375-Z

Fritzen, C. P. (2005). Vibration-Based Structural Health Monitoring – Concepts and Applications. Key Engineering Materials, 293–294, 3–20. https://doi.org/10.4028/www.scientific.net/KEM.293-294.3

Fritzen, C.-P., Kraemer, P., & Klinkov, M. (2011). An Integrated SHM Approach for Offshore Wind Energy Plants BT - Structural Dynamics, Volume 3 (T. Proulx (ed.); pp. 727–740). Springer New York.

G

Gass, V., Strauss, F., Schmidt, J., & Schmid, E. (2011). Assessing the effect of wind power uncertainty on profitability. Renewable and Sustainable Energy Reviews, 15(6), 2677–2683.

Gellermann, T. (2013). Extension of the scope of Condition Monitoring Systems for multi-MW and offshore wind turbines.

Germanischer Lloyd (GL). (2010). Guideline for the Certification of Wind Turbines.

Germanischer Lloyd (GL). (2012). Guideline for the Certification of Offshore Wind Turbines.

Ghaisas, N. S., & Archer, C. L. (2016). Geometry-Based Models for Studying the Effects of Wind Farm Layout. Journal of Atmospheric and Oceanic Technology, 33(3), 481–501. https://doi.org/10.1175/JTECH-D-14-00199.1

Gillijns, S., & De Moor, B. (2007). Unbiased minimum-variance input and state estimation for linear discrete-time systems with direct feedthrough. Automatica, 43(5), 934–937. https://doi.org/https://doi.org/10.1016/j.automatica.2006.11.016

Glauert, H. (1926). The Analysis of Experimental Results in the Windmill Brake and Vortex Ring States of an Airscrew. H.M. Stationery Office.

Glinka, G., & Kam, J. C. P. (1987). Rainflow counting algorithm for very long stress histories. International Journal of Fatigue, 9(4), 223–228. https://doi.org/https://doi.org/10.1016/0142-1123(87)90025-9

H

Häfele, J., Hübler, C., Gebhardt, C. G., & Rolfes, R. (2018). A comprehensive fatigue load set reduction study for offshore wind turbines with jacket substructures. Renewable Energy, 118, 99–112. https://doi.org/https://doi.org/10.1016/j.renene.2017.10.097

Hameed, Z., Hong, Y. S., Cho, Y. M., Ahn, S. H., & Song, C. K. (2009). Condition monitoring and fault detection of wind turbines and related algorithms: A review. Renewable and Sustainable Energy Reviews, 13(1), 1–39. https://doi.org/https://doi.org/10.1016/j.rser.2007.05.008

Hansen, M. (2015). Aerodynamics of Wind Turbines (3rd ed.). Routledge. https://doi.org/https://doi.org/10.4324/9781315769981

Hansen, M. H. (2007). Aeroelastic instability problems for wind turbines. Wind Energy, 10(6), 551–577. https://doi.org/https://doi.org/10.1002/we.242

Hau, E. (2006). Wind Turbines: Fundamentals, Technologies, Application, Economics (2nd ed.). Springer. https://doi.org/https://doi.org/10.1007/3-540-29284-5

HBM-FiberSensing. (2015). FS62: Athermal Strain Sensor. A4252-1.2.

Helbing, G., & Ritter, M. (2018). Deep Learning for fault detection in wind turbines. Renewable and Sustainable Energy Reviews, 98, 189–198. https://doi.org/https://doi.org/10.1016/j.rser.2018.09.012

Hindersmann, A. (2019). Confusion about infusion: An overview of infusion processes. Composites Part A: Applied Science and Manufacturing, 126, 105583. https://doi.org/https://doi.org/10.1016/j.compositesa.2019.105583

Hjelm, H., Brincker, R., Graugaard-Jensen, J., & Munch, K. (2005). Determination of stress histories in structures by natural input modal analysis. In Conference Proceedings: IMAC-XXIII: A Conference & Exposition on Structural Dynamics Society for Experimental Mechanics.

Hoffmann, K. (2012). An introduction to stress analysis and transducer design using strain gauges. HBM Test and Measurement.

Howland, M. F., Bossuyt, J., Martínez-Tossas, L. A., Meyers, J., & Meneveau, C. (2016). Wake structure in actuator disk models of wind turbines in yaw under uniform inflow conditions. Journal of Renewable and Sustainable Energy, 8(4). https://doi.org/10.1063/1.4955091

Hu, Wei-Hua, Thöns, S., Rohrmann, R. G., Said, S., & Rücker, W. (2015). Vibration-based structural health monitoring of a wind turbine system Part II: Environmental/operational effects on dynamic properties. Engineering Structures, 89, 273–290. https://doi.org/https://doi.org/10.1016/j.engstruct.2014.12.035

Hu, W-H. (2011). Operational Modal Analysis and Continuous Dynamic Monitoring of Footbridges. Faculdade de Engenharia da Universidade do Porto.

Hübler, C., Weijtjens, W., Rolfes, R., & Devriendt, C. (2018). Reliability analysis of fatigue damage extrapolations of wind turbines using offshore strain measurements. Journal of Physics: Conference Series, 1037, 32035. https://doi.org/10.1088/1742-6596/1037/3/032035

Hyers, R. W. et al. (2006) 'Condition monitoring and prognosis of utility scale wind turbines', Energy Materials, 1(3), pp. 187–203. doi: 10.1179/174892406X163397.

Hyers, R. W., Mcgowan, J. G., Sullivan, K. L., Manwell, J. F., & Syrett, B. C. (2006). Condition monitoring and prognosis of utility scale wind turbines. Energy Materials, 1(3), 187–203. https://doi.org/10.1179/174892406X163397

I

Iliopoulos, A., Shirzadeh, R., Weijtjens, W., Guillaume, P., Hemelrijck, D. Van, & Devriendt, C. (2016). A modal decomposition and expansion approach for prediction of dynamic responses on a monopile offshore wind turbine using a limited number of vibration sensors. Mechanical Systems and Signal Processing, 68–69, 84–104. https://doi.org/https://doi.org/10.1016/j.ymssp.2015.07.016

Iliopoulos, A., Weijtjens, W., Van Hemelrijck, D., & Devriendt, C. (2016). Full-Field Strain Prediction Applied to an Offshore Wind Turbine BT - Model Validation and Uncertainty Quantification, Volume 3 (S. Atamturktur, T. Schoenherr, B. Moaveni, & C. Papadimitriou (eds.); pp. 349–357). Springer International Publishing.

Im, S., & Choung, J. (2021). Comparison of Fatigue Provisions in Various Codes and Standards-Part 1: Basic Design S-N Curves of Non-Tubular Steel Members. J. Ocean Eng. Technol., 35(2), 161–171. https://doi.org/10.26748/KSOE.2021.001

International Electrotechnical Commission. (2009). IEC 61400-3 Wind turbines – Part 3: Design requirements for offshore wind turbines.

International Electrotechnical Commission. (2014). IEC 61400-1 Wind turbines –Part 1: Design requirements.

International Electrotechnical Commission. (2015). IEC 61400-13 Wind Turbine Generator Systems - Part 13: Measurement of Mechanical Loads.

IRENA (2018) Renewable capacity statistics 2018. Abu Dhabi. doi: 978-92-9260-057-0.

J

J. van der Tempel. (2006). Design of support structures for offshore wind turbines. Technisce Universiteit Delft.

Jacquelin, E., Bennani, A., & Hamelin, P. (2003). Force reconstruction: analysis and regularization of a deconvolution problem. Journal of Sound and Vibration, 265(1), 81–107. https://doi.org/https://doi.org/10.1016/S0022-460X(02)01441-4

Jayalakshmi, V., Lakshmi, K., & Mohan Rao, A. R. (2018). Dynamic force reconstruction techniques from incomplete measurements. Journal of Vibration and Control, 24(22), 5321–5344. https://doi.org/10.1177/1077546317752709

Jin, X., Fan, J., & Chow, T. W. S. (2019). Fault Detection for Rolling-Element Bearings Using Multivariate Statistical Process Control Methods. IEEE Transactions on Instrumentation and Measurement, 68(9), 3128–3136. https://doi.org/10.1109/TIM.2018.2872610

Joe, H.-E., Yun, H., Jo, S.-H., Jun, M. B. G., & Min, B.-K. (2018). A review on optical fiber sensors for environmental monitoring. International Journal of Precision Engineering and Manufacturing-Green Technology, 5(1), 173–191. https://doi.org/10.1007/s40684-018-0017-6

Johnson, R. A. and Wichern, D. W. (1988) Applied Multivariate Statistical Analysis. USA: Prentice-Hall, Inc.

Jonkman, J. et al. (2009) Definition of a 5-MW Reference Wind Turbine for Offshore System Development. 38060. United States. doi: 10.2172/947422.

K

Kaminski, M., Laurin, F., & Maire, J.-F. (2015). Fatigue Damage Modeling of Composite Structures: the ONERA Viewpoint. Life Prediction Methodologies for Materials and Structures, 1. https://doi.org/10.12762/2015.AL09-06

Katnam, K. B., Comer, A. J., Roy, D., da Silva, L. F. M., & Young, T. M. (2015). Composite Repair in Wind Turbine Blades: An Overview. The Journal of Adhesion, 91(1–2), 113–139. https://doi.org/10.1080/00218464.2014.900449

Kim, H.-C., Kim, M.-H., & Choe, D.-E. (2019). Structural health monitoring of towers and blades for floating offshore wind turbines using operational modal analysis and modal properties with numerical-sensor signals. Ocean Engineering, 188, 106226. https://doi.org/https://doi.org/10.1016/j.oceaneng.2019.106226

Kim, S.-H., Shin, H.-K., Joo, Y.-C., & Kim, K.-H. (2015). A study of the wake effects on the wind characteristics and fatigue loads for the turbines in a wind farm. Renewable Energy, 74, 536–543. https://doi.org/https://doi.org/10.1016/j.renene.2014.08.054

Kong, Z., Tang, B., Deng, L., Liu, W., & Han, Y. (2020). Condition monitoring of wind turbines based on spatio-temporal fusion of SCADA data by convolutional neural networks and gated recurrent units. Renewable Energy, 146, 760–768. https://doi.org/https://doi.org/10.1016/j.renene.2019.07.033

L

Larsen, T. J. and Hansen, A. M. (2007) 'How 2 HAWC2, the user's manual'. Roskilde, Denmark: Risø National Laboratory Technical University of Denmark.

Lee, K. H. (2005). Responses of Floating Wind Turbines to Wind and Wave Excitation. Massachusetts Institute of Technology.

Lee, S., Churchfield, M. J., Moriarty, P. J., Jonkman, J., & Michalakes, J. (2013). A Numerical Study of Atmospheric and Wake Turbulence Impacts on Wind Turbine Fatigue Loadings. Journal of Solar Energy Engineering, 135(3). https://doi.org/10.1115/1.4023319

LEE, Y.-L. (2005). 10 - FATIGUE ANALYSIS IN THE FREQUENCY DOMAIN (Y.-L. LEE, J. W. O. PAN, R. B. HATHAWAY, & M. E. B. T.-F. T. and A. BARKEY (eds.); pp. 369–394). Butterworth-Heinemann. https://doi.org/https://doi.org/10.1016/B978-075067719-6/50011-7

Lekou, D. J., & Mouzakis, F. (2009). WT Load Measurement Uncertainty: Load-Based Versus Analytical Strain-Gauge Calibration Method. Journal of Solar Energy Engineering, 131(1). https://doi.org/10.1115/1.3027508

Liao, C., Shi, K., & Zhao, X. (2019). Predicting the Extreme Loads in Power Production of Large Wind Turbines Using an Improved PSO Algorithm. In Applied Sciences (Vol. 9, Issue 3). https://doi.org/10.3390/app9030521

Liu, P, & Barlow, C. Y. (2016). The environmental impact of wind turbine blades. IOP Conference Series: Materials Science and Engineering, 139, 12032. https://doi.org/10.1088/1757-899x/139/1/012032

Liu, Pu, & Barlow, C. Y. (2017). Wind turbine blade waste in 2050. Waste Management, 62, 229–240. https://doi.org/https://doi.org/10.1016/j.wasman.2017.02.007

Liu, Z., Li, Q., Ishihara, T., & Peng, J. (2020). Numerical simulations of fatigue loads on wind turbines operating in wakes. Wind Energy, 23(5), 1301–1316. https://doi.org/https://doi.org/10.1002/we.2487

Loraux, C. T. (2018). Long-term monitoring of existing wind turbine towers and fatigue performance of UHPFRC under compressive stresses. École Polytechnique Fédérale de Lausanne.

Loraux, C., & Brühwiler, E. (2016). The use of long term monitoring data for the extension of the service duration of existing wind turbine support structures. Journal of Physics: Conference Series, 753, 72023. https://doi.org/10.1088/1742-6596/753/7/072023

Lourens, E., Papadimitriou, C., Gillijns, S., Reynders, E., De Roeck, G., & Lombaert, G. (2012). Joint input-response estimation for structural systems based on reduced-order models and vibration data from a limited number of sensors. Mechanical Systems and Signal Processing, 29, 310–327. https://doi.org/https://doi.org/10.1016/j.ymssp.2012.01.011

Lund, E., & Stegmann, J. (2005). On structural optimization of composite shell structures using a discrete constitutive parametrization. Wind Energy, 8(1), 109–124. https://doi.org/https://doi.org/10.1002/we.132

M

M .Klinkov, & Fritzen, C. (2010). Wind load observer for a 5MW wind energy plant. Proceedings of IMAC XXVIII International Modal Analysis Conference.

M. López Aenlle, Hermanns, L., Fernández, P., & Fraile, A. (2013). Stress estimation in a scale model of a symmetric two story building. Proceedings of the 5th International Operational Modal Analysis Conference, IOMAC 2013.

Ma, K.-T., Luo, Y., Kwan, T., & Wu, Y. (2019). Chapter 6 - Fatigue analysis (K.-T. Ma, Y. Luo, T. Kwan, & Y. B. T.-M. S. E. for O. S. Wu (eds.); pp. 115–137). Gulf Professional Publishing. https://doi.org/https://doi.org/10.1016/B978-0-12-818551-3.00006-5

Maes, K. et al. (2016) 'Dynamic strain estimation for fatigue assessment of an offshore monopile wind turbine using filtering and modal expansion algorithms', Mechanical Systems and Signal Processing, 76–77, pp. 592–611. doi: https://doi.org/10.1016/j.ymssp.2016.01.004.

Maes, K., Iliopoulos, A., Weijtjens, W., Devriendt, C., & Lombaert, G. (2016). Dynamic strain estimation for fatigue assessment of an offshore monopile wind turbine using filtering and modal expansion algorithms. Mechanical Systems and Signal Processing, 76–77, 592–611. https://doi.org/https://doi.org/10.1016/j.ymssp.2016.01.004

Maes, K., Smyth, A. W., De Roeck, G., & Lombaert, G. (2016). Joint input-state estimation in structural dynamics. Mechanical Systems and Signal Processing, 70–71, 445–466. https://doi.org/https://doi.org/10.1016/j.ymssp.2015.07.025

Magalhães, F. (2010). Operational Modal Analysis for Testing and Monitoring of Bridges and Special Structures. Faculdade de Engenharia da Universidade do Porto.

Magalhães, F. and Cunha, Á. (2011) 'Explaining operational modal analysis with data from an arch bridge', Mechanical Systems and Signal Processing, pp. 1431–1450. doi: 10.1016/j.ymssp.2010.08.001.

Magalhães, F., Cunha, A. and Caetano, E. (2012) 'Vibration based structural health monitoring of an arch bridge: From automated OMA to damage detection', Mechanical Systems and Signal Processing, 28, pp. 212–228. doi: https://doi.org/10.1016/j.ymssp.2011.06.011.

Mandell, J., & Reed, R. (1992). Fatigue of fiberglass wind turbine blade materials. Sandia National Laboratory Contractor Report: SAND92-7005.

Manwell, J. F., McGowan, J. G., & Rogers, A. L. (2010). Wind Energy Explained: Theory, Design and Application (2nd ed.). John Wiley & Sons.

Marine Insight (2021) ABS Classification Makes 'WindFloat Atlantic' The World's First Classed Offshore Windfarm. Available at: https://www.marineinsight.com/shipping-news/abs-classification-makes-windfloat-atlantic-the-worlds-first-classed-offshore-windfarm/ (Accessed: 16 November 2021).

Marulo, F., Petrone, G., D'Alessandro, V., & Di Lorenzo, E. (2014). Operational modal analysis on a wind turbine blade.

Matsuishi, M., & Endo, T. (1968). Fatigue of metals subjected to varying stress. Proceedings of the Kyushu Branch of Japan Society of Mechanics Engineering, 37–40.

McGugan, M., & Mishnaevsky, L. (2020). Damage Mechanism Based Approach to the Structural Health Monitoring of Wind Turbine Blades. In Coatings (Vol. 10, Issue 12). https://doi.org/10.3390/coatings10121223

McMillan, D., & Ault, G. W. (2007). Quantification of Condition Monitoring Benefit for Offshore Wind Turbines. Wind Engineering, 31(4), 267–285. https://doi.org/10.1260/030952407783123060

Mihailov, S. J. (2012). Fiber Bragg grating sensors for harsh environments. Sensors (Basel, Switzerland), 12(2), 1898–1918. https://doi.org/10.3390/s120201898

Milella, P. P. (2013). Fatigue and Corrosion in Metals. Springer Milan. https://doi.org/10.1007/978-88-470-2336-9

Miner, M. A. (1945). Cumulative Damage in Fatigue. Journal of Applied Mechanics, 12(3), 159–164.

Mishnaevsky Jr., L. (2019). Toolbox for optimizing anti-erosion protective coatings of wind turbine blades: Overview of mechanisms and technical solutions. Wind Energy, 22(11), 1636–1653. https://doi.org/https://doi.org/10.1002/we.2378

Mishnaevsky, L. (2012). Composite materials for wind energy applications: micromechanical modeling and future directions. Computational Mechanics, 50(2), 195–207. https://doi.org/10.1007/s00466-012-0727-5

Mishnaevsky, L. (2019). Repair of wind turbine blades: Review of methods and related computational mechanics problems. Renewable Energy, 140, 828–839. https://doi.org/https://doi.org/10.1016/j.renene.2019.03.113

Mishnaevsky, L. (2021) 'Sustainable End-of-Life Management of Wind Turbine Blades: Overview of Current and Coming Solutions', Materials . doi: 10.3390/ma14051124.

Mishnaevsky, L., Branner, K., Petersen, H. N., Beauson, J., McGugan, M., & Sørensen, B. F. (2017). Materials for Wind Turbine Blades: An Overview. Materials (Basel, Switzerland), 10(11), 1285. https://doi.org/10.3390/ma10111285

Morrison Hershfield Limited. (2012). Wind Turbine Specification Report. HAF Wind Energy Project.

Moutinho, C. and Cunha, Á. (2019) 'Contribution to new solutions of instrumentation of Civil structures for continuous dynamic monitoring', in IX ECCOMAS Thematic Conference on Smart and Materials (SMART 2019). Paris, France: IX ECCOMAS Thematic Conference on Smart and Materials (SMART 2019).

Mouzakis, F., Morfiadakis, E., & Dellaportas, P. (1999). Fatigue loading parameter identification of a wind turbine operating in complex terrain. Journal of Wind Engineering and Industrial Aerodynamics, 82(1), 69–88. https://doi.org/https://doi.org/10.1016/S0167-6105(98)00211-6

Moynihan, B., Moaveni, B., Liberatore, S., & Hines, E. (2022). Estimation of blade forces in wind turbines using blade root strain measurements with OpenFAST verification. Renewable Energy, 184, 662–676. https://doi.org/https://doi.org/10.1016/j.renene.2021.11.094

N

N. W. M. Bishop. (1988). The use of frequency domain parameters to predict structural fatigue [University of Warwick]. http://wrap.warwick.ac.uk/34794/

Nash, R., Nouri, R., & Vasel-Be-Hagh, A. (2021). Wind turbine wake control strategies: A review and concept proposal. Energy Conversion and Management, 245, 114581. https://doi.org/https://doi.org/10.1016/j.enconman.2021.114581

Noppe, N, Weijtjens, W., & Devriendt, C. (2015). Reliable empirical analysis of effects of turbulent air in an operating wind farm based on unreliable SCADA-dat. Poster at EAWE PhD Seminar Stuttgard.

Noppe, Nymfa, Hübler, C., Devriendt, C., & Weijtjens, W. (2020). Validated extrapolation of measured damage within an offshore wind farm using instrumented fleet leaders. Journal of Physics: Conference Series, 1618(2), 22005. https://doi.org/10.1088/1742-6596/1618/2/022005

O

Oliveira, G, Magalhães, F., Cunha, Á., & Caetano, E. (2017). Dynamic monitoring system for utility-scale wind turbines: damage detection and fatigue assessment. Journal of Civil Structural Health Monitoring, 7(5), 657–668. https://doi.org/10.1007/s13349-017-0250-7

Oliveira, G. (2016) Vibration-based structural health monitoring of wind turbines. Faculty of Engineering of the University of Porto. Available at: https://repositorio-aberto.up.pt/handle/10216/83690.

Oliveira, G. et al. (2018a) 'Continuous dynamic monitoring of an onshore wind turbine', Engineering Structures, 164(January), pp. 22–39. doi: 10.1016/j.engstruct.2018.02.030.

Oliveira, G. et al. (2018b) 'Vibration-based damage detection in a wind turbine using 1 year of data', Structural Control and Health Monitoring, 25(11). doi: 10.1002/stc.2238.

Oliveira, G., Magalhães, F., Cunha, Á., & Caetano, E. (2016). Development and implementation of a continuous dynamic monitoring system in a wind turbine. Journal of Civil Structural Health Monitoring, 6(3), 343–353. https://doi.org/10.1007/s13349-016-0182-7

Orifici, A. C., Herszberg, I., & Thomson, R. S. (2008). Review of methodologies for composite material modelling incorporating failure. Composite Structures, 86(1), 194–210. https://doi.org/https://doi.org/10.1016/j.compstruct.2008.03.007

Ortegon, K., Nies, L. F. and Sutherland, J. W. (2013) 'Preparing for end of service life of wind turbines', Journal of Cleaner Production, 39, pp. 191–199. doi: https://doi.org/10.1016/j.jclepro.2012.08.022.

Ovenden, M., Wang, Q., Huang, S., Zhao, W., & Wang, S. (2019). Real-Time Monitoring of Wind Turbine Blade Alignment Using Laser Displacement and Strain Measurement. Journal of Nondestructive Evaluation, Diagnostics and Prognostics of Engineering Systems, 2(3). https://doi.org/10.1115/1.4043850

Owen, M., & Bishop, P. (1974). Prediction of static and fatigue damage and crack propagation in composite materials. In: AGARD Conference Proceedings, Munich, West Germany, 13–19.

P

Palanisamy, R. P., Cho, S., Kim, H., & Sim, S.-H. (2015). Experimental validation of Kalman filter-based strain estimation in structures subjected to non-zero mean input. Smart Structures and Systems, 15(2), 489–503. https://doi.org/https://doi.org/10.12989/sss.2015.15.2.489

Papadimitriou, C., Fritzen, C.-P., Kraemer, P., & Ntotsios, E. (2011). Fatigue predictions in entire body of metallic structures from a limited number of vibration sensors using Kalman filtering. Structural Control and Health Monitoring, 18(5), 554–573. https://doi.org/https://doi.org/10.1002/stc.395

Park, T., Kim, M., Jang, B., Lee, J., & Park, J. (2014). A nonlinear constant life model for the fatigue life prediction of composite structures. Advanced Composite Materials, 23(4), 337–350. https://doi.org/10.1080/09243046.2013.871172

Pedersen, N. L. (2017). On analysis and redesign of bolted L-flanged connections. Wind Energy, 20(6), 1069–1082. https://doi.org/https://doi.org/10.1002/we.2080

Peeters, B. (2000). System Identification and Damage Detection in Civil Engineering. Katholieke Universiteit Leuven.

Peeters, B. et al. (2004) 'The PolyMAX Frequency-Domain Method: A New Standard for Modal Parameter Estimation?', Shock and Vibration, 11, p. 523692. doi: 10.1155/2004/523692.

Pelayo, F. et al. (2011) 'Operational modal analysis of two wind turbines with foundation problems', in 4th International Operational Modal Analysis Conference (IOMAC). Istanbul, Turkey.

Pelayo, F., López-Aenlle, M., Fernández-Canteli, A., & Cantieni, R. (2011). Operational modal analysis of two wind turbines with foundation problems. 4th International Operational Modal Analysis Conference (IOMAC).

Philippidis, T. P., & Vassilopoulos, A. P. (2004). Life prediction methodology for GFRP laminates under spectrum loading. Composites Part A: Applied Science and Manufacturing, 35(6), 657–666. https://doi.org/https://doi.org/10.1016/j.compositesa.2004.02.009

Pimenta, F., Branco, C. M., Teixeira, C. M., & Magalhães, F. (2019). Calibration of onshore wind turbine numerical model using experimental data. 15th EAWE PhD Seminar on Wind Energy.

Pollino, M. C., & Huckelbridge, A. A. (2012). In-situ measurements of fatigue demands on a wind turbine support structure. 2012 IEEE Energytech, 1–5. https://doi.org/10.1109/EnergyTech.2012.6304680

Post, N. (2016). Improving Bending Moment Measurements on Wind Turbine Blades. 2016 Wind Energy Research Workshop, NREL.

Prendergast, L. J., Gavin, K. and Doherty, P. (2015) 'An investigation into the effect of scour on the natural frequency of an offshore wind turbine', Ocean Engineering, 101, pp. 1–11. doi: https://doi.org/10.1016/j.oceaneng.2015.04.017.

R

R., L. Z., & S., L. S. (2006). Force Identification Based on Sensitivity in Time Domain. Journal of Engineering Mechanics, 132(10), 1050–1056. https://doi.org/10.1061/(ASCE)0733-9399(2006)132:10(1050)

Randall, R. B., & Sawalhi, N. (2011). A New Method for Separating Discrete Components from a Signal. Sound and Vibration, 45, 6–9.

Rani, M., Choudhary, P., Krishnan, V., & Zafar, S. (2021). A review on recycling and reuse methods for carbon fiber/glass fiber composites waste from wind turbine blades. Composites Part B: Engineering, 215, 108768. https://doi.org/https://doi.org/10.1016/j.compositesb.2021.108768

Rebelo, C., Veljkovic, M., Matos, R., & Silva, L. S. D. (2012). Structural monitoring of a wind turbine steel tower - Part II: monitoring results. 15(4), 301–311. https://doi.org/https://doi.org/10.12989/WAS.2012.15.4.301

Reder, M. D., Gonzalez, E. and Melero, J. J. (2016) 'Wind Turbine Failures - Tackling current Problems in Failure Data Analysis', Journal of Physics: Conference Series, 753, p. 72027. doi: 10.1088/1742-6596/753/7/072027.

Rice, R. C. (1988). Fatigue design handbook (S. of A. Engineers (ed.)). Society of Automotive Engineers.

Riziotis, V. A., & Voutsinas, S. G. (2000). Fatigue loads on wind turbines of different control strategies operating in complex terrain. Journal of Wind Engineering and Industrial Aerodynamics, 85(3), 211–240. https://doi.org/https://doi.org/10.1016/S0167-6105(99)00127-0

Roger, N. (2006). Fatigue life prediction and strength degradation of wind turbine rotor blade composites. TU Delft.

Rolfes, R., Tsiapoki, S., & Häckell, M. W. (2014). 19 - Sensing solutions for assessing and monitoring wind turbines. In M. L. Wang, J. P. Lynch, & H. B. T.-S. T. for C. I. Sohn (Eds.), Woodhead Publishing Series in Electronic and Optical Materials (Vol. 56, pp. 565–604). Woodhead Publishing. https://doi.org/https://doi.org/10.1533/9781782422433.2.565

Rubiella, C., Hessabi, C. A., & Fallah, A. S. (2018). State of the art in fatigue modelling of composite wind turbine blades. International Journal of Fatigue, 117, 230–245. https://doi.org/https://doi.org/10.1016/j.ijfatigue.2018.07.031

Rychlik, I. (1987). A new definition of the rainflow cycle counting method. International Journal of Fatigue, 9(2), 119–121. https://doi.org/https://doi.org/10.1016/0142-1123(87)90054-5

Rytter, A. (1993). Vibrational Based Inspection of Civil Engineering Structures (Ph.D. Thes). Dept. of Building Technology and Structural Engineering, Aalborg University.

S

Sakellariou, N. (2018) 'Current and potential decommissioning scenarios for end-of-life composite wind blades', Energy Systems, 9(4), pp. 981–1023. doi: 10.1007/s12667-017-0245-9.

Schijve, J. (2003). Fatigue of structures and materials in the 20th century and the state of the art. International Journal of Fatigue, 25(8), 679–702. https://doi.org/https://doi.org/10.1016/S0142-1123(03)00051-3

Schlechtingen, M., & Santos, I. F. (2014). Wind turbine condition monitoring based on SCADA data using normal behavior models. Part 2: Application examples. Applied Soft Computing, 14, 447–460. https://doi.org/https://doi.org/10.1016/j.asoc.2013.09.016

Schroeder, K., Ecke, W., Apitz, J., Lembke, E., & Lenschow, G. (2006). A fibre Bragg grating sensor system monitors operational load in a wind turbine rotor blade. Measurement Science and Technology, 17(5), 1167–1172. https://doi.org/10.1088/0957-0233/17/5/s39

Sedaghatizadeh, N., Arjomandi, M., Kelso, R., Cazzolato, B., & Ghayesh, M. H. (2018). Modelling of wind turbine wake using large eddy simulation. Renewable Energy, 115, 1166–1176. https://doi.org/https://doi.org/10.1016/j.renene.2017.09.017

Shapiro, C. R., Gayme, D. F., & Meneveau, C. (2018). Modelling yawed wind turbine wakes: a lifting line approach. Journal of Fluid Mechanics, 841, R1. https://doi.org/DOI: 10.1017/jfm.2018.75

Siemens Gamesa (2021) 'The winds of change have never been stronger: The SG 14-222 DD', Siemens Gamesa Renewable Energy, S.A.

Smyth, A., & Wu, M. (2007). Multi-rate Kalman filtering for the data fusion of displacement and acceleration response measurements in dynamic system monitoring. Mechanical Systems and Signal Processing, 21(2), 706–723. https://doi.org/https://doi.org/10.1016/j.ymssp.2006.03.005

Sobrinho, M., Pimentel, M., & Magalhães, F. (2021). Monitoring of onshore wind turbine foundation. 17th EAWE PhD Seminar on Wind Energy, Porto, Por.

Söker, H. (1995). Monitoring fatigue loads using cycle counting data acquisition systems. DEWI Magazin, 7, 74–79.

Söker, H. (1996). Determination of Fatigue Loads on Large Wind Turbines. DEWI Magazin, 8, 45–58.

Sørensen, J. D., & Sørensen, J. (2011). Wind Energy Systems: Optimising Design and Construction for Safe and Reliable Operation (Woodhead P). Woodhead Publishing.

Sørensen, S., & Ibsen, L. (2013). Assessment of foundation design for offshore monopiles unprotected against scour. Ocean Engineering, 63, 17–25. https://doi.org/10.1016/j.oceaneng.2013.01.016

Sprague, M., Jonkman, J. M., & Jonkman, B. (2015). FAST Modular Framework for Wind Turbine Simulation: New Algorithms and Numerical Examples. In: Proc. 33rd Wind Energy Symposium.

Sun, H., & Yang, H. (2018). Study on an innovative three-dimensional wind turbine wake model. Applied Energy, 226, 483–493. https://doi.org/https://doi.org/10.1016/j.apenergy.2018.06.027

Sutherland, H. (1996). Frequency Domain Analysis of the Fatigue Loads on Typical Wind Turbine Blades. Journal of Solar Energy Engineering, 118(4), 204–211. https://doi.org/10.1115/1.2871779

Sutherland, H. J. (2000). A summary of the fatigue properties of wind turbine materials. Wind Energy, 3(1), 1–34. https://doi.org/https://doi.org/10.1002/1099-1824(200001/03)3:1<1::AID-WE28>3.0.CO;2-2

T

Tang, M., Chen, W., Zhao, Q., Wu, H., Long, W., Huang, B., Liao, L., & Zhang, K. (2019). Development of an SVR Model for the Fault Diagnosis of Large-Scale Doubly-Fed Wind Turbines Using SCADA Data. In Energies (Vol. 12, Issue 17). https://doi.org/10.3390/en12173396

Tchakoua, P., Wamkeue, R., Ouhrouche, M., Slaoui-Hasnaoui, F., Tameghe, T. A., & Ekemb, G. (2014). Wind Turbine Condition Monitoring: State-of-the-Art Review, New Trends, and Future Challenges. In Energies (Vol. 7, Issue 4). https://doi.org/10.3390/en7042595

Tcherniak, D., & Mølgaard, L. L. (2017). Active vibration-based structural health monitoring system for wind turbine blade: Demonstration on an operating Vestas V27 wind turbine. Structural Health Monitoring, 16(5), 536–550. https://doi.org/10.1177/1475921717722725

Tcherniak, D., Chauhan, S., & Hansen, M. H. (2010). Applicability Limits of Operational Modal Analysis to Operational Wind Turbines. Paper Presented at the XXVIII International Modal Analysis Conference (IMAC), Florida, USA.

Thompson, M. T. (2014). Chapter 14 - Analog Low-Pass Filters (M. T. B. T.-I. A. C. D. (Second E. Thompson (ed.); pp. 531–583). Newnes. https://doi.org/https://doi.org/10.1016/B978-0-12-405866-8.00014-0

Thomsen, K., & Sørensen, P. (1999). Fatigue loads for wind turbines operating in wakes. Journal of Wind Engineering and Industrial Aerodynamics, 80(1), 121–136. https://doi.org/https://doi.org/10.1016/S0167-6105(98)00194-9

Turan Dirlik. (1985). Application of computers in fatigue analysis [University of Warwick]. http://wrap.warwick.ac.uk/2949/

U

UNFCCC (2015) Adoption of the Paris Agreement., United Nations Framework Convention on Climate Change. Paris, France.

V

van Kuik, G. A. M., Peinke, J., Nijssen, R., Lekou, D., Mann, J., Sørensen, J. N., Ferreira, C., van Wingerden, J. W., Schlipf, D., Gebraad, P., Polinder, H., Abrahamsen, A., van Bussel, G. J. W., Sørensen, J. D., Tavner, P., Bottasso, C. L., Muskulus, M., Matha, D., Lindeboom, H. J., … Skytte, K. (2016). Long-term research challenges in wind energy a research agenda by the European Academy of Wind Energy. Wind Energy Science, 1(1), 1–39. https://doi.org/10.5194/wes-1-1-2016

Van Overschee, P. and De Moor, B. (1996) 'Subspace identification for linear systems. Theory, implementation, applications. Incl. 1 disk', in Springer Science & Business Media, p. xiv + 254. doi: 10.1007/978-1-4613-0465-4.

Vasel-Be-Hagh, A., & Archer, C. L. (2017). Wind farms with counter-rotating wind turbines. Sustainable Energy Technologies and Assessments, 24, 19–30. https://doi.org/https://doi.org/10.1016/j.seta.2016.10.004

Veers, P. S., Ashwill, T. D., Sutherland, H. J., Laird, D. L., Lobitz, D. W., Griffin, D. A., Mandell, J. F., Musial, W. D., Jackson, K., Zuteck, M., Miravete, A., Tsai, S. W., & Richmond, J. L. (2003). Trends in the Design, Manufacture and Evaluation of Wind Turbine Blades. Wind Energy, 6(3), 245–259. https://doi.org/https://doi.org/10.1002/we.90

Veljkovic, M., Feldmann, M., Naumes, J., Pak, D., Simões, L., da Silva, & Rebelo, C. (2011). 9 - Wind turbine tower design, erection and maintenance. In John D Sørensen & J. N. B. T.-W. E. S. Sørensen (Eds.), Woodhead Publishing Series in Energy (pp. 274–300). Woodhead Publishing. https://doi.org/https://doi.org/10.1533/9780857090638.2.274

Vera-Tudela, L., & Kühn, M. (2017). Analysing wind turbine fatigue load prediction: The impact of wind farm flow conditions. Renewable Energy, 107, 352–360. https://doi.org/https://doi.org/10.1016/j.renene.2017.01.065

Verein Deutscher Ingenieure. (2015). Systematic calculation of highly stressed bolted joints- Joints with one cylindrical bolt (VDI guidel). VDI MANUALS.

Vermeer, L. J., Sørensen, J. N., & Crespo, A. (2003). Wind turbine wake aerodynamics. Progress in Aerospace Sciences, 39(6), 467–510. https://doi.org/https://doi.org/10.1016/S0376-0421(03)00078-2

W

Wagner, H.-J. (2020). Introduction to wind energy systems. EPJ Web Conf., 246. https://doi.org/10.1051/epjconf/202024600004

Walford, C. A. (2006) Wind turbine reliability :understanding and minimizing wind turbine operation and maintenance costs. United States. doi: 10.2172/882048.

Weijtens, W., Noppe, N., Verbelen, T., Iliopoulos, A., & Devriendt, C. (2016). Offshore wind turbine foundation monitoring, extrapolating fatigue measurements from fleet leaders to the entire wind farm. Journal of Physics: Conference Series, 753, 92018. https://doi.org/10.1088/1742-6596/753/9/092018

Weijtjens, W., Noppe, N., Verbelen, T., & Devriendt, C. (2016). Fleet-wise structural health monitoring of (offshore) wind turbine foundations. In Proceedings of the 8th EuropeanWorkshop on Structural Health Monitoring, 5–8.

Weipao, M., Chun, L., Jun, Y., Yang, Y., & Xiaoyun, X. (2016). Numerical Investigation of Wake Control Strategies for Maximizing the Power Generation of Wind Farm. Journal of Solar Energy Engineering, 138(3). https://doi.org/10.1115/1.4033110

WindEurope (2018) Wind in Power 2017: Annual combined onshore and offshore wind energy statistics. Brussels, Belgium.

WindEurope (2021) Wind energy in Europe 2020 Statistics and the outlook for 2021-2025. Brussels, Belgium.

WindEurope (2022) Wind Energy in Europe 2021 Statistics and the outlook for 2022-2026. Brussels, Belgium.

Wöhler, A. (1860). Versuche zur Ermittlung der auf die Eisenbahnwagenachsen einwirkenden Kräfte und die Widerstandsfähigkeit der Wagen-Achsen. Zeitschrift Für Bauwesen, 10(1860), 160–161.

Worden, K., Farrar, C. R., Manson, G., & Park, G. (2007). The fundamental axioms of structural health monitoring. Proceedings of the Royal Society A: Mathematical, Physical and Engineering Sciences, 463(2082), 1639–1664. https://doi.org/10.1098/rspa.2007.1834

Wymore, M. L., Van Dam, J. E., Ceylan, H., & Qiao, D. (2015). A survey of health monitoring systems for wind turbines. Renewable and Sustainable Energy Reviews, 52, 976–990. https://doi.org/https://doi.org/10.1016/j.rser.2015.07.110

Y

Yang, W., Tavner, P. J., Crabtree, C. J., & Wilkinson, M. (2010). Cost-effective condition monitoring for wind turbines. IEEE Transactions on Industrial Electronics, 57(1), 263–271. https://doi.org/10.1109/TIE.2009.2032202

Yang, W., Tavner, P. J., Crabtree, C. J., Feng, Y., & Qiu, Y. (2014). Wind turbine condition monitoring: technical and commercial challenges. Wind Energy, 17(5), 673–693. https://doi.org/https://doi.org/10.1002/we.1508

Yin, S., & Yu, F. T. S. (2002). Fiber Optic Sensors. CRC Press. https://doi.org/10.1201/9780824744571

Z

Zhao, W., & Baker, M. J. (1992). On the probability density function of rainflow stress range for stationary Gaussian processes. International Journal of Fatigue, 14(2), 121–135. https://doi.org/https://doi.org/10.1016/0142-1123(92)90088-T

Zuo, P., Srinivasan, D. V, & Vassilopoulos, A. P. (2021). Review of hybrid composites fatigue. Composite Structures, 274, 114358. https://doi.org/https://doi.org/10.1016/j.compstruct.2021.114358

Zwick, D., & Muskulus, M. (2015). The simulation error caused by input loading variability in offshore wind turbine structural analysis. Wind Energy, 18(8), 1421–1432. https://doi.org/https://doi.org/10.1002/we.1767